

# **Improvements to MOS CCD Technology for Future X-ray Astronomy Missions**

Thesis submitted for the degree of

Doctor of Philosophy

at Brunel University

by

Neil John Murray

Imaging for Space and Terrestrial Applications Group

School of Engineering and Design

Brunel University

19<sup>th</sup> August 2008

# Improvements to MOS CCD Technology for Future X-ray Astronomy Missions

Neil John Murray

## Abstract

This thesis is concerned with the development of MOS charge-coupled device (CCD) technology for future applications in X-ray astronomy. Of particular interest is increased detection efficiency of high energy X-ray photons and increased pixel readout speed for large area sensors. Chapter 2 reviews the generation of X-rays, methods for extra-terrestrial X-ray observations, detectors and provides an overview of X-ray astronomy missions. Chapter 3 discusses the CCD and introduces some of the recent technological developments that improve their overall performance for optical and X-ray photon detection. Chapter 4 presents the basic laboratory equipment and methods used to carry out the experimental work of this thesis. Chapter 5 presents the characterisation of new high resistivity devices that were manufactured by e2v technologies during the work of this thesis. Chapter 6 describes a method for estimating the depletion depth of a CCD by analysing the X-ray event patterns that are generated in CCD image data. Chapter 7 presents the equipment developed and experimental measurements taken to evaluate the high energy X-ray quantum efficiency of a high resistivity CCD. Finally, Chapter 8 describes the ongoing development and characterisation of low noise ASICs that are intended for use in future X-ray astronomy missions.

## Declaration

I hereby declare that no part of this thesis has been previously submitted to this or any other university as part of the requirement for a higher degree. The work described herein was conducted solely by the undersigned except for those colleagues and other workers acknowledged in the text.

Neil John Murray

19<sup>th</sup> August 2008

## Dedication

To my mother, father and my love.

## Acknowledgements

I would like to acknowledge quite a lot of people for their help and encouragement over the duration of my thesis work.

Thanks to my supervisors Andrew Holland and Peter Pool for their guidance and technical support.

Thanks to Chris Castelli, Adrian Martin and David Burt for imparting fractions of their vast knowledge and experiences on me.

Thanks to the remaining ISTA members, Ian Hutchinson, Richard Ingley, John Osmond, David Simpson, Gopal Jeyesundra, George Seabroke, Jordi Calafell, Thomas Greig, Amir Intisar, Jason Gow, David Hall and Billy Kinchin, who provided friendship and entertainment for some, if not all, of my time in the group.

Thanks to Mohamed Abdelrazik for suggesting the PhD way back in 2004.

Thanks to Les Botwright, Paul Mardle, Linda Paul, Tony Wood, Michael Latteo, Tony Morris, Iran Adil-Smith and last but not least Nigel Fudge for all their help and good deeds around campus during my time at Brunel.

Thanks to Rob Sareen, Bob Daniel, Greg Bale, Andrew Pike, John Kemp, Paul Jorden and Pritesh Mistry at e2v technologies for their help with devices, equipment and information.

I would like to gratefully acknowledge the financial support received from the Science and Technology Facilities Council and e2v technologies during my research studentship.

Finally, a big thank you to David Smith for his continued enthusiasm, friendship and support with my work, teaching me to write better English, checking I have used the correct fonts and offering timely distractions with his endless conversations about film and video games (and BBC news article links via MSN).

## Contents

<b>Abstract</b>	ii
<b>Declaration</b>	iii
<b>Dedication</b>	iv
<b>Acknowledgements</b> .....	iv
Chapter 1: Introduction .....	8
1.1 X-ray astronomy.....	8
1.2 Research goals .....	8
1.3 Thesis organisation .....	9
1.4 Publications.....	11
1.5 References .....	11
Chapter 2: X-ray physics and astronomy .....	12
2.1 Introduction .....	12
2.2 X-ray sources.....	13
2.2.1 The X-ray tube.....	13
2.2.2 Synchrotron Light.....	15
2.2.3 Radioactive decay .....	17
2.2.4 Thermal excitation .....	17
2.3 X-ray astronomy.....	17
2.3.1 Detection platforms.....	17
2.3.2 X-ray telescopes .....	19
2.4 X-ray Detectors .....	22
2.4.1 Scintillation.....	23
2.4.2 Geiger-Müller / Ionisation tube .....	24
2.4.3 Proportional/gas counter.....	24
2.4.4 Micro channel plate (MCP) .....	24
2.4.5 Bolometer/calorimeters .....	25

2.4.6	Transition edge sensor (TES).....	25
2.4.7	Charge-coupled device (CCD).....	26
2.5	CCD based X-ray missions .....	26
2.5.1	XMM-Newton .....	26
2.5.2	XEUS .....	28
2.6	Summary .....	31
2.7	References .....	31
Chapter 3:	The charge-coupled device .....	35
3.1	Introduction .....	35
3.2	Charge generation.....	37
3.2.1	The photoelectric effect.....	37
3.2.2	Photon absorption .....	39
3.2.3	Charge diffusion .....	40
3.2.4	Quantum efficiency.....	42
3.2.5	QE Enhancements .....	43
3.3	Charge storage .....	46
3.3.1	The pixel structure .....	46
3.3.2	The buried-channel .....	47
3.3.3	The potential well model .....	48
3.4	Charge Transfer.....	49
3.4.1	Moving charge .....	49
3.4.2	Charge trapping.....	53
3.4.3	Frame transfer architecture.....	54
3.5	Signal Measurement .....	55
3.5.1	The output node capacitor .....	55
3.5.2	The output circuit.....	55
3.5.3	Multi-stage output amplifiers .....	57
3.6	Noise sources .....	58

3.6.1	Dark current .....	58
3.6.2	Reset noise .....	59
3.6.3	Cosmetic defects .....	59
3.6.4	Cosmic rays .....	59
3.7	Summary .....	60
3.8	References .....	61
Chapter 4:	Instrumentation, equipment and techniques.....	63
4.1	Introduction .....	63
4.2	Camera system.....	63
4.2.1	Clock sequencing.....	63
4.2.2	Clock and bias voltages .....	67
4.2.3	Image pixels, under/over-scan and pixel binning .....	67
4.2.4	CCD image acquisition.....	69
4.3	Laboratory equipment .....	71
4.3.1	X-ray sources .....	71
4.3.2	Cooling .....	72
4.3.3	Evacuation.....	74
4.3.4	Light shielding .....	76
4.4	Noise reduction.....	76
4.4.1	Filtering .....	76
4.4.2	Output pre-amplification .....	78
4.4.3	Correlated double sampling.....	79
4.4.4	Common mode rejection .....	82
4.5	Device characterisation.....	83
4.5.1	System noise calibration .....	83
4.5.2	Responsivity .....	84
4.6	X-ray events .....	84
4.7	Summary .....	85

4.8	References .....	86
Chapter 5:	Electro-optic characterisation of high resistivity CCDs .....	88
5.1	Introduction .....	88
5.2	The 'high-rho' CCD217 and CCD247 .....	88
5.3	Experimental Setup.....	90
5.3.1	Camera setup .....	90
5.3.2	X-ray source .....	92
5.4	Test results.....	94
5.4.1	Leakage and cosmetic quality .....	94
5.4.2	Anomalous charge injection .....	95
5.5	X-ray measurements.....	96
5.5.1	XRF Spectrum .....	96
5.5.2	Output node responsivity .....	97
5.5.3	Noise performance .....	99
5.5.4	Spectral resolution .....	101
5.6	Problems and observations .....	101
5.6.1	Pixel size .....	101
5.6.2	Cosmic events .....	102
5.6.3	Serial register events.....	102
5.6.4	XRF angle of incidence .....	103
5.6.5	Package isolation.....	104
5.7	p-Channel (CCD227) testing.....	104
5.8	Conclusions .....	106
5.8.1	CCD217 Design .....	106
5.8.2	CCD247 Design .....	107
5.8.3	p-Channel .....	107
5.9	Further work .....	108
5.10	References .....	108

Chapter 6:	Depletion depth modelling & estimates by event analysis .....	110
6.1	Introduction .....	110
6.2	Measurement methods .....	111
6.2.1	High energy ionising particle analysis .....	111
6.2.2	X-ray spread event analysis.....	111
6.2.3	Quantum efficiency model fitting.....	112
6.3	The depletion model.....	112
6.3.1	Calculations.....	112
6.3.2	Average depletion driving potential .....	113
6.3.3	Potential profile .....	114
6.3.4	Depletion depth .....	115
6.4	Front illuminated CCD photon transmission model .....	116
6.5	X-ray split events.....	119
6.5.1	Location of ionisation (location) .....	119
6.5.2	Size of e-h cloud (size).....	120
6.5.3	Charge diffusion to collection (distance) .....	121
6.6	Depletion depth estimate method .....	121
6.7	Event counting .....	122
6.8	Results.....	123
6.8.1	Errors.....	123
6.8.2	Depletion boundary estimate example .....	124
6.8.3	Estimates.....	124
6.9	Depletion depth uniformity .....	125
6.10	Conclusions .....	127
6.11	Further work .....	128
6.12	References .....	128
Chapter 7:	X-ray quantum efficiency modelling & measurements .....	129
7.1	Introduction .....	129

7.2	Front illuminated CCD247 QE model .....	130
7.3	The QE measurement facility.....	131
7.3.1	Possible QE measurement chamber designs.....	132
7.3.2	The SiLi reference detector.....	133
7.3.3	The design .....	135
7.3.4	The X-ray source .....	138
7.3.5	Radiation safety .....	139
7.4	Method .....	140
7.4.1	Data acquisition .....	141
7.4.2	Data processing.....	141
7.4.3	Errors.....	143
7.5	Results.....	144
7.6	Conclusions .....	145
7.7	Further work .....	145
7.8	References .....	146
Chapter 8:	High throughput video processing ASICs .....	147
8.1	Introduction .....	147
8.1.1	High pixel throughput .....	147
8.1.2	Multiple readout channels.....	148
8.1.3	Reduced mass .....	149
8.1.4	Reduced power consumption .....	150
8.1.5	Reduced noise through layout.....	150
8.1.6	Reduced noise through CDS.....	150
8.2	The 2-channel CDS ASIC .....	151
8.2.1	Testing and results .....	153
8.3	The 4-channel CDS ASIC .....	153
8.3.1	Initial 4-channel CDS ASIC Evaluation board.....	157
8.3.2	Initial setup .....	158

8.3.3	Operation .....	159
8.3.4	Data acquisition and processing .....	161
8.3.5	Channel cross-talk evaluation .....	163
8.3.6	Noise contribution .....	165
8.4	Conclusions .....	166
8.5	Further work .....	167
8.6	References .....	169
Chapter 9:	Conclusions and further work .....	170
9.1	Electro-optic characterisation of high resistivity CCDs .....	170
9.2	Depletion depth modelling and estimates by event analysis .....	171
9.3	X-ray quantum efficiency modelling and measurements .....	172
9.4	High throughput video processing ASICs .....	173

## Chapter 1: Introduction

### 1.1 X-ray astronomy

X-rays occupy the shorter, ionising, wavelengths ( $10^{-8}$  to  $10^{-11}$  m) of the electromagnetic spectrum and are produced by the most energetic cosmological events and travel through the Universe with low attenuation by the inter-galactic/stellar medium. X-rays arriving from distant objects can be imaged to give a visible representation of their source that it is not possible to see in the optical. The energies of X-ray photons can be measured to ascertain the nature of the source from its characteristic energy lines and continuum (density/temperature). Recording the arrival times of X-ray photons, it is possible to determine variable emission, such as that emitted from an X-ray pulsar. Like the Sun, other stars in the universe emit X-rays because of their high surface temperature. Some of the more dense objects, such as white dwarfs and black holes, can also produce X-rays by pulling matter into them from companion stars. The strong gravitational force of the dense star pulls matter in that is accelerated and heated, eventually becoming hot enough to emit X-rays. Neutron stars and accretion-powered pulsars can produce X-rays by the acceleration of charged particles about their strong magnetic field. Other events in the life time of a star can also produce thermally emitted X-rays, such as the explosive force of a supernova, or the superheating of matter as it is pulled in towards the event horizon of a black hole [Gorenstein & Zombeck 1990].

One of the key questions scientists and astronomers wish to address is the evolution of the Universe. The observation of X-rays can help to answer this question by probing regions of high temperature or strong gravity.

The advantages of CCDs for astronomy have long been recognised since the launch of the Galileo mission in 1989 and the launch of the Hubble Space Telescope (HST) in 1990. In more recent times, major advances in charge-coupled device technology have led to larger imaging areas, smaller pixels, increased detection efficiency, higher pixel throughput and lower noise. Of all these improvements, increased detection efficiency and lower noise being the most important to X-ray astronomy [Lumb et al 1990].

### 1.2 Research goals

The work carried out for this thesis comprises of two themes relevant to the improvement of metal oxide semiconductor (MOS) CCD technology for future X-ray astronomy missions. Two studies evaluated recent developments in the manufacture of deep depletion CCDs at e2v

technologies using high resistivity bulk silicon. In the first study a method was developed to provide estimates of the thickness of the depletion depth for the CCD217 and CCD247 by X-ray analysis when operating at various substrate potentials. This was particularly desirable to e2v to provide corroborative measurements to their own Modulation Transfer Function (MTF) analyses, demonstrating the ability to fully deplete the 100  $\mu\text{m}$  back thinned variants of high resistivity CCD manufactured for infra-red astronomy applications. With the increased thickness of device depletion depth required for infra-red applications, comes increased detection efficiency for X-ray photons, offering benefits to X-ray astronomy in terms of energy spectroscopy. The second study provided quantum efficiency measurements of the high resistivity devices to demonstrate the increased detection efficiency of deep depletion CCDs for high energy photons compared with standard resistivity CCDs.

A third study was to evaluate recent developments in Application Specific Integrated Circuit (ASIC) technology made by Brunel University in collaboration with the Science and Technology Facilities Council (STFC), for low noise, multi-channel X-ray applications. This included measuring the additional noise component of the ASIC to the camera system and assessing the cross-talk between parallel processing channels.

The work carried out for this thesis was funded by a Co-operative Award in Science and Engineering (CASE) studentship from STFC in collaboration with e2v technologies of Chelmsford, Essex, UK.

### 1.3 Thesis organisation

This thesis is organised into nine chapters including this introduction. Chapter 2 reviews the generation of X-rays with particular reference to the electrical X-ray tube that enables the widespread application of X-rays. The technology developed to facilitate the acquisition of X-ray data from astronomical sources is discussed with particular reference to the CCD that has revolutionised X-ray astronomy in the last 20 years. Overviews of the European Space Agency's (ESA) current and future X-ray astronomy missions are reviewed, including discussion of the key improvements to MOS CCD technology that would be beneficial to the proposed X-ray Evolving Universe Spectroscopy (XEUS) mission [Gondoin et al 2008].

Chapter 3 describes how the buried channel CCD works, how charge is generated from incoming photons, collected within the pixel structures and transferred to the serial output circuit. The requirement of deeper depletion depth to increase the detection efficiency at higher energy and longer wavelength is discussed. Improvements to output circuit design

are also reviewed, to allow increased pixel throughput for large area CCDs. Common CCD noise sources are discussed including, dark current, reset noise, cosmetic defects and cosmic rays.

Chapter 4 presents an overview of the laboratory equipment and methods used to operate and characterise the performance of CCDs for this thesis work. This includes: the camera system electronics that drive the CCD, two methods of image acquisition, X-ray sources and cryogenic equipment for minimising the dark current. Four basic techniques for noise reduction are discussed, including low pass filtering, pre-amplification of the output, correlated double sampling and common mode rejection. Methods are presented to measure the system noise and output responsivity. Finally, the patterns observed in a CCD image generated by X-ray photons are described.

Chapter 5 presents the design and general characterisation of the new CCDs manufactured by e2v technologies that have been fabricated on high resistivity bulk silicon. The basic laboratory setup is described including the electrical connections to the CCDs and the method of generating X-ray photons for spectroscopy. Analysis of cosmetic quality and leakage current, measurements of output amplifier responsivity, noise and spectral resolution are also presented. Finally, a p-channel variant of the high resistivity device is described along with the modifications made to the laboratory equipment to perform the initial testing of the device.

Chapter 6 describes three methods of estimating the depletion depth of high resistivity CCDs using high energy photons. The experimental setup is presented to provide depletion depth estimates of the CCD using the X-ray spread event analysis method. Software developed to recognise and count the different types of X-ray events generated in the CCD image is described, enabling the fraction of photons absorbed beyond the depletion depth to be approximated. Models of the electrostatic potential and X-ray photon transmission are presented for the CCD pixel structure that allow estimates to be made on the device's depletion depth based on the event statistics.

Chapter 7 reviews the existing methods for making quantum efficiency measurements of a CCD using a calibrated reference detector. The SiLi reference detector is introduced that will be used to provide the flux measurement, due to its  $\sim 100\%$  collection efficiency at the X-ray energy range of interest (6 keV to 20 keV). A new test facility design is then presented to satisfy the requirement to have minimal spatial and temporal displacement between measurements whilst accommodating the SiLi detector and ensuring the safe use of X-rays.

The experimental procedure and data analysis methods are then described, including the anticipated errors on the measurements. Finally, results are presented for X-ray photons of energies between 8,047 eV to 17,478 eV.

Chapter 8 describes the ongoing work that is being undertaken in collaboration with STFC (RAL) into the development of ASICs for the low noise readout of X-ray CCDs. The benefits of ASIC technology to future X-ray astronomy missions are discussed, including: higher pixel throughput, concurrent processing of multiple video channels, reduced mass, reduced power consumption and in particular reduced noise. The design and testing of an early two channel ASIC design is reviewed before the development of test equipment is then presented to enable the characterisation of a four video channel ASIC in terms of channel isolation and noise. Finally, results are presented; highlighting the suitability of such technology to future X-ray CCD based astronomy missions.

The final chapter, Chapter 9, recounts the main conclusions arising from the work of this thesis and assess the possible directions for further work that could be undertaken.

## 1.4 Publications

Some of the results in this thesis are contained within the following publications.

Jorden, P. et al., 2006. Commercialisation of full depletion scientific CCDs. *Proc. SPIE*, Vol. 6276. [Chapter 5]

**Murray, N.J.** et al., 2007. High-throughput video processing ASICs for X-ray CCDs. *Proc. SPIE*, Vol. 6686. [Chapter 8]

**Murray, N.J.** et al., 2008. The X-ray performance of high resistivity (high-rho) scientific CCDs. *Proc. SPIE*, Vol. 7021. [Chapter 5,6 & 7]

**Murray, N.J.** et al., 2008. The X-ray quantum efficiency measurement of high resistivity CCDs. *Nuc. Inst. And Meth.*, Vol. A. [Chapter 7]

## 1.5 References

Gorenstein, P. & Zombeck, M., 1990. High resolution X-ray spectroscopy of cosmic plasmas. *Proc. IAU Colloquium*, 115.

Lumb, D.H. et al., 1990. Applications of charge-coupled devices to X-ray astrophysics missions. *Nuclear Instruments and Methods*, Vol. A288, p. 219-226.

Gondoin P. et al., 2008. Overview of ESA study activities on XEUS. *Proc. SPIE*, Vol. 7011.

## Chapter 2: X-ray physics and astronomy

### 2.1 Introduction

X-rays were discovered by accident in 1895 by Wilhelm Röntgen, who observed that his cathode ray generator could cause a barium platinocyanide screen to fluoresce without the interaction of visible photons. Röntgen won the Nobel Prize for physics in 1901 for experimenting with the transmission properties of these phenomena through various materials [Röntgen 1896]. It was not until 1923 that Arthur H. Compton confirmed that these were photons by demonstrating that these rays could be reflected at glancing angles by polished surfaces. Compton also won a Nobel Prize in 1927 for the discovery of the interaction between X-ray photons and electrons, now known as Compton Scattering [Compton 1923].

X-rays occupy the shorter, ionising, wavelengths ( $10^{-8}$  m to  $10^{-11}$  m) of the electromagnetic spectrum shown in Figure 2.1.

<i>Band</i>	<i>Radio</i>	<i>Microwave</i>	<i>IR</i>	<i>Visible</i>	<i>UV</i>	<i>X-ray</i>	<i>Gamma-ray</i>
<b>Temp (°K)</b>		$1 \times 10^0$	$1 \times 10^1$	$1 \times 10^3$		$1 \times 10^6$	$1 \times 10^9$
<b>Frequency (Hz)</b>	$3 \times 10^8$ $3 \times 10^9$	$3 \times 10^{10}$ $3 \times 10^{11}$	$3 \times 10^{12}$ $3 \times 10^{13}$	$3 \times 10^{14}$ $3 \times 10^{15}$	$3 \times 10^{16}$ $3 \times 10^{17}$	$3 \times 10^{18}$ $3 \times 10^{19}$	$3 \times 10^{20}$
<b>Wavelength (m)</b>	$1 \times 10^0$ $1 \times 10^{-1}$	$1 \times 10^{-2}$ $1 \times 10^{-3}$	$1 \times 10^{-4}$ $1 \times 10^{-5}$	$1 \times 10^{-6}$ $1 \times 10^{-7}$	$1 \times 10^{-8}$ $1 \times 10^{-9}$	$1 \times 10^{-10}$ $1 \times 10^{-11}$	$1 \times 10^{-12}$
<b>Energy (eV)</b>	$1 \times 10^{-6}$ $1 \times 10^{-5}$	$1 \times 10^{-4}$ $1 \times 10^{-3}$	$1 \times 10^{-2}$ $1 \times 10^{-1}$	$1 \times 10^0$ $1 \times 10^1$	$1 \times 10^2$ $1 \times 10^3$	$1 \times 10^4$ $1 \times 10^5$	$1 \times 10^6$

**Figure 2.1** The electromagnetic spectrum

This chapter reviews the sources of X-ray photons from both manmade and natural phenomena that are available for laboratory use. The technologies developed to enable X-ray astronomy are reviewed, including the instruments employed to detect X-rays. These instruments include detectors based on:

- Scintillation
- Ionisation tubes
- Proportional counters
- The micro channel plate (MCP)
- Calorimeters
- Transition edge sensors (TES)
- The charge-coupled device (CCD)

The achievement of the science goals of the European Space Agency's (ESA) XMM-Newton observatory is briefly reviewed in Section 2.5, with particular reference to the MOS CCD technology that was developed in the UK for the mission. ESA's proposed follow up mission to XMM-Newton, XEUS (X-ray Evolving Universe Spectroscopy) is also discussed in Section 2.5, that seeks to improve upon the detection sensitivity of XMM-Newton by 100 times. Further advancements in MOS CCD technology are required to achieve increased sensitivity aims of XEUS and some of these developments form the basis of this thesis.

## 2.2 X-ray sources

X-ray photons can be generated by two methods; accelerating an electrical charge or by the quantum transition of energy states in a charged particle either by electromagnetic radioactive decay or thermal excitation. In the first method the X-ray generator must provide a source of free unbound electrons and an electric field to accelerate them [Sokolov & Ternov 1967]. The electrical generation of X-rays has a major safety advantage over radioactive decay and hot body sources for laboratory use as the source can be deactivated immediately by switching it off.

### 2.2.1 The X-ray tube

The X-ray tube as shown in Figure 2.2 is the most common method of electrical X-ray production due to its simplicity.

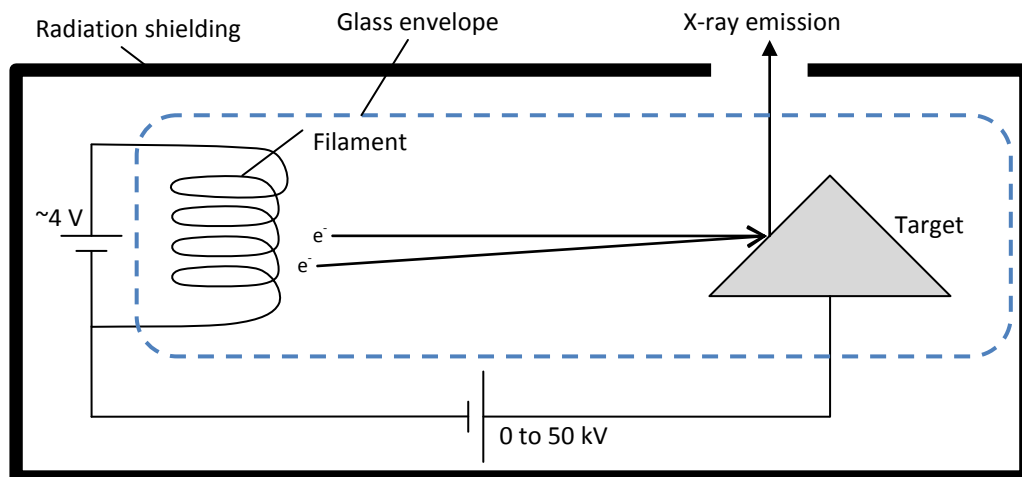


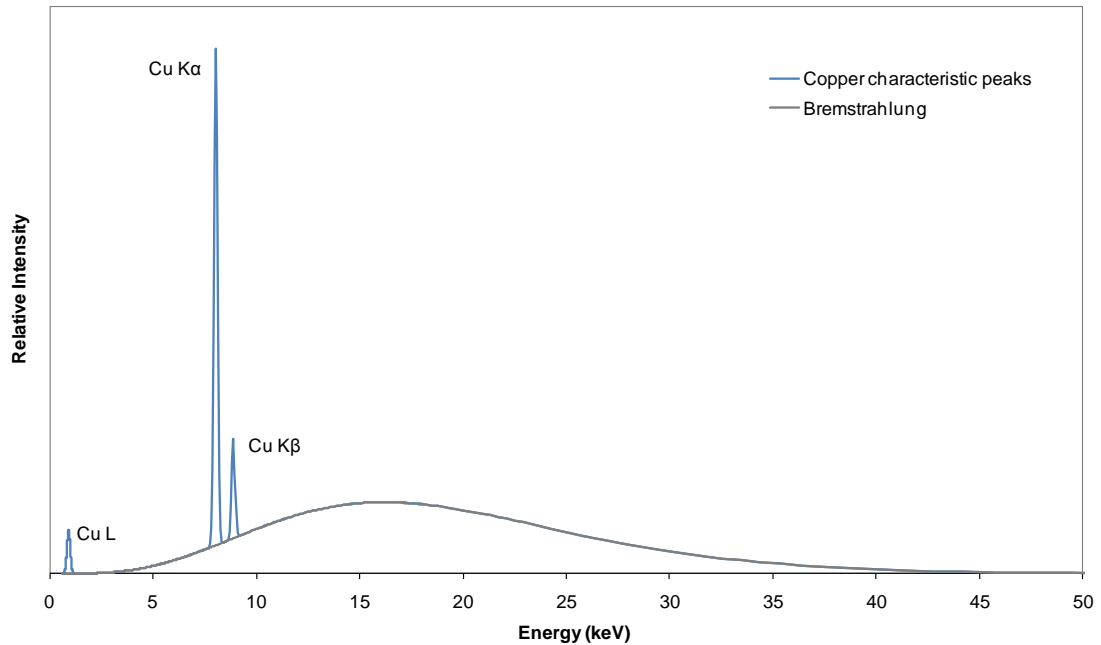
**Figure 2.2** Schematic of an electric X-ray generator tube

An evacuated tube houses a wire filament that passes an electric current that heats up and emits electrons. The vacuum ensures there is no oxygen present to oxidise the filament. The current flowing through the filament determines the number of electrons that are produced and hence the X-ray flux. These electrons are accelerated by an electric field towards an

anode target. The point of interaction of the electrons with the target can generate a large amount of thermal energy [Brown 1975].

The electron can interact with the target material by two methods to produce X-ray radiation. Firstly, the most commonly occurring method, the incident electron passes close to and is deflected by the nucleus of the atom. This deflection causes the electron to not only change direction but to lose kinetic energy by emitting a photon of an unknown energy. This electron then continues on through the target material until it encounters another atom and loses more kinetic energy, slowing down, producing another X-ray photon of unknown energy. This method of radiation is termed *Bremsstrahlung*, coming from the German translations *brems* (brake) and *strahlung* (radiation) [Young & Freedman 1996]. The severity of each interaction varies with the position of the incident electron to the nucleus and therefore the X-ray photon emission spectrum is continuous up to the maximum applied field energy. That is a maximum energy photon is created for a head on collision with the nucleus, where upon all kinetic energy is lost in the first interaction. The majority of photons will be emitted over a number of atomic interactions, when the electron passes close to the nucleus. The peak energy intensity, ignoring any characteristic peaks caused by K-shell emissions from the target, is roughly 1/3 of the maximum energy and can be seen in Figure 2.3 [Knoll 2000].

In the second instance, the incident electron can directly displace an orbital electron in the atoms target material; this vacancy is immediately filled by an electron from a higher orbit shell. The difference in binding energies between the two shells is released as an X-ray photon or Auger electrons. The energy of an X-ray photon released is characteristic of the atomic element due to the uniqueness of the atomic binding energies [Bearden 1967]. The emission of X-ray photons by this process is known as X-ray fluorescence (XRF). The characteristic nature of photon emission enables a target material to be chosen to provide a desirable X-ray photon energy peak above that of the continuous *Bremsstrahlung* output.



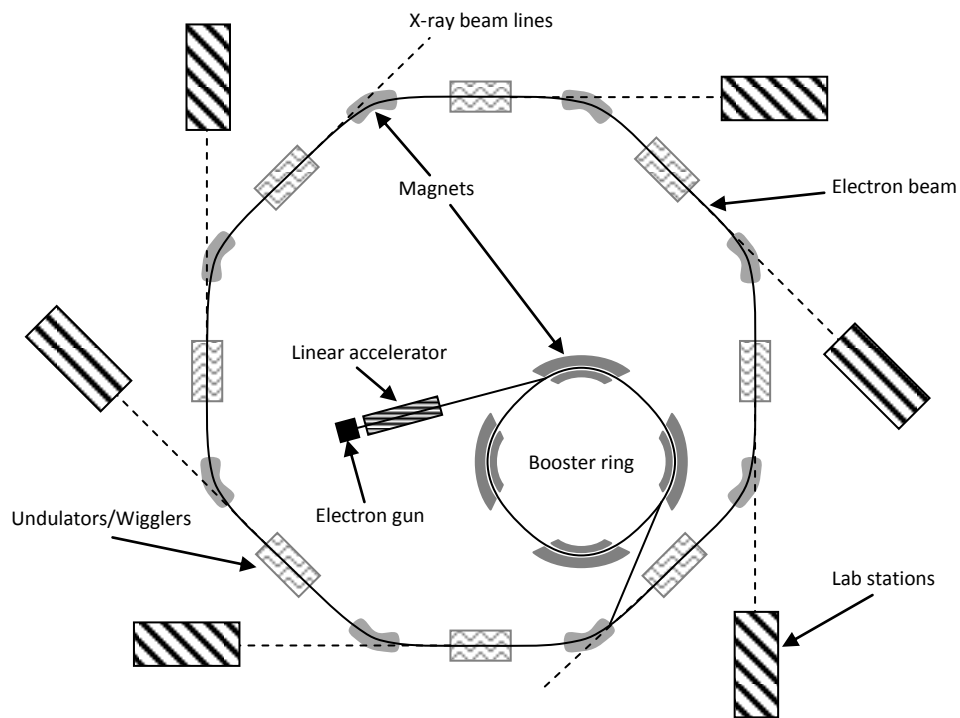
**Figure 2.3** X-ray tube output energy spectrum

Figure 2.3 shows the radiation produced by a 50 kV field using a copper target anode. There is a 1:1 relationship between the accelerating field potential and the kinetic energy gained by the electron where maximum energy transfer equals the accelerating potential, therefore the x-axis of Figure 2.3 is given in electron Volts (eV). Using a copper target for the anode there are clear radiation intensity peaks above that of the Bremsstrahlung spectrum at the two atomic K-shell edges at 8,047 eV and 8,904 eV and at the L-shell at 928 eV. The fluorescence yield for L-shell emission is very low ( $\sim 8\%$ ) relative to the K-shell emissions [Krause 1979].

### 2.2.2 Synchrotron Light

An alternative electrical production of X-ray photons is with a synchrotron facility, shown in Figure 2.4. Electrons are produced in an electron gun by a current flowing through an element that are then accelerated through a pinhole by an electric field. The velocity of the electrons is then increased further towards the speed of light in a linear accelerator by modulation with radio and microwaves. A series of magnetic elements direct the electron beam to travel in a circle around the booster ring. Further electromagnetic energy is imparted onto the electrons in the booster ring to increase their kinetic energy to 1.5 GeV to 2.9 GeV. The electron beam is fed into a larger storage ring that again channels the electrons into a circular path by magnetic force. The storage ring is evacuated to minimise any unwanted deflection and loss of energy in the electron beam by stray atoms. Synchrotron light is generated when high energy electrons are deflected by the magnets, similar to the

process at the atomic level in Bremsstrahlung radiation. High energy photons are emitted at a tangent to the ring at each directing magnet and are manipulated by use of monochromators and filters at independent stations for the desired energy for the experiment [Helliwell 1998].



**Figure 2.4** A typical synchrotron facility (adapted from Canadian Light Source)

Synchrotron X-ray radiation offers three key advantages over the tube method: directivity, wavelength and power. The emission of X-ray photons from an X-ray tube anode is isotropic, only a small fraction of those produced can be directed towards the experiment. In synchrotron radiation the energy is always directed and polarised to a tangential path of the ring. This reduces the energy wasted creating unusable X-ray photons and then having to provide shielding to ensure the safety of the user of the system. The use of undulators and monochromators can be used to provide exact wavelengths over a wide band of energies, allowing for X-ray absorption fine structure (XAFS) spectroscopic analysis of materials [Keay 1997]. Electrons in the synchrotron do not generate X-ray photons by interacting at the atomic level and therefore do not generate the same thermal energy as the X-ray tube. Higher flux can therefore be produced by synchrotron radiation that would otherwise melt the anode in an X-ray tube. The disadvantages of the synchrotron are primarily its large size, such facilities can occupy a number of buildings. The beam line can also be too intense for some applications without suitable filtering, causing radiation damage to the detector.

### 2.2.3 Radioactive decay

An unstable atomic nucleus, caused by an imbalance of protons to neutrons, enters a stable state by capturing an orbiting electron to cancel the charge of the extra proton. The captured electron, usually from the K-shell, creates a vacancy that is then filled by the transition of an electron from a higher orbit state. During this transition the binding energy difference between the two states is lost as an X-ray photon or Auger electrons. The process is termed a 'decay' because the number of atomic protons are reduced by one, hence a reduction in the atomic number to a different element [Krane 1988].

### 2.2.4 Thermal excitation

Where sufficient thermal energy is applied to the atom it is also possible for an electron to be excited into a higher state. This creates a vacancy that must be filled by another electron dropping down from a higher orbital shell. X-ray photons are emitted from objects in this manner where the temperature is of the order  $> 10^6$  K [Helfand et al 1980].

## 2.3 X-ray astronomy

In Chapter 1 the importance of X-ray astronomy to scientists was discussed. The following sections present an overview of the technologies man has created enabling X-ray astronomy.

### 2.3.1 Detection platforms

Astronomers could not observe the sky at X-ray wavelengths before the invention of rocket motors and satellites in the 1950's due to the attenuation of X-ray photons by the Earth's atmosphere.

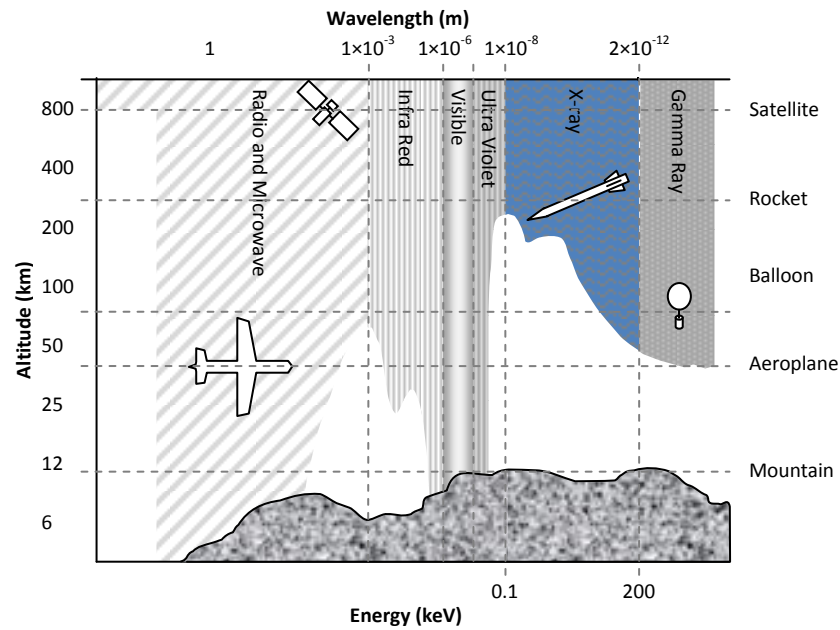


**Figure 2.6** Penetration of e-m waves through the atmosphere (adapted from NASA)

Figure 2.6 shows the altitudes required to place a detector to measure photons of different energies taking into account the atmospheric absorption. Whilst X-rays can be observed from very high altitude aircraft, the X-ray band of the electromagnetic spectrum is beyond the reach of typical aircraft flight. Three methods therefore exist whereby detectors can be sited to measure extra-terrestrial X-ray sources.

High energy (hard) X-rays,  $> 35$  keV, can be measured by detectors suspended in the upper atmosphere by balloons. An example of such a balloon is the High Resolution Gamma-ray and Hard X-ray Spectrometer (HIREGS) that was initially launched in 1992 with 2 week mission duration. Scientists collected data on gamma-ray and hard X-rays from solar flares during this time to ascertain the elemental composition of the solar atmosphere and learn more about the process causing the flares [Boggs 1998].

Sounding rockets that momentarily leave the Earth's atmosphere can allow detectors to be placed with an un-restricted view of the entire X-ray band of extra-terrestrial sources. X-ray observations made with rockets began in 1948 by the US Navy Research Laboratory (NRL). In three separate missions, detectors were placed in the rocket's nose cone to observe X-rays from the Sun. The first X-ray mission to inadvertently discover X-rays from beyond the solar system was in 1962. Whilst observing X-rays from the Sun, another source was discovered that originated from the Scorpius constellation and was labelled Scorpius X-1. The source was later called Sco X-1, after the discovery [Giacconi et al 1962]. Sounding rockets do not

have enough energy to reach an Earth orbit, so mission durations are short and hence the observation times, lasting typically a few minutes.

For longer observations, satellite based detectors are required where missions can last for many years. Like the sounding rocket missions, the full energy spectrum of X-rays can be measured as there is no atmospheric absorption. The satellite platform has enabled astronomers to make use of telescopes specifically for the X-ray wavelength.

### 2.3.2 X-ray telescopes

Due to the very small wavelengths of X-ray photons the telescope design must be different to that of traditional optical telescopes. Standard optics do not work in the X-ray wavelength as the X-ray photons either pass straight through, unaffected by the optic, or are completely absorbed by the optic material. The only process available to manipulate the path of an X-ray photon on to the detector is by total external reflection. The application of Snell's law can be used to find the critical angle for total external reflection of X-ray photons; hence  $\theta_c$  the grazing angle is given by [Kahn et al 2005]:

$$\theta_c = \sqrt{2(2\pi\lambda^2 r_0 N_e)} \quad (\text{ii-i})$$

Where  $\lambda$  is the wavelength of the X-ray photon,  $r_0$  is the classical electron radius and  $N_e$  is the electron density of the reflector material. The grazing angle is therefore proportional to the wavelength of the X-ray and inversely proportional to its energy. Therefore the higher the energy of the incident photon, the smaller the angle by which it can be reflected. The atomic number of the reflective material is also proportional to the grazing angle, as the electron density  $N_e$  is related to the atomic number. A popular material for use in X-ray optics is gold that can be easily deposited in coatings, doesn't tarnish and has an atomic number of 79. Therefore gold retains a high reflection coefficient up to 10 keV for angles less than  $0.5^\circ$  as shown in Figure 2.7 [Henke et al 1993].

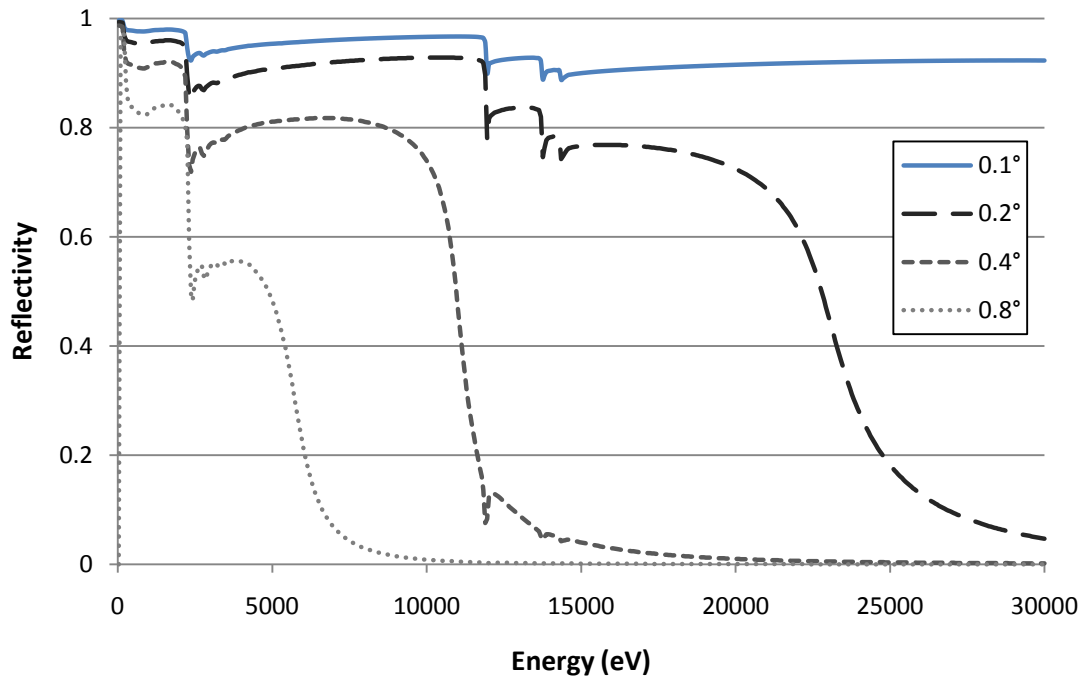


**Figure 2.7** X-ray reflectivity of gold as a function of incident grazing angle

Problems associated with the optics for telescope design are: the surface smoothness of the reflecting mirror, to ensure the grazing angle remains below  $\theta_c$ . The X-ray focussing mirror assembly must remain mechanically stable but be low enough in mass for launch into orbit. The focal length of the X-ray telescope will need to be large due to small grazing angles used in the total external reflection of X-ray photons.

The telescope design, proposed by Giacconi and Rossi in 1960, shown in Figure 2.8 has a parabolic profile mirror that perfectly focuses on-axis targets. However any off-axis image suffers from the Coma defect, whereby these photons are magnified by different amounts, causing oval like distortions [Giacconi & Rossi 1960].

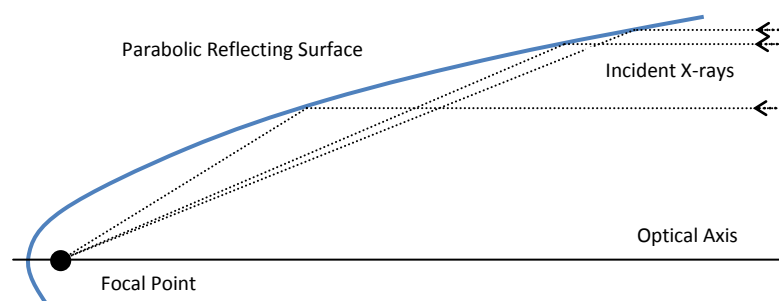


**Figure 2.8** Giacconi and Rossi optic

The solution to the coma defect was to incorporate a second stage reflector on a hyperboloid (Wolter type I/II) or ellipsoid (Wolter type III) plane as shown in Figure 2.9 [Giacconi et al 1969].

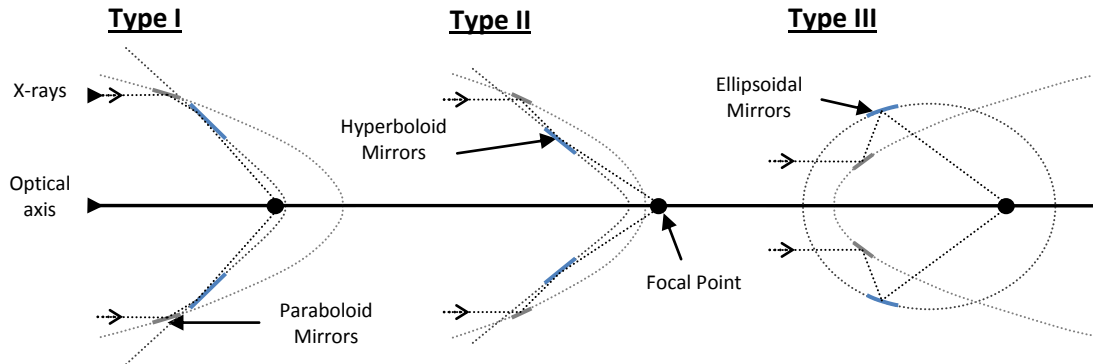


**Figure 2.9** Wolter type I, II and III optics

Wolter types I and II can be built very compact, type 1 being used in Swift, Suzaku, Chandra and the XMM-Newton observatory launched in 1999 [Burrows 2005] [Serlemitsos et al 2007] [Weisskopf 2003] [Gondoin et al 2003]. The grazing incidence mirrors showed are revolved about the optical axis to produce a ring. Only photons that strike the mirror shell can be focussed. Therefore many mirror shells are nested at different radii to the optical axis to increase the field of view as shown in Figure 2.10. Fifty-eight shells were included in each XMM-Newton mirror module [Gondoin et al 2003].

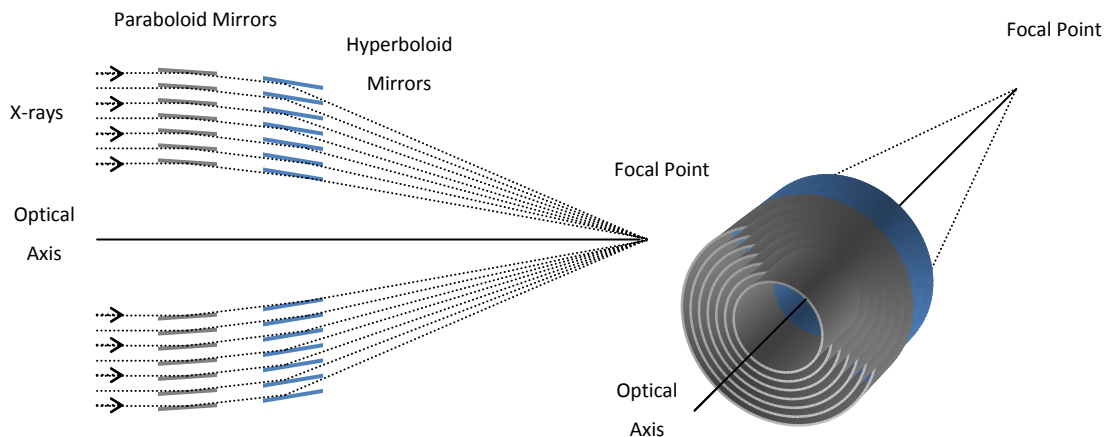


**Figure 2.10** Wolter I nested mirror optic.

A practical application of the Wolter type I parabolic/hyperbolic nested mirror rings optic can be seen in Figure 2.11 of the ROSAT telescope launched in 1990. With an outer mirror shell of 0.82 m, ROSAT had an effective focal area of  $1,140 \text{ cm}^2$  and a focal length of only 2.4 m. The gaps in the four mirror rings are support struts ensuring mechanical stability. Each

mirror has a polished gold coating to a surface finish of  $3 \text{ \AA}$  and is 50 cm in length [Aschenbach 1988].

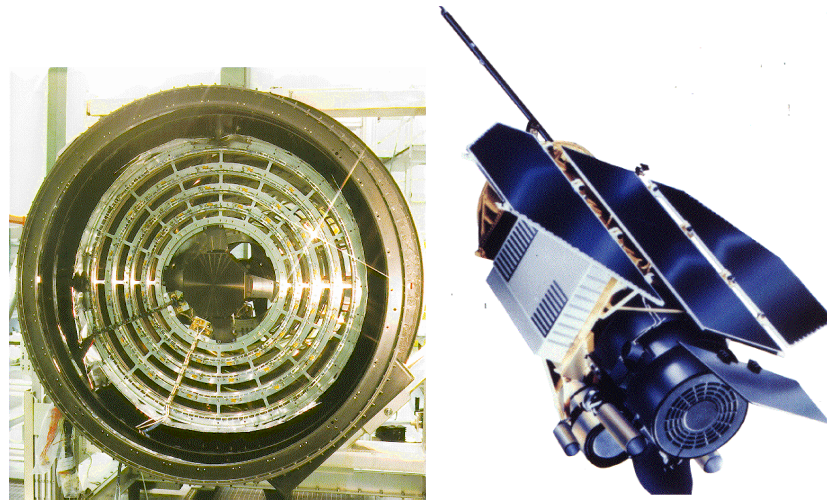


**Figure 2.11** Entrance aperture (left) and the ROSAT telescope (right)

(courtesy of Max-Planck-Institut für extraterrestrische Physik)

Later mirror designs, such as XMM-Newton, still based on Wolter type 1 optics, have increased the number of mirror rings and hence the effective collecting area of the optic. Electroplated nickel shells were manufactured to a thickness of  $\sim 1 \text{ mm}$ , allowing the shells to be closely stacked together, reducing the ‘dead’ space in between.

In all X-ray telescopes it is vital to ensure only those X-rays coming from the target focus are detected, preventing interference from any spurious ‘stray’ light sources. This is achieved by providing adequate shielding by means of a baffle to it at all other angles.

## 2.4 X-ray Detectors

X-rays interact strongly with electrons. An X-ray photon can transfer all of its energy to semiconductor electrons bound in the atomic structure of a material by the process of photoelectric absorption. Whereby, a photon provides enough kinetic energy to an electron orbiting the valence-band of an atom for it to be excited into the conduction-band. When electrons are excited to the conduction band, they are free to move through neighbouring atoms in the material structure and can be measured as a charge relative to the incident X-ray photon [Hall 1936].

An X-ray detector makes use of the photoelectric absorption of X-ray photons to quantify the energy of incident X-ray photons and in some cases the spatial position of their arrival to the detector.

“What would be the ideal detector for satellite-borne X-ray astronomy? It would possess high spatial resolution with a large useful area, excellent temporal resolution with the ability to handle large count rates, good energy resolution with unit quantum efficiency over a large bandwidth. Its output would be stable on timescales of years and its internal background of spurious signals would be negligibly low. It would be immune to damage by the in-orbit radiation environment and would require no consumables. It would be simple, rugged, and cheap to construct, light in weight and have a minimal power consumption. It would have no moving parts and a low output data rate. Such a detector does not exist” [Fraser 1989].

There are a number of X-ray photon detector technologies in existence, each one capable of meeting only a handful of the requirements suggested by Fraser. The following sections review these common X-ray detector technologies.

### 2.4.1 Scintillation

A Scintillator is a crystal that converts high energy X-ray photons into visible light that can then be measured. The total light output is proportional to the energy of the incident X-ray photon. Inorganic crystals such as sodium iodide (NaI) and caesium iodide (CsI) are the typical choice for Scintillators as these materials offer a high X-ray attenuation and hence good X-ray stopping power. These materials can be made into large area crystals and have a high efficiency at producing light [Wagner et al 2000]. Optical photons are then converted in a photomultiplier tube to electrons and measured as an electric signal proportional to the incident X-ray energy. The first stage of a photomultiplier tube shown in Figure 2.12 is the photocathode that converts photons into electrons by the photoelectric effect. A series of dynodes at increasing potentials accelerate and magnify the charge through the vacuum tube to the anode, where the final charge is collected to be measured [Kyushima et al 1994].

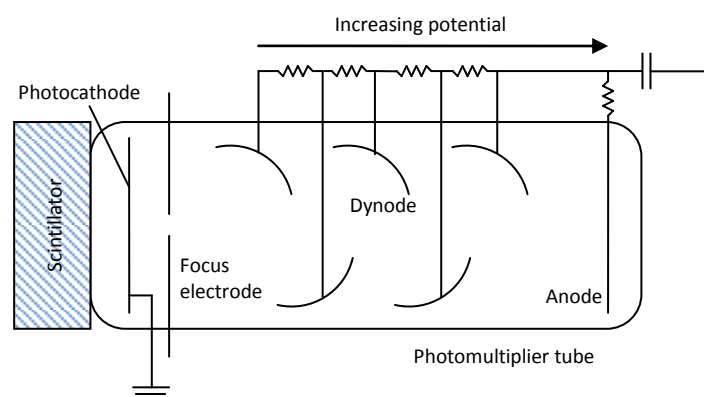


**Figure 2.12** Schematic of the photomultiplier tube X-ray detector

### 2.4.2 Geiger-Müller / Ionisation tube

The Geiger-Müller type detector operates by the photo-ionisation of an inert gas by an incoming charged particle or high energy photon that allows temporary conduction through the gas that can be measured. This is due predominantly to the photoelectric effect at energies below 50 keV; the incoming photon liberates a primary photo-electron, Auger electrons and fluorescent photons. The missing photoelectron from the atom creates a positively charged ion, hence ionisation. Such devices can be used to measure the rate of events [Duffendack et al 1937].

### 2.4.3 Proportional/gas counter

The proportional counter is similar to the Geiger-Müller tube; X-rays are detected by the photo-ionisation of an inert gas, such as Argon or Helium, but with a lower operating voltage. There is a linear relationship between the number of ion pairs collected by the anode and the operating voltage, therefore energy resolution of incoming photons and particles is possible. The time between interactions can also be measured to determine the radioactivity (rate). An array of proportional counters (PCA) can be manufactured to allow spatial resolution of incoming particles and photons [Fraser 1989]. Proportional counters were used in Einstein (1978), Ginga (1987) and ROSAT (1990) [Giacconi et al 1979] [Turner et al 1989] [Truemper 1982].

### 2.4.4 Micro channel plate (MCP)

The micro channel plate, shown in Figure 2.13, is an array of high gain, compact lead glass channel elements. Each channel in the micro channel plate is an independent dynode photomultiplier allowing spatial resolution of incident X-ray photons [Wiza 1979]. MCPs were employed on ROSAT (1990) and Chandra (1999) [Truemper 1982] [Weisskopf 2003].

Very high spatial resolution is achievable with typically 10 M channels in the detector array. Incoming X-ray photons with energies  $< 5$  keV will be measured within a single channel, at higher energies 'channel crossing' occurs, whereby cascading electrons can pass into neighbouring channels. The gain of the channel is dependent on its length and diameter and is typically of the order  $10^6$  to  $10^8$ , yielding a large, easily detected signal. The potential gradient across the channel accelerates and multiplies the photo-electrons through the channel to a phosphor coated fibre optic. The phosphor coated fibre optic converts the electrons into visible light that can be imaged.

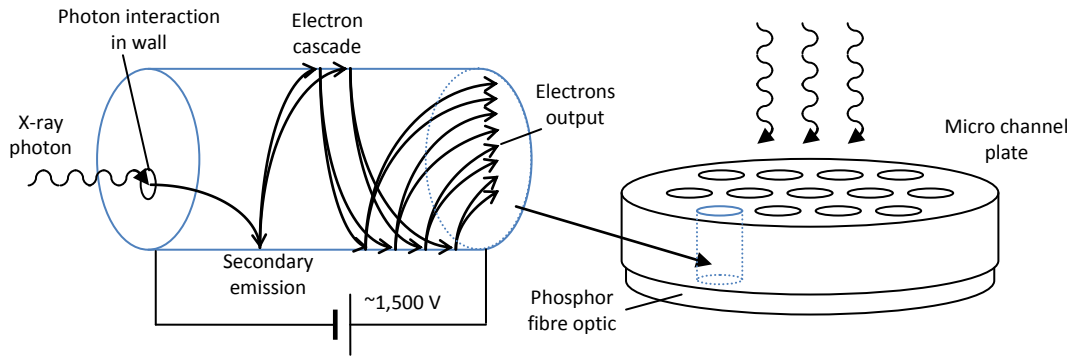


**Figure 2.13** Schematic of the micro channel plate X-ray imager

#### 2.4.5 Bolometer/calorimeters

Calorimeters have absorber crystals that are directly heated by thermal agitation of an incoming X-ray photon. The incoming photon liberates an electron loose from the atom of the absorber material that moves about the crystal, generating heat. The amount of temperature rise in the crystal is directly proportional to the energy of the incident photon. A thermometer is used to measure the temperature from which the absorbed energy can be calculated. The absorber is connected by a thermal link to a heat-sink that continually refreshes its temperature state. The thermal change produced by an incoming photon is small, therefore the device must be kept at a very low temperature so that the change is large relative to any fluctuation in the thermal link. An array of small calorimeters (microcalorimeters) can be used to spatially resolve incident X-ray photons [de Korte 2000]. The use of a microcalorimeter in space has been unsuccessful so far with the explosion of ASTRO-E (2000) and the cryogenic failure of Suzaku (2005) [Takahashi et al 1998] [Mitsuda et al 2007].

#### 2.4.6 Transition edge sensor (TES)

A TES is a highly sensitive superconducting thermometer used to measure the change in temperature in a bolometer or calorimeter. The sensor is biased at its transition temperature, whereupon it is in a superconducting state. Any incoming photon raises the temperature of the sensor material above the transition edge and it loses its super-conductivity. The change in resistance across the material is used to determine the amount of energy deposited by the incident photon [Moseley et al 1984]. Transition edge sensors have yet to be included in any X-ray missions but are in consideration for future mission such as NeXT [Tawara et al 2003].

### 2.4.7 Charge-coupled device (CCD)

The CCD is a semiconductor solid state imaging device, usually made from high purity doped silicon and has higher quantum efficiency (QE) than the counters mentioned previously, but at a cost to noise. The dominant noise source is thermally generated electrons in the silicon, this effect can be minimised by cooling the device during operation. An incident photon excites electrons into the conduction band due to the photoelectric effect. The silicon the device is fabricated on liberates 1 electron hole pairs for every 3.65 eV of energy that is absorbed at room temperature. A pixelated structure allows the arrival position of photon to be determined and is formed by column implants and surface electrodes. Under each pixel a potential well is formed by applying a potential difference between a surface electrode and the substrate. Charge generated in the silicon, proportional to the energy of the incoming photon is held within the nearest potential well. Charge is then transferred across the device to a readout amplifier by sequentially changing the potentials of the surface electrodes, i.e. charge coupling (see Chapter 3).

CCDs allow not only spatial imaging resolution of incident X-ray photons but also energetic spectroscopy. CCDs offer a  $\times 10$  improvement over X-ray measurements obtained with position sensitive proportional counters (PSPCs), scintillators and micro-channel plates.

CCDs have proved to be a popular choice of detection instrument with their inclusion in ASCA (1993), XMM-Newton (1999), Chandra (1999), Swift(2004), Suzaku (2005) and future missions such as NeXT (2010) [Tanaka et al 1994] [Holland et al 1996] [Weisskopf 1987] [Burrows 2005] [Mitsuda et al 2007] [Kunieda et al 2004].

## 2.5 CCD based X-ray missions

### 2.5.1 XMM-Newton

The X-ray Multi-Mirror (XMM) Newton telescope, shown in Figure 2.14, was launched by an Ariane V rocket on December 10<sup>th</sup> 1999. XMM-Newton is currently in orbit although coming close to its projected life time of 10 years.



**Figure 2.14** The XMM-Newton telescope (courtesy of ESA)

XMM-Newton provided a major advance in sensitivity over previous missions such as EINSTEIN by the combination of the European Photon Imaging Camera (EPIC) cameras and the XMM optics. XMM-Newton has been successful in helping astronomers to understand the diffuse X-ray background and establish its principle components. It has also been successful in achieving its mission aims of [Eggel et al 1996]:

- Mapping many clusters of galaxies for their temperature and elemental abundances
- Spectral surveys of galaxies and supernova remnants
- Studies of stellar X-rays and stellar flare events
- Studies of accreting binary systems.
- Gravitational redshift of light emitted from neutron stars

Instrumentation on board XMM-Newton comprises EPIC, the Reflection Grating Spectrometer (RGS) and an Optical Monitor.

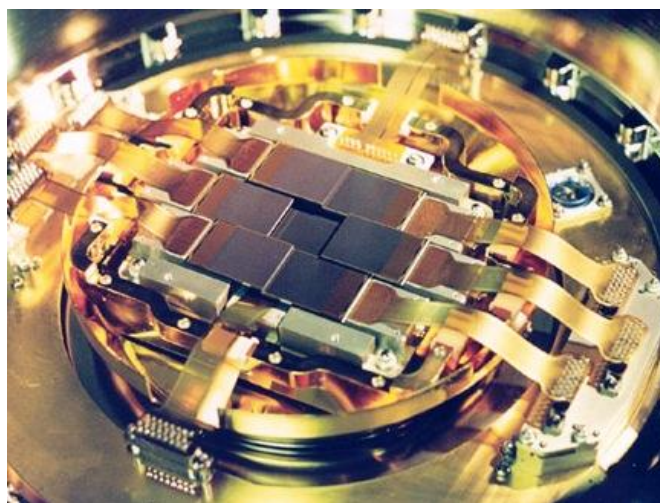


**Figure 2.15** An EPIC-MOS focal plane array (courtesy of ESA)

EPIC consists of two MOS CCD arrays (EPIC-MOS) and one pn-CCD array (EPIC-Maxi), each array is aligned to one of the three openings visible in Figure 2.14 [Bignami et al 1990]. The EPIC-MOS camera shown in Figure 2.15 was developed and built at Leicester University and each camera has seven e2v frame transfer CCD22 devices with  $600 \times 600 \times 40 \mu\text{m}$  square pixels that are arranged into the focal plane. The central CCD is lowered with respect to the other six to account for the small curvature of the focussing optics and allows for maximum fill factor as the readout section is overlapped by the imaging region of another CCD. The CCDs employ open-electrodes to give improved low energy QE of ( $\sim 30\%$  @ 277 eV) and are depleted to  $30 \mu\text{m}$  to improve high energy QE ( $20\%$  @ 10 keV) [Holland et al 1996]. The EPIC-MOS CCDs were the first to employ tapered pixel geometries allowing the frame transfer of  $40 \times 40 \mu\text{m}$  pixels to be reduced into  $40 \times 12 \mu\text{m}$  pixels in the store section. This enabled the CCDs comprising the array to be positioned closely together, minimising the loss of imaging area between CCDs across the focal plane. The reduced store pixel size also ensured a maximum possible imaging area for the frame transfer CCD could be fabricated within the limits of the wafer size [Holland et al 1996].

The work of this thesis relates to the development of MOS CCD technology beyond that employed by the EPIC cameras for the potential inclusion on ESA's XEUS mission.

### 2.5.2 XEUS

The X-ray Evolving Universe Spectroscopy (XEUS) mission is ESA's proposed follow on mission to XMM-Newton to launch  $\sim 2030$ . Sensitivity of the detector instruments will be up to  $\times 100$  greater than those employed on XMM-Newton. The focal length of the telescope is to be increased from 7 m to  $\sim 35$  m, requiring the focussing optics to be located in a separate spacecraft to that of the detector instruments [Gondoin et al 2008]. Figure 2.16 shows a model of the two spacecraft in orbit about the earth in a carefully controlled formation ensuring the focus to within  $\pm 2$  mm is maintained. XEUS will be inserted into orbit at the second Lagrange point where it will be able to make uninterrupted observations of the X-ray sky but be subjected to solar proton irradiation that may damage instruments and increase the background of measurements.

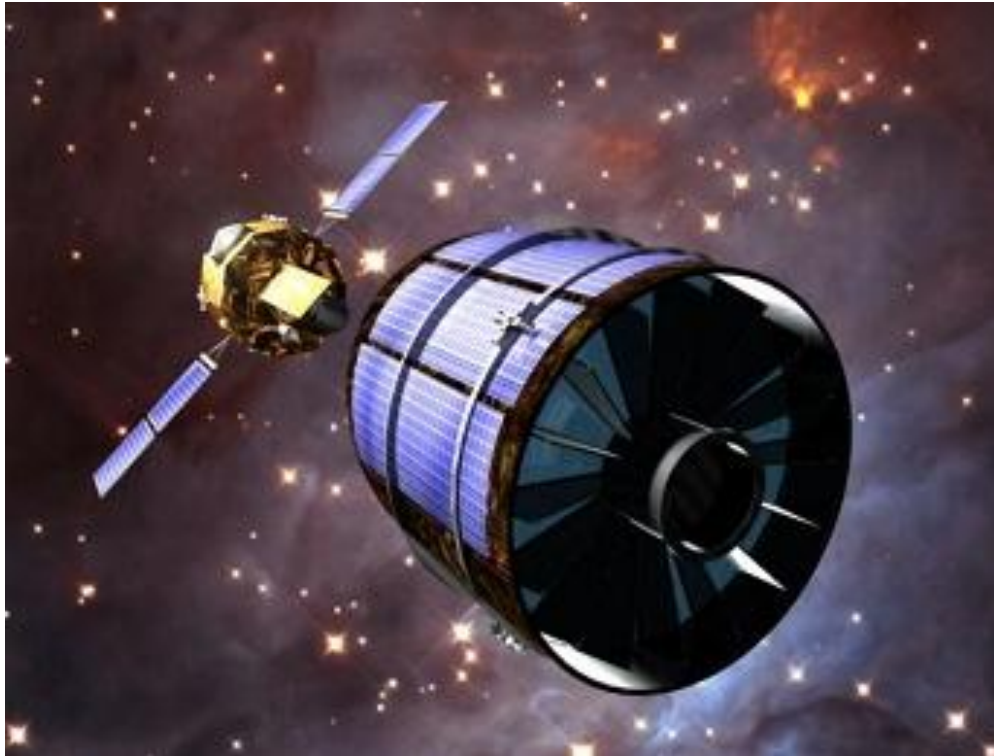


**Figure 2.16** The XEUS telescope (courtesy of ESA)

XEUS will observe the very faint objects from the early universe, specifically targeting:

- The 1<sup>st</sup> Black holes formed in the early Universe
- Galaxy groups
- Clusters
- The interstellar medium

XEUS will comprise three main instruments utilising the primary focus of the optic. An active pixel DEPFET wide-field imager (WFI), developed by the Max Planck Institute, will provide images with a 7 arcmin field of view at resolutions of 50 eV full-width-half-maximum (FWHM) at carbon-K (277 eV) and 125 eV FWHM at manganese  $K\alpha_1$  (5,898 eV) [de Korte et al 2008]. The WFI will also be used to guide the focus of X-ray sources onto the higher sensitivity narrow-field imagers (NFIs) that have a 1 arcmin field of view (FOV). The two narrow-field imagers employ superconductor tunnel junction (STJ) and transition edge sensor technology and will resolve the fine structure of X-ray emission. The NFI's will have a resolution of 1 eV to 10 eV FWHM over the energy range 0.1 keV to 30 keV [Bavdaz et al 1999].

The XEUS telescope optic will provide a field of view greater than 20 arcmins that will not be entirely covered by the baseline as shown in Figure 2.17.

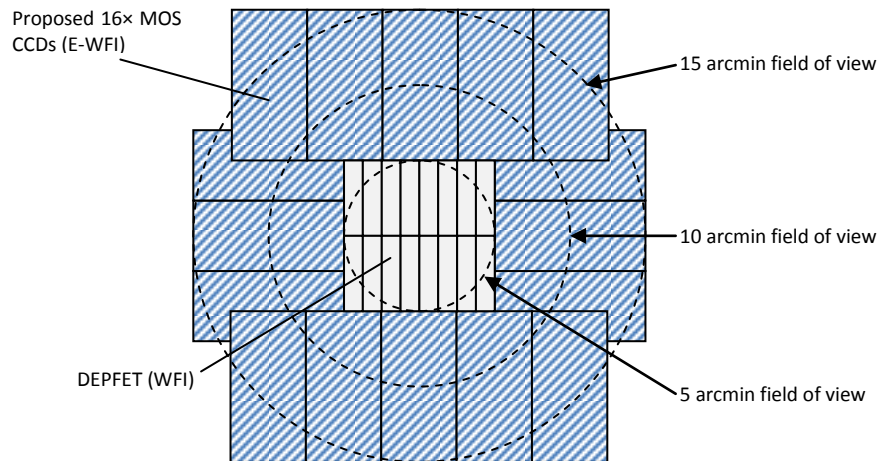


**Figure 2.17** Possible FOV of the XEUS mirror on the detector space craft

Therefore it is possible to include additional imagers to serendipitously find events of cosmological interest that can later be imaged with the primary instruments. The inclusion of up to sixteen MOS CCDs is proposed to surround the DEPFET imager, creating the extended wide-field imager (E-WFI) that will increase the collecting area of the XEUS telescope by 9 times [Holland et al 2005]. The MOS CCDs for the XEUS E-WFI would include the following technological developments since the launch of XMM-Newton:

- Increased quantum efficiency over the energy range 0.1 keV to 20 keV
- High pixel throughput using multi-channel ASICs
- Low amplifier read noise
- Improved radiation hardness for increased lifetime

The former two technological developments, increased QE and pixel throughput, form the subject of this thesis.

The detection efficiency for low energy X-rays can be increased by the use of open electrode phases as demonstrated by the EPIC-MOS CCDs [Holland et al 1996]. However the pinned implant used in the open area of the pixel has a negligible effect on the depletion of the pixel, thus reducing the high energy sensitivity (see Chapter 3). The high energy sensitivity of an open electrode CCD can be restored by the deposition of a very thin polysilicon layer (40 nm) that is biased to drive the pixel's depletion below the open phase [Pool 2006].

High pixel throughputs and low noise performance is achieved by the use of multiple output nodes around the CCD allowing the parallel read out of pixels. Modern output nodes contain multi-stage amplifiers that allow greater impedance matching between the CCD and the read out electronics allowing higher pixel rates without the time penalty of capacitive loading (see Chapter 3).

A reduction in read noise leads to an increased spectral resolution of the CCDs, allowing the fainter X-ray sources to be imaged.

The radiation hardness of CCDs for use in space applications is paramount as it directly affects the useable life of the detector. The proposed life time of the XEUS telescope is up to 10 years, therefore a CCD based E-WFI would need to be able to withstand high energy particle irradiation for this amount of time. The use of p-type silicon to produce the buried channel rather than n-type for the XEUS E-WFI CCDs would improve upon the radiation hardness of the detector as the boron atom is less susceptible to being displaced by protons than the phosphorus used in n-type silicon (see Chapters 3 and 5).

## 2.6 Summary

This chapter reviewed the generation of X-rays by both manmade and natural phenomena with particular reference to the electrical X-ray tube and synchrotron sources that enable the widespread application of X-rays.

The technology man has developed to facilitate the acquisition of X-ray data from astronomical sources was also presented. Some of the established methods for X-ray detection were discussed with particular reference to the CCD that has revolutionised X-ray astronomy in the last 20 years.

Overviews of the current and future X-ray astronomy missions for the ESA were discussed in Section 2.5. The key improvements to CCD technology were highlighted that would be vital amongst other requirements for the inclusion of MOS CCDs in the future XEUS mission that aspects of this thesis seek to address. Chapter 3 will discuss the CCD in detail.

## 2.7 References

Aschenbach, B., 1988. Design, construction, and performance of the ROSAT high-resolution X-ray mirror assembly. *Applied Optics*, Vol. 27, No. 8, p. 1404-1413.

Bavdaz, M. et al., 1999. X-ray evolving universe spectroscopy mission (XEUS). *Proc. SPIE*, Vol. 3766.

Bearden, J.A., 1967. X-ray wavelengths. *Review of Modern Physics*, Vol. 39, p. 78-124.

Biggami, G.F. et al., 1990. European photon imaging camera for X-ray astronomy. *Proc. SPIE*, Vol. 1344, p. 144-153.

Boggs, S.E., 1998. A high resolution gamma-ray and hard X-ray spectrometer (HIREGS) for long duration balloon flights. *Advances in Space Research*, Vol. 21, p. 1015-1018.

- Brown, J.G., 1975. X-rays and their applications. *Plenum*, p. 13.
- Burrows, D.N., 2005. The Swift X-ray telescope. *Space Science Reviews*, Vol. 120, p. 165-195.
- Compton, A.H., 1923. A quantum theory of the scattering of X-rays by light elements. *Physical Review*, Vol. 21, p. 483-502.
- de Korte, P.A.J., 2000. Cryogenic imaging spectrometers for X-ray astronomy. *Nuclear Instruments and Methods*, Vol. A444, p. 163-169.
- de Korte, P.A.J. et al., 2008. The XEUS focal plane instruments. *Proc. SPIE*, Vol. 7011.
- Duffendack, O.S. et al., 1937. Production, characteristics, and reliability of Geiger-Muller Counters. *Physical review*, Vol. 52, p. 1231-1237.
- Eggel, H. et al., 1996. ESA XMM Mission. *Proc. SPIE*, Vol. 2808.
- Fraser, G.W., 1989. X-ray detectors in astronomy. *Cambridge Astrophysics*.
- Giacconi, R. & Rossi, B., 1960. A 'Telescope' for soft X-ray astronomy. *Geophysical Research*, Vol. 65, p. 773-775.
- Giacconi, R. et al., 1969. Grazing-incidence telescopes for X-ray astronomy. *Space Science Reviews*, Vol. 9, p. 3-57.
- Giacconi, R. et al., 1979. The Einstein /HEAO 2/ X-ray observatory. *Astrophysics Journal*, Vol. 230, p. 540-550.
- Giacconi, R. et al., 1962. Evidence for X-rays from sources outside the solar system. *Physical Review Letter*, Vol. 9, p. 439-443.
- Gondoin, P. et al., 2003. Calibration of the first XMM flight mirror module: I. Image quality. *Proc. SPIE*, Vol. 3444, p. 278-289.
- Gondoin P. et al., 2008. Overview of ESA study activities on XEUS. *Proc. SPIE*, Vol. 7011.
- Hall, H., 1936. The theory of photoelectric absorption for X-rays and  $\gamma$ -rays. *Review of Modern Physics*, Vol.8, p. 358-397.
- Helfand, D.J. et al., 1980. Thermal X-ray emission from neutron stars. *Nature*, Vol. 283, p. 337-343.
- Helliwell, J.R., 1998. Synchrotron radiation facilities. *Nature Structural Biology*, Vol. 5, p. 614-617.

- Henke, B.L. et al., 1993. X-ray interactions: Photoabsorption, scattering, transmission, and reflection at  $E = 50\text{-}30,000$  eV,  $Z = 1\text{-}92$ . *Atomic Data and Nuclear Data Tables*, Vol. 54, p. 181-343.
- Holland, A.D. et al., 1996. MOS CCDs for the EPIC on XMM. *Proc. SPIE*, Vol. 2808, p. 414-420.
- Holland, A.D. et al., 2005. MOS CCDs for the wide field imager on the XEUS spacecraft. *Proc. SPIE*, Vol. 5898.
- Kahn, S.M. et al., 2005. High-energy spectroscopic astrophysics. *Springer*, p. 113.
- Keay, A., 1997. An investigation of fine structure effects in CCDs developed for JET-X. *University of Leicester*, Ph.D. thesis.
- Knoll, G.F., 2000. Radiation detection and measurement. *Wiley*, 3rd Ed, p. 13.
- Krane, K.S., 1988. Introductory nuclear physics. *Wiley*, p. 160.
- Krause, M.O., 1979. Atomic radiative and radiationless yields for K and L shells. *Physical and Chemical Reference Data*, Vol. 8, p. 307-327.
- Kunieda, H. et al., 2004. New X-ray telescope mission (NeXT). *Proc. SPIE*, Vol. 5168, p. 77-89.
- Kyushima, H. et al., 1994. Photomultiplier tube of new dynode configuration. *Nuclear Science, IEEE*, Vol. 41, p. 725-729.
- Mitsuda, K. et al., 2007. The X-ray observatory Suzaku. *Astronomical Society of Japan*, Vol. 59, p. S1-S7.
- Moseley, S.H. et al., 1984. Thermal detectors as X-ray spectrometers. *Applied Physics*, Vol. 56, p. 1257-1262.
- Pool, P.J., 2006. Thin poly process report. E2V-Brunel-TP-RP-02.
- Röntgen, W.C., 1896. On a new kind of rays. *Science*, Vol. 3, p. 227-231.
- Serlemitsos, P.J. et al., 2007. The X-ray telescope onboard Suzaku. *Astronomical Society of Japan*, Vol. 59, p. S9-S21.
- Sokolov, A.A. & Ternov, I.M., 1967. Synchrotron radiation. *Russian Physics*, Vol. 10, p. 39-47.
- Takahashi, T. et al., 1998. Astro-E mission and the X-ray survey. *Astronomische Nachrichten*, Vol. 319, p. 159-162.
- Tanaka, Y. et al., 1994. The X-ray astronomy satellite ASCA. *Astronomical Society of Japan*, Vol. 46, p. L37-L41.

- Tawara, Y. et al., 2003. Broadband X-ray imaging mission NeXT. *Proc. SPIE*, Vol. 4851, p. 324-330.
- Truemper, J., 1982. The ROSAT mission. *Advances in Space Research*, Vol. 2, p. 241-249.
- Turner, M.J.L. et al., 1989. The large area counter on Ginga. *Astronomical Society of Japan*, Vol. 41, p. 345-372.
- Wagner, A. et al., 2000. Energy resolution and energy-light response of CsI (Ti) scintillators for charged particle detection. *Nuclear Instruments and Methods*, Vol. A456, p. 290-299.
- Weisskopf, M.C., 2003. The Chandra X-ray observatory: An overview. *Advances in Space Research*, Vol. 32, p. 2005-2011.
- Weisskopf, M.C., 1987. The advanced X-ray astrophysics facility - an overview. *Astrophysical Letters*, Vol. 26, p. 1-6.
- Wiza, J.L., 1979. Microchannel plate detectors. *Nuclear Instruments and Methods*, Vol. 162, p. 587-601.
- Young, H.D. & Freedman, R.A., 1996. University physics. *Addison Wesley*, 9th Ed., p. 1252.

## Chapter 3: The charge-coupled device

### 3.1 Introduction

The CCD, Figure 3.1, was devised by William S. Boyle and George E. Smith in 1969 at Bell Laboratories as a solid state memory device capable of transferring charge packets of data through a semiconductor material [Boyle and Smith 1970]. It was soon demonstrated by Smith that by using this technology with the photo-absorption properties of silicon, a 2-dimensional imager could be formed.

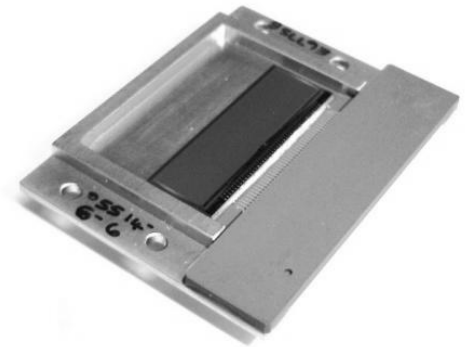


Figure 3.1 The charge-coupled device

The 2-D array of charge storing picture elements (pixels) shown in Figure 3.2 is formed by the creation of metal-oxide-semiconductor (MOS) capacitors under vertically spaced electrodes and horizontally spaced implants that run the length of the imaging area. The electrodes are manufactured by the deposition of polycrystalline silicon onto the epitaxial silicon that is grown from the silicon substrate wafer, or directly onto bulk silicon and are electrically isolated by the formation of the native oxide. The implant regions are formed by introducing dopants into the epitaxial or bulk silicon by either ion implantation or molecular beam epitaxy (MBE) and have a fixed charge that repels the generated signal charge from them and into discrete columns. The electrodes are usually manufactured as a repeating structure of three or four independent electrodes (3/4-phase) such that vertical separation can be achieved by alternating the biases applied to them [Burt 2006].

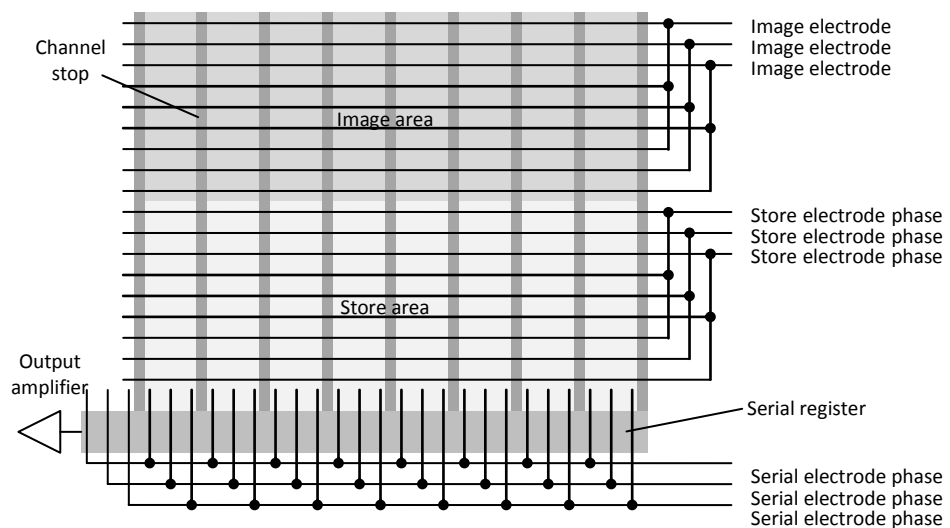
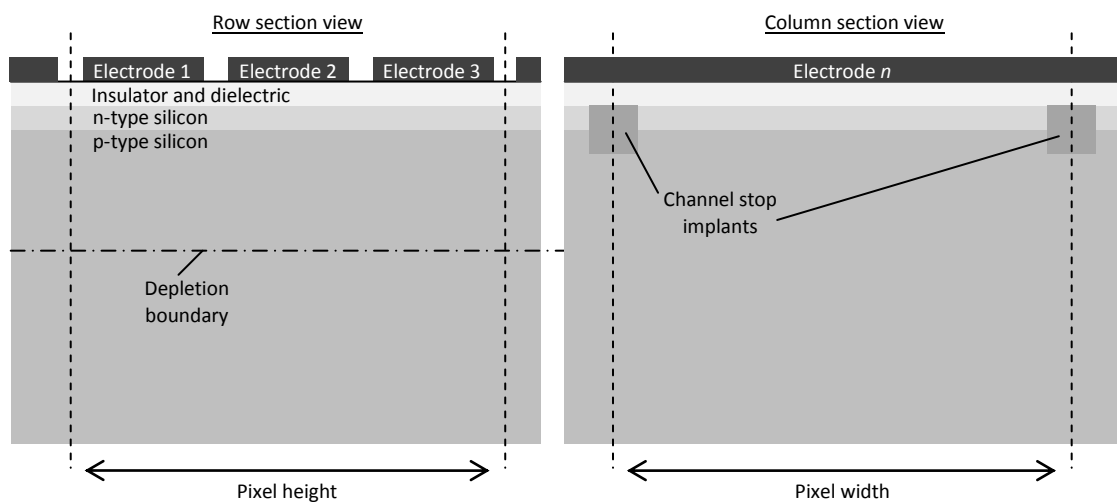


Figure 3.2 Schematic of a 3-phase frame transfer CCD

During operation, each MOS capacitor generates a potential well below it, that attracts any locally photo-generated electric charge into it. The level of charge stored in these potential wells will vary with the intensity of light focussed on to the CCD surface and exposure time. The charge packets are then transferred, one row at a time, by a sequence of applied electrode biases, into a serial register. This charge is then transferred by a similar clocking scheme along the serial register to an output node that is used to modulate the gate of an output field-effect-transistor (FET). The output of the CCD is therefore a series of voltages that correspond to discrete sampling areas of the image.

The initial MOS capacitor design, known as the 'surface channel CCD', allowed collected electrons to come into contact with hole-vacancies caused by 'dangling bonds' at the oxide/silicon interface, presenting an unknown loss of signal charge that is unacceptable for scientific applications. Thus the buried channel CCD was devised, to keep the collected electrons a safe distance from these surface recombination sites. The potential wells of a buried channel CCD are formed by p-n diode structures rather than MOS capacitors and are arranged in a similar 2-D array [Howes & Morgan 1979]. Figure 3.3 shows the cross-section views of Figure 3.2 in both vertical and horizontal directions respectively for one pixel in the buried channel CCD.



**Figure 3.3** Buried channel CCD cross-section

The first layers that comprise the electrode structures, insulator and dielectric are referred to as the 'dead' layers as any photons that are absorbed within these will not be detected. The depletion boundary indicates the distance into the p-type silicon of the p-n diode where the electrostatic potential has reduced to 0 V. The depletion boundary defines the effective charge collecting depth boundary of the pixel and is discussed further in Section 3.2.5.

This chapter reviews the physical principles behind the operation of the buried channel CCD, its manufacture, and technological developments to improve the performance and is organised into the following sections:

- Charge generation
- Charge storage
- Charge transfer
- Signal measurement
- Noise sources

## 3.2 Charge generation

### 3.2.1 The photoelectric effect

The silicon used for device fabrication is in crystalline form. The four outermost electrons of each atom are paired with those of four adjacent atoms to form the chemical bonds that hold the structure together.

The photoelectric effect is the process by which an incident photon provides enough energy for one of the bonding electrons to break away and move freely throughout the lattice. The resultant lack of an electron in the lattice is called a hole (hence the term electron-hole pair generation), this can also move through the lattice via transportation with other bonding electrons [Kane 1962]. An illustration of this mechanism is shown in Figure 3.4. The path the electron and hole take after generation due to the electric field is indicated by the dotted lines.

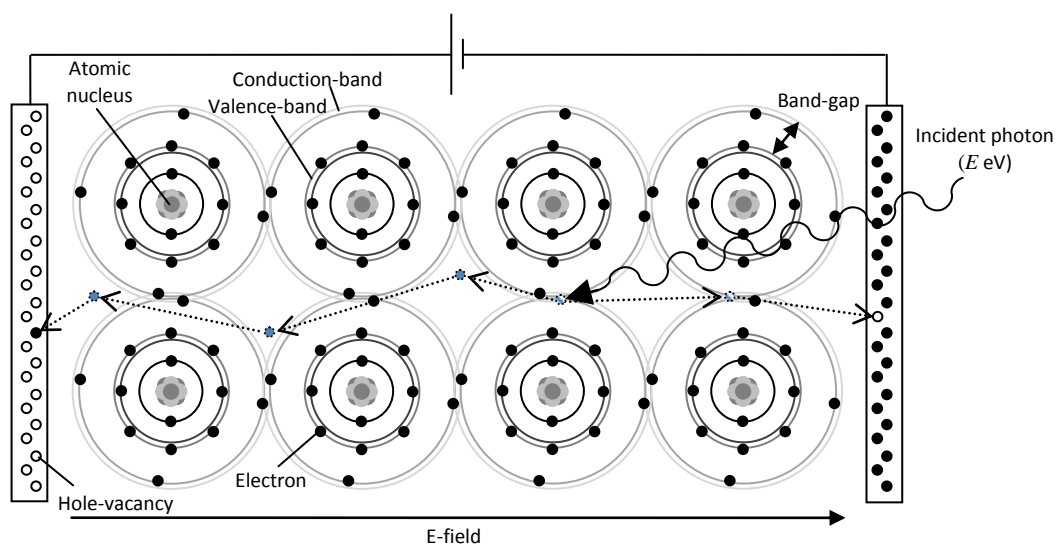


**Figure 3.4** e-h pair generation and collection in silicon from a high energy photon

The relationship between a photon's energy  $E$  and wavelength  $\lambda$  was discovered in 1904 by Albert Einstein and is:

$$E = \frac{hc}{\lambda} \quad (\text{iii-i})$$

Where  $h$  is Planck's constant ( $4.14 \times 10^{-15}$  eV sec<sup>-1</sup>) and  $c$  ( $3 \times 10^8$  m sec<sup>-1</sup>) is the speed of light.

In the case of optical photons, the energy required to directly release an electron is a minimum of about 3.65 eV, corresponding to a wavelength of about 340 nm (UV). However, it is also possible for the thermal energy of the bonding electron to be added to the energy of the photon and at 273 K, the minimum photon energy to release an electron is actually about 1.11 eV. This quantity is effectively the energy level threshold between the valence and conduction-bands and is therefore termed the 'band-gap'.

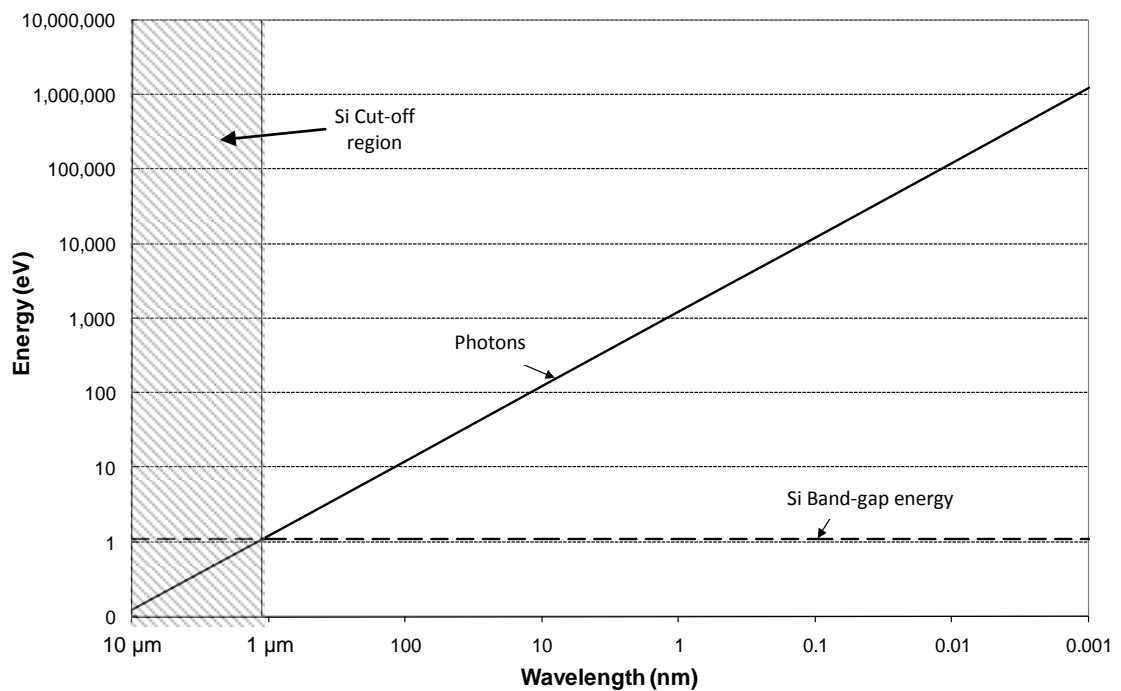


**Figure 3.5** Planck's relationship between photon frequency and energy

Figure 3.5 shows that light at wavelengths longer than 1.1  $\mu\text{m}$  (far Infra-red) does not have enough energy to cause electrons to cross the silicon band-gap and is therefore undetectable by a silicon CCD (Si Cut-off).

Incident photons of energy between 1.11 eV and  $\sim 3.65$  eV, the Infra-red to ultra-violet band of the electromagnetic spectrum, generate only 1 electron-hole (e-h) pair per photon. At higher photon energies a greater number of e-h pairs can be generated by impact ionisation of the photo-generated electron with valence-band electrons of other atoms. If the energy of the electron is sufficient, as will be the case of innermost electrons being ejected from the silicon

atom by interactions with X-rays, an Auger transition can occur, whereby both the photo-generated electron and the valence-band electron will jump into the conduction-band. Two e-h pairs are formed in such an event; two unbound electrons are freed from the atom where the Auger transition took place as well as one hole in the valence-band. The second hole exists at the valence-band of the atom where the primary photo-electric interaction occurred. If the two electrons ejected from the valence-band of the primary Auger transition have enough energy to cause subsequent Auger transitions in other atoms, an avalanche of impact ionisations can occur, generating many e-h pairs [Geist 1983]. This effect is commonly termed the formation of an 'e-h cloud' due to its roughly isotropic formation in the 3-dimensional silicon lattice. The subsequent drift and collection of electrons in a CCD is essentially localised by the electrical field arising from the electrode potentials applied during integration, this causes the electrons to be collected in the discrete picture elements (pixels).

The number of e-h pairs generated in a cloud,  $n_i$ , can be calculated by the ideal quantum yield equation [Geist & Zalewski 1979]:

$$n_i = \frac{E}{E_{e-h}} \quad (\text{iii-ii})$$

Where  $E_{e-h}$  is the energy required to generate 1 e-h pair and has an average value of 3.65 eV in silicon at 293 K [Bertolini & Coche 1968].  $E$  (eV) is the incident photon energy. This relationship is paramount for a CCDs ability to perform energetic spectroscopy of X-ray radiation, as different energies can be distinguished based on the quantity of electrical charge they generate as signal in the silicon.

### 3.2.2 Photon absorption

When a photon travels through a material, the probability of interaction via the photoelectric effect is a function of the distance travelled. The distance is also a function of the wavelength of the incident photon, density of the absorber material and position of the valence-band electrons around the atomic nucleus. The position of the valence-band electrons can be assumed to be random, therefore this distance cannot be quoted as a precise figure, but as a statistical average for a number of photons. This characteristic distance is called the absorption length ( $X_{abs}$ ) and is the  $1/e$  depth into the material at which 36.7 % of the number of incident photons have been absorbed.

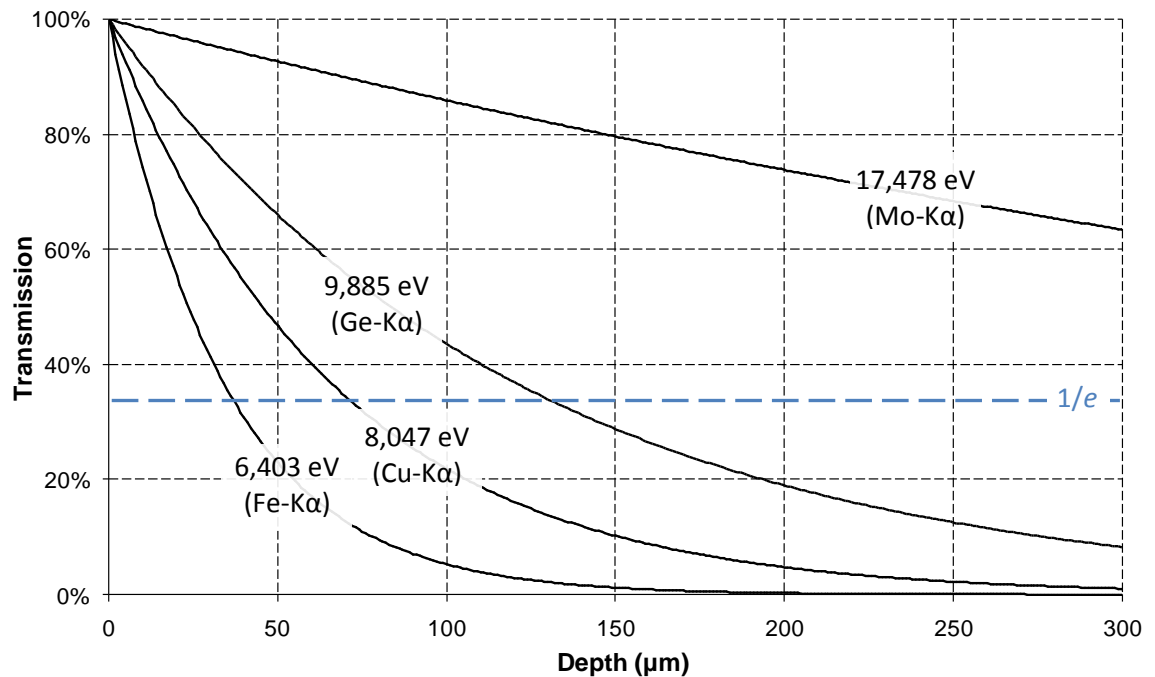


**Figure 3.6** Photon energy effect of absorption in silicon [McMaster et al 1969]

Figure 3.6 shows that energy/wavelength has a strong influence on the thickness of silicon required to absorb all the photons. For CCDs, this presents two problems; firstly the electric field needs to extend deep enough into the silicon to collect electrons generated by infra-red or X-ray photons deep into the p-substrate before they can recombine or diffuse into neighbouring pixels. Secondly, at the other end of their spectral range, the traditional electrode structures will significantly attenuate any blue light or soft X-ray photons before they reach the active silicon.

The photon absorption length of a material increases with a reduction in temperature. This is because the band-gap is increased with the reduction in the contribution of the electron's thermal energy.

### 3.2.3 Charge diffusion

The electron component of the e-h cloud generated by the photoelectric effect will tend to diffuse in the silicon as it propagates towards the potential well of a pixel. The amount of electron diffusion depends on the strength of the electric field the electron cloud is subjected to as it is generated and during its drift towards the potential well [Hopkinson 1983]. Charge clouds that are generated in the field-free region of the silicon (beyond the depletion regions below the electrodes) will exhibit the greatest diffusion and are likely to suffer partial recombination in the substrate and at the rear surface and as a result, be collected in multiple

pixels due to lateral diffusion. Reduced spatial resolution thus results. Re-combination also results in poor energy resolution as an unknown quantity of charge is lost.

The initial electron-hole cloud generated by the photoelectric effect and subsequent impact ionisations will have a maximum radius described by the following equation [Everhart & Hoff 1971]:

$$R(\mu\text{m}) = 0.0171 \times E^{1.75} \quad (\text{iii-iii})$$

Where  $R$  ( $\mu\text{m}$ ) is the maximum distance an impact ionised electron may form from a photo-generated electron and  $E$  (keV) is the energy of the photo-generated electron. Statistically, e-h clouds will have a  $1\sigma$  radius that is  $0.25 \times R$  [Fitting et al 1978]. This equates to a charge cloud diameter of less than  $1 \mu\text{m}$  in silicon for photon energies of less than 10 keV. The typical CCD pixel size is usually greater than  $10 \mu\text{m}$  in both width and height and therefore charge diffusion within the depleted region has a negligible impact on the spatial resolution of the detector. However, a charge cloud may be formed in either the depleted or field-free regions of the silicon as shown in Figure 3.7. In the latter case, independent studies confirm that the radial diffusion of the charge cloud in the field-free region to be dominant in the degradation of spatial resolution [Hopkinson 1983] [Pavlov & Nousek 1999].

If the photon is absorbed in the field-free region, the e-h cloud diffuses isotropically. Some of the charge will eventually diffuse into the electric field of the depleted region, where it will drift towards collection in the potential well. The resultant charge spreading is now greater than if the absorption were in the depletion region.

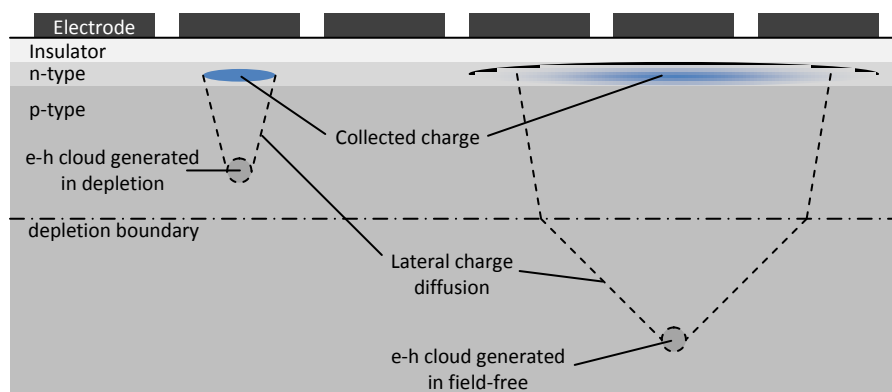


**Figure 3.7** e-h cloud diffusion in depleted and field-free region of the CCD

The effects of charge diffusion are discussed in Chapter 6 and are used to evaluate the depletion depth of a CCD.

### 3.2.4 Quantum efficiency

The quantum efficiency (QE) is a measurement of the CCD efficiency at detecting incoming photons and is essentially the fraction of the number of incident photons that generate useful signal. The QE is a monochromatic measurement and a graph of values measured over a broad range of wavelengths/energies, termed the spectral response.

The X-ray QE of a CCD is highly affected by the energy of the incident photons, due to the consequences of the photon absorption length in silicon. The QE can be reduced both for low energy photons ( $< 0.5$  keV), due to very high absorption of photons in the dead layers on the surface, and for high energy photons, because of the large absorption length resulting in very low absorption. Thus, in traditional front illuminated CCDs, very poor QE is realised at short wavelengths such as blue light, ultra-violet and soft X-ray because of absorption in the electrodes. Equally, the depletion region of traditional devices does not extend sufficiently deeply into the silicon to efficiently collect charge generated by higher energies ( $> 10$  keV) [Burt 2006].

Another major contributor to the reduced optical QE of CCDs is the reflection of light from the surface, caused by a mismatch in refractive indices. This can be reduced by deposition of an anti-reflection coating on the CCD surface that is optimised for a particular wavelength of light, depending on the application.

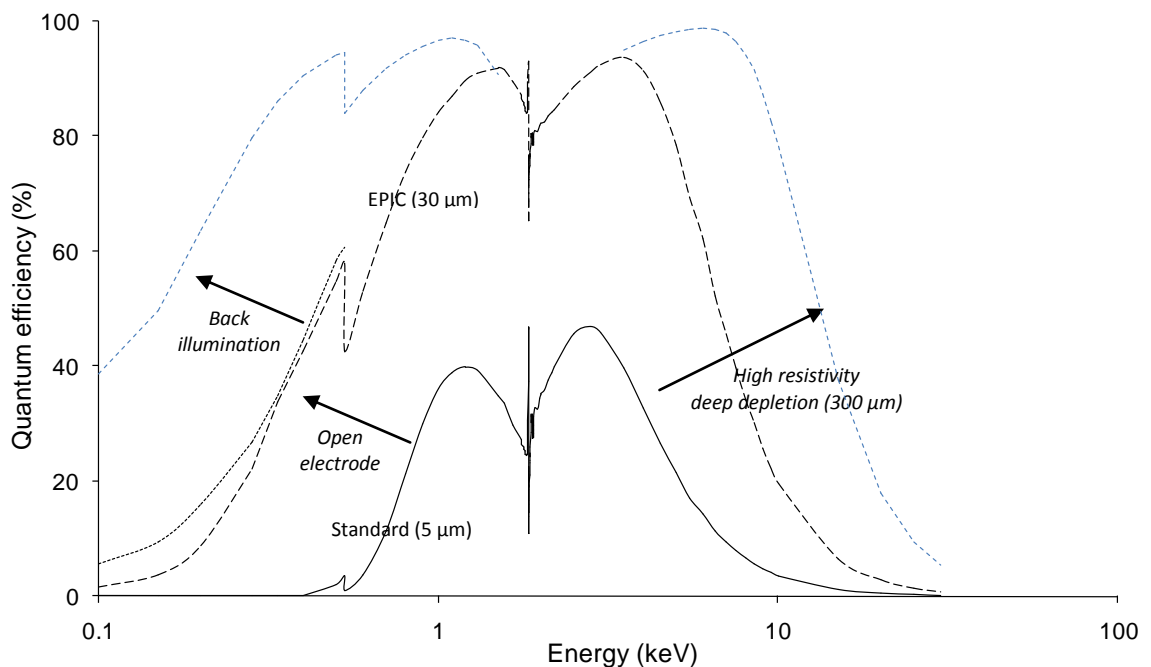


**Figure 3.8** Typical QE and improvement strategies

A number of technologies have been established to overcome these problems, improving the QE of the CCD over a broad band of wavelengths. Examples of backside illumination, high resistivity and open electrode phase effects are shown in Figure 3.8 and are described in detail in the following sections.

The practical measurement of the quantum efficiency of a CCD is described and compared to that of a theoretical model in Chapter 7.

### 3.2.5 QE Enhancements

#### 3.2.5.1 Backside illumination

Backside illumination increases QE at blue and UV wavelengths (short), by reducing absorption in the surface layers of the silicon. The CCD is manufactured in the same manner as a conventional front-illuminated device; however the light is focussed onto the back surface to avoid any attenuation through the electrode structures [Shortes et al 1974]. High QE is achieved by chemically etching the backside, a process known as ‘thinning’, to a thickness where the electric field extends to the rear surface with a linear gradient. This ensures the majority of photons generate e-h pairs in the active silicon, within clearly defined pixel boundaries to prevent lateral diffusion.

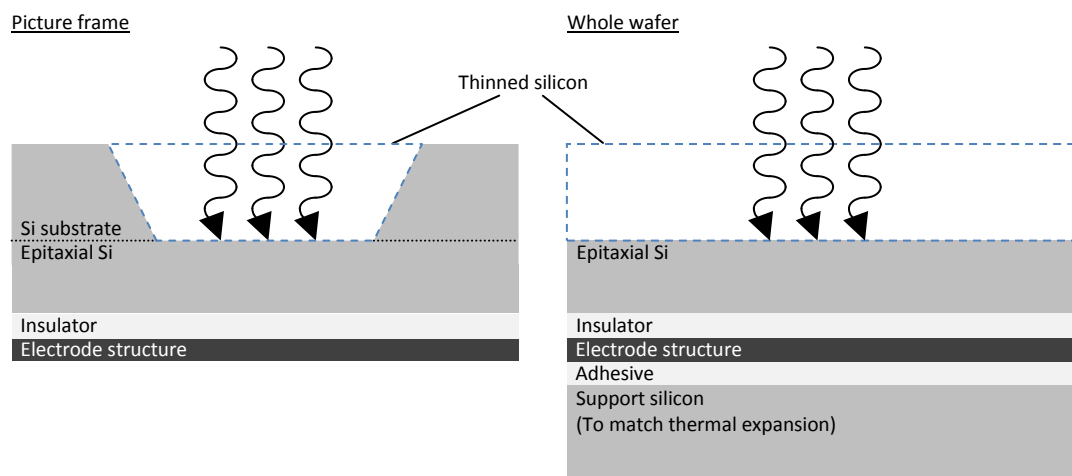


**Figure 3.9** ‘Back thinned’ CCD manufacturing examples

Figure 3.9 demonstrates two practical methods of producing back-thinned CCDs. The example on the left shows an early method of thinning that removes a section of the substrate over the imaging surface. The ‘thinned’ section is very delicate and prone to breaking under mechanical stress and CCD is prone to suffering a greater number of dark current artefacts. It is usual for the manufacturing yield of this process to be low, especially for large imaging area CCDs. The method adopted by e2v technologies for producing back-thinned CCDs is shown on

the right of Figure 3.9. The CCD is adhered to a support wafer prior to thinning and the entire substrate is then removed by mechanical lapping and chemical etching down to the epitaxial layer. A resistive-selective etching solution can be chosen to only affect silicon at the doping concentration of the substrate and not that of the epitaxial layer, resulting in a clean flat surface. A final non-selective etch is applied for a short time to remove any irregularities at the epitaxial interface [Burt 2006].

After the etching process, a native oxide layer ( $< 10 \text{ \AA}$ ) naturally grows on the rear surface. The ability of an oxygen atom to be able to share only two electrons in the crystal lattice creates hole-vacancies at the silicon interface, giving both positive charge and recombination centres. This charge results in a depleted region at the back surface that will sweep any photo-generated charge into the oxide before re-combining. This backside depletion counteracts any sensitivity that was gained in the shorter wavelengths by back-illumination and therefore needs to be eliminated by bringing the back surface into accumulation, which is known as 'passivation'. The accumulated region has an excess of free majority carriers (holes) and provides a negative charge that repels any photo-generated minority carriers, i.e. electrons, from the rear surface and towards the CCDs potential wells [Huang et al 1989].

There are two popular methods employed to passivate the hole-carriers in the native oxide. The hole-vacancies can be filled with electrons prior to use, by exposing the device (pre-charging) with UV light in the presence of oxygen. UV light ( $\sim 5 \text{ eV}$ ) passes through the native oxide and is immediately absorbed by the denser silicon immediately below the rear surface. Electrons are released from the valence-band of the Si atoms that pass into the conduction-band of the oxide, causing the adsorption of  $\text{O}_2$  ions at the oxide surface, negatively charging it. The  $\text{O}_2$  ions need to be periodically replaced with subsequent UV exposures as they desorb in time, particularly under thermal cycling and hence 'UV flooding' can only be a short term solution [Janesick et al 1985].

A back-surface doping technique ('delta-doping') is a long term solution with no requirement to re-charge the recombination centres over time and gives the back illuminated CCD a reflection limited response (100 % internal QE). Once the back thinning process has been completed, a layer of boron ions ( $\text{p}^+$ ) are implanted below the back surface by molecular beam epitaxy or ion-implantation. This introduces a potential step in the electric field that repels electrons from the back surface and towards the potential wells [Nikzad et al 1994]. Some damage to the silicon lattice is caused by the above process that is repaired by annealing with a laser, although this process can itself leave undesirable artefacts that can be observed in flat-field illuminations.

### 3.2.5.2 High resistivity

The infra-red and X-ray sensitivity of a CCD can be enhanced by extending the depletion depth into the p-region of the p-n diode structures by forming a larger depletion potential through the thickness of silicon [Groom et al 2000]. This is achieved by increasing the potential that reverse biases the p-n diode structures. High resistivity silicon can be produced by lowering the donor/acceptor dopant concentration that will allow full depletion of the wafer thickness before breakdown occurs. Traditionally doped CCDs suffer from breakdown of the p-n diodes at the potential difference required to deplete the thickness of the wafer (300  $\mu\text{m}$  to 500  $\mu\text{m}$ ) [Rusu & Bulucea 1979]. Figure 3.10 demonstrates the difference in potential profiles through a standard CCD and a high resistivity CCD. The standard device in the example has a potential difference of 11 V between the electrode structure and the substrate potential connection. The high resistivity device uses a negative substrate potential (-20 V) to provide the large potential drop across the p-n diode. Practically, the substrate bias is lowered, rather than raising the electrode potential, to maintain the potential well.

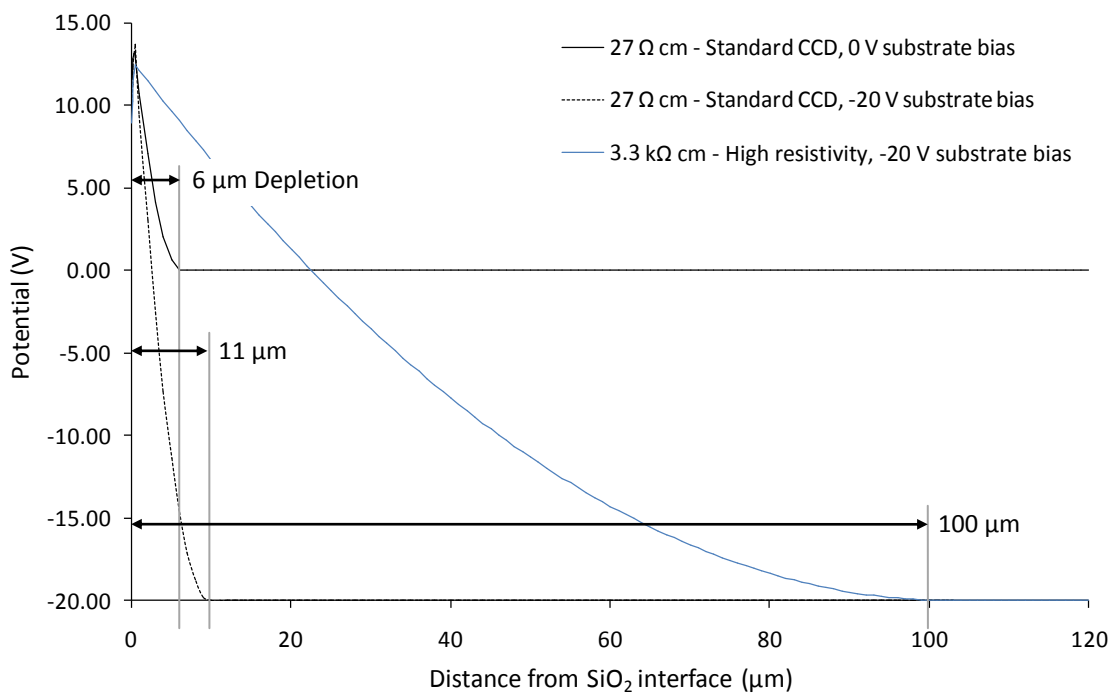


**Figure 3.10** Buried channel CCD potential profiles

The depletion of the CCD extends into the silicon to the depth where the gradient of the potential profile falls to zero. Figure 3.10 shows that the greater the potential applied across the diode structure, the greater the depletion. By increasing the resistivity of the silicon the same applied potential yields a greater device depletion depth. The increased active silicon cross-section in high resistivity CCDs, leads them to be referred to as 'thick'.

Thicker back illuminated CCDs also suffer less from the optical fringing problem associated with back illuminated CCDs. The longer wavelength photons have a very low probability of travelling far enough through the silicon to be reflected twice before they are absorbed.

### 3.2.5.3 *Open and Thin electrodes*

The 'blue' (475 nm) to 'soft X-ray' (< 0.5 keV) response of CCDs can be improved for front-illuminated devices by reducing the thickness of the overlying electrode structure, hence reducing the amount of photon absorption. The two adopted methods to achieve this are to either manufacture the CCD with one of the electrode phases larger in area but thinner in cross section, or to provide an 'open area' over the pixel by removing portions of an electrode phase [Lumb et al 1991]. Figure 3.11 shows examples of these two methods. The thin electrode region of the JET-X CCD shown on the left of Figure 3.11 has a dead layer of only 340 nm. The EPIC structure shown on the right has approximately 40% of the pixel area free from polysilicon and has been successfully employed on XMM-Newton.

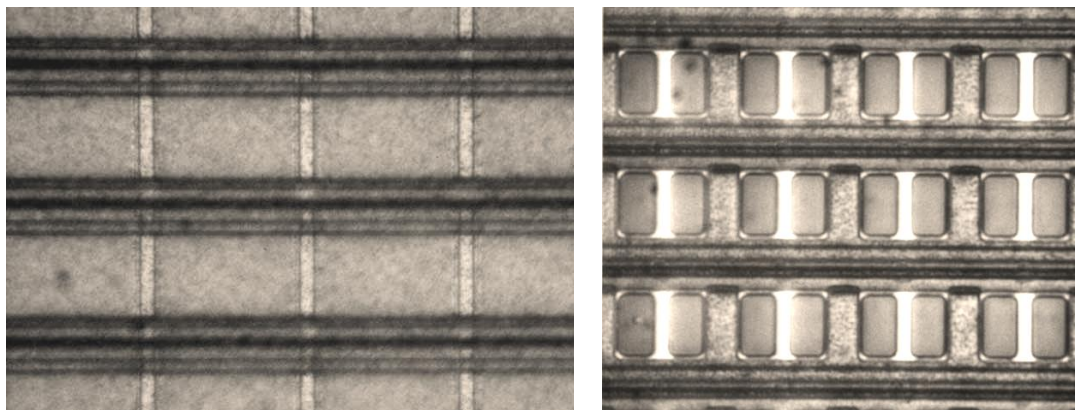


**Figure 3.11** Thin electrode (left) and open electrode (right) structures (courtesy A.D. Holland)

## 3.3 Charge storage

### 3.3.1 The pixel structure

The CCD imaging area comprises a discrete number of picture elements (pixels) that are defined by electrodes and channel stops as shown in Figure 3.12.

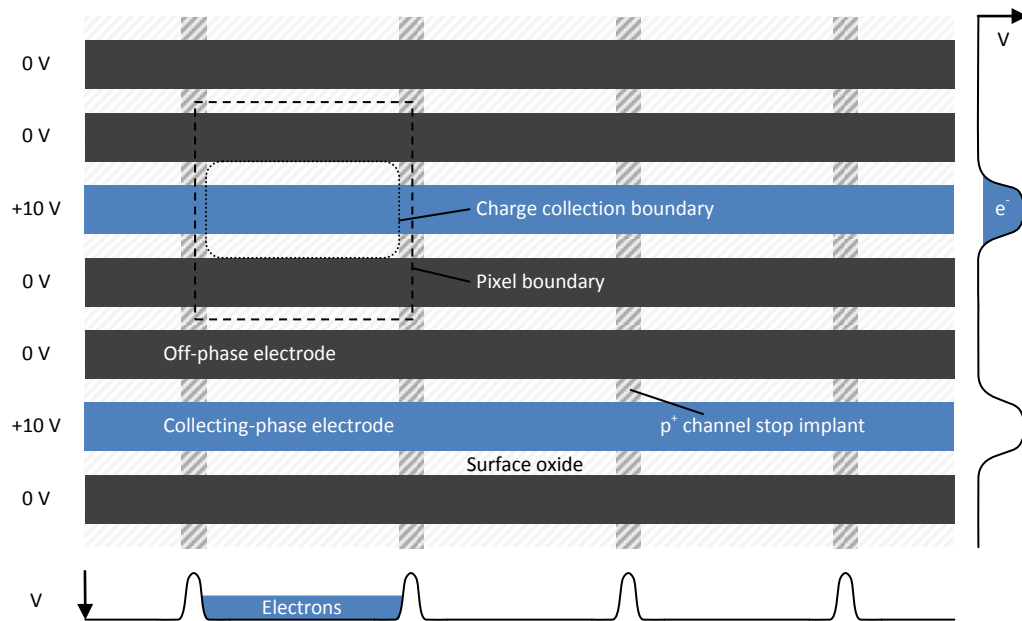


**Figure 3.12** The pixelated structure of a CCD

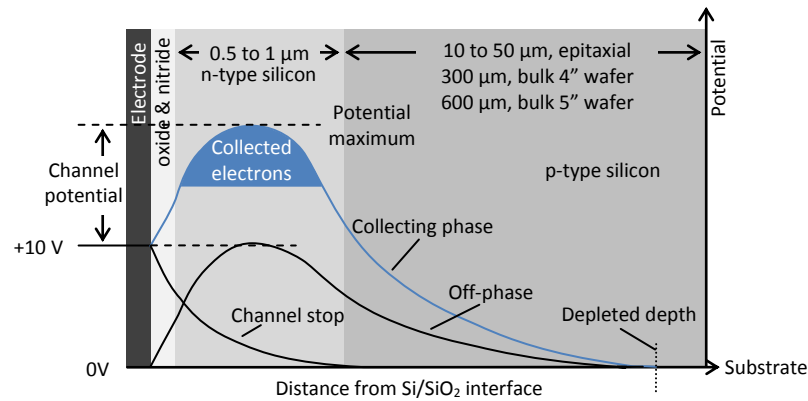
The electrode structures, running in the horizontal direction, are suitably biased to confine the pixel boundaries in the vertical-axis. The collecting-phase electrode is biased with a high potential to define the vertical centre of the pixel in the array by depleting the silicon below it. This creates an electric field that will cause any mobile electrons to drift towards its potential maximum (collecting point). The off-phases are biased at a lower potential (typically 0 V) with respect to the substrate potential to define clear boundaries between the vertical pixels.

The channel stops are formed by  $p^+$  implants that confine pixels in the horizontal axis by repelling signal electrons from their fixed negative charge.

### 3.3.2 The buried-channel

Early CCDs (surface channel) were constructed such that the charge was stored at the silicon surface and suffered poor charge transfer efficiency (CTE) and energy resolution as the oxide interface with the silicon surface generates hole-carriers that can trap electrons [Sze 1981].

The buried channel CCD was devised to overcome the problem of the collected charge recombining with the hole-carrier states found at the  $\text{SiO}_2$  interface ( $< 0.1 \mu\text{m}$ ) by holding the stored/transferred charge away from the surface ( $\sim 0.5 \mu\text{m}$ ). This is achieved by superimposing a secondary potential gradient onto that generated by the applied electrode by means of a depleted p-n junction. The p-n junction is reversed biased by a sufficient potential difference to deplete the entire n-region of electrons. The donor concentration in the n-region is far higher than that of the acceptor in the p-region and therefore the depletion extends further into the p-region to ensure charge conservation [Howes & Morgan 1979].



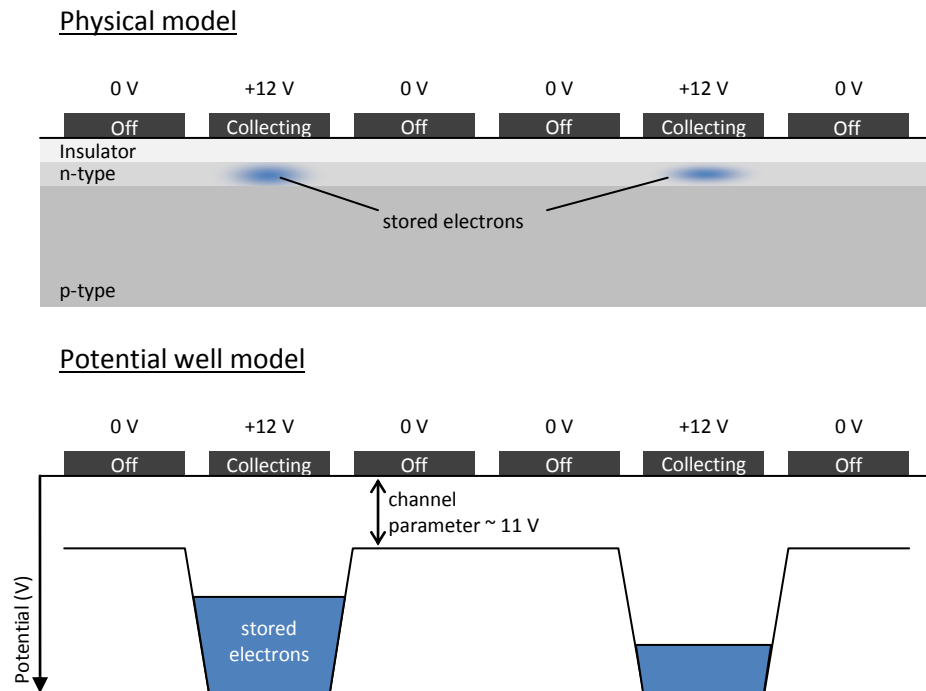
**Figure 3.13** The buried-channel potential well

Figure 3.13 shows the potential profile through the depth of silicon for the three regions of interest in a pixel. The depleted depth is the distance of active silicon that will efficiently collect charge generated by the photo-electric effect. The potential maximum of the collecting-phase is the location where any photo-generated charge will be stored. The buried channel potential of the e2v CCD247 is modelled in Chapter 6 to ascertain the depletion depth for an applied substrate potential.

The buried channel n-regions are formed by doping sections of the epitaxial silicon with phosphorus by ion-implantation. All modern scientific CCDs incorporate a buried channel; therefore the remaining sections of this thesis assume the use of this technology.

### 3.3.3 The potential well model

The potential well model, shown in Figure 3.14, is used to illustrate the location of charge collection within a cross-section of the CCD. It is analogous to a series of buckets collecting water at their lowest point due to gravity.



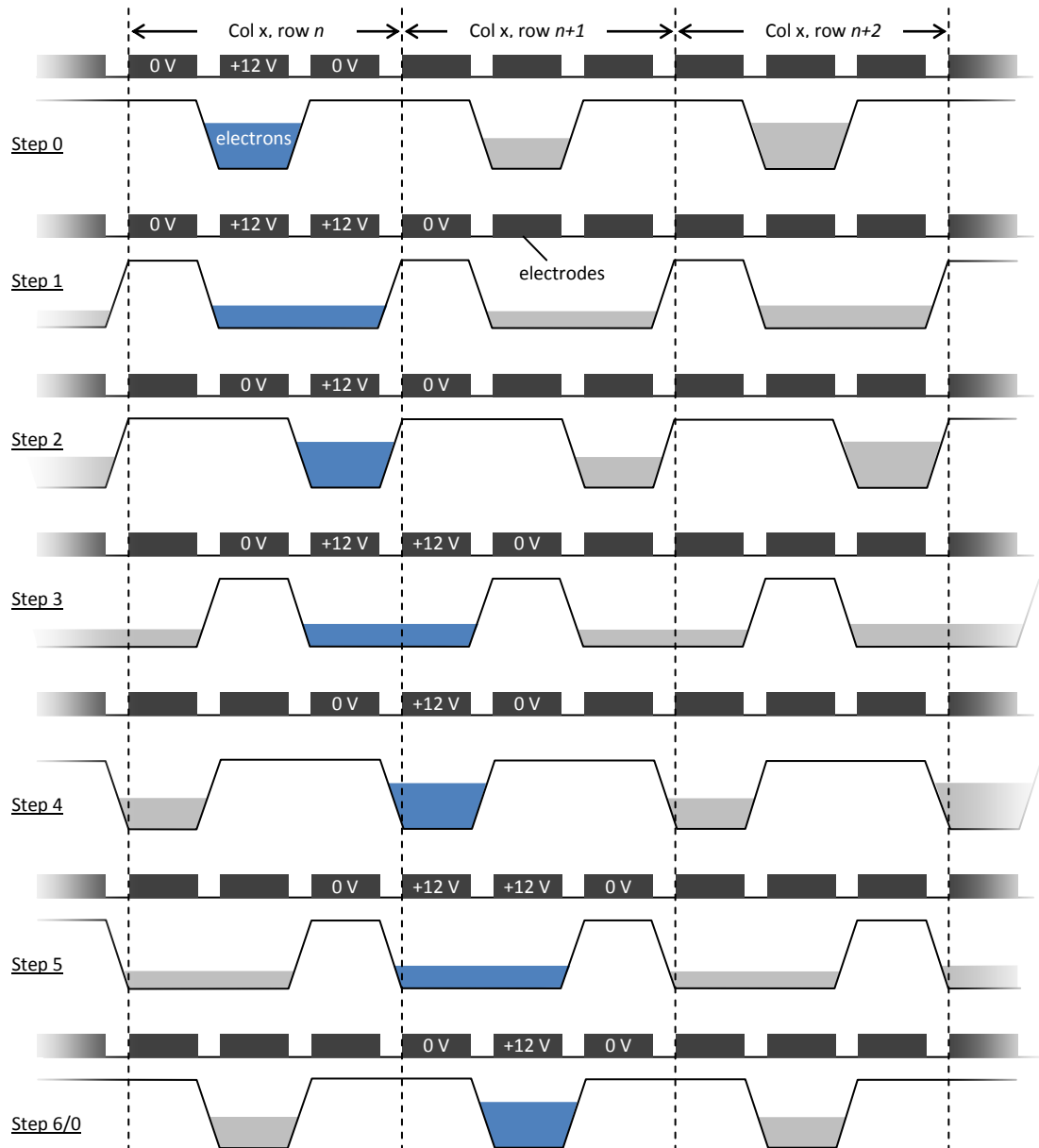
**Figure 3.14** Buried channel CCD potential well model

## 3.4 Charge Transfer

### 3.4.1 Moving charge

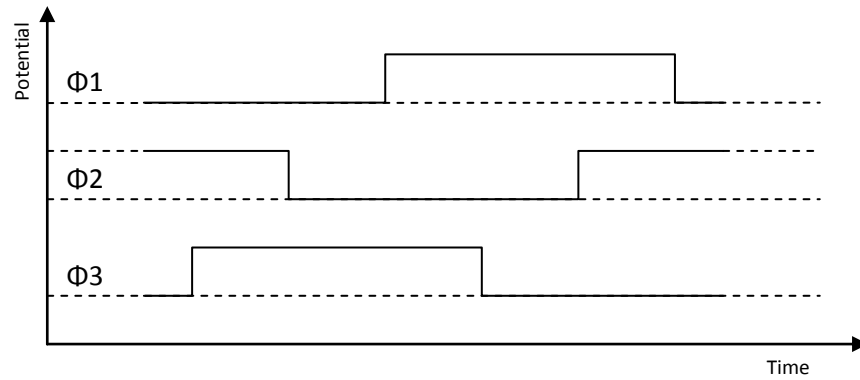
Charge is transferred vertically from all pixels in the image one row at a time into a horizontal (serial) register, which is read out sequentially in between row transfers. The mechanism for moving pixel charge packets through the silicon is by changing the location of the potential wells. This is achieved by altering the biases of the collecting-phase and off-phase electrodes sequentially.

Figure 3.15 shows the sequence of steps that transfer pixel charge packets vertically in a three phase CCD. At step 0 the charge has been collected and stored in the potential well during the integration of the image. In step 1, the off-phase electrode of the pixel towards the direction of desired charge transfer is biased at the same potential as the collecting-phase. This widens the potential well under the pixel as the charge is now distributed below two electrodes. The original collecting-phase electrode is then biased to 0 V in step 2 to complete the transition of charge by one electrode across the CCD. Steps 3 to 6 repeat the same processes to complete the transfer of the pixel charge packets by 1 pixel row (3 electrode transfers) across the imaging area.



**Figure 3.15** Charge transfer in a three phase CCD with 100 % overlap

The sequencing of the three electrode phases are shown in Figure 3.16. that allows the charge transfer in Figure 3.15. The vertical transfer operation moves an entire row of pixels together and is therefore commonly termed a 'parallel transfer'.



**Figure 3.16** Overlapping clock sequence for electrode phases

The serial register, located at the end of the imaging area, has a similar multi-electrode structure to transfer pixel charge packets horizontally towards the output amplifier(s) and is referred to as 'serial transfer'.

The electrode structure in Figure 3.15 shows gaps in between the electrode structures. In practice these gaps allow a thicker surface oxide to grow during manufacture. The potential across the oxide layer,  $V_{OX}$ , can be calculated by [Howes & Morgan 1979]:

$$V_{OX}(V) = \frac{2qN_A t^2}{\epsilon_{Si}} \left(1 + \frac{\epsilon_{Si} d}{\epsilon_{OX} t}\right)^2 \quad (\text{iii-iv})$$

Where  $q$  is the electronic charge,  $N_A$  is the acceptor doping concentration,  $t$  is the thickness of the buried channel,  $\epsilon_{Si}$  is the permittivity of silicon,  $d$  is the thickness of the oxide and  $\epsilon_{OX}$  is the permittivity of the silicon dioxide.

When the thickness of the oxide is increased, the potential well underneath the electrode gap is also increased. This creates an uneven potential well profile along the charge transfer channel that can cause charge to become trapped in 'pockets'. It is therefore vital to minimise the spacing between electrodes to ensure a smooth potential well profile is formed along the transfer channel. Figure 3.17 demonstrates 'pockets' between the potential wells that can exist in a buried channel CCD when the electrode spacing is too large. This causes poor charge transfer efficiency (CTE) as some of the charge becomes trapped between transfers.

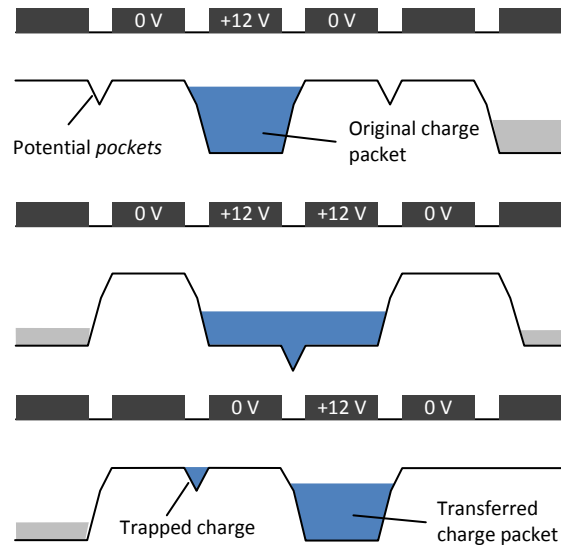


**Figure 3.17** Charge trapping of inter-electrode gap potential ‘pockets’

The charge trapping effect is reduced with electrode separations of less than  $1\ \mu\text{m}$ , although such a small spacing is difficult to manufacture in the standard etch process [Burt 2006]. The standard method CCD manufacturers use to fabricate sub-micron electrode separations is with an overlapping electrode structure, shown in Figure 3.18 and 3.19. This process allows a very narrow gap to be formed down to the thickness of the insulation ( $\sim 100\ \text{nm}$ ) between electrodes [Burt 2006].

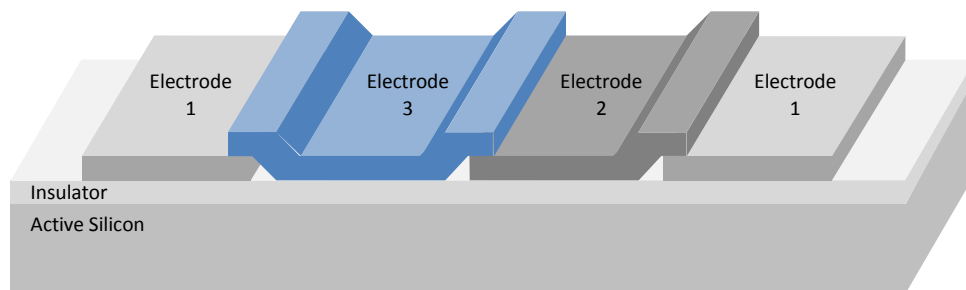


**Figure 3.18** Overlapping CCD electrodes

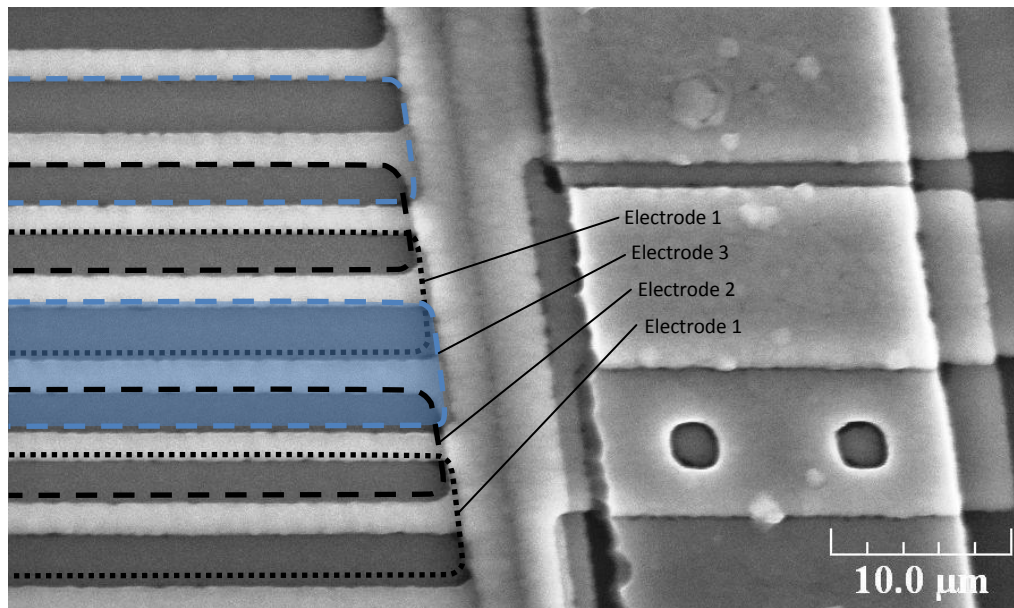


**Figure 3.19** SEM image of the overlapping electrode structure

For future reference the electrode phases will be referred to as numbers and the type indicated by (I) for image, (S) for store and (R) for the serial readout register. Therefore the 3 phases in the serial readout register section become RΦ3, RΦ2 and RΦ1.

### 3.4.2 Charge trapping

Charge traps extract a portion of the signal charge as it is transferred through the CCD giving the effect of smearing over a number of pixels as the charge is slowly released into subsequent pixels. This effect gives charge transfer inefficiency (CTI) that is typically better than 1 occurrence in  $10^6$  pixels in modern buried channel CCDs [Janesick 2001]. Figure 3.20 demonstrates deferred charge tails in a CCD image of X-ray events in the vertical axis.

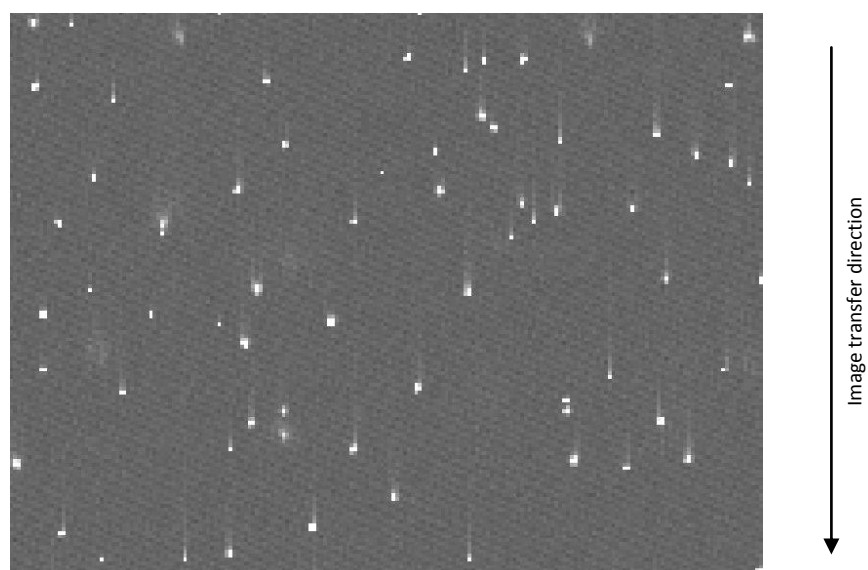


**Figure 3.20** Charge smearing in the parallel direction due to CTI

The inclusion of the buried channel effectively eliminates charge trapping at the surface interface although other sources still exist. Any impurities added during the growth of the silicon crystal or introduced during fabrication can cause defects in the lattice, leading to bulk traps. These are the most dominant source in modern CCDs [Janesick 2001].

Other sources leading to a degradation of CTE are energetic particles that can damage the silicon lattice by displacing dopant atoms in the buried channel used to transfer the charge. This presents a major problem in space bound CCD applications as the exposure to such particles is higher because of the lack of protection from the Earth's magnetic field. The radiation damage of CCDs is extensively discussed in the thesis works of Smith (2004) and Holland (1990). The boron atom is considered to be less susceptible than phosphorus to displacement by proton irradiation [Janesick et al 1991] [Hopkinson 1999]. Therefore CCDs for space applications are currently being developed with boron doped buried channels (p-type) on n-type substrates to improve tolerance to high energy particles ('radiation hardness') [Dawson et al 2008]. These p-channel CCDs collect and measure holes rather than electrons from the photo-generation of e-h pairs and are discussed in Chapter 5.

### 3.4.3 Frame transfer architecture

A frame transfer CCD is used to capture an image with a short integration time to reduce image smear during readout. The image is collected in the upper section of the CCD before being rapidly transferred into a store region below it where it can be read out at a slower rate. A subsequent frame can be integrated in the image section during the readout of the previous frame. Frame transfer specific CCDs will usually have an additional layer of opaque material, usually aluminium, over the store section to prevent any further integration of light signal during readout. The architecture of a frame transfer CCD is shown in Figure 3.2

### 3.5 Signal Measurement

#### 3.5.1 The output node capacitor

At the end of the serial register is a capacitor formed by a region of  $n^+$  silicon that stores the pixel charge packets. In between the serial transfer of pixel charge packets this capacitor is reset by the activation of a field effect transistor (FET) that connects a fixed potential bias to the capacitor. The amount of charge stored in this capacitor will vary between resets; the reason for this is discussed in Section 3.6.2 of this chapter.

#### 3.5.2 The output circuit

The output circuit comprises a MOSFET amplifier and reset FET that are connected to the output node capacitance. The potential applied to the gate by the charge stored in the output node capacitor controls the flow of electrons from the source to the drain potential. A load is placed between the output MOSFET source and a suitably lower potential than the drain as shown in Figures 3.21 and 3.22 [Burt 2006]. The potential drop across an external load is measured to give a representation of the pixel signal.

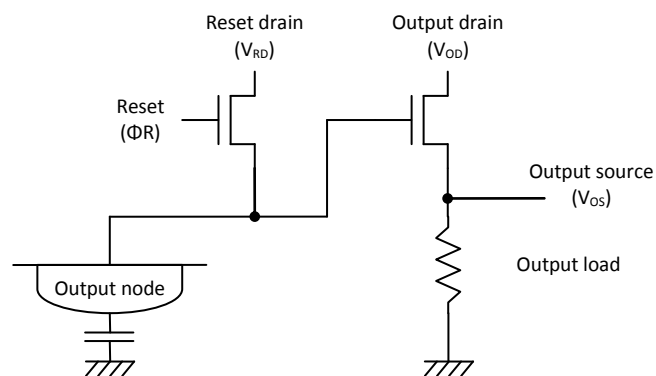


Figure 3.21 CCD output circuit schematic

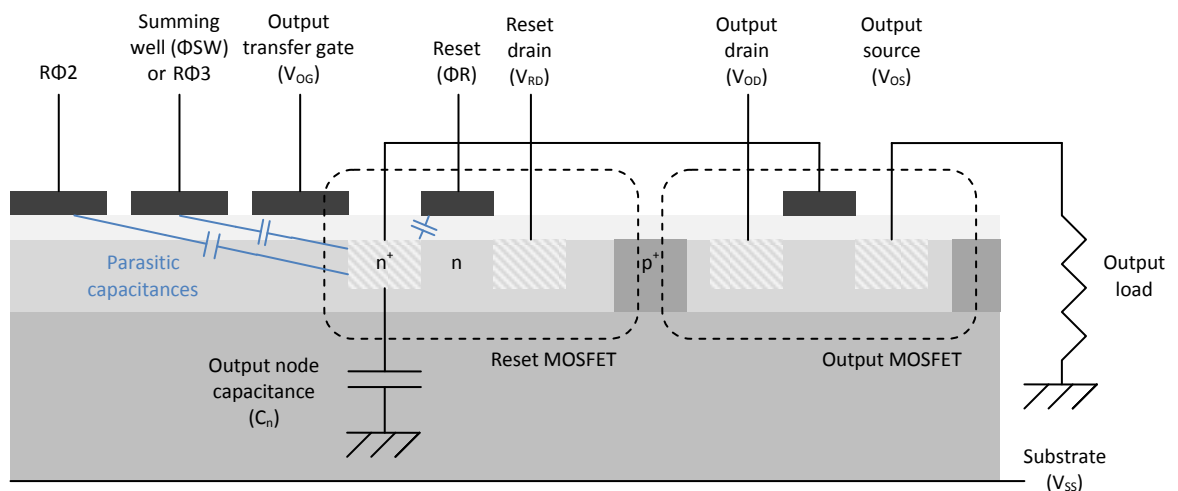
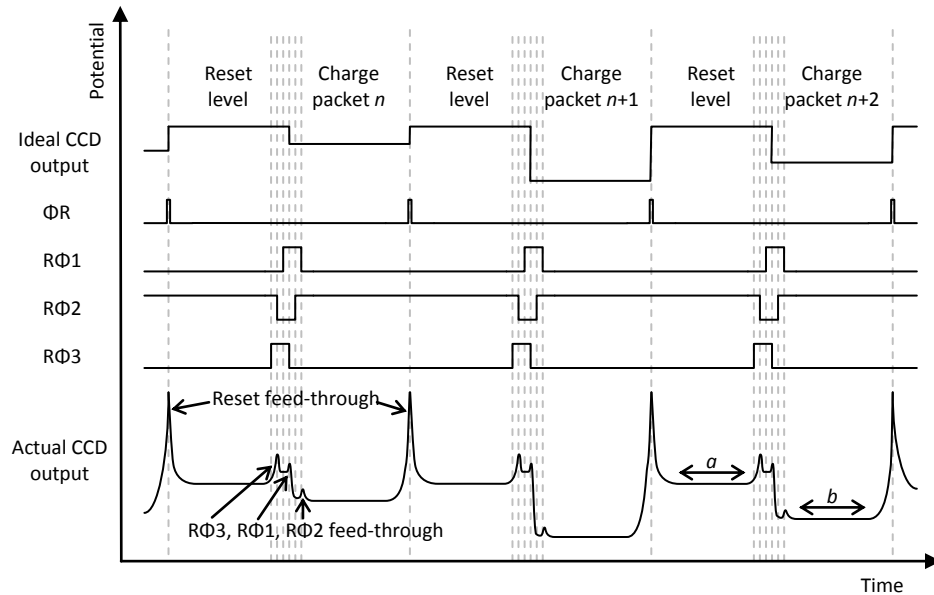


Figure 3.22 CCD Output circuit

Parasitic capacitances exist between the output node and local electrode connections. These include the gate of the reset FET ( $\Phi_R$ ) and the closest serial register electrodes ( $R\Phi_3$ ,  $R\Phi_2$  &  $R\Phi_1$ ). When these change potential levels during the clocked sequence some of the A.C. charge is fed through to the output node and appears at the output. Figure 3.23 shows the typical capacitive feed-through onto the CCD output.



**Figure 3.23** Capacitive feed-through of CCD control clocks onto output node potential

The closer the source of the parasitic capacitance is to the output node, the greater the amplitude of the A.C. feed-through. Therefore the gate of the reset FET induces the feed-through with the greatest amplitude onto the CCD output, followed by R $\Phi_3$ , R $\Phi_2$  and finally R $\Phi_1$ . Care must be taken to sample the CCD output after the settling of the feed-through potentials, indicated by regions *a* *b* in Figure 3.23.

The output MOSFET and output node capacitor are sized to yield a typical potential increase of 1 to 6  $\mu\text{V}$  for every electron added to the output node capacitor and is termed  $R_n$ , the responsivity. The responsivity at the node is defined by [Burt 2006]:

$$R_n = \frac{q}{C_{node}} \quad (\text{iii-v})$$

Where  $q$  is the electronic charge and  $C_{node}$  is the output node capacitance that is governed by the output node diffusion size and its proximity to neighbouring features. Therefore the responsivity can be tuned by altering the feature size of the output node diffusion and hence its capacitance, the smaller the capacitance the higher the responsivity. Higher responsivity

yields reduced charge handling capacity and hence high responsivity CCDs are only suitable for low signal applications such as X-ray spectroscopy.

The rate at which the output amplifier can provide pixel values for sampling is determined by its time response, governed by the output impedance of the amplifier and the load capacitance. To increase the output rate and hence pixel throughput of the CCD, the output impedance of the amplifier must be lowered. This is achieved in practice by including extra amplifier stages.

### 3.5.3 Multi-stage output amplifiers

Additional amplifier stages can be used to lower the output impedance, reducing the time constant of the output load, allowing it to be changed at a higher rate [Janesick 2001]. The output impedance is progressively reduced by each stage by increasing the width of the MOSFETs, increasing their current flow capacity and hence lowering the impedance. The 1<sup>st</sup> stage MOSFET and output node capacitance must be kept to the original sizing to preserve the sensitivity of the amplifier. Figure 3.24 shows a 2-stage output amplifier schematic that is employed in some of e2v's scientific CCDs.

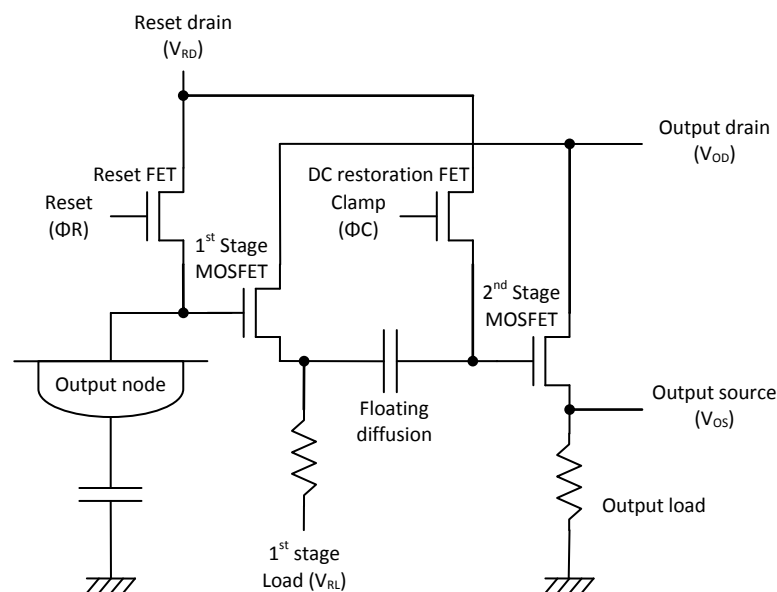


**Figure 3.24** CCD multi-stage output circuit schematic

It is necessary to periodically reset the charge held in the floating diffusion to prevent it from saturating and is achieved similarly to the reset of the output node capacitor. A clamp signal ( $\Phi_C$ ) activates the D.C. restoration FET that resets the floating diffusion to the reset drain ( $V_{RD}$ ) potential. The clamp operation need only be performed once per CCD row due to the

relatively large size of the floating diffusion compared to the output node and hence is connected to the image clock  $I\Phi 3$  in e2v devices.

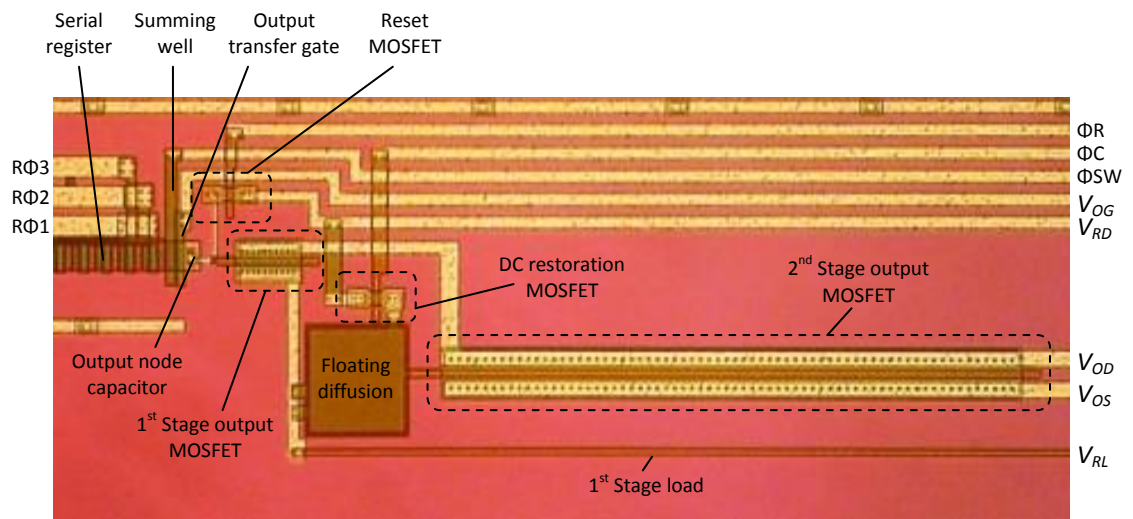


**Figure 3.25** 2-stage output amplifier

Figure 3.25 shows a photograph of the output region of the 2-stage output CCD218. The output of the 1<sup>st</sup> stage MOSFET is stored in a large floating diffusion that acts as the 2<sup>nd</sup> output node capacitance. The charge stored in this 2<sup>nd</sup> output node controls the gate of the 2<sup>nd</sup> stage MOSFET that drives the external output load between the output source ( $V_{OS}$ ) and 0 V. In this example the 1<sup>st</sup> stage load ( $V_{RL}$ ) is fabricated on the CCD and biased to 0 V. It is important to note the 2<sup>nd</sup> stage MOSFET is clearly a number of times wider than the 1<sup>st</sup> stage to provide the reduced output impedance.

The summing well ( $\Phi_{SW}$ ) connection shown in Figure 3.25 facilitates on chip-binning and is usually connected to  $R\Phi 3$  in applications where binning is not required.

### 3.6 Noise sources

Of the many noise sources generated within the CCD the two major contributors are the dark current and reset level noise both of which must be suppressed to enable good X-ray spectroscopy. Consideration also has to be given to cosmetic defects and the generation of cosmic ray traces generated in the prototype CCDs used in the experimental work of this thesis.

#### 3.6.1 Dark current

Thermal energy can excite electrons into the conduction-band of the silicon atom and is termed 'dark current' as the CCD will measure this random electrical charge. This charge cannot be distinguished from the photo-generated charge measured, therefore it is important

to cool the silicon to minimise the occurrence [Burt 2006]. For X-ray photon induced charge packets to be measured with an acceptable SNR the CCD must be cooled to at least 233 K.

### 3.6.2 Reset noise

Reset level noise has a large impact on the SNR and must be eliminated to make X-ray spectroscopy with CCDs at all possible. Reset noise is found on all CCD output signals and is caused by the Johnson noise in the reset FET. Johnson noise is a random fluctuation in the current flow in a conductor as the free electrons collide with one another [Johnson 1928]. Figure 3.26 demonstrates that this noise can cause a variation in the charge flowing through the reset FET (b) from the potential bias of the reset drain (a) to the output node and causes a non-deterministic reset value to be stored in the output node (c) when the FET is closed.

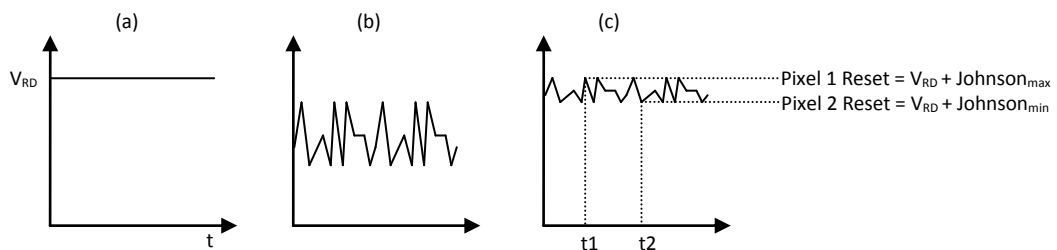


**Figure 3.26** Johnson noise modulation of output node

The signal charge packet of a pixel is added to the reset level held in the output node during the serial clocking operation. Therefore both the reset level and ‘clocked’ signal level contain exactly the same reset noise component. By measuring the reset level and using it as a reference to subtract from the signal level the exact signal charge packet can be found. This practice is called correlated double sampling (CDS) and effectively eliminates the reset noise [Janesick 2001]. The remaining noise is that due to the source follower transistor(s).

### 3.6.3 Cosmetic defects

Defects in the silicon, manufacturing processes and radiation damage can all cause regions of the CCD to not perform correctly. Such defects can manifest as bright or dark pixels or columns in the imaging area and tend to occur at consistent locations. In X-ray spectroscopy it is possible to simply ignore the areas affected by cosmetic defects by setting an exclusion zone around them.

### 3.6.4 Cosmic rays

Cosmic rays constantly bombard the Earth, imparting energy into the matter they encounter and hence can be observed with CCD detectors. Cosmic rays are generated by high energy protons from the Sun and other celestial sources that interact with the Earth’s stratosphere

generating secondary particles. It is the secondary particles that can be observed by the CCD and are incident at an undeterminable direction and time. Cosmic rays are therefore a problem for images taken at observatories with long integration times as they are unavoidable. At sea level cosmic rays appear at a rate of approximately  $90 \text{ hour}^{-1} \text{ cm}^{-2}$  [Janesick 2001]. A CCD with an imaging area of  $1.9 \text{ cm}^2$ , such as the  $2048 \times 512 \times 13.5 \mu\text{m}^2$  pixel devices used in the experimental work in this thesis, will encounter cosmic rays at a rate of 1 in every  $\sim 21$  seconds. At a read out rate of  $150 \text{ k pixels sec}^{-1}$  the image taken by the CCD can have a minimum integration time of  $\sim 10.7$  seconds. It is therefore possible to acquire frames that do not contain any cosmic ray interactions. For the device characterisation work in this thesis it is possible to simply ignore and re-acquire any frames that do contain cosmic rays.

### 3.7 Summary

This chapter described the generation of electronic charge within silicon by incoming photons and the dependence of the photons wavelength with the amount of charge generated. The absorption of photons within silicon was discussed to highlight the requirement of thicker CCDs to efficiently detect high energy and long wavelength photons such as the infra-red and X-ray. Charge diffusion of the electron-hole pairs generated in silicon by the photoelectric effect was described to introduce the problem of spatial resolution in CCDs with the deeper ionising photons. The QE metric for CCDs was presented with some of the technological developments for improvement.

The buried channel CCD was discussed to introduce the pixelated imaging structure produced by the depletion of an array of p-n diodes. The charge coupling mechanism that enables the transfer of pixel charge packets through the CCD structure towards the output amplifier was described. The problem of charge trapping was discussed along with the development of overlapping electrodes, buried channel and p-channel technology to overcome trapping.

The method for measuring the pixel charge packets of the image as a serial voltage output was described in Section 3.5. The improvement in readout speed was also presented by the use of multiple stage outputs.

The final section of this chapter reviewed the major noise source contributions that had to be overcome in the experimental work in this thesis. These were the dark current, reset noise, cosmetic defects in the imaging area and cosmic rays.

The next chapter will present the laboratory equipment used to allow the characterisation of CCD detectors with particular reference to the use of CDS to eliminate reset noise.

### 3.8 References

- Bertolini, G. & Coche, A., 1968. Semiconductor devices. *Elsevier Science*.
- Boyle, W.S. & Smith, G.E., 1970. Charge-coupled semiconductor devices. *Bell System Technical*, Vol. 49, p. 587-593.
- Burt, D.J., 2006. Private communication.
- Dawson, K. et al., 2008. Radiation tolerance of fully-depleted p-channel CCDs designed for the SNAP satellite. Submitted to *IEEE*.
- Everhart, T.E. & Hoff, P.H., 1971. Determination of kilovolt electron energy dissipation vs. penetration distance in solid materials. *Applied Physics*, Vol. 42, p. 5837.
- Fitting, H.J. et al., 1978. Attenuation length and escape depth of excited electrons in solids. *Surface Science*, Vol. 75, p. 267-278.
- Geist, J. & Zalewski, E.F., 1979. The quantum yield of silicon in the visible. *Applied Physics Letters*, Vol. 35, p. 503-505.
- Geist, J. et al., 1983. New calculations of the quantum yield of silicon in the near ultraviolet. *Physical Review, Rev. B*, Vol. 27, p. 4841-4847.
- Groom, D.E. et al., 2000. Back-illuminated, fully depleted CCD image sensors for use in optical and near-IR astronomy. *Nuclear Instruments and Methods*, Vol. A442, p. 216-222.
- Hopkinson, G.R., 1983. Charge diffusion effects in CCD X-ray detectors. I. Theory. *Nuclear Instruments and Methods*, Vol. 216, p. 423-429.
- Hopkinson, G.R., 1999. Proton damage effects on p-channel CCDs. *IEEE Transactions on Nuclear Science*, Vol. 46, p. 1790-1796.
- Howes, M.J. & Morgan, D.V., 1979. Charge-coupled devices and systems. *Wiley*.
- Huang, C.M. et al., 1989. A new process for thinned, back-illuminated CCD imager devices. *IEEE Proc. VLSI Technology, Systems and Applications*, Vol. 3-3 p. 98-101.
- Janesick, J.R. et al., 1985. Backside charging of the CCD. *Proc. SPIE*, Vol. 570, p. 46-79.
- Janesick, J.R. et al., 1991. Effects of proton damage on charge-coupled devices. *Proc. SPIE*, Vol. 1447, p. 87-108.
- Janesick, J.R., 2001. Scientific charge-coupled devices. *SPIE Press*.
- Johnson, J.B., 1928. Thermal agitation of electricity in conductors. *Physical Review*, Vol. 32, p. 97-109.

- Kane, E.O., 1962. Theory of photoelectric emission from semiconductors. *Physical Review*, Vol. 127, p. 131-141.
- Lumb, D.H. et al., 1991. Charge-coupled devices (CCDs) in X-ray astronomy. *Experimental Astronomy*, Vol. 2, p. 179-201.
- McMaster, W.H. et al., 1969. Compilation of X-ray cross sections. *Atomic data and nuclear data tables*.
- Nikzad, S. et al., 1994. Delta-doped CCDs: High QE with long term stability at UV and visible wavelengths. *Proc. SPIE*, Vol. 2198, p. 907-915.
- Pavlov, G.G. & Nousek, J.A., 1999. Charge diffusion in CCD X-ray detectors. *Nuclear Instruments and Methods*, Vol. A428, p. 348-366.
- Rusu, A. & Bulucea, C., 1979. Deep-depletion breakdown voltage of silicon-dioxide/silicon MOS capacitors. *IEEE Transactions on Electronic Devices*, Vol. 26, p. 201-205.
- Shortes, S.R. et al., 1974. Characteristics of thinned backside-illuminated charge-coupled device imagers. *Applied Physics Letters*, Vol. 24, p. 565-567.
- Streetman, B.G. & Banerjee, S., 2005. Solid state electronic devices. *Prentice Hall*, 6th Ed.
- Sze, S.M., 1981. Physics of semiconductor devices. *Wiley*, 2nd Ed. p. 423.

## Chapter 4: Instrumentation, equipment and techniques

### 4.1 Introduction

This chapter reviews the laboratory equipment and techniques used in the experimental work of this thesis and covers the 3<sup>rd</sup> party CCD camera system, cryogenic equipment, noise optimisation methods and processing of X-ray events observed in CCD images.

### 4.2 Camera system

The CCD is operated and read from by a commercially available camera system that allows the operator to customise key parameters, ensuring the optimum performance can be achieved for any given device. The camera system parameters are: clock sequencing and delays, clock and bias voltages, image dimensions, pixel binning and system gain. These are described in detail in the following subsections. The camera system is controlled by a USB interface to a Windows XP® PC running a proprietary GUI that allows easy fine tuning of the operating parameters.

#### 4.2.1 Clock sequencing

The various electrode phases of the CCD are biased high and low in sequence to integrate the CCD image and then transfer it to the output amplifier as described in Chapter 3. This operation of switching electrode biases from high to low is commonly termed 'clocking' due to the importance of the timings between such operations. Electrode phases are often referred to as 'clocks' for this reason. The sequence of clocking events used to generate and read out a CCD image is written in assembler code by the user as a series of loop operations that are executed by a digital signal processor (DSP) in the 'sequencer' of the camera. The DSP is connected to an interface circuit within the camera system that buffers and amplifies the signals required to 'clock' the CCD. A number of custom sequencer programs were developed under the work of this thesis.

Additional delay loops and no-operation (NOP) instructions are included in the sequence program to match the instruction cycle time of the DSP to the optimum timings for the CCD. Figure 4.1 shows a flowchart of the CCD sequence program for a full frame image.

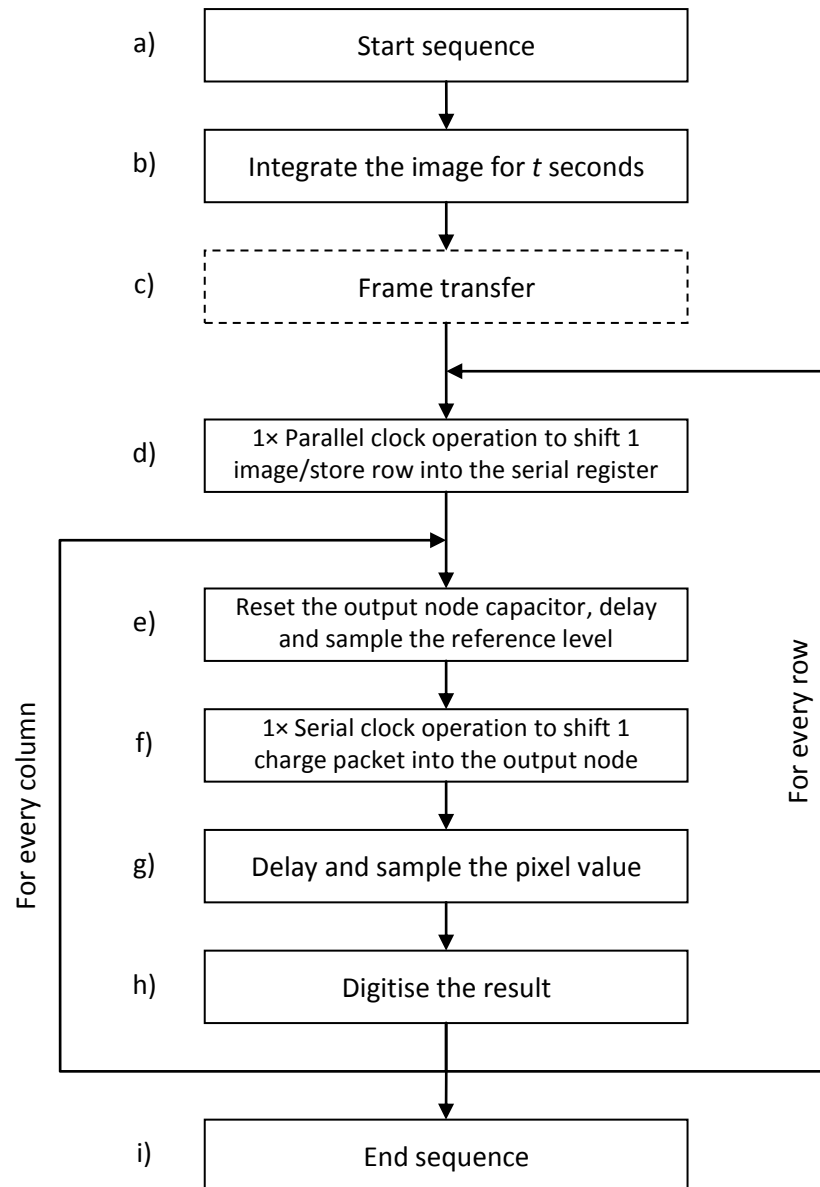


**Figure 4.1** CCD image capture and readout sequence flow diagram

The first operations of the sequence program are to set up the input and output flags of the DSP that are used to drive the electrode clock signals and readout circuitry. The image is then integrated by biasing one or two of the image electrode phases high for the duration of a user specified time delay. Biasing two electrodes high during integration allows the p-n diodes of each pixel to have a greater depletion, as the weighted-average potential driving depletion in the pixel area is higher.

The first row of pixels is then transferred into the serial register by calling the first parallel clock loop d). All rows in the image become shifted down by 1 row during this operation. The parallel clock loop performs the sequence of steps 0 to 7 shown in Figure 4.2.

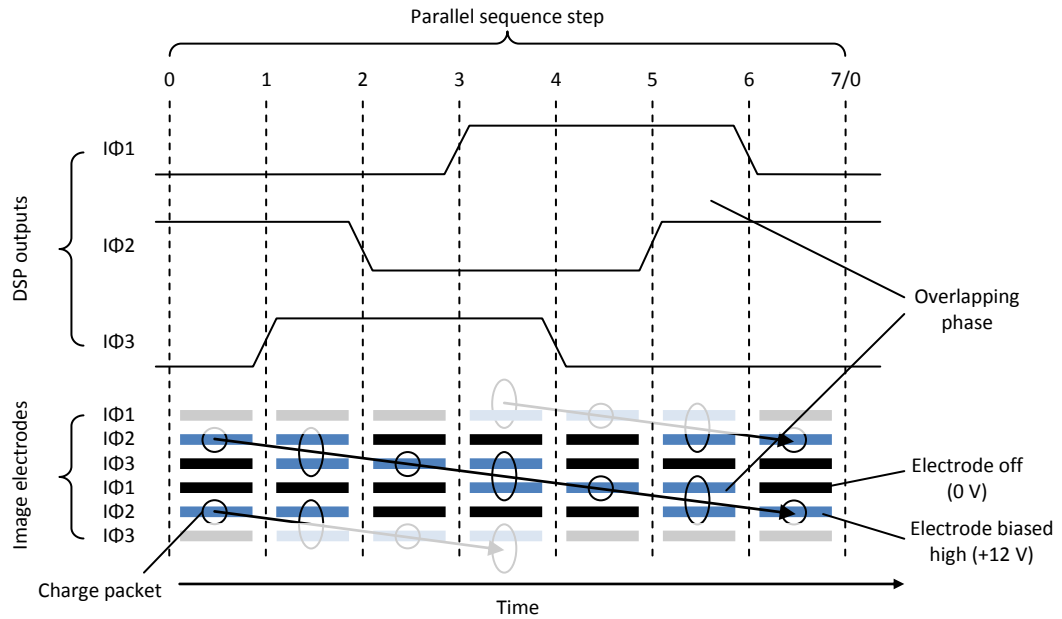


**Figure 4.2** Parallel clock transfer sequence

An electrode phase of the serial register is also biased high during the parallel transfer to collect the charge as it reaches the end of the imaging area. During the transfer, the image electrode phases are said to overlap, as the neighbouring electrode is held high before the charge storage electrode is switched off, increasing the charge transfer efficiency (CTE).

Before the serial transfer, the charge in the output node capacitor is reset to a reference charge by the activation of the reset FET with the signal  $\Phi_R$  and is defined by the potential applied to the reset drain ( $V_{RD}$ ), typically of the order 17 V. All potentials cited are with respect to the clock low level of 0 V. The reference signal is sampled either using a clamp and sample scheme, or more often for low noise applications, a dual slope integrator system. In this instance, the reference level is integrated for a fixed period and held.

The electrodes in the serial register, now holding all the charge packets of the bottom row, perform a similar sequence to the parallel transfer to move the charge packets one-by-one to the output amplifier. The charge applied to the node capacitance causes a potential shift. This is coupled to the output FET (assuming a single stage output circuit as shown in Figure 4.3) causing a change in  $V_{DS}$ , thereby altering  $I_{DS}$  and hence the potential difference across the external load resistance, thereby generating an output voltage signal. This is then sampled by an analogue to digital converter (ADC) at the request of an enable clock signal (ENB) from the DSP.

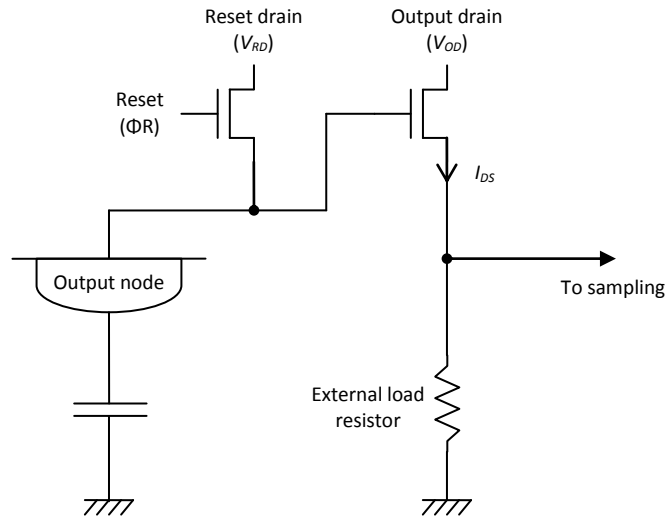


**Figure 4.3** CCD Output circuit

The output node is then reset and the next pixel charge packet is clocked in with the same serial transfer loop. Figure 4.4 shows the sequence of events that follow the parallel clock transfer sequence to transfer and sample 10 pixel charge packets in the serial register.

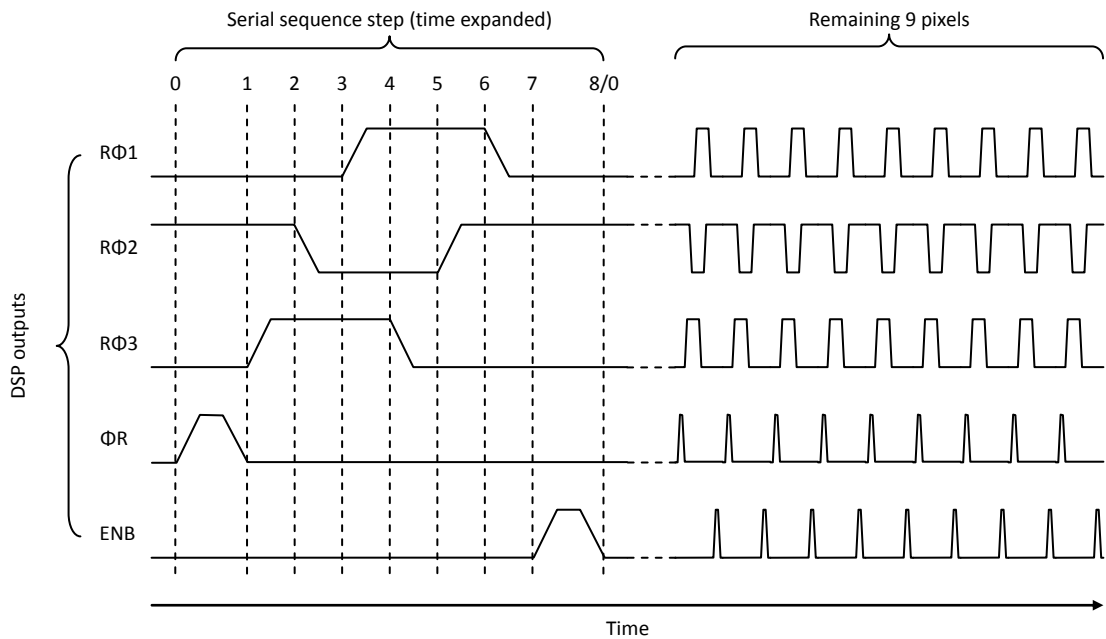


**Figure 4.4** Serial clock transfer and output sampling

Once the entire row of pixel charge packets has been sampled by the ADC the parallel clock sequence is called to transfer the next row of the image into the serial register for sampling. The process is repeated until every pixel in every row has been sampled and recorded.

### 4.2.2 Clock and bias voltages

Clock voltages are programmed via the GUI to output between 0 V and +15 V for logic high and 0 V for logic low. The potential biases applied to the CCD during operation are provided internally to the camera drive electronics by a power supply module with eight software adjustable outputs. The camera system allows six of these to be set with 8-bits of resolution between 0 V and 30 V and a further two up to 35 V. Table 4.1 lists the typical bias potentials and values applied to operate a non inverted mode (NIMO) CCD.

Label	Description	Typical DC potential (V)	Clock high (V)	Clock low (V)
I $\Phi$ #	Image/store clocks	-	9	0
R $\Phi$ #	Serial clocks	-	10	0
$\Phi$ R	Reset clock	-	7	0
V <sub>SS</sub>	Substrate	0	-	-
V <sub>RD</sub>	Reset MOSFET drain	17	-	-
V <sub>OD</sub>	Output MOSFET drain	29	-	-
V <sub>OG</sub>	Output transfer gate	3	-	-
V <sub>DD</sub>	Dump drain	24	-	-

**Table 4.1** Typical CCD operating potentials

### 4.2.3 Image pixels, under/over-scan and pixel binning

The number of pixels in the image is input by the user via the GUI and are forwarded to the sequencer program as the variables for the number of row and column loops to perform. Most CCDs have a number of serial register stages leading to the output node that will not have charge packets added to them from the imaging area during the parallel transfer. These allow the output circuit to be located away from the sides of the CCD, allowing an array of devices to be closely positioned together. The extra serial register elements manifest themselves as virtual pixels at the beginning of each line that must be read out from the CCD before the image data can be obtained. The virtual pixel data is referred to as 'pre' or 'under'-scan and the number of these pixels must be added to the physical number of pixels in each row to obtain the full image.

The image can be over-scanned, whereby additional pixels are clocked from the output node that carry no integrated charge, in the parallel and serial directions by increasing the row and column counts beyond the physical pixel dimensions respectively. For example Figure 4.5 shows a 10 $\times$ 5 pixel image with four over-scan pixels in the serial direction and three in the parallel. To achieve the image in Figure 4.5 the row count must be set to eight and the column count set to sixteen.

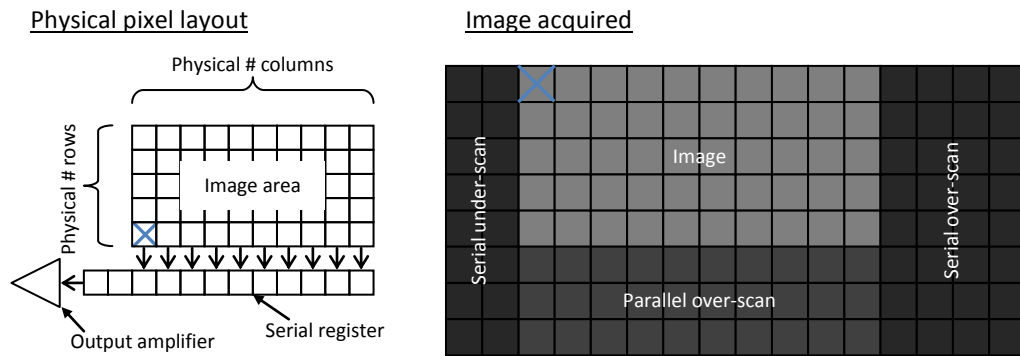


**Figure 4.5** Under and over-scanned CCD image

Over-scanned pixels can be used for calibration as they provide the pixel data containing closest to zero signal as they contain only the leakage current accumulated during readout.

Pixel binning allows the summation of neighbouring pixels in the image array, allowing for images with effectively larger pixels but at a cost to spatial resolution. The binning operation can be performed by including additional charge transfers in both the parallel and serial directions between pixel resets. An example of a  $2 \times 2$  binned image is shown in Figure 4.6, the first parallel clock sequence transfers the charges of row  $n$  into the serial register. A second parallel transfer then adds the charges of row  $n + 1$  of the original image into the serial register. Two consecutive serial transfers then sum the charges of the first two elements of the serial register at the output node.

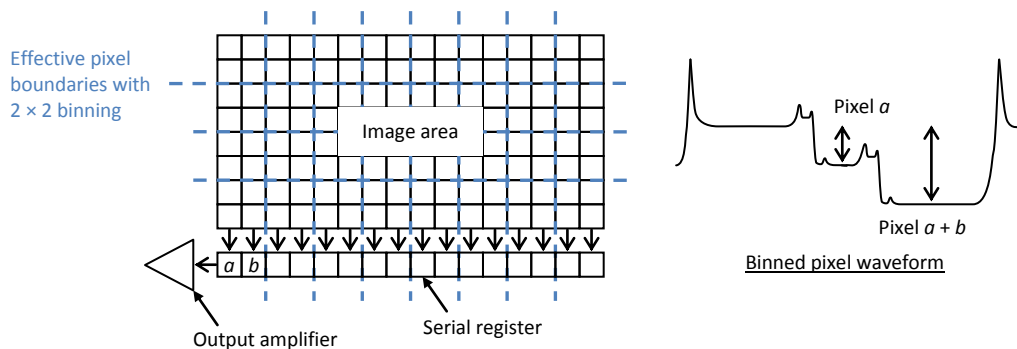


**Figure 4.6**  $2 \times 2$  Pixel binning example

An alternative method for binning is supported in some e2v devices where a summing well is included between the serial register and the output node. This can be biased during two consecutive serial clock sequences to sum two adjacent charge packets before being 'clocked' into the output node.

Care must be taken when pixel binning that the summed charge packets does not exceed the capacity of the output node causing saturation.

#### 4.2.4 CCD image acquisition

A programmable gain stage is used to match the output of the pre-amplifier stage to the input range of the ADC, maximising the resolution of the system. It also serves to amplify the very small signals in low noise applications. The ADC is used to sample the pixel values of the image during the high period of the ENB clock signal.

Two methods were used for the acquisition of CCD image frames; the first method was using the software provided with the camera system. The second was devised under the work of this thesis. The camera system automatically runs the sequence program described in Figure 4.1 as an indefinite loop, such that pixels are constantly being sampled by a 16-bit ADC. Additional DSP output flags are used to identify the beginning of the frame (Frame-Sync) and the start of each row (Line-Sync) before the 1<sup>st</sup> pixel is clocked into the output amplifier. Upon request of an image by the operator, sampled values from the ADC begin to be stored in a temporary array following the next Frame-Sync. The temporary array is used to store one row of pixel values at a time and is copied into the row of a 2-D image array at each Line-Sync. Subsequent rows are copied across into the image array until the next Frame-Sync signifies the completed frame. The array is then output to the display as a greyscale image scalable in both contrast and brightness. A histogram function enables the user to plot the pixel values from either the entire image or a user specified region of interest (ROI). In X-ray applications, such a plot provides the energy spectrum of the photons incident on the CCD. Figure 4.7 shows an example 10×10 pixel image and the energy spectrum obtained from the histogram.

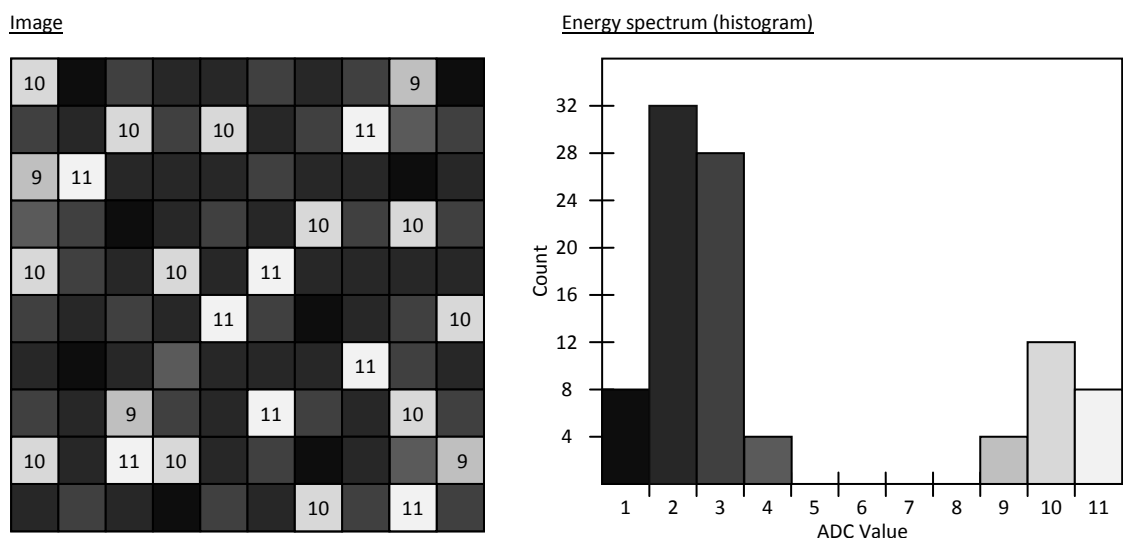


**Figure 4.7** Example image and energy spectrum

A Gaussian fitting routine can be used to ascertain statistics within the histogram plot to derive the signal's mean and standard deviation that can be used to calibrate an energy scale for the system to evaluate the noise and energy resolution.

The second method for acquiring CCD images, developed by the author, employs the commercially available Measurement Computing DAS4020/12 PCI ADC shown in Figure 4.8. The DAS4020/12 has four analogue input channels that are multiplexed to a single 12-bit ADC that has a programmable input range of  $\pm 1$  to  $\pm 5$  V. BNCs were used to make the external connections the analogue input channels, the fifth BNC connector is an analogue trigger input connected to ENB. Sampling was possible up to a maximum rate of 20 M samples per second (MSPS) divided between the number of ADC channels in use. Therefore, where all four analogue input channels were used the maximum sample rate was 5 MSPS. A Visual Basic library was included with the DAS4020/12 that enabled a custom program to be written to sample the CCD output at the correct timings.

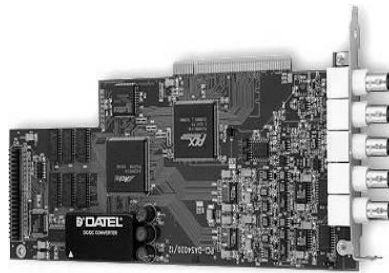


**Figure 4.8** Measurement Computing DAS4020/12 PCI ADC

To reduce the effect of noise pickup on the analogue path between the output FET of the CCD and the ADC, multiple samples were taken of each pixel value and averaged to improve the SNR by  $\sqrt{N}$ , where  $N$  is the number of samples taken per pixel. This was achieved by using the analogue input scan function (*cbAinScan*) of the ADC board that allows a predefined number of samples to be taken following an analogue trigger. The software program then sums up the values sampled and divides by  $N$  to find the mean and stored this in an array. The time delay between acquiring two consecutive input scans triggered by the external BNC trigger was of the order 1 ms. The typical pixel read period from the CCD was less than 10  $\mu$ s; therefore it was not possible to retain the spatial resolution of the image using this external trigger method. It was therefore necessary to acquire pixel data with the analogue input scan operation for the duration of the row readout, triggered by the Line-Sync trigger.

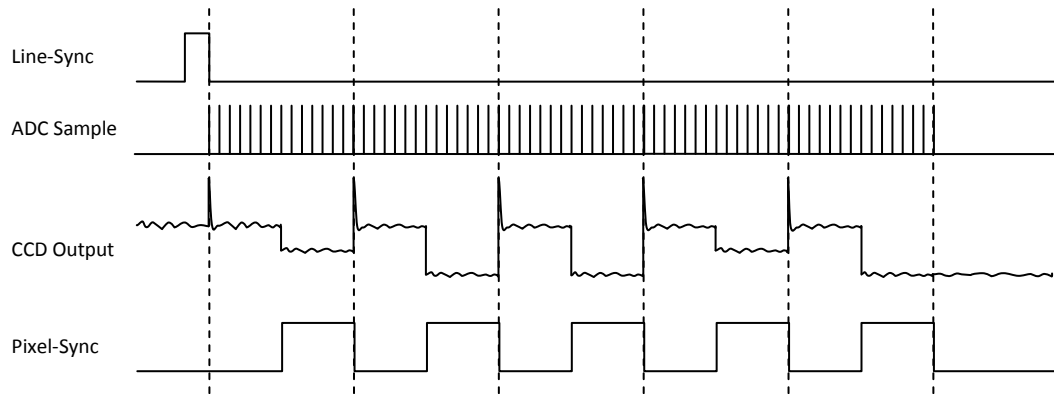


**Figure 4.9** DAS4020/12 CCD pixel acquisitions

The undesirable data sampled during the serial clocking and reset of the output FET were removed in software by timing with an additional pixel trigger clock (Pixel-Sync) that was generated by an output flag of the DSP as shown in Figure 4.9. The Pixel-Sync samples were then stored into an array of logic 1's and 0's that are subsequently multiplied with the CCD output array, shown in Figure 4.10. The resultant array contained the  $N$  number of samples per pixel separated by zeros in between. The software then calculated the mean of the  $N$  pixel samples and stores them as a row in a 2-D image array.

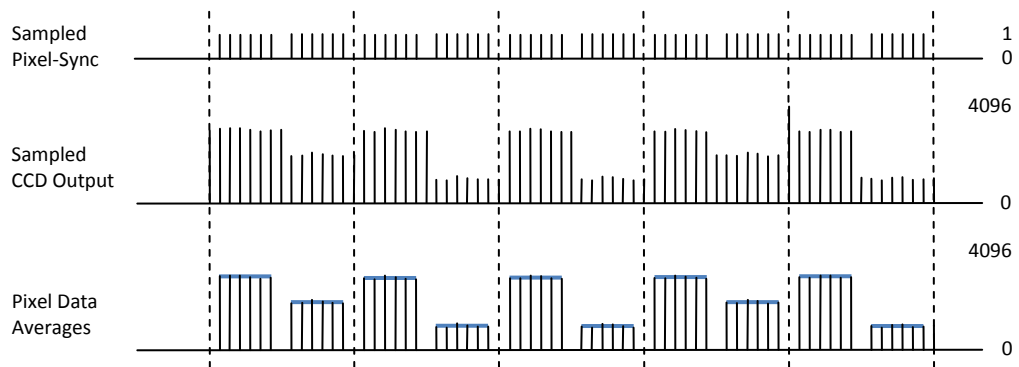


**Figure 4.10** DAS4020/12 Software processing example

The parallel transfer time for the next row into the serial register was sufficient for the DAS4020/12 to set up the next triggered input scan. Subsequent rows in the image are sampled by the ADC by the same method and stored in the array with an incremental row value.

## 4.3 Laboratory equipment

### 4.3.1 X-ray sources

Two sources of X-rays were used during this thesis work. A radioactive isotope of iron ( $\text{Fe}^{55}$ ) was used primarily for calibrating the energy spectrum of the CCD with the measured ADC values for X-ray photons. The  $\text{Fe}^{55}$  source produces characteristic X-ray photons of 5,898 eV

and 6,490 eV when the iron atoms decay into manganese. The calibration method is discussed in Section 4.5 of this chapter as it is paramount in determining the gain of noise in terms of electrons r.m.s. of the system.

The second X-ray source was an Oxford Instruments X-ray tube containing a tungsten target. This provided a source of X-ray radiation up to 50 keV, but was electronically limited to 24 keV for safety after filter transmission calculations showed the possibility of 30 keV photons leaking through the stainless steel vacuum test chamber. The Bremsstrahlung radiation from this tube was used to generate secondary X-ray photons by fluorescence from a number of materials, providing characteristic photon energies to illuminate a CCD. The particular experimental arrangement, developed by the author to measure a high resistivity CCDs depletion depth and X-ray QE, is discussed in Chapter 6 and 7.

### 4.3.2 Cooling

The operation of the CCD at low temperatures is necessary to suppress the leakage current that is thermally generated in the silicon by electrons hopping from the valence-band into the conduction-band. In standard CCD X-ray photon counting applications, where  $\leq 5 e^-$  r.m.s. noise is required, it is necessary to cool the device below 210 K before dark current is acceptably reduced to less than  $1 e^-/\text{pixel}/\text{second}$ . The three standard laboratory methods for cooling detectors such as CCDs are with liquid nitrogen ( $\text{LN}_2$ ), a refrigeration pump or a thermoelectric cooler (TEC). In all cases their use under vacuum aids performance by reducing the heat load due to conduction/convection and preventing condensation of the surrounding air onto the cooled detector.

The use of  $\text{LN}_2$  allows an operating temperature close to the boiling point of nitrogen that is 77 K. The  $\text{LN}_2$  is stored in an insulated flask to prevent unnecessary heat loss to the surrounding environment. A material with high thermal conductivity, usually copper, at the base of the flask couples the liquid to the detector. This material is commonly referred to as the 'cold finger' due to it usually having a long thin shape in order for it to reach the detector whilst minimising the radiative heat coupling with the environment. When  $\text{LN}_2$  is used to cool the thermal load of a detector it will evaporate and therefore needs to be topped-up at regular intervals, presenting potential hazards such as cold burns.

Sealed refrigeration systems, such as the CryoTiger<sup>®</sup> used in the experimental work in this thesis, offer the ability to cool the heat load of a CCD to approximately 150 K without the need for regular maintenance. A compressor unit compresses a refrigerant gas into a liquid form that is then transported via flexible pipes to a 'cold head'. At the cold head the liquid is passed

through a small opening that allows it to rapidly expand into a gaseous state, absorbing heat through vaporisation, before the gas returns to a radiator in the compressor housing. Air is forced over this radiator by a fan to assist in removing the heat. The cold head has the ability to remove heat from the load at a rate determined by the plot in Figure 4.11.

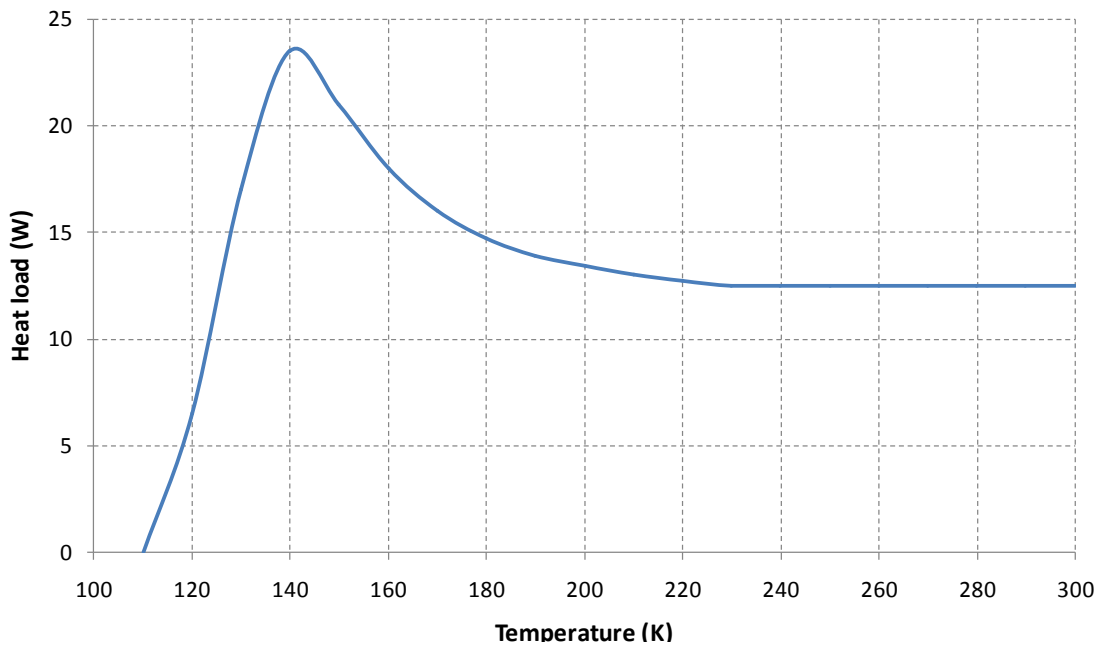


**Figure 4.11** CryoTiger® PT-30 cold head cooling capacity (courtesy of Polycold)

Vibrations from the compressor can be transferred to the 'cold head' that can affect the spatial sensitivity of the detector and are reduced in practice by mechanically decoupling the refrigeration head from the detector with a flexible link.

Using either the LN<sub>2</sub> or CryoTiger® method to cool the detector, it is possible to maintain a specific temperature, higher than that of the method's minimum, by generating additional heat in the cold finger with a high power resistor as demonstrated in Figure 4.12. A temperature controller varies the power dissipated in this resistor in accordance with the input from a platinum resistance thermometer (PRT) that constantly monitors the temperature of the cold finger. The maximum operating temperature available using the CryoTiger® is 223 K without overloading the 'cold head'.

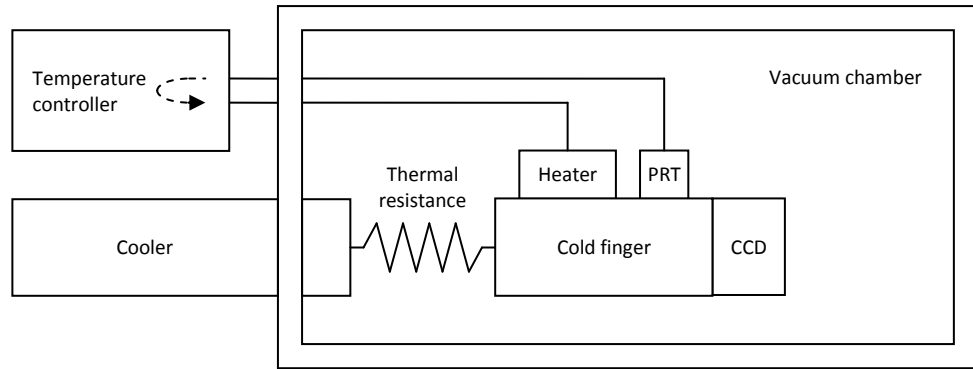


**Figure 4.12** CCD temperature control with feedback

For operating temperatures above 223 K, the use of a TEC is ideal. The TEC is a solid state heat pump that transfers heat from one side to the other. The rate at which the transfer takes place is dependent on the current flowing through the device and therefore can be set to maintain the detector at a specific temperature.

### 4.3.3 Evacuation

When cooling any material below the dew point, any moisture present in the air will begin to condense on to the materials surface. In the case of a CCD this is to be avoided as the formation of water and ice will potentially damage the device and could induce short circuits if the device is biased when it is heated above 273 K. It is therefore necessary to remove the air and hence moisture from the CCD's surrounding environment or lower the dew point by altering the air pressure when cooling. In both cases a sealed vacuum chamber houses the CCD and headboard to prevent the ingress of fresh air.

The first method is to displace the air inside the container with a lower density gas such as nitrogen as shown in Figure 4.13.

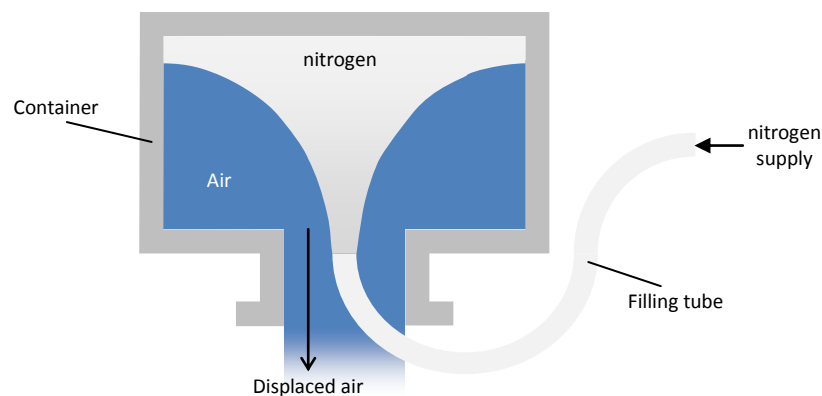


**Figure 4.13** Air displacement with nitrogen

Nitrogen is fed into a sealable opening at the lowest point of the container so that the nitrogen is forced up by the denser air as it is expelled from the low opening. After a sufficient time the container is full of nitrogen and sealed for cooling to begin.

The second method uses a pump system to remove air from the container, forming a partial vacuum at a pressure of approximately  $1 \times 10^{-6}$  mbar that changes the temperature of the phase transition of water into a solid from 273 K to approximately 160 K.

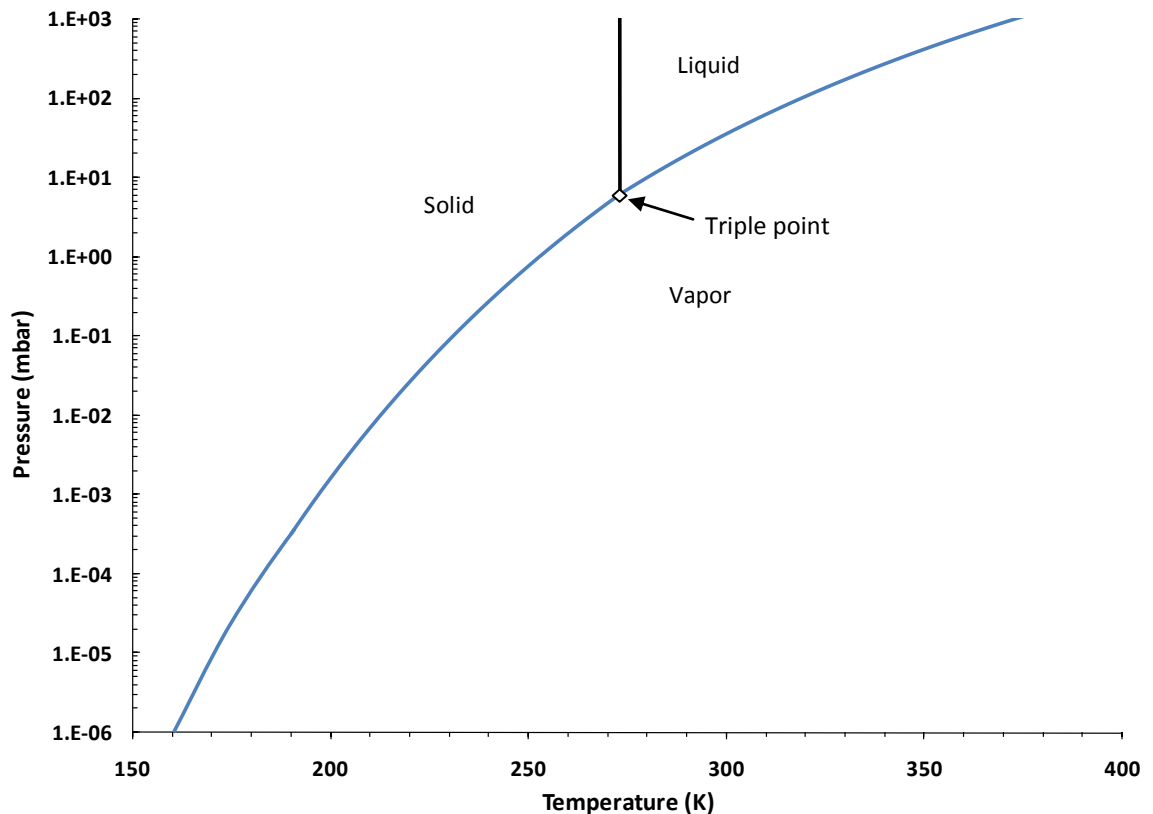


**Figure 4.14** Phase transition of water curve (data courtesy of ChemicalLogic)

Figure 4.14 shows that the CCD can be cooled to  $\sim 160$  K before ice begins to form at the cold head from the remaining moisture in the evacuated container. The vacuum pump system used to evacuate the container in the experimental work described in Chapters 5, 6 and 7 is a single unit that employs two pump technologies. To begin the 'pumping down' operation a first stage diaphragm pump removes air to a pressure of  $\sim 1 \times 10^{-3}$  mbar. A turbomolecular pump then removes the remaining air down to a pressure of  $\sim 1 \times 10^{-6}$  mbar. The pressure is monitored constantly with a Pfeiffer PKR-251 combination gauge that uses a Pirani gauge and cold cathode sensor for high and low pressure respectively.

The container that holds the vacuum must have high compressive strength to prevent it from imploding. The vacuum container(s) that are used in the experimental work were

manufactured from welded stainless steel, with a minimum wall thickness of 2 mm. This thickness of steel also serves to contain X-ray photons of energies up to 30 keV.

#### 4.3.4 Light shielding

In X-ray photon counting applications, optical light increases leakage current and adds to the noise reducing the SNR, hence broadening the FWHM energy resolution. It is therefore vital to ensure the CCD is not illuminated by any other light source by accommodating it in a light-tight container. The steel vacuum container used for cryogenic operation will usually be sufficient in shielding the CCD from stray light, although it has been found that some of the coloured sealing gaskets can permit light to enter. Passage of light through these gaskets was removed, by the use of black adhesive tape. It was also found during the work of this thesis that the Pirani gauge used to measure the vacuum pressure emitted a small quantity of unwanted light during operation. This was avoided by relocating the gauge away from the detector by using an elbow vacuum adapter piece.

### 4.4 Noise reduction

The following methods are commonly employed to increase the measured charge signal to noise ratio, improving the performance of the devices under test.

#### 4.4.1 Filtering

The bias connections ( $V_{OD}$  etc.) to the CCD are equipped with 1<sup>st</sup> order low pass resistor-capacitor ( $RC$ ) filters in close proximity to the CCD to arrest any spurious high frequency noise pickup in the wiring between the CCD and the power supply unit. The low pass filter is designed to have a cut-off frequency  $f_c$  of  $\sim 70$  Hz, whereby all signals of higher frequency are significantly attenuated that can be calculated by [Horowitz & Hill 1989]:

$$f_c (\text{Hz}) = \frac{1}{2\pi RC} \quad (\text{iv-i})$$

Where  $R$  is the value of resistance in ohms and  $C$  is the value of capacitance in Farads, shown in Figure 4.15. Typical values used in CCD headboard circuits for  $R$  and  $C$  are  $100 \Omega$  and  $22 \mu\text{F}$  respectively.

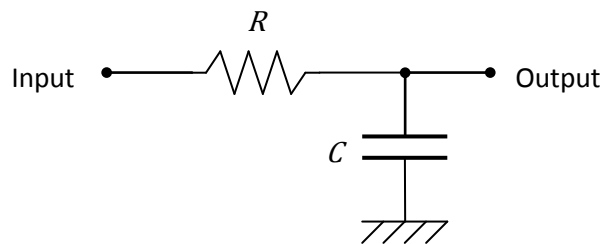


**Figure 4.15** The 1<sup>st</sup> order low pass filter

The low pass filter is a frequency dependant potential divider of which the output varies with the reactance of the capacitor. Therefore as the frequency increases, the reactance of the capacitor falls, causing a greater potential drop across the resistor and hence attenuation of the signal. The response of the typical low pass filter is shown in Figure 4.16. The region to the left of the cut-off frequency is called the Passband, whereby signals pass through the filter with minimum attenuation. To the right of the Cut-off frequency are the frequencies that are attenuated by the filter. The gradient of the curve in the Stopband is -20 dB per decade, that means as the frequency doubles the magnitude is halved.

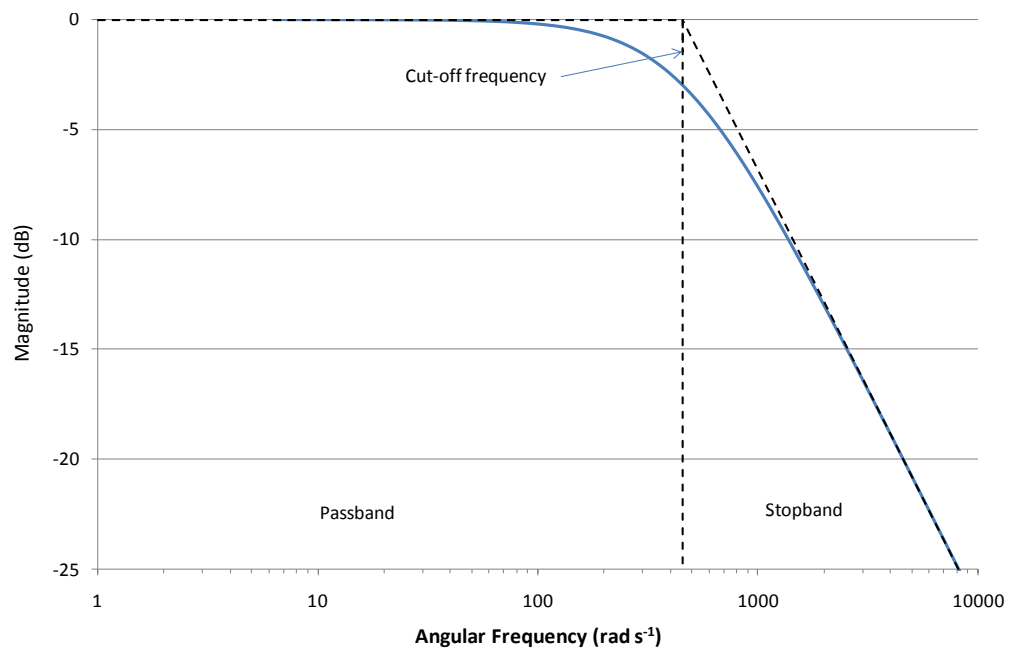


**Figure 4.16** The low pass filter response

Figure 4.17 shows a photograph of a CCD located adjacent a small circuit board that contains the RC power supply filters.



**Figure 4.17** e2v CCD227 and bias filtering 'headboard' developed under this work

The clock electrode lines are not filtered as the high frequency components are needed to provide the high rate of transition between high and low levels during operation.

#### 4.4.2 Output pre-amplification

The gain conversion of the CCD output amplifier is termed the 'responsivity' and is typically  $5 \mu\text{V}/e^-$  in e2v's scientific CCDs. Figure 4.18 demonstrates the level of output of three devices when used for X-ray spectroscopy.

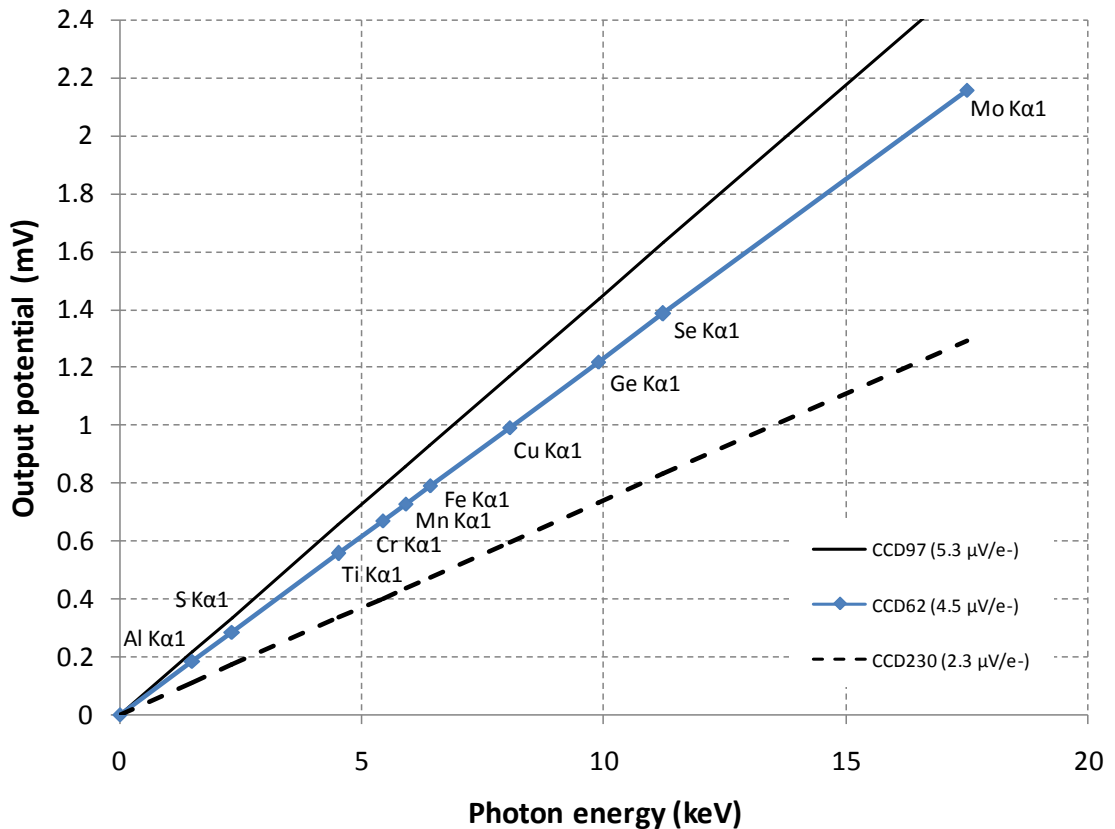


**Figure 4.18** The voltage swing of e2v X-ray CCDs

In X-ray spectroscopy applications the output signal produced by the CCD is relatively low ( $\sim 1 \text{ mV}$ ) compared to that of optical ( $\sim 500 \text{ mV}$ ) and will be greater affected by spurious noise pickup on the connection to the acquisition electronics. The serial output of the CCD is typically A.C. coupled into a voltage pre-amplifier with a typical gain of  $\times 11$  to increase the SNR of the signal from the ADC noise. The operational amplifier (op-amp) is chosen to have a fast voltage response time, such as the Analog Devices AD829 or the National Semiconductor LM7171. This ensures the op-amp output has settled before it is sampled, when operating at high pixel rates ( $> 200 \text{ k Pixels/Sec}$ ). Figure 4.19 shows the typical voltage pre-amplifier circuit used in X-ray CCD applications [Horowitz & Hill 1989].

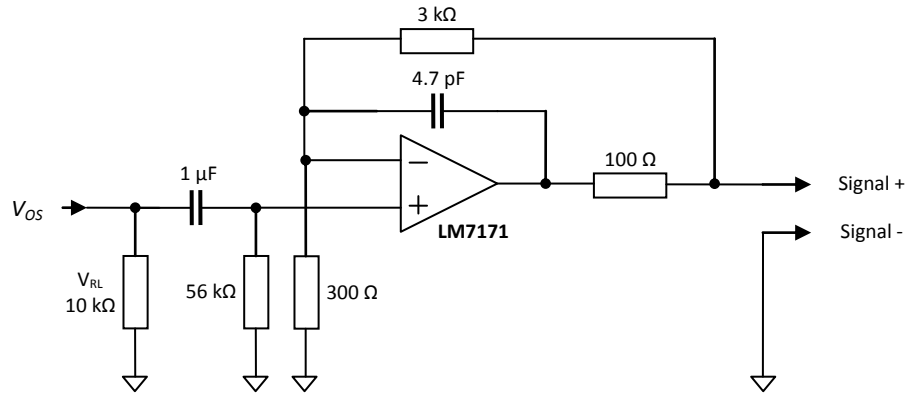


**Figure 4.19** Schematic of the CCD headboard voltage pre-amplifier circuit

#### 4.4.3 Correlated double sampling

The correlated double sampling method is standard practice for the readout of scientific CCDs. The primary function of CDS is to eliminate the reset noise from the signal, as discussed in Chapter 3. For every pixel, the initial reset charge of the output node is sampled before the pixel charge packet is added onto the output node and is referred to as the reset reference level. The pixel charge packet is then clocked into the output node and is the difference between the current value and the reset reference level [White et al 1974]. Figure 4.20 demonstrates the output of one pixel and the timings of the two sample points.

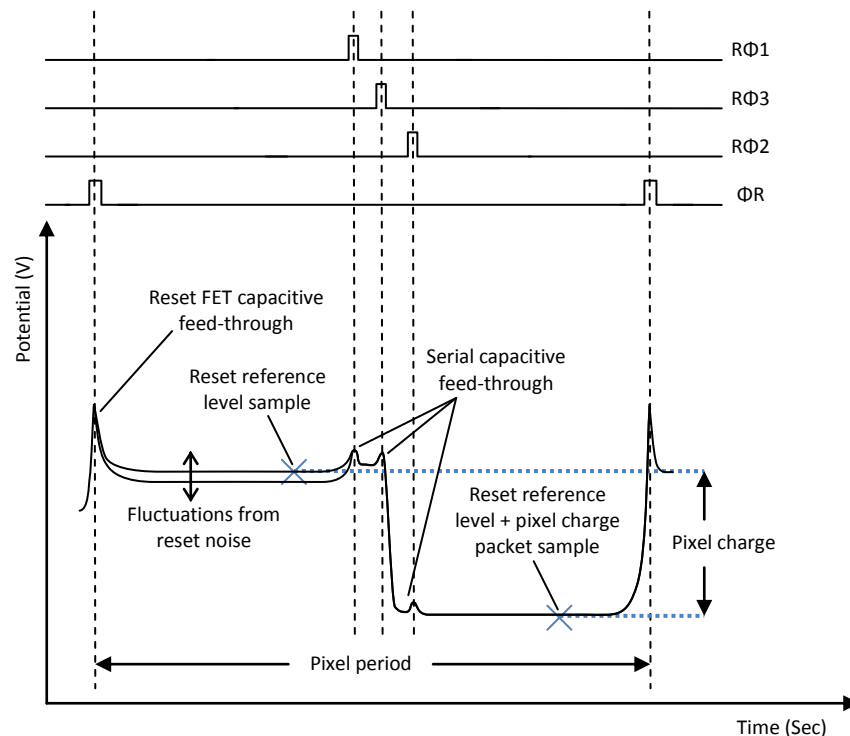


**Figure 4.20** Correlated double sampling of a CCD pixel

Capacitive coupling from parasitic components in the vicinity of the FET allow some portion of the reset and the clocking operations to be superimposed onto the output waveform; such peaks are referred to as feed-through. In slow-scan scientific systems these are simply ignored by taking the CDS samples after a suitable time delay following the cause of the feed-through. The time delays and sample requests are incorporated into the clock sequencer program discussed in Section 4.2.1.

CDS can be achieved practically by three common methods; clamp and sample, the dual slope integrator and digital double sampling. The latter method is now possible due to the development of fast and low cost ADC/DSP/FPGA technology.

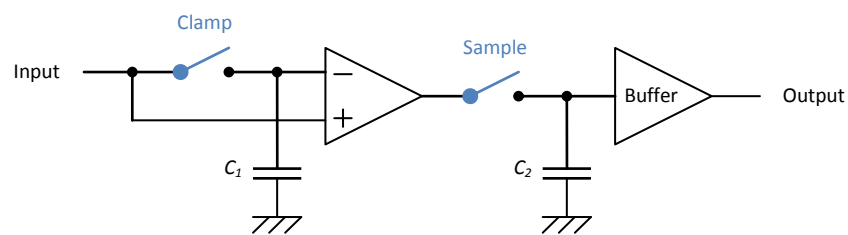


**Figure 4.21** Typical clamp and sample CDS processor

Figure 4.21 shows a typical clamp and sample circuit that uses a differential pre-amplifier to evaluate pixel values by comparing the 'clocked' charge at the non-inverting input to the reset reference level that was stored earlier in  $C_1$  by the momentary closing of the clamp switch. The sample switch stores the output of the differential amplifier onto capacitor  $C_2$ , where the charge is suitably buffered for input to an ADC [Hynecek 1986]. The relative timings for the clamp and sample CDS processor are shown in Figure 4.16.



**Figure 4.16** Clamp and sample CDS timings

The clamp and sample method is the simplest to produce although suffers the greatest from noise on the video signal, as either the clamp or sample value may be taken during a noise spike that can significantly affect the output.

An improved CDS method is the dual slope integrator, shown in Figure 4.17, that uses an average of the CCDs output for both the reference and the signal levels [Janesick 2001].

The effect of any noise on the output is therefore reduced as it is likely to be present in both samples and effectively self-cancelling as it has similar magnitudes. The dual slope integrator method is adopted in the camera system used for some of the work in this thesis that is described in Section 4.2.

The CCD video signal is input to a preamplifier stage that has a suitable gain to match the input range of the ADC. The signal is then clamped to ground during the pixel reset that sets a reference point for the integrator.

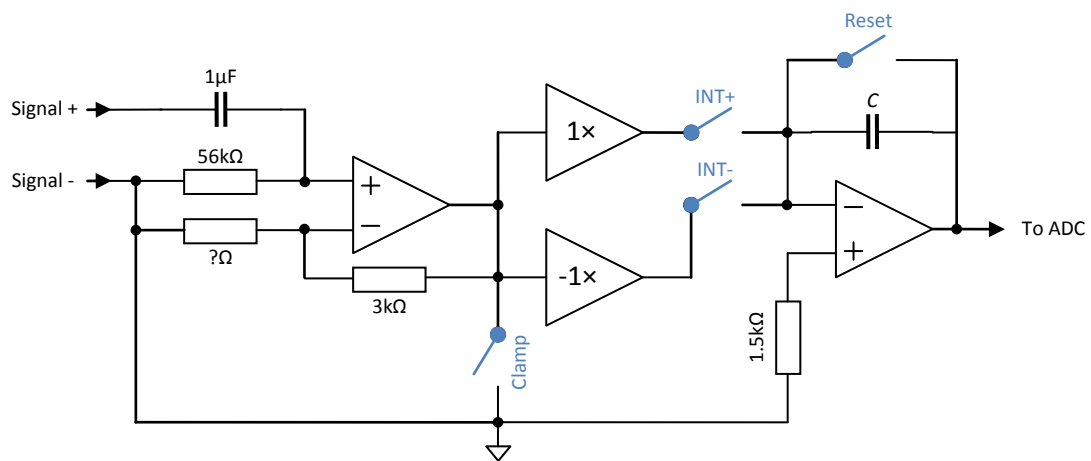


**Figure 4.17** The dual slope integrator CDS circuit

The pixel reference potential level is then integrated negatively across the capacitor  $C$  for the periods that switch  $INT-$  is closed due to the  $-1$  gain of the amplifier. This causes the output of the integrator to slope negatively (down) with a linear gradient for the period switch  $INT-$  is closed. Before the serial clocking of the pixel charge packet into the CCD output, switch  $INT-$  is opened, freezing the reference level at the output of the integrator. After the pixel charge packet is added to the CCD output node, switch  $INT+$  is then closed, that begins to add a positive integration (upwards slope) of the pixel charge onto the reference level. Switch  $INT+$  is then closed and the value of the pixel is stored at the output of the integrator that is then sampled by the ADC. Finally, during the CCD pixel reset, the clamp switch is closed to reset the reference level and a reset switch shorts the feedback capacitor of the integrator to discharge it ready for the next pixel. This sequence of events is shown in Figure 4.18.

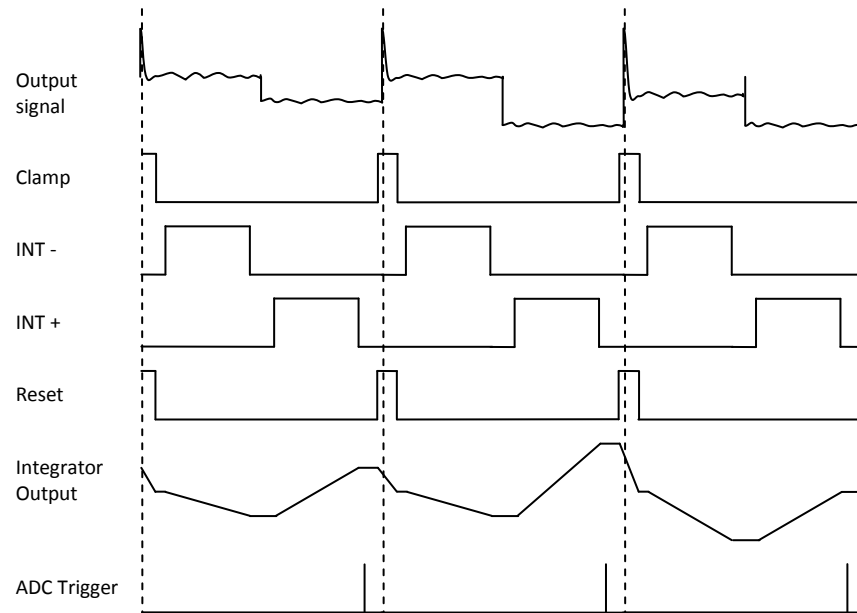


**Figure 4.18** Dual slope integrator timings

The digital double sampling method uses an ADC to sample the pre-amplified output from the CCD; the data acquired is then post-processed to form the image. The sampling rate of the ADC is sufficient that each pixel is sampled at least four times in both periods of the reference and pixel charge levels. The average of the samples for the pixel charge is then subtracted from the reference level average to determine the individual pixel value. Figure 4.19 shows the timings of the ADC samples acquired used to generate the average pixel values.

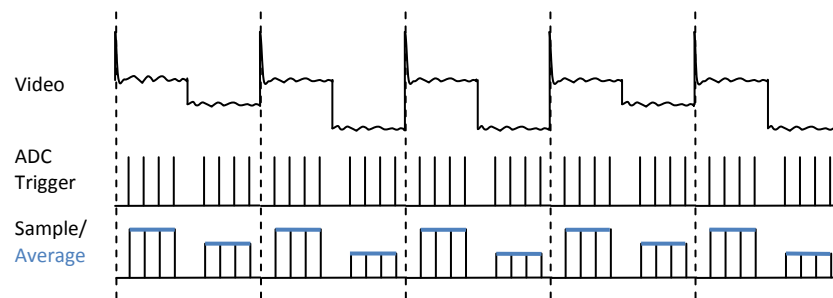


**Figure 4.19** Digital double sampling example

#### 4.4.4 Common mode rejection

The common mode rejection (CMR) technique can eliminate the capacitive feed-through sources that are superimposed onto the output. This enables higher pixel read rates to be achieved as the output circuit does not require additional time to respond to these peaks. An example is shown in Figure 4.20. The output of the CCD is input to a differential amplifier that has its 2<sup>nd</sup> input connected to a dummy output node clocking zero charge. The capacitive feed-through to both output nodes are equal in magnitude and are therefore cancelled in the differential operation. The remaining difference of the operation is the reference and pixel

charge levels that are output by the amplifier [Burt 2006]. However since two outputs are combined, the noise is a factor  $\sqrt{2}$  higher than a single output.

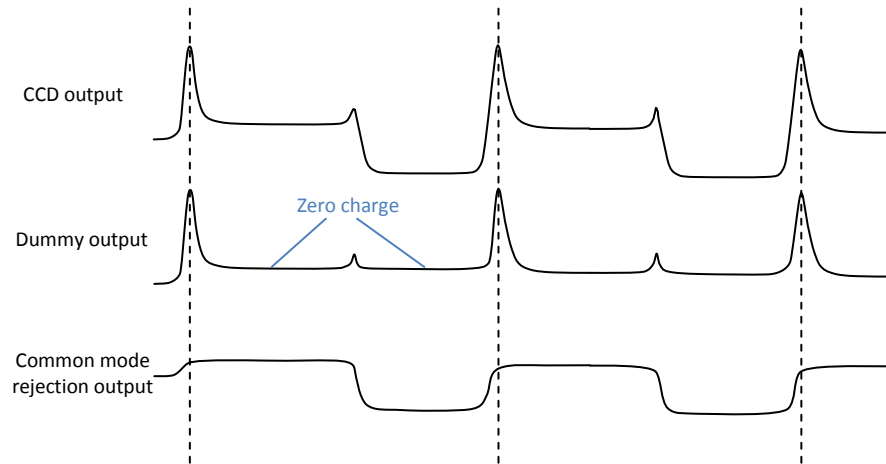


**Figure 4.20** Common mode rejection waveforms

## 4.5 Device characterisation

### 4.5.1 System noise calibration

The camera system noise was measured by finding the sigma of the background signal obtained from the CCD image. This was presented in terms of the uncertainty on the signal in electrons r.m.s. by initially calibrating with a known photon energy, usually an  $\text{Fe}^{55}$  source producing Mn-K $\alpha$  (5,898 eV) photons and converting into the noise equivalent signal by dividing by the quantum yield for silicon, as discussed in Chapter 3.

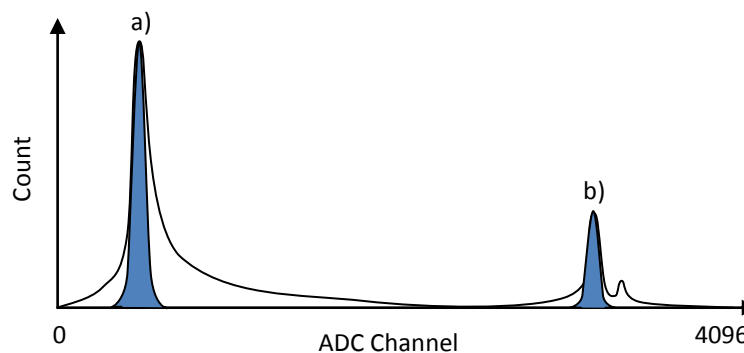


**Figure 4.21** CCD X-ray image histogram

The output from the CCD was quantised by the ADC and sorted into a histogram such as that shown in Figure 4.21. Gaussian curves were fitted to both peaks observed at a) the background and b) the known X-ray energy to determine the peak location and  $\sigma$ . The known energy was then divided by the number of analogue to digital units (ADUs) between the two peak locations to give the energy conversion scale with 0 eV at the background peak location.

$\sigma$  for the background peak was then multiplied by the energy conversion scale to determine its value in eV. Finally this value was divided by the 3.68 eV per  $e^-$  to convert it into the noise equivalent signal in electrons, since the quantum yield for silicon at 173 K is 3.68 eV [Geist & Zalewski 1979].

#### 4.5.2 Responsivity

The responsivity of the CCD is the conversion gain of the output amplifier and is usually designed to be between  $1.5 \mu\text{V}/e^-$  to  $5 \mu\text{V}/e^-$  in e2v devices. Responsivity can be measured by analysing the X-ray events in an image obtained using a known X-ray energy and with knowledge of the gain of the camera electronics [Holland 2004].

The pre-amplifier gain stage on the CCD headboard is usually designed to be  $\times 11$  in X-ray applications, this was measured by inputting a sinusoid signal to pin 2 of the AD829 and observing the output at pin 6. The gains of CDS and ADC electronics were also found by inputting a sinusoidal signal and recording the value sampled by the ADC. The knowledge of these gains was used to determine the input voltage range of the ADC in Volts per ADU. Once the V/ADU is known for the system it is necessary to illuminate the CCD with a known signal. Various X-ray energies, Ti-K $\alpha$ , Cu-K $\alpha$  and Ge-K $\alpha$  were used to provide input signals of 1,226  $e^-$ , 2,187  $e^-$  and 2,686  $e^-$ . The ADC channel numbers for the peaks of these X-ray lines were found and multiplied by the input voltage range to determine the CCD responsivity in  $\text{V}/e^-$ .

### 4.6 X-ray events

X-ray photons incident at the CCD arrive as point sources, generating a roughly spherical e-h cloud upon ionisation [Hopkinson 1983]. The diameter of this cloud is energy dependent although is small compared to the pixel size at energies less than 10 keV. Due to the random arrival and depth of absorption of the X-ray photon in the pixel structure, any of the pixelated patterns described below can be imaged.

Where the X-ray photon is absorbed close to or on the pixel boundary, charge will be shared between neighbouring pixels. Figure 4.22 demonstrates the four types of event that can be observed in the CCD image where this has happened. Where the charge is collected over a greater number of pixels, the charge per pixel is reduced and is indicated by a darker shade of grey in Figure 4.22. The  $2 \times 1$  and  $2 \times 2$  events can be summed to the equivalent charge value of a  $1 \times 1$ , or isolated, event.

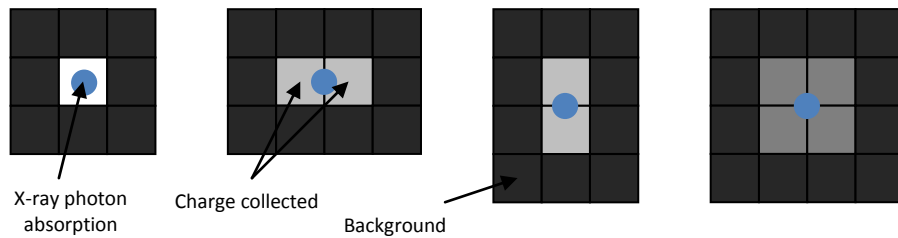


**Figure 4.22** X-ray events in CCDs – Pixel boundary split events

The next set of X-ray events, shown in Figure 4.23, occur when the e-h cloud diffuses in the silicon and partially spreads into neighbouring pixels. This occurs both within and beyond the depleted region, although the greater effect is observed beyond depletion. Where diffusion occurs outside the depletion, some portion of the charge will be lost to recombination in the bulk silicon; therefore such events cannot be reliably summed to an isolated value.

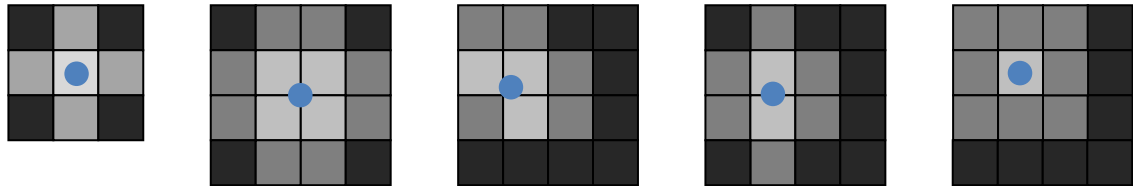


**Figure 4.23** X-ray events in CCDs – Diffusion split events

The remaining three examples, shown in Figure 4.24, are of events where two photons have been absorbed in close proximity such that the charges merge into the same split event pattern. This can occur where two or more photons simply arrive to the CCD in close proximity or when the initial photon fluoresces a silicon atom within the pixel, causing a secondary photon that is ionised a small distance away within a neighbouring pixel.

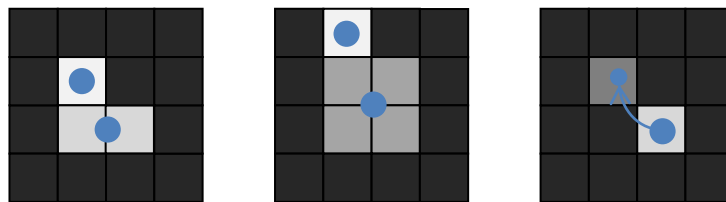


**Figure 4.24** X-ray events in CCDs – Multiple photons

X-ray event recognition and summation software is described in Chapter 7 that was developed to provide statistics for the different event patterns observed in X-ray images.

## 4.7 Summary

This chapter reviewed the laboratory equipment used to complete the experimental work of this thesis. The 3<sup>rd</sup> party camera system electronics that were used to bias and clock CCDs were described and examples were given for a typical clock sequence. The methods for image

acquisition were discussed, the first method using the hardware and software included with the 3<sup>rd</sup> party camera system, the second, using a PCI card was later developed to offer greater flexibility with the work associated with the CDS ASICs.

The practical aspects of operating the scientific CCD in the laboratory have been presented. Topics included the X-ray sources used for energy calibration, cryogenic operation and shielding from stray light.

The four basic techniques employed to maximise signal to noise ratio in scientific CCD were discussed. These techniques were the use of low pass filters to prevent electro-magnetic pickup interfering with the bias of the CCD, pre-amplifying the output to minimise the effect of any further pickup, employing correlated double sampling to remove reset noise and common mode rejection to increase the readout frequency.

The methods to measure the system noise and CCD responsivity were discussed. The system noise measurement was extensively used throughout the practical work of this thesis to verify the correct operation of the CCDs under test.

Finally, examples of the patterns observed in a CCD image that are generated by X-ray photons. These can be categorised into 3 types; those generated at the pixel boundary, those that have diffused within the silicon before collection and finally those that were generated by multiple photons. These patterns form the basis of the event recognition algorithms presented in Chapter 7.

Chapter 5 will present the electro-optical characterisation of a new CCD using the methods described in this chapter.

## 4.8 References

Burt, D.J., 2006. Private communication.

Geist, J. & Zalewski, E.F., 1979. The quantum yield of silicon in the visible. *Applied Physics Letters*, Vol. 35, p. 503-505.

Holland, A.D., 2004. Private communication.

Hopkinson, G.R., 1983. Charge diffusion effects in CCD X-ray detectors. I. Theory. *Nuclear Instruments and Methods*, Vol. 216, p. 423-429.

Horowitz, P. & Hill, W., 1989. The art of electronics. *Cambridge University Press*, 2<sup>nd</sup> Ed. p.37.

Hynecek, J., 1986. High-resolution 8-mm CCD image sensor with correlated clamp sample and hold charge detection unit. *IEEE Transactions on Electronic Devices*, Vol. 33, p. 850-862.

Janesick, J.R., 2001. Scientific charge-coupled devices. *SPIE*, p. 578.

White, M. et al., 1974. Characterization of surface channel CCD image arrays at low light levels. *IEEE Journal of Solid-State Circuits*, Vol. 9, p. 1-12.

## Chapter 5: Electro-optic characterisation of high resistivity CCDs

### 5.1 Introduction

This chapter reviews the general characterisation methods and design of the new high resistivity scientific CCDs manufactured by e2v technologies fabricated on bulk silicon that were used in the work of this thesis. The basic laboratory setup is described including the electrical connections to the CCDs and the method of generating X-ray photons for spectroscopy.

Characterisation of the devices is presented, including analysis of cosmetic quality and leakage current. Measurements of output amplifier responsivity, noise and hence the spectral resolution are also presented.

The p-channel variant of the 1<sup>st</sup> generation high resistivity device is described along with the early testing of the device; although these devices are generally not manufactured in quantity for routine use.

### 5.2 The ‘high-rho’ CCD217 and CCD247

The CCD217 and CCD247 are the 1<sup>st</sup> and 2<sup>nd</sup> generation devices of the high resistivity programme at e2v that were manufactured during the work of this thesis. Based on the design of the popular astronomy 2 k × 4 k pixel format, e.g. the CCD42, the starting bulk silicon is of a far higher resistivity (~ 8 kΩ cm) than that of standard CCDs (20 to 1,500 Ω cm) allowing for a greater depletion depth into the p-substrate region. Depletion depth can be extended further by increasing (negatively) the substrate potential. In epitaxial devices the depletion depth would be constrained to the thickness of the epitaxial layer, bulk material has no such restrictions, potentially allowing wafer thick depletion. Gate protection structures are omitted to allow input of the higher bias potentials, increasing the risk of electrostatic damage [Jordan et al 2006].

The ‘spreading resistance’ technique was used by Semiconductor Assessment Services Ltd. to determine the doping concentration ( $N_A$ ) of the bulk silicon wafers used to manufacture these devices. This involves measuring the electrical resistance between 2 probes, a number of depths from the material’s surface. Practically this is achieved by slicing the material at a shallow angle to increase the surface area of the edge to be probed [Mazur & Dickey 1966]. The average doping concentration was found to be approximately  $1.7 \times 10^{12}$  cm for the majority of the silicon thickness, suggesting a device resistivity of 8 kΩ cm. The increased bulk resistivity of these devices should allow for an applied gate to substrate potential of up to

150 V before breakdown of the p-n junctions comprising the pixelated structure [e2v technologies 2007].

In the 1<sup>st</sup> generation design (CCD217) the spacing between the n<sup>+</sup> and p<sup>+</sup> regions of the output circuit was increased from that of the CCD42 design to avoid avalanche breakdown at the high electric field potential applied to drive depletion. It was found during the early work of this thesis that this was at a cost to increased parasitic capacitance of the output node, reducing the sensitivity of the amplifier and hence giving a poor noise performance [Murray et al 2008].

The 2<sup>nd</sup> generation devices were designed to overcome the shortfalls experienced with a 'spaced' layout and therefore resorted to a similar closely spaced, high performance 2-stage output circuit to the CCD42, but surrounded by an independent substrate region, isolated from the main substrate by a guard drain. The new substrate regions are called the local substrate ( $V_{LSS}$ ) and are biased to a standard CCD substrate potential typically 0 V to 9 V. The layout reduction between the two generations of high resistivity device can be seen Figure 5.1 [Murray et al 2008].

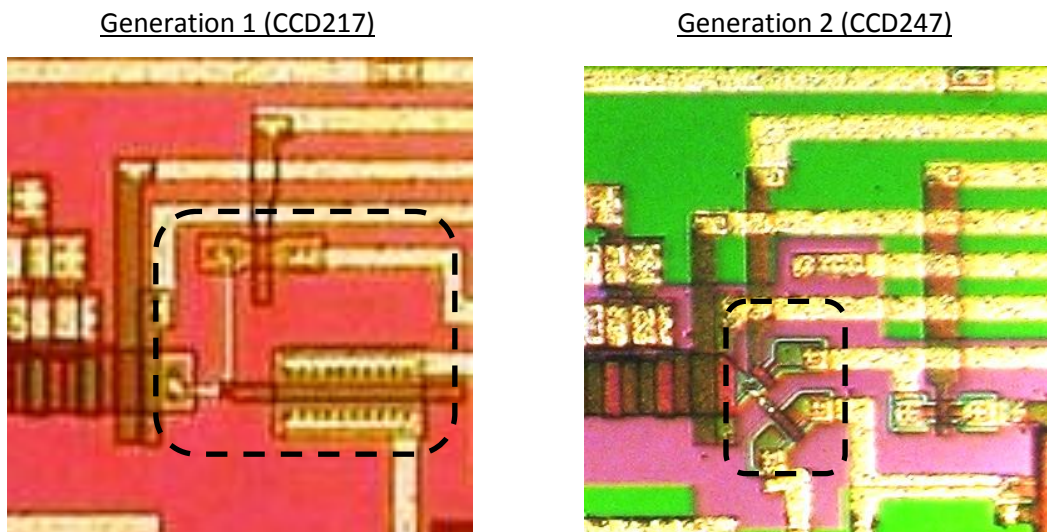


**Figure 5.1** Photographs of the output circuit of CCD217 (left) and CCD247 (right)

The devices have been manufactured using the standard e2v stitching process that allows wafer size limited devices. The samples tested for the work presented in this chapter were n-channel front face illuminated, single 'stitch' devices of  $2108 \times 512 \times 13.5$  pixels mounted in invar/ceramic characterisation packages with a 42-pin PGA connector as shown in Figure 5.2

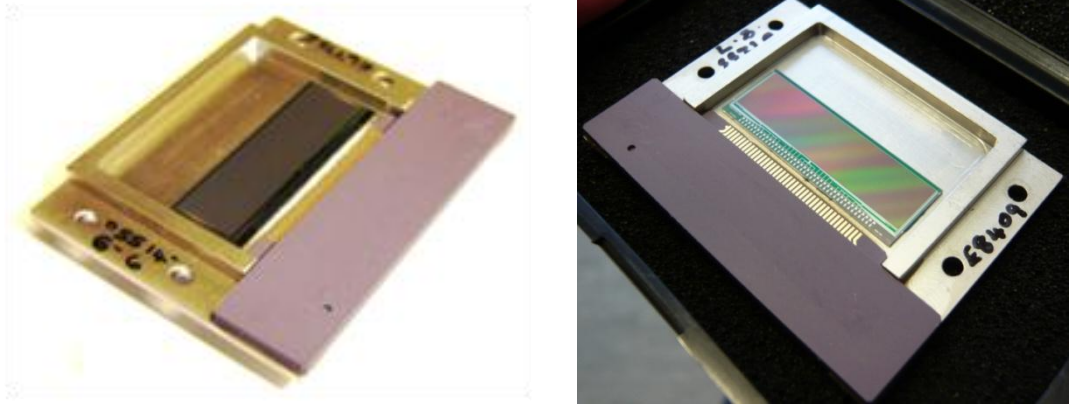


**Figure 5.2** The packaged 1<sup>st</sup> generation CCD217 (left) and 2<sup>nd</sup> generation CCD247 (right)

### 5.3 Experimental Setup

The following section describes the general setup of laboratory equipment to perform the characterisation work.

#### 5.3.1 Camera setup

The CCD was mounted in a vacuum chamber and the air was pumped out until a pressure of  $\sim 1 \times 10^{-6}$  mbar was achieved, to minimise the water content in the remaining air. The temperature of the CCD was then reduced to  $\sim 170$  K by use of a CryoTiger<sup>®</sup> refrigeration system to adequately suppress the dark current.

The CCD potential biases supplied by the camera system were capable of being set between 0 V and 35 V. Due to the increased gate to substrate potential capability of the CCD217 and CCD247 it was necessary to provide an extra 0 V to -130 V supply, connected in series with the substrate bias ( $V_{SS}$ ) as shown in Figure 5.3. Electrical connections to the CCD are given in Table 5.1.

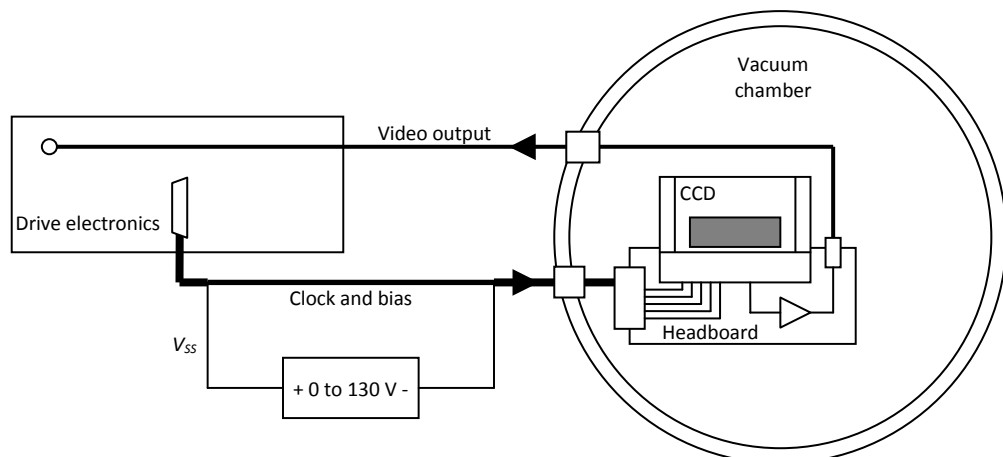


**Figure 5.3** Laboratory setup

Name		CCD247 pin connections	Headboard	Vacuum feed-through	Drive box
Substrate	$V_{SS}$	1, 8, 13, 28, 35, 40	23	23	23
Image $\emptyset 3$	$I\emptyset 3$	5, 38	2	2	2
Image $\emptyset 1$	$I\emptyset 1$	6, 39	1	1	1
Image $\emptyset 2$	$I\emptyset 2$	7, 34	14	14	14
Output source	$V_{OS}$	9	N/A	N/A	N/A
Output drain	$V_{OD}$	10	9	9	9
Guard drain	$V_{GD}$	11, 32, 27, 26, 25, 29, 33, 31, 36	10	10	10
Reset drain	$V_{RD}$	12	22	22	22
Output gate	$V_{OG}$	14	11	11	11
Local Substrate	$V_{LSS}$	15, 30	13	13	13
Summing well	$\emptyset SW$	16	3	3	3
Clamp	$\emptyset C$	17	4	4	4
Reset pulse	$\emptyset R$	18	7	7	7
Register $\emptyset 2$	$R\emptyset 2$	19, 23	18	18	18
Register $\emptyset 1$	$R\emptyset 1$	20, 22	5	5	5
Register $\emptyset 3$	$R\emptyset 3$	24	6	6	6
+15 V		N/A	8	8	8
0 V		N/A	20	20	20
-15 V		N/A	21	21	21
Video		N/A	MCX	4-Way	BNC
Current source	$V_{IOS}$	N/A	12	12	12

**Table 5.1** CCD247 Electrical connections

Table 5.2 states the optimum clock and bias potentials that were found by X-ray calibration for non inverted mode operation (NIMO) of the CCDs.

Label	Description	CCD217 DC potential (V)	CCD247 DC potential (V)	Clock high (V)	Clock low (V)
$I\emptyset\#$	Image/store clocks	-	-	11	0
$R\emptyset\#$	Serial clocks	-	-	11	0
$\emptyset R$	Reset clock	-	-	10	0
$V_{SS}$	Substrate	0 to -70	0 to -100	-	-
$V_{LSS}$	Local substrate	-	7	-	-
$V_{RD}$	Reset MOSFET drain	18	18	-	-
$V_{OD}$	Output MOSFET drain	29	29	-	-
$V_{OG}$	Output transfer gate	2	2	-	-
$V_{GD}$	Guard drains	24	24	-	-

**Table 5.2** 'Hi-rho' CCD217 and CCD247 operating potentials

The optimum local substrate potential for the CCD247 was determined experimentally to be  $6.5 \text{ V} \pm 1 \text{ V}$  for all applied substrate potentials [Murray et al 2008].

The full frame CCD247 was sequenced in time delay integration (TDI) mode, whereby the image was integrated during the parallel transfer to the readout register [Burt 2006]. The camera system constantly 'clocks' out images that are only stored at the request of the user. Therefore each row of pixels equally integrates charge for the time it takes to be clocked from row 1 to row  $512 + 1$ , the serial register. The pixel integration time was calculated by measuring the row transfer time and multiplying by the physical number of rows in the image area.

### 5.3.2 X-ray source

#### 5.3.2.1 Generation

X-ray photons were generated by a commercially available X-ray tube manufactured by Oxford Instruments Ltd. The tube has a tungsten target anode with a maximum power output of 50 kV at 1 mA, allowing continuous Bremsstrahlung radiation up to 50 keV. For safety, the output was limited to 25 keV at the power supply to prevent transmission of X-ray photons through the vacuum chamber walls. A vacuum interlock circuit also prevented the tube from powering on without first establishing a sealed vacuum. The interlock circuit developed under this work is described in Chapter 7.

#### 5.3.2.2 Fluorescence

The X-ray source was mounted as shown in Figure 5.4 so that it illuminated a target at an obtuse angle. The target was interchangeable for various materials, allowing a number of characteristic X-ray photons to illuminate the CCD [Bearden 1967].

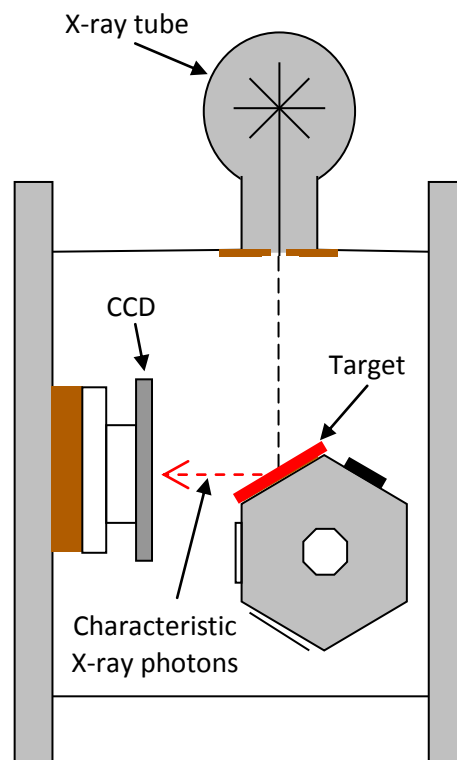


**Figure 5.4** X-ray fluorescence setup

### 5.3.2.3 Filtering

The primary energy used for the characterisation work was 8,047 eV, generated by the K $\alpha$  fluorescence of a copper target. However, photons of other energies were also incident on the CCD that were undesirable; sourced from backscatter, fluorescence of other vacuum chamber materials and the K $\beta$  line of the target. These X-ray lines were effectively filtered from the CCD by attenuation through a 15  $\mu\text{m}$  nickel foil, shown in Figure 5.5, which has a K-shell absorption edge at 8,333 eV [McMaster et al 1969]. The filter transmission is shown in Figure 5.6, alongside the sampled spectrums both with (Filtered) and without (Raw) the nickel filter in place [Henke et al 1993]. There was a reduction in X-ray flux of the Cu-K $\alpha$  of approximately 46 %, although this can be compensated for by increasing the output of the X-ray tube.

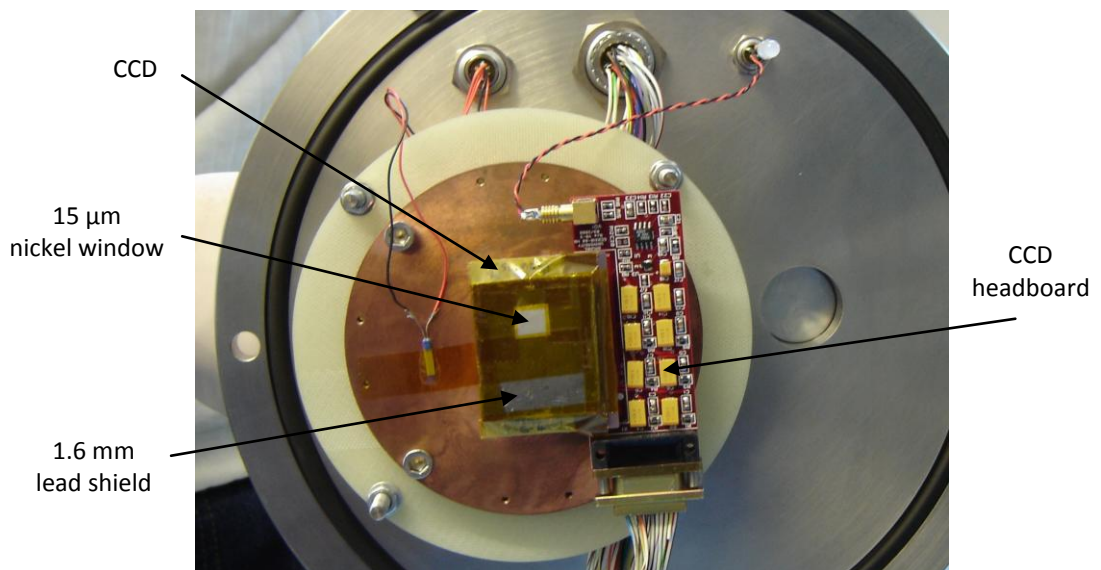


**Figure 5.5** 15  $\mu\text{m}$  thick nickel filter and lead mask on CCD217

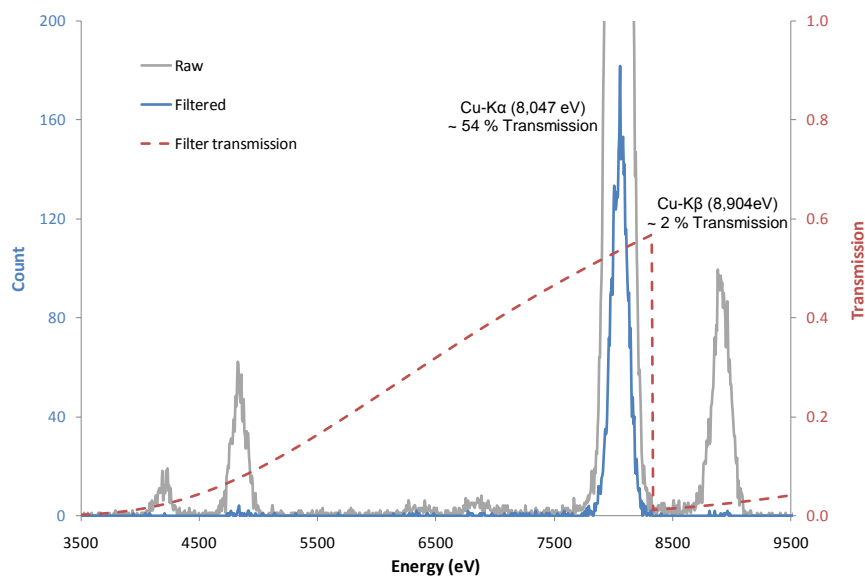


**Figure 5.6** X-ray photon transmissions through a 15  $\mu\text{m}$  nickel window

## 5.4 Test results

### 5.4.1 Leakage and cosmetic quality

The increased gate to substrate potentials of high resistivity devices leads to increased bulk dark current generation, however this was small in comparison to the surface generation present at all gate to substrate potentials. Figure 5.7 shows this small increase in bulk dark current generation for substrate potentials of -10 V and -70 V for the CCD217. Total dark current generation was measured by e2v to be  $1 \text{ nA cm}^{-2}$  at 293 K, equivalent to that of standard n-channel devices [Jorden et al 2006].

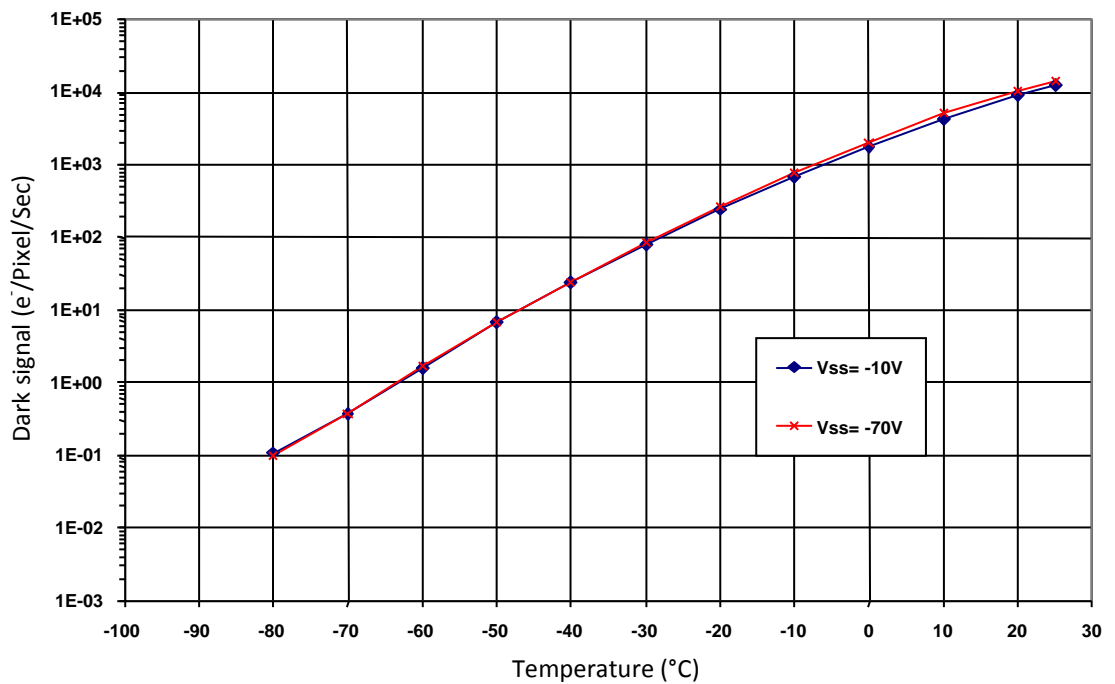


**Figure 5.7** Dark current generation in CCD217

The leakage current of the CCD247 was measured to be  $36 \text{ k e}^- \text{ pix}^{-1} \text{ sec}^{-1}$  at  $20 \text{ }^\circ\text{C}$ , similar to that of low resistivity devices and is shown in Figure 5.8.

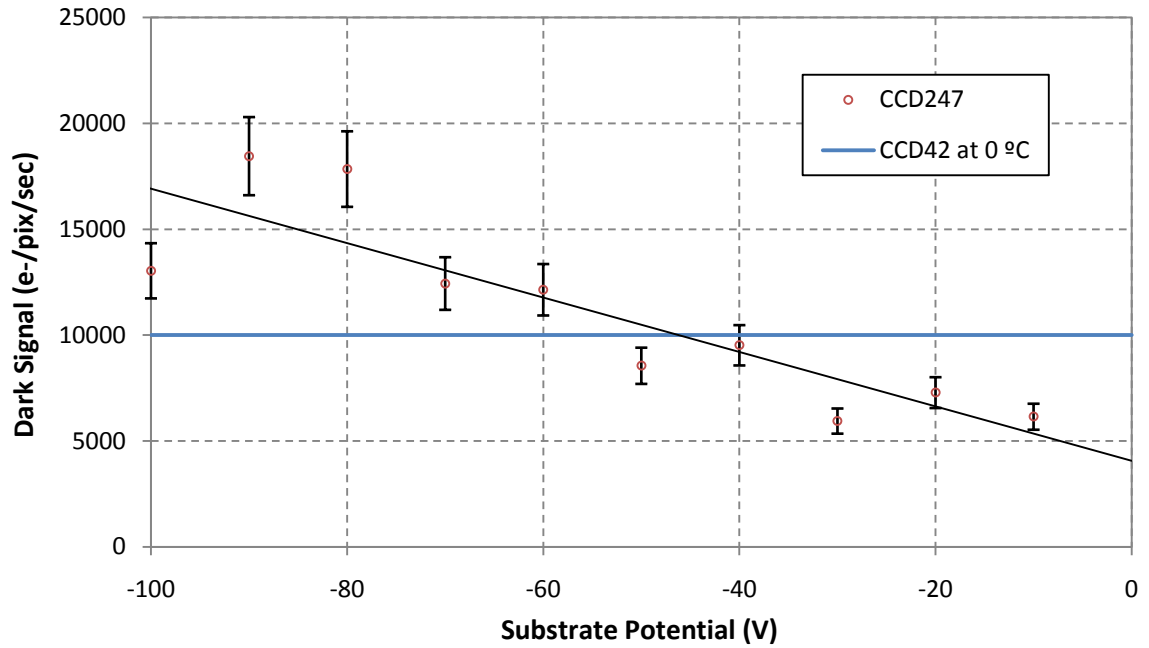


Figure 5.8 Dark current generation in CCD247

#### 5.4.2 Anomalous charge injection

At substrate potentials more negative than -90 V, anomalous leakage current was observed in the first few columns of each CCD image, as shown in Figure 5.9. The severity of the leakage increases with a more negative potential. This was not believed to be caused by the output circuit due to the geometry of the leakage, nor from the image bus lines as the phenomena was not symmetrical with the right hand image area.

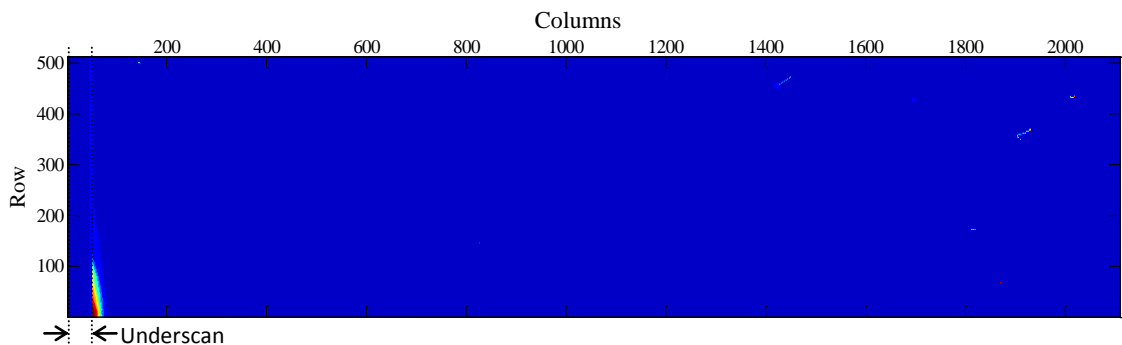
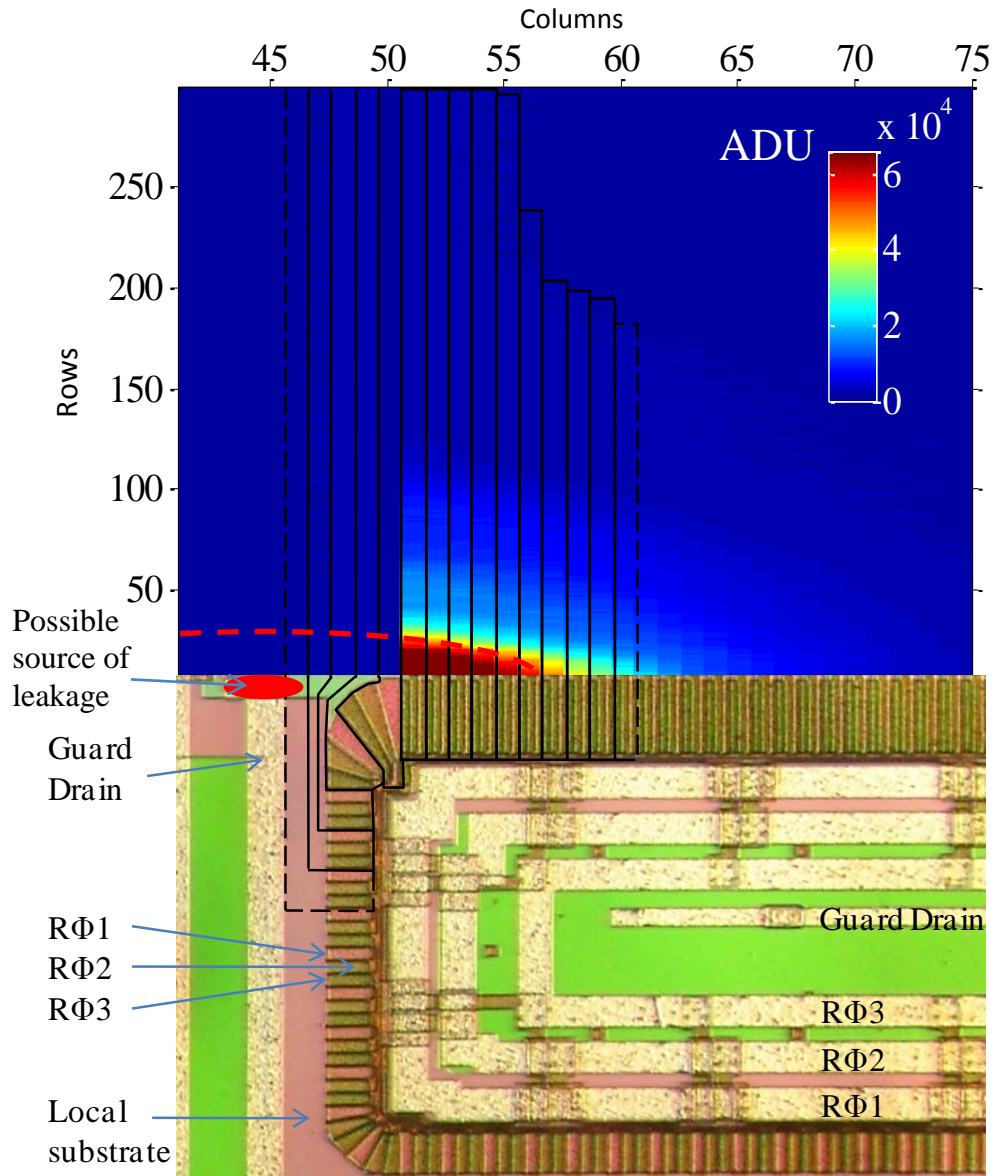


Figure 5.9 Leakage observed in CCD247 image at  $V_{SS} = -120$  V

Figures 5.9 and 5.10 show the typical leakage in an image acquired at a substrate potential of -120 V. The profile of the leakage pattern suggests that the source is away from the serial register electrodes. Initial analysis of the curvature of the leakage suggests that the leakage component is due to the proximity of a guard drain contact to the local substrate region. This could be examined in further work by using an electron-multiplication CCD (EMCCD) microscope to determine if the leakage is caused by a glow and locate its origin.



**Figure 5.10** Leakage profile aligned to the CCD247 output circuit

The effect is not observed in the CCD217 as the design does not include a local substrate.

## 5.5 X-ray measurements

### 5.5.1 XRF Spectrum

X-ray spectra were acquired with the CCD217 and CCD247 for a number of target materials to characterise the spectroscopic performance of the devices. These are produced by plotting the histogram of pixel values in the image and then converting the x-axis into an energy scale by calibration to a known energy peak. Clearly resolved characteristic X-ray lines for chromium, iron, copper and molybdenum are observed in Figure 5.11, acquired by the CCD247.

The Mo-K $\alpha$  peak at 17,478 eV would simply not be resolvable, given the same exposure with standard resistivity, low depletion depth (< 10  $\mu\text{m}$ ) devices.

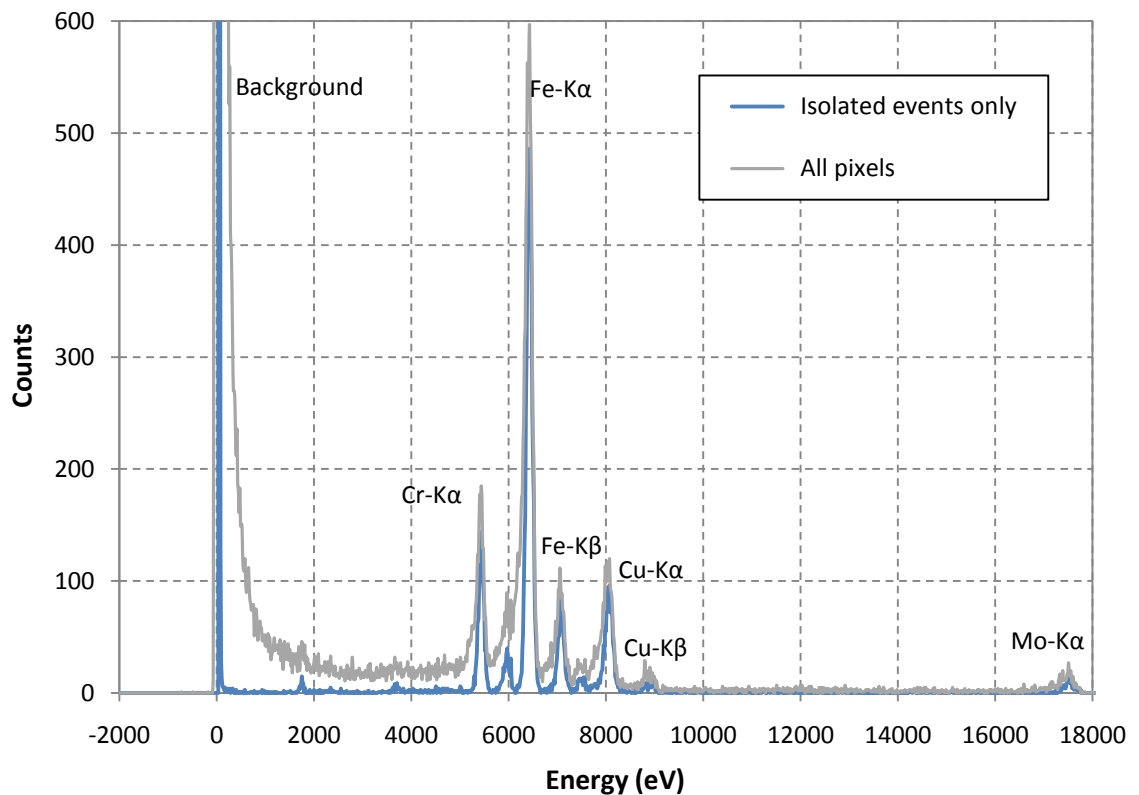


**Figure 5.11** XRF spectra acquired from a multi-element target for raw and isolated pixel events

In the example spectrum of Figure 5.11, on-chip binning was employed to increase the effective pixel area to  $81 \times 81 \mu\text{m}$  in order to prevent the oversampling of the larger charge clouds that are generated by the higher energy photons.

### 5.5.2 Output node responsivity

Responsivity was measured by finding the peak channel for isolated events of a known X-ray energy and V/ADU in terms of the CCD output before pre-amplification and the camera system gain. The X-ray peak was produced by a number of photo-generated electrons that was approximately the value of the X-ray energy divided by the  $3.68 \text{ eV/e}^-$  silicon conversion factor. The number of ADU between the background and the X-ray peak was multiplied by V/ADU for the CCD and finally divided by the number of electrons at the energy to determine the CCD responsivity in  $\text{V/e}^-$ .

Responsivity of the CCD247 was measured to be similar to that of the CCD42, due to the smaller output circuit layout. A smaller layout has reduced parasitic capacitances to the

output node that increases the sensitivity of the amplifier and hence the responsivity by greater than twice that of the 1<sup>st</sup> generation CCD217 devices.

By taking the substrate potential more negative, the responsivity increases due to a second order effect common to all CCD output circuits [Burt 2006]. The relationship between increased responsivity and the substrate potential appears to be linear and is shown by the trend lines in Figure 5.12. The reduced gradient of the trend line for the CCD247 data over that of the CCD217 shows that the local substrate and guard drain structure have had some success at isolating the output circuit from the substrate bias potential. Results presented in Figures 5.12 and 5.13 were obtained by the X-ray method are consistent with those obtained by e2v technologies from mean vs. variance curves. Further, general device characterisations showed, as expected, that decreasing the device temperature increases the amplifier responsivity.

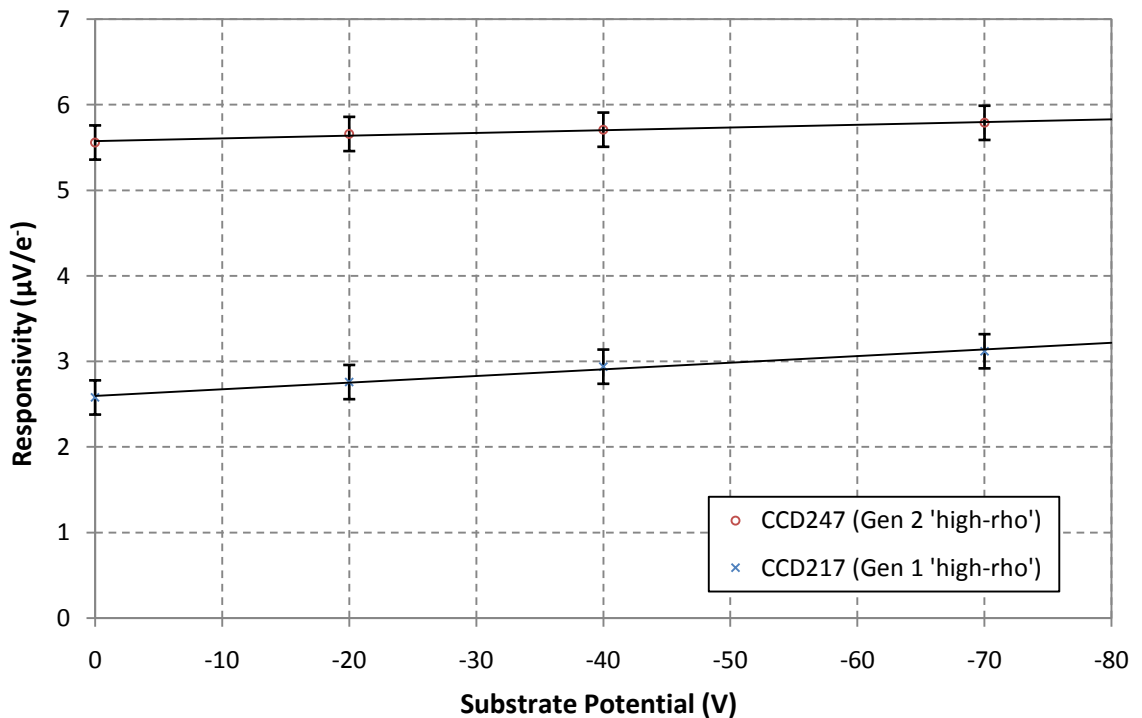


**Figure 5.12** Responsivity vs. substrate potential for CCD217 and CCD247

Responsivity of the CCD247 was also measured whilst varying the local substrate potential ( $V_{LSS}$ ) at substrate potentials of 0 V and -70 V. In all measurements, the results for  $V_{SS} = 0$  V are lower than that for  $V_{SS} = -70$  V, supporting the data shown in Figure 5.12. Increasing the local substrate potential gradually decreases the responsivity until around  $V_{LSS} = 8$  V, at which point the responsivity measurement rapidly reduces as shown in Figure 5.13. This was caused by the onset of deferred charge in the serial register (poor CTE), leading to the incorrect measurement of the X-ray peak ADC channel.

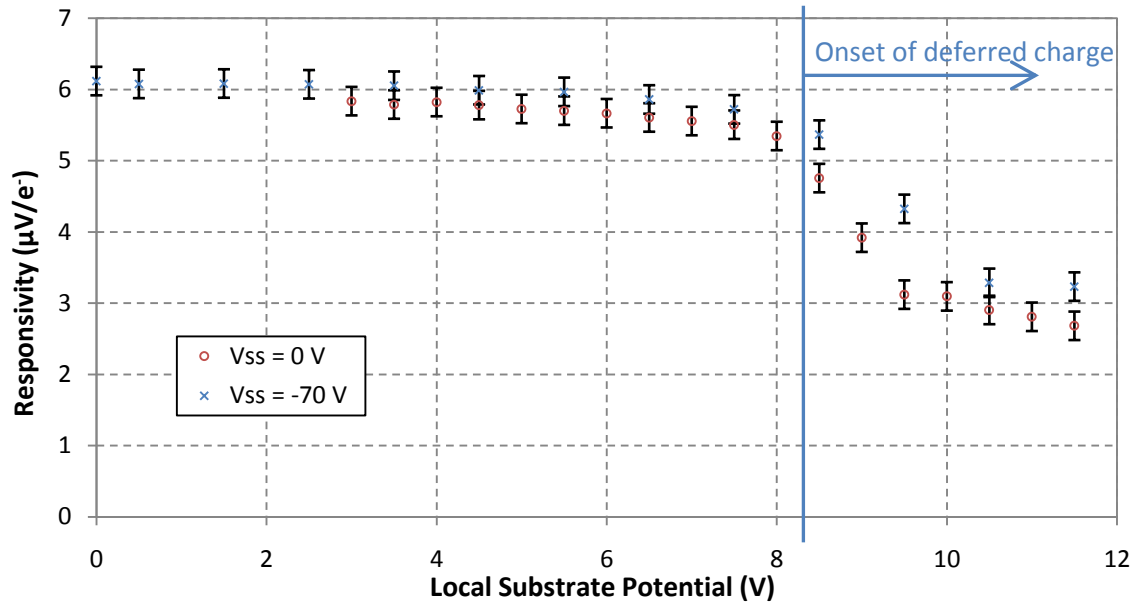


**Figure 5.13** Responsivity vs. local substrate potential for CCD247 at two substrate potentials

### 5.5.3 Noise performance

Device noise was measured by determining the standard deviation in measured signal across a large number of pixels in a dark signal frame. This was then converted into the noise equivalent signal in electrons r.m.s. by initially calibrating with inputs of known X-ray energies. Gaussian models were fitted to the peaks observed in a histogram of the image pixel values to determine the peak channel and  $\sigma$  for the background and known X-ray energy. The energy of the X-ray line was divided by the number of analogue to digital units (ADUs) between the background and X-ray peak channels to find the energy conversion scale, with 0 eV at the background peak location. The background  $\sigma$  was then multiplied by the energy conversion scale to determine its value in eV. Finally this value was divided by the 3.68 eV to convert it into the noise equivalent signal in electrons r.m.s.

Where the device was operated within the intended operating potentials for substrate and local substrate, the CCD247 has a comparable noise to the CCD42. Due to the reduced responsivity of the CCD217, noise measurements are significantly higher.

Where the local substrate ( $V_{LSS}$ ) of the CCD247 was raised in potential towards inversion, ( $> 8$  V) the noise increases due to what was believed to be clock-induced charge (CIC), shown in Figure 5.14. This could be generated by the impact ionisation of holes repelled from the surface, initially sourced from pinned elements in the latter stage of the readout register that are within the region of local substrate. The effect is reproducible for all substrate potentials. The results show, that the severity is reduced as device temperature increases, as is generally expected for impact ionisations [e2v technologies 2004].

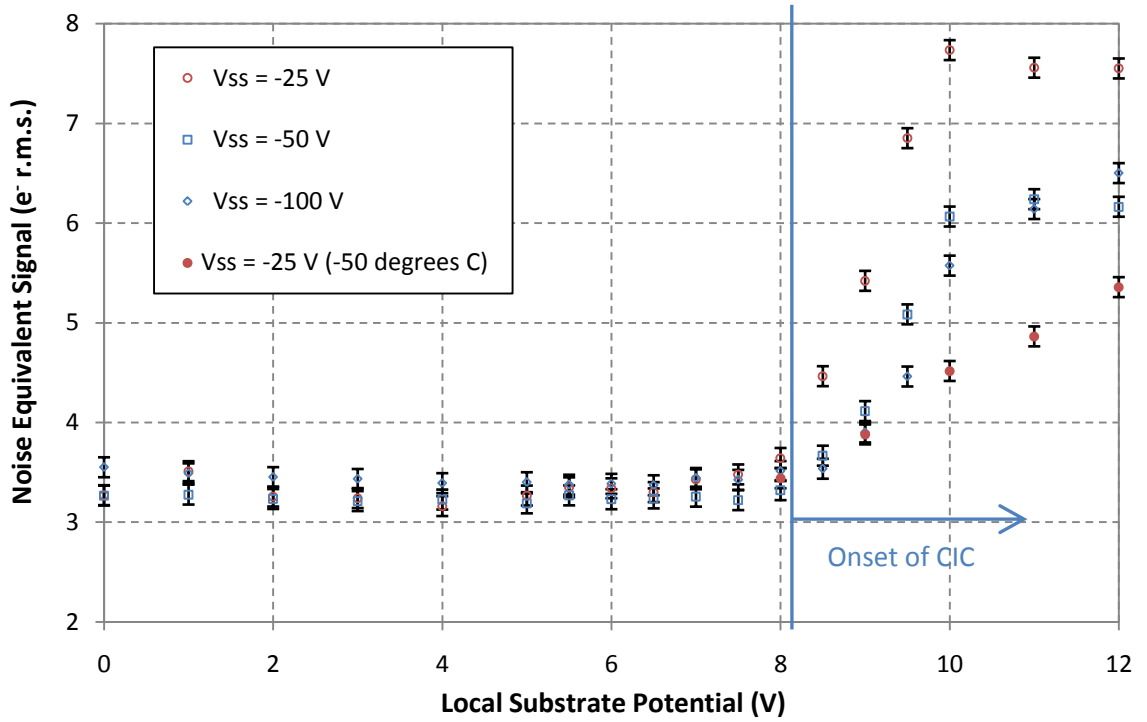


Figure 5.14 Noise vs. local substrate potential  $V_{LSS}$  at 100 kHz pixel read rate

For substrate potentials higher than -100 V the device performs with a readout noise lower than 4 electrons r.m.s. Where the potential was taken more negative than -100 V, the guard drain structure becomes incapable of blocking the conduction path between to local substrate and the main substrate, the resulting leakage current being the likely cause of the increased noise. This is shown by the exponential increase in the noise measurements of Figure 5.15.

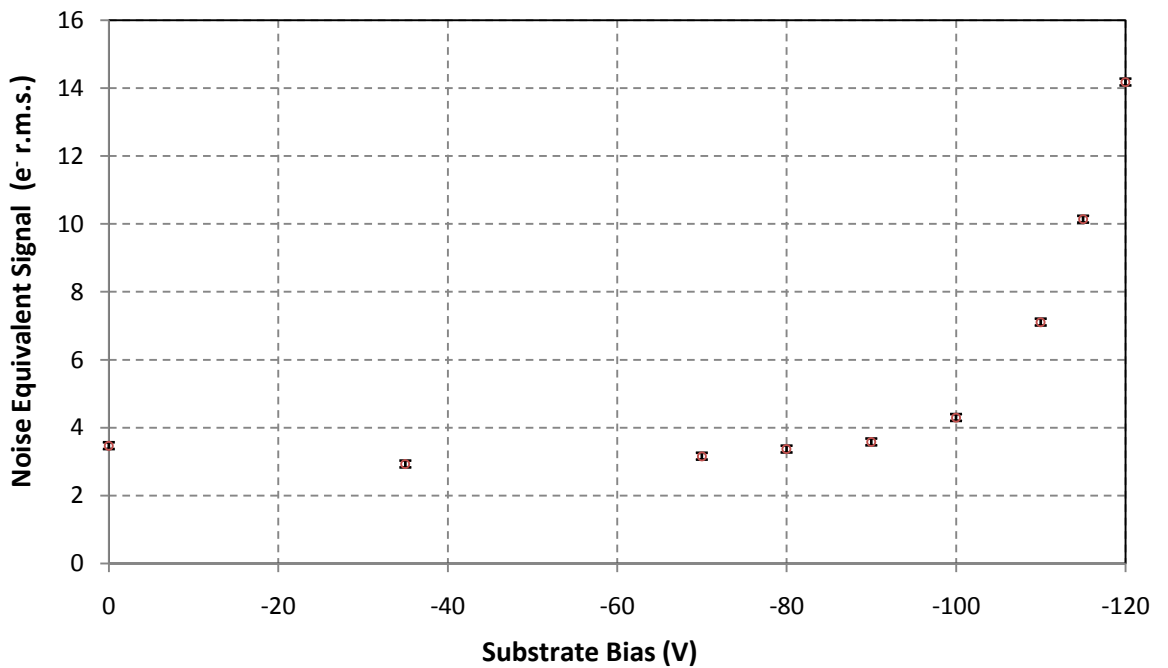
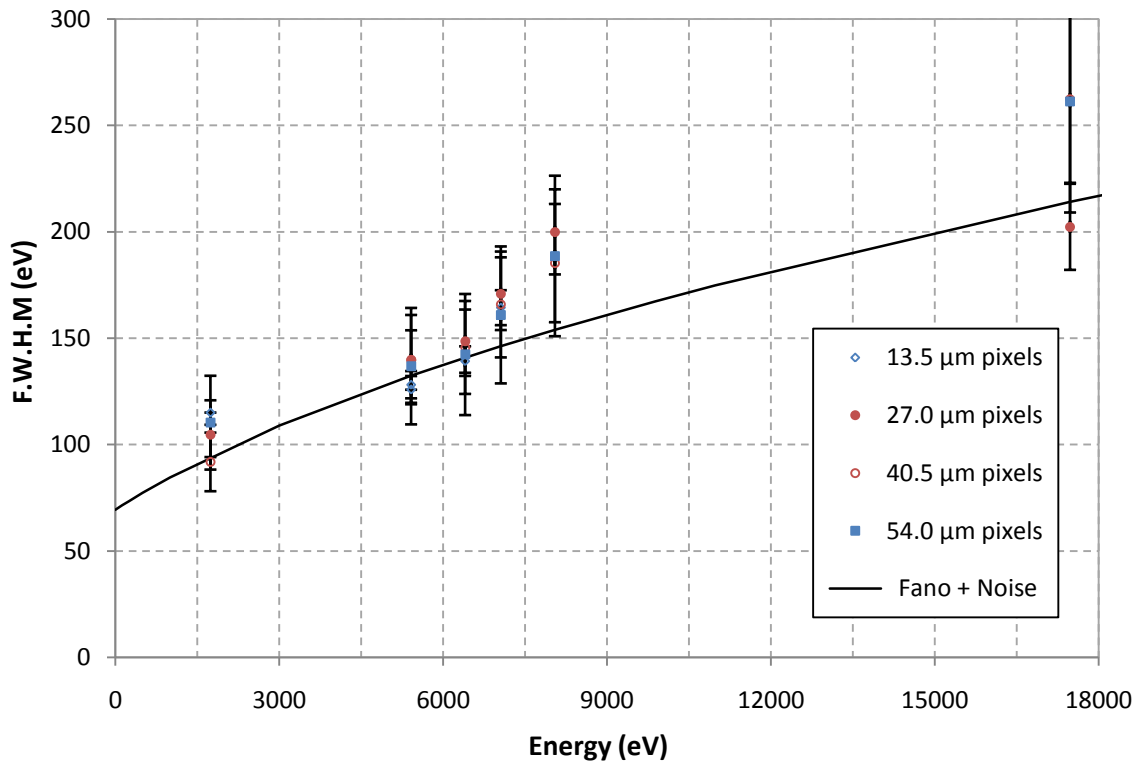


Figure 5.15 Noise vs. substrate potential  $V_{SS}$  with local substrate  $V_{LSS} = 7$  V

The results shown in Figures 5.14 and 5.15 define the useful operating range of the CCD247.

### 5.5.4 Spectral resolution

The spectral resolution of the device at different X-ray energies was found by measuring the FWHM of a Gaussian model fitted to the X-ray peaks in the histogram of the image in terms of eV. Results are plotted in Figure 5.16.



**Figure 5.16** Spectral resolution vs. substrate potential

The increased responsivity of the output circuit yields Fano limited + noise spectral resolution for energies below 6.5 keV. At higher energies the X-ray charge cloud was over-sampled by the 13.5 μm pixels and therefore on-chip binning was necessary to maintain an acceptable, although reduced, performance.

## 5.6 Problems and observations

### 5.6.1 Pixel size

The pixel size (13.5 μm) is small in comparison to the charge cloud generated by the X-ray event for energies above ~ 6 keV. This leads to spread events in the image caused by the charge traversing pixel boundaries both within and beyond depletion. This causes the oversampling of the X-ray event and hence poor FWHM due to errors involved in the event reconstruction that was necessary to determine the original X-ray energy. This effect was

resolved by performing on-chip binning, described in Chapter 4, to effectively increase the pixel size by  $n$  times the original pixel size, where  $n$  was the number of bins.

### 5.6.2 Cosmic events

Energetic particles from space interact with atoms in the upper atmosphere, creating secondary particles that can be imaged by the CCD, such particles are known as ‘cosmic rays’. The shape and spatial distribution of the event that is imaged depends on the particle’s angle of incidence and the depletion of the device. The increased depletion of high resistivity CCDs allows a greater portion of the charge generated by particles of shallow incidence to be fully collected, therefore producing longer traces than observed in standard devices. Figure 5.17 demonstrates a cosmic ray trace generated by a particle entering the front face of a CCD217 at a shallow angle that was observed during X-ray tests.

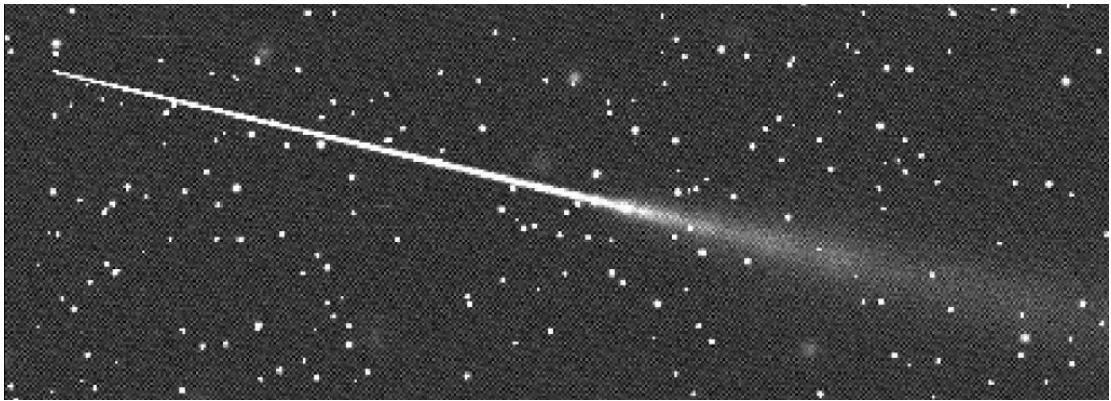


**Figure 5.17** Ionising particle track observed in CCD217

The particle deposits charge as it passes diagonally across the imaging area of the device and into the bulk silicon from left to right. The overall physical length of interaction was approximately 8 mm. Initially the charge was generated within the depleted region of the CCD and therefore was confined to within a few pixels perpendicular to its path. Roughly 2/3 of the distance along the trace ( $\sim 6$  mm) the particle enters the undepleted bulk silicon and the charge distribution becomes diffuse.

### 5.6.3 Serial register events

Both CCD217 and CCD247 are full frame devices that, when illuminated by an un-collimated X-ray source, may collect charge in the serial register elements. This was confirmed by ‘back-clocking’ the parallel register and therefore only reading out the charge generated under the serial register as shown in Figure 5.18.

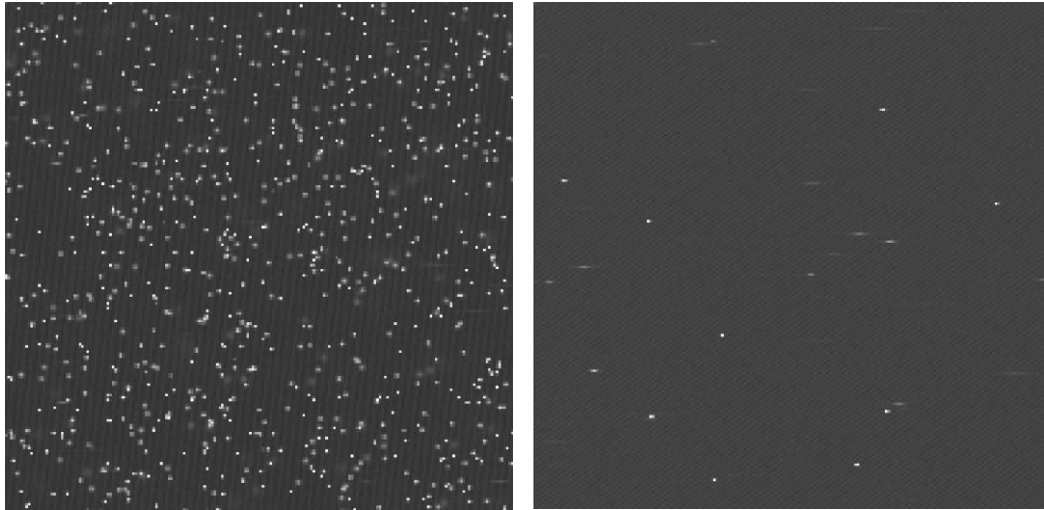


**Figure 5.18** Serial register X-ray events with parallel forward (left) and back (right) clocking

X-rays ionising directly in the serial register were observed to generate events that were 2 to 10 pixels in width. The excess width over standard split events observed in the imaging area of the device (2 to 3 pixels) was attributed to repulsion from the bulk p-material bounding the lower edge of the serial register. To overcome the problem of extra events being generated in the serial register, a lead screen was placed over the lower edge of the CCD to cover the serial register.

#### 5.6.4 XRF angle of incidence

The CCD was illuminated by an XRF target that was in close proximity ( $\sim 100$  mm) to the CCD imaging surface. The angle of dispersion from the target was therefore found to be large at the horizontal extremes of the imaging area. This allowed higher energy photons ionising towards the horizontal extremes of the imaging area to be collected within the depletion region that otherwise would have been ionised beyond the depletion region and only partially collected. Figure 5.19 shows example images of events observed by X-ray fluorescence of a copper target at different substrate potentials. The spread events caused by photons ionising beyond the depletion region have been highlighted in light grey to demonstrate their distribution across the imaging area. Where the gate to substrate potential was increased, depletion of the device was also increased and hence the number of spread events decreased.

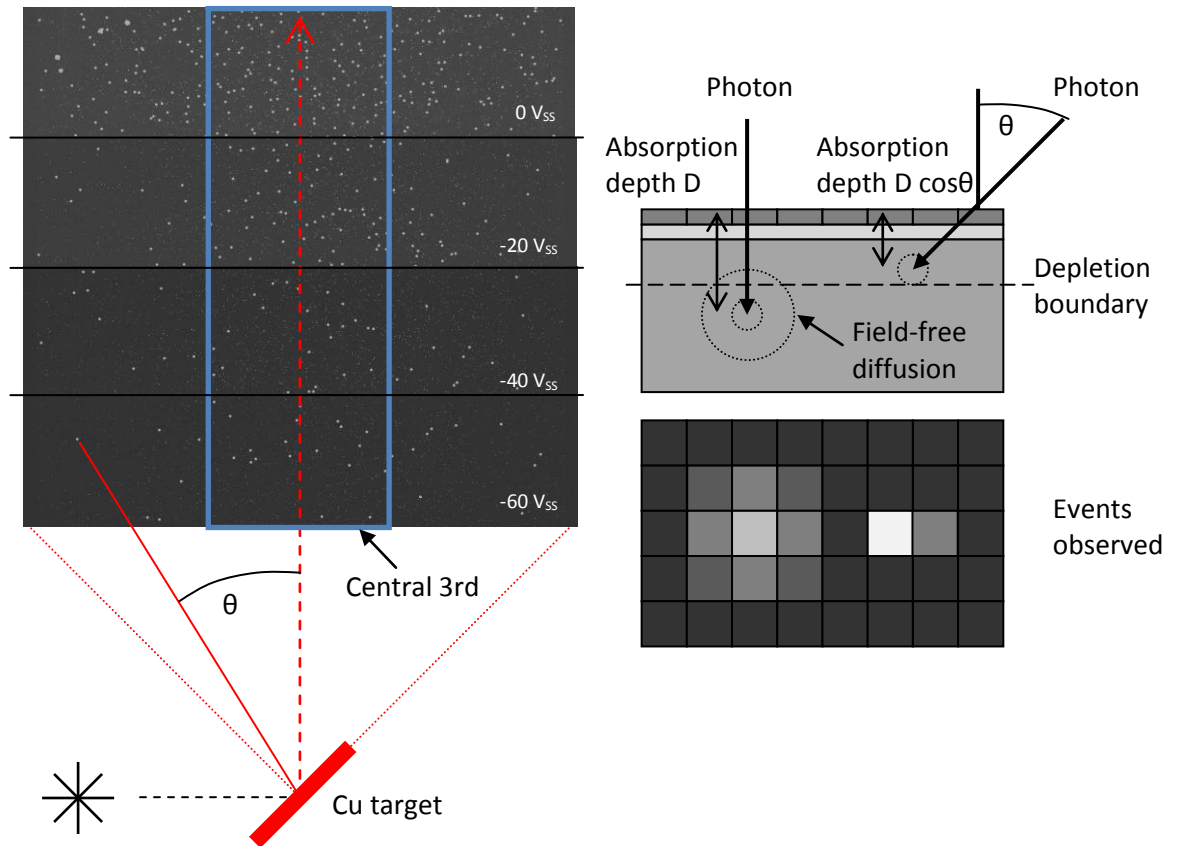


**Figure 5.19** Deep ionising event distribution from XRF

For un-collimated X-ray images, only the centre 1/3 of the imaging area (bounded blue) was used to provide event statistics as the dispersion was low minimising the number of X-ray events incorrectly identified as occurring within the depleted region.

### 5.6.5 Package isolation

The epoxy used to hold the CCD in the characterisation package was found to allow a conduction path between the rear surface ( $V_{ss}$ ) and the invar package grounded via the metal of the cold finger and vacuum chamber. The CCD package was electrically isolated from the cold finger by a single piece of Kapton film and the supporting machine screws were replaced by nylon alternatives.

## 5.7 p-Channel (CCD227) testing

For future X-ray astronomy missions it is planned to use p-channel CCDs as the buried channel is less susceptible to proton induced displacement damage [Hopkinson 1999] [Bebek et al 2001]. p-Channel devices were manufactured by exactly the same process steps as conventional n-channel devices, although the dopants are reversed [Jorden et al 2006]. The drive potentials for clock and bias lines are inverted and the signal carriers of the photo-

generated charge are holes, rather than electrons. Due to the reversed operating potentials, a new headboard, shown in Figure 5.20, was developed to ensure the correct polarisation of the tantalum capacitors used in the low pass filters of the D.C. biases.



**Figure 5.20** High resistivity p-channel CCD (CCD227) and headboard

The camera system used to drive the CCD that was described in Chapter 4 was only capable of providing bias potentials between 0 V to +30 V and clock signals of 0 V to +15 V. Therefore two methods were tried to operate the p-channel CCD227 at inverse potentials.

Firstly the clocking scheme was inverted as shown in Figure 5.21 and D.C. offsets were added to the clock signals to provide a virtual ground at +20 V, the OFF periods of the clocks becoming the logic high periods in the scheme.

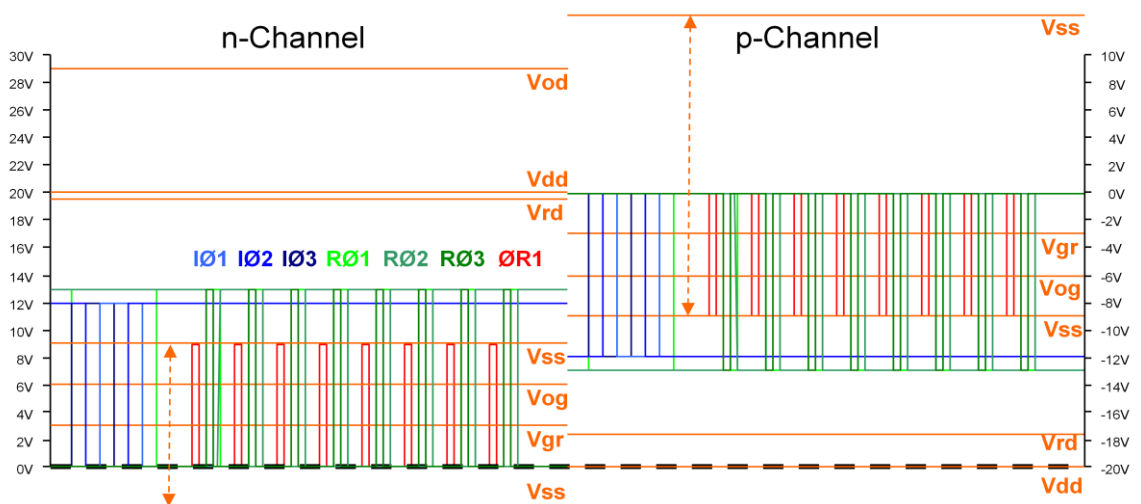


**Figure 5.21** p-Channel inversion scheme. D.C. offsets are added to all clocks

Unfortunately this method did not work due to a minor mistake in the sequencing program that was not discovered until the equipment was dismantled for conventional n-channel

characterisation work. The pixel reset clock ( $\Phi_R$ ) had not been inverted, meaning the output node was being reset during the addition of the pixel charge packet and hence no change could be sampled.

The second method was to operate the device with a standard n-channel sequencer program and clock and bias potentials but with each connection input into an array of independent operational amplifiers each with a gain of -1. The LM7171 was chosen for the task as it has a high slew rate allowing it to accurately follow the high switching of the output clocks and large operating voltage range.

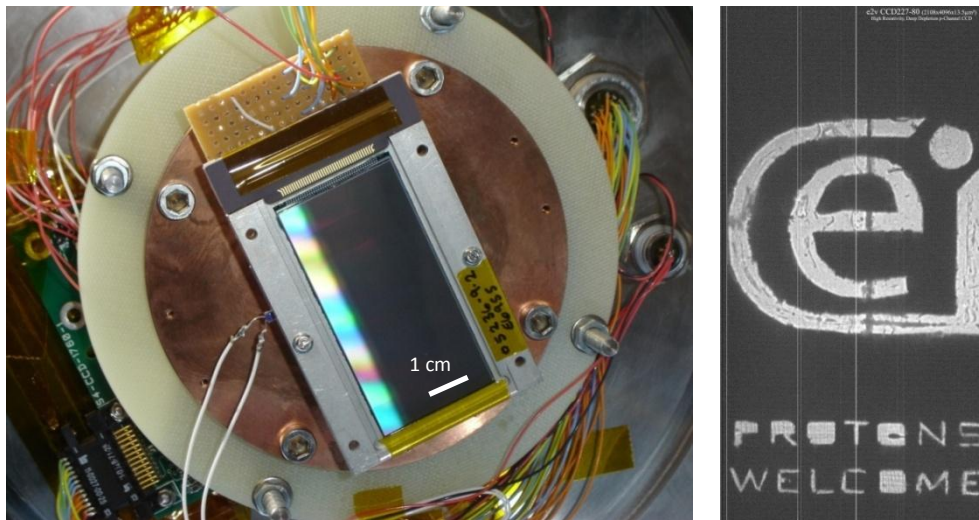


**Figure 5.22** Large area 2 k × 4 k CCD227 (left) and optical test image acquired (right)

This method proved successful and the optical test image shown in Figure 5.22 was acquired using a card mask.

## 5.8 Conclusions

### 5.8.1 CCD217 Design

The CCD217 was successful in proving the concept of fabricating CCDs using e2v's standard processes on high resistivity bulk silicon, that could be operated at large negative substrate potentials (-70 V) to increase the depletion depth of the device. However the extra spacing required between components of the output circuit to prevent avalanche breakdown led to increased parasitic capacitance of the output node, reducing output amplifier responsivity. The responsivity of the CCD217 was measured by X-ray to between 1-2  $\mu\text{V}/e^-$ . Corroborating measurements were made by e2v technologies using the mean vs. variance technique. The low responsivity had a negative impact on the noise, which was measured to be  $7.2 e^- \pm 0.5 e^-$  r.m.s at a pixel rate of 120 kHz, ultimately hindering the spectral performance of the device.

### 5.8.2 CCD247 Design

The inclusion of a separate substrate region around the output circuit in the CCD247 design allowed the layout of the output circuit to be reduced to a similar size to the CCD42, whilst retaining the ability to operate at large negative substrate potential. Responsivity was therefore increased to  $5.75 \mu\text{V}/e^- \pm 0.5 \mu\text{V}/e^-$ , almost halving the noise to  $3.4 e^- \pm 0.5 e^-$  r.m.s. and increasing the spectral resolution to an acceptable 140 eV at 6.4 keV. The guard drain structure however was found not to completely isolate the output circuit from the main substrate as demonstrated by the gradient of Figure 5.12. The main substrate potential was still having some, if reduced, effect on the responsivity of the output circuit.

The CCD247 was found to function correctly for substrate potentials between 0 V and -130 V. It was found that the most negative substrate potential that could be applied to the CCD247 whilst maintaining an acceptable  $< 5 e^-$  system noise was -100 V. The local substrate potential was found to have little impact on the noise in the range 0 V to 8 V, at higher potentials it is believed the onset of clock induced charge is observed, increasing the noise measurement. The CCD247 was never intended to operate with a local substrate potential of  $> 7$  V and therefore further investigation was not necessary.

Leakage current generation occurred at the expected rate for substrate potentials less negative than -90 V. Where the substrate potential was taken more negative an extra leakage effect was observed at the bottom left hand side of the imaging area. The severity of this effect was proportional to substrate potentials more negative than -90 V. Early analysis shows the leakage to be sourced from a section of the guard drain that overlaps a region of the left hand side local substrate. This could be verified in future work by biasing the right hand side local substrate to the same potential as the left (during the characterisation work described the right hand side local substrate was left floating). From this work, e2v now recognise a redesign of the CCD247 is necessary to avoid this problem.

In both CCD217 and CCD247 designs, it was observed that the pixel size should be matched to the incident X-ray energy for optimum performance. This prevents the oversampling of the event, that increases the noise due to the assumptions made of the background levels of the component pixels during event reconstruction. For high energy X-ray applications (up to 20 keV), it would be desirable to have 40  $\mu\text{m}$  to 50  $\mu\text{m}$  pixels.

### 5.8.3 p-Channel

Modifications were made to existing laboratory equipment to operate the p-channel devices with a complete set of inverted inputs. Images were acquired, although the leakage current

was found to be a factor 5 times higher than the equivalent n-channel CCDs, showing a greater dependence on the gate to substrate potential. Cosmetic quality was also found to be considerably poorer than that of the n-channel devices and this may be attributable to the starting bulk silicon used in the manufacture being of inferior quality [Jordan et al 2006]. It was not possible to adequately suppress the leakage current to observe X-ray photons.

## 5.9 Further work

It would be beneficial to the development of high resistivity CCDs to investigate the I-V characteristics of both the guard drain to main substrate and guard drain to local substrate of the CCD247, to ascertain the source of the extra leakage current observed at  $V_{ss} < -90$  V. This could lead to a modification of the design that would allow substrate potentials down to  $-130$  V, whilst maintaining  $< 5$  e<sup>-</sup> r.m.s. Such a redesign is currently being considered by e2v.

Further work would also include a comparative proton irradiation study of both p-channel and n-channel variants of the high resistivity CCDs to investigate the reduction in charge transfer inefficiency (CTI) in the p-channel devices.

## 5.10 References

- Bearden, J.A., 1967. X-ray wavelengths. *Review of Modern Physics*, Vol. 39, p. 78-124.
- Bebek, C. et al., 2001. Proton radiation damage in p-channel CCDs fabricated on high-resistivity silicon. *IEEE Nuclear Science*, Vol. 1, p. 72-75.
- Burt, D.J., 2006. Private communication.
- e2v technologies Ltd., 2004. Low-light technical note 4: dark signal and clock-induced charge in L3vision CCD sensors. A1A-Low-Light TN4. Issue 2.
- e2v technologies Ltd., 2007. High-rho project progress summary. *Commercial in Confidence*.
- Henke, B.L. et al., 1993. X-ray interactions: Photoabsorption, scattering, transmission, and reflection at  $E = 50$ -30,000 eV,  $Z = 1$ -92. *Atomic Data and Nuclear Data Tables*, Vol. 54, p. 181-343.
- Hopkinson, G.R., 1999. Proton damage effects on p-channel CCDs. *IEEE Transactions on Nuclear Science*, Vol. 46, p. 1790-1796.
- Jordan, P. et al., 2006. Commercialisation of full depletion scientific CCDs. *Proc. SPIE*, Vol. 6276.
- Mazur, R.G. & Dickey, D.H., 1966. A spreading resistance technique for resistivity measurements on silicon. *Electrochemical society*, Vol. 113, p. 255-259.

McMaster, W.H. et al., 1969. Compilation of X-ray cross sections. *Atomic data and nuclear data tables*.

Murray, N.J. et al., 2008. The X-ray performance of high resistivity (high-rho) scientific CCDs. *Proc. SPIE*, Vol. 7021.

## Chapter 6: Depletion depth modelling & estimates by event analysis

### 6.1 Introduction

This chapter describes three methods using X-ray photons to estimate the depletion depth of high resistivity CCDs. The experiment and measurements are presented for the X-ray spread event analysis method that are later compared to measurements obtained by the quantum efficiency (QE) method following the work described in Chapter 7.

Models of the potential profile under a CCD pixel and X-ray photon transmission are presented for the high resistivity CCD217 and CCD247, the devices designed and manufactured by e2v technologies that are used in the experimental work of this chapter. The potential profile models are produced by solving a series of analytical equations that determine the theoretical depth of depleted silicon for a given gate to substrate potential. The photon transmission model defines the attenuation of X-ray photons as they traverse the CCD structure and hence gives an indication of the transmission at any depth into the device. The transmission model is used to correlate the measured X-ray flux at a given incident photon energy to the depth of depleted silicon required to make that measurement.

The complete collection of charge generated by an X-ray event usually depends on the depth of depleted material into the p-region of a CCD's p-n junction (n-region for p-channel devices), referred to as the device's depletion depth. (In front illuminated devices the charge generation and collection of soft X-ray events can occur within the n-region) Where the X-ray photon interacts within the depletion region, nearly all of the charge generated is collected within one or more neighbouring pixels. The component pixel values of an X-ray event that is split over a number of pixels can usually be summed to a value equivalent to that expected by the incident photon. The charge generated by X-ray photons that interact beyond the depletion region, referred to as field-free events, will only be partially collected over a number of potential wells as it diffuses isotropically through the silicon before entering the depleted region. The remaining charge recombines in the bulk within a few microns and is not measured.

It is possible to determine the fraction of field-free events (events occurring beyond the depletion region) by analysing a large sample of monochromatic X-ray events in a CCD image and summing the pixel values of split events. The software developed to recognise and count the different types of X-ray events generated in the CCD image is described in this chapter, allowing the fraction of field-free X-ray events to be determined. This fraction can be directly

referenced to the photon transmission model to determine an approximation of the device's depletion depth. Results are presented for the estimated depletion depths of the CCD247 for different applied substrate potentials by spread event analysis using characteristic Cu-K $\alpha$  (8,047 eV) photons.

## 6.2 Measurement methods

The depth of depleted material in a CCD can be estimated by three methods: analysis of high energy ionising particles, X-ray spread event analysis and by QE model fitting [Prigozhin et al 1998]. The following subsections briefly describe these methods:

### 6.2.1 High energy ionising particle analysis

High energy particles illuminate the CCD at a shallow angle  $\theta$  to the CCD surface, the length  $x$  of charge deposited within a tightly confined 'corridor' of pixels is then measured. Where the particle trace becomes diffuse it is assumed to have penetrated beyond the depletion region as demonstrated in Figure 6.1. The depth of depletion  $y$  can be estimated to be the length of the trace multiplied by  $\tan \theta$  [Prigozhin et al 1998] [Awaki et al 2002].

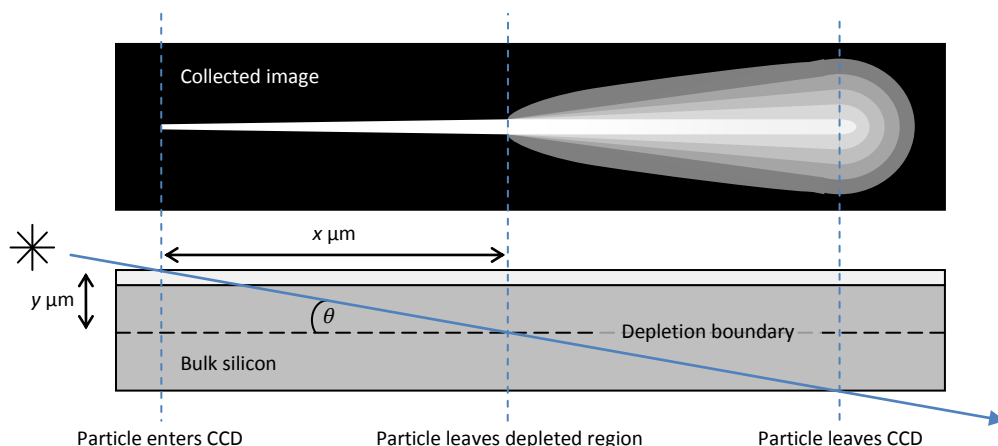


**Figure 6.1** Ionising particle trace analysis example, image (top) and cross-section (bottom)

### 6.2.2 X-ray spread event analysis

In X-ray point spread function analysis, the fraction of incident X-ray photons sampled beyond the depleted region are referenced to the photon transmission model of the CCD structure [Prigozhin et al 1998]. This model shows the corresponding thickness of the CCD material the photon has travelled and hence an estimate of the depletion depth can be made. All X-ray events in a CCD image must be analysed to determine the fraction of those that have been generated beyond depletion. Some fraction of events will occur too deeply in the CCD to be counted, due to the varying length a photon may travel through the silicon before interacting, hence leading to a systematic under estimate of the depletion depth by this method.

### 6.2.3 Quantum efficiency model fitting

Measurements of the X-ray QE of the CCD are compared to a theoretical QE model of the device. The depletion parameter of the model is adjusted until a fit is made to the measured data points.

The X-ray spread event analysis method is adopted in this chapter to provide estimates for the depletion depth over a range of gate to substrate potentials. The results of this method will later be compared with the QE model fit method using the QE data presented in Chapter 7.

## 6.3 The depletion model

The 1-D electrostatic potential profile of the high resistivity CCD217 and CCD247 at a given gate to substrate field potential can be modelled analytically for the n and p-type regions in the buried-channel CCD using the equations in Section 6.3.1 below [Howes & Morgan 1979].

### 6.3.1 Calculations

Table 6.1 lists the constants that are used in the following equations to model the front illuminated CCD217 and CCD247 devices.

Symbol	Units	Description	Value
$q$	C	Electronic charge	$1.60 \times 10^{-19}$
$\epsilon_{Si}$	F cm <sup>-1</sup>	Permittivity of silicon	$1.03 \times 10^{-12}$
$N_A$	cm <sup>-3</sup>	silicon acceptor dopant concentration	$4.00 \times 10^{12}$
$N_D$	cm <sup>-3</sup>	silicon donor dopant concentration	$1.00 \times 10^{16}$
$V_G$	V	Gate electrode potential	11
$t$	cm	Depth of n-channel	$1.00 \times 10^{-4}$
$\Phi_{ch0}$	V	Empty (buried) channel potential	11

**Table 6.1** Depletion model constants

The potential maximum of the buried channel,  $V_{max}$ , can be found by:

$$V_{max} = \Phi_{ch0} \left( 1 + \frac{N_A}{N_D} \right) \quad (\text{vi-i})$$

Where  $\Phi_{ch0}$  is the unbiased, empty channel potential created by the p-n junction,  $N_A$  and  $N_D$  are the acceptor and donor concentrations respectively. The acceptor concentration  $N_A$ , was taken as an average value for the bulk silicon based on the spreading resistance measurement of a sample of the material, described in Chapter 5. For e2v devices,  $\Phi_{ch0}$  is designed to have a potential of between 10 V to 12 V, so an average value of 11 V was used in the model.

The depth the depletion region extends into the p-region,  $x_p$ , can be approximated by:

$$x_p = \sqrt{\frac{2 \Phi_{ch0} \epsilon_{Si}}{q N_A}} \quad (\text{vi-ii})$$

Where  $q$  is the electronic charge and  $\epsilon_{Si}$  is the permittivity of silicon.

The depth of the potential maximum from the silicon dioxide interface,  $x_n$ , can be found by:

$$x_n = t - \left( x_p \frac{N_A}{N_D} \right) \quad (\text{vi-iii})$$

Where  $t$  is the depth of the n-channel.

The electrostatic potential of the n-type buried channel, at a depth  $x$  cm from the silicon dioxide interface,  $V_{n\text{-type}}$ , is then found by:

$$V_{n\text{-type}} = V_{max} - \frac{qN_D}{(2\epsilon_{Si})} (x - x_n)^2 \quad (\text{vi-iv})$$

The electrostatic potential of the p-type bulk silicon, at a depth  $x$  cm from the silicon dioxide interface,  $V_{p\text{-type}}$ , is then found by:

$$V_{p\text{-type}} = \frac{qN_A}{2\epsilon_{Si}} (x - t - x_p)^2 \quad (\text{vi-v})$$

### 6.3.2 Average depletion driving potential

The electric field driving depletion is provided by the applied gate electrode potential of + 11 V ( $V_G$ ), the buried channel potential ( $\Phi_{ch0}$ ) and the substrate bias ( $V_{SS}$ ). Each pixel has at least one electrode phase off during integration to maintain the vertical spatial resolution in the CCD image. The area of the pixel the off-electrodes occupy will therefore make a smaller contribution to depletion. Horizontal separation from neighbouring pixels is made by regions of channel stop that will also make a smaller contribution to depletion. Therefore, an average potential driving depletion ( $V_{AVG}$ ) over the area of one pixel and hence the entire imaging area, was found to increase the accuracy of the potential model. The average potential was derived from four different regions of the pixel structure, labelled 1-4 in Figure 6.2.

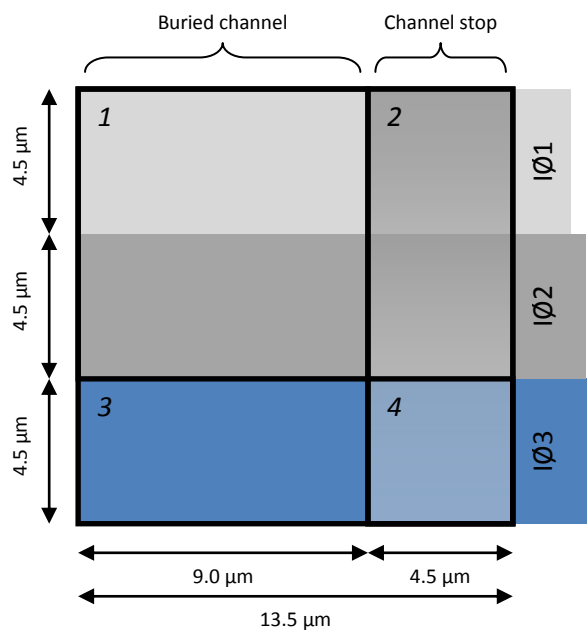


Figure 6.2 CCD217 and CCD247 pixel geometry

In general operation, the CCD was biased with one gate electrode high during integration and this is indicated by the shaded blue section of Figure 6.2. This region will introduce the gate potential of 11 V during integration. The buried-channel region of the pixel has an intrinsic empty channel potential formed by the p-n junction that occurs in regions 1 and 3 of Figure 6.2. This channel potential is designed to be between 10 V to 12 V for devices manufactured by e2v technologies and therefore an average of 11 V was used in the model. The channel stop region of the pixel labelled 2 in Figure 6.2 has an insignificant negative potential and was therefore modelled as having zero potential. The channel stop region labelled 4 in Figure 6.2 contributes only the gate potential towards the depletion (similarly to the surface channel CCD). All regions of the pixel (1-4) are subjected to the substrate bias potential ( $V_{SS}$ ) that was applied uniformly to the backside of the CCD. Table 6.2 summarises the four pixel regions shown in Figure 6.2 and gives the potential contribution made towards depletion in each case.

Region	Composition	Potential (V)	Area (%)	Component (V)
1	Buried-channel and substrate	$11 - V_{SS}$	44.5	$4.9 - V_{SS}$
2	Substrate only	$- V_{SS}$	22.2	$0 - V_{SS}$
3	Gate, buried-channel and substrate	$11 + 11 - V_{SS}$	22.2	$4.9 - V_{SS}$
4	gate and substrate	$11 - V_{SS}$	11.1	$1.2 - V_{SS}$
Average		$V_{AVG} - V_{SS}$	100.0	$11 - V_{SS}$

**Table 6.2** Depletion field components in a single pixel

Therefore, with an applied gate electrode potential of 11 V and an empty buried channel potential of 11 V the average potential driving the depletion depth of one pixel was 11 V, less the applied substrate potential.

A more accurate determination of the depletion depth could be made by the use of 3-D modelling software, but this was not available during the time of this investigation.

### 6.3.3 Potential profile

Figure 6.3 shows the electrostatic potential profile of the CCD217 and CCD247, calculated by equations (vi-iv) and (vi-v) for both the n and p regions of the CCD respectively. The buried channel (n-type material) was assumed to have a depth of 1  $\mu\text{m}$  and a doping concentration of  $1 \times 10^{16} \text{ cm}^{-3}$ . The potential maximum was observed to be between 0.91  $\mu\text{m}$  and 0.99  $\mu\text{m}$  from the silicon dioxide interface, depending on the substrate bias applied. The potentials in the n-type material are calculated at 0.1  $\mu\text{m}$  intervals from the silicon dioxide interface to the p-n junction. The remaining p-type material is plotted at 1  $\mu\text{m}$  steps until the electrostatic potential equals the applied substrate bias and the curve has an approximate gradient of zero. This is the depletion depth for the device at the applied substrate potential.

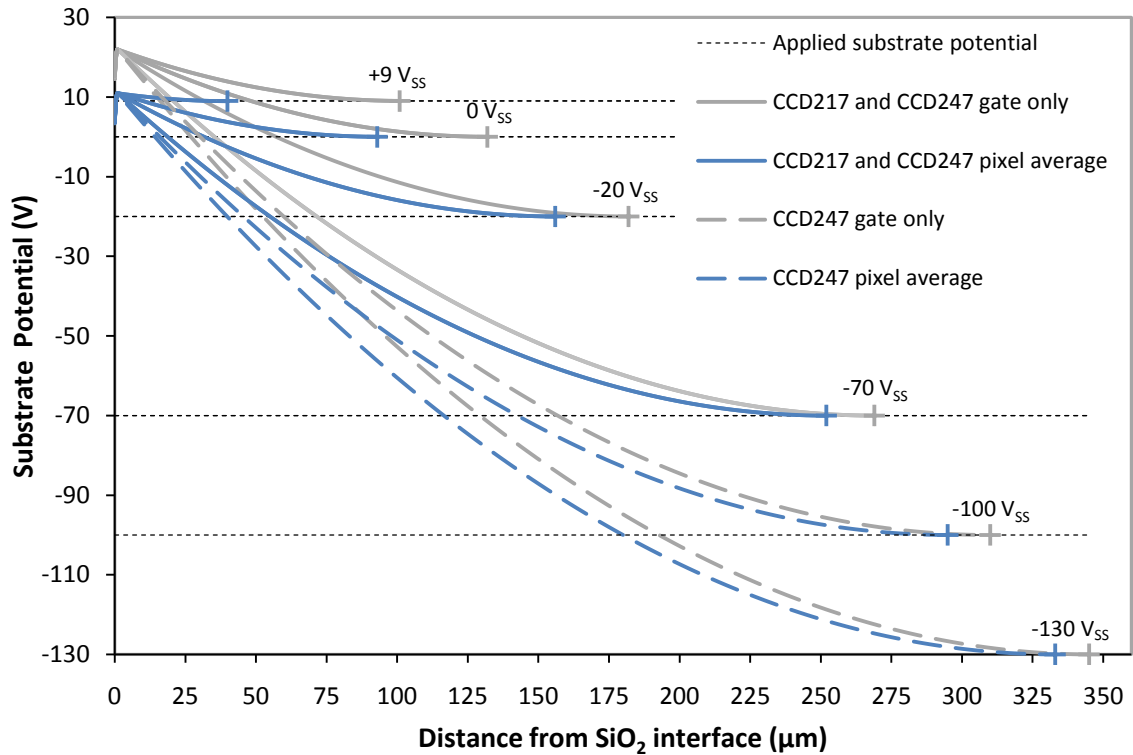


**Figure 6.3** CCD217 and CCD247 electrostatic potential models

The blue plots of Figure 6.3 indicate the potentials that have been calculated using the average driving potential ( $V_{AVG}$ ) in the pixel at the five different substrate biases. The depletion depth of the grey plots could be achieved by biasing all image electrode phases high during integration, but would remove the vertical spatial resolution of the CCD.

### 6.3.4 Depletion depth

The theoretical depletion depth from the surface,  $x_d$ , for a number of applied substrate potentials was obtained using [Howes & Morgan 1979]:

$$x_d (\mu\text{m}) = 1000 \sqrt{\frac{2\epsilon_{Si}(V_{AVG} - V_{SS})}{qN_A}} \quad (\text{vi-vi})$$

Where  $V_{AVG}$  is the average driving potential of the pixel.

Figure 6.4 shows the theoretical depletion depths achievable for applied gate to substrate potentials in three different p-type dopant concentrations of silicon. The higher the resistivity of the material, the greater the depletion for the same gate to substrate potential. Where the average was taken over the pixel area for the depletion driving potential, shown by the blue plots, the depletion is reduced.

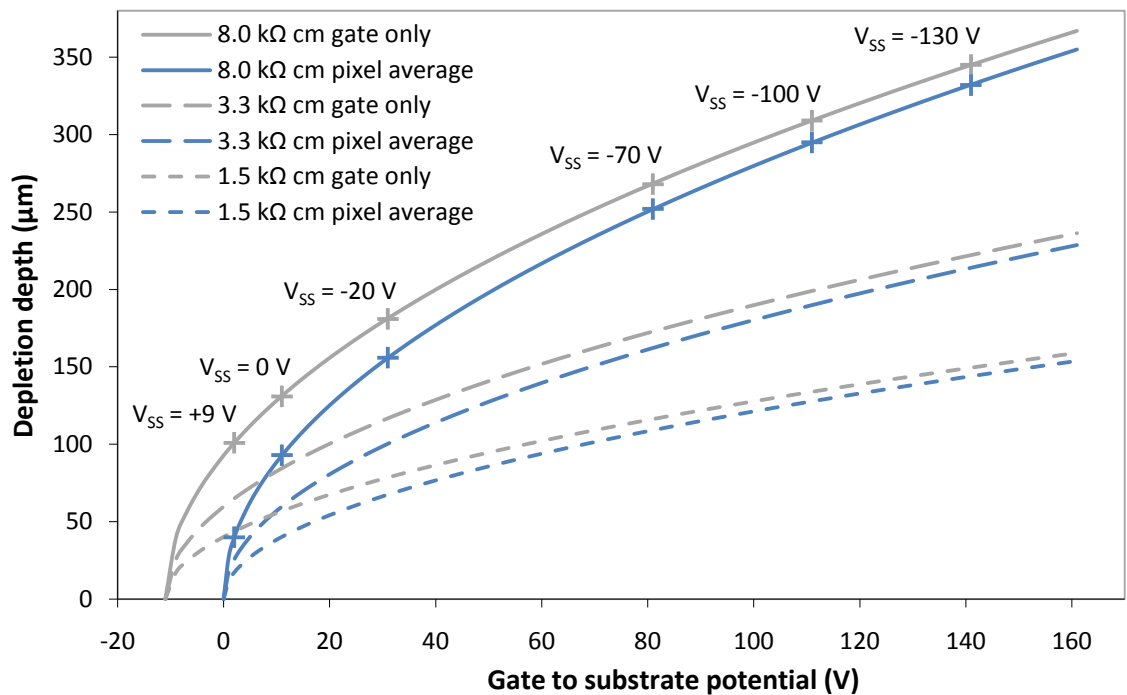


**Figure 6.4** High resistivity CCD depletion depths

Table 6.3 summarizes the theoretical depletion depths for applied gate to substrate potentials, including the difference in values obtained when taking the average driving potential of the pixel.

Substrate potential (V)	Gate depletion (µm)	Pixel average depletion (µm)	Difference (µm)
+9	101	40	61
0	131	93	38
-20	181	156	25
-70	268	252	16
-100	309	295	14
-130	345	332	13

**Table 6.3** CCD217 & CCD247 depletion depth model summary

The weighted mean of the pixel potential must be used when using low substrate potentials as it has a strong effect on the depletion depth. For large negative substrate potentials using the weighted average effect is less significant.

## 6.4 Front illuminated CCD photon transmission model

In manufacturing the front illuminated CCD a number of layers of material are formed on the surface of the silicon substrate to facilitate charge collection and transfer. Before incoming photons generate electrons in the active silicon they must first pass through these layers, with some fraction of the photons being absorbed before they reach the silicon substrate.

The front of the CCD217 and CCD247 comprise four layers deposited onto the silicon. The top surface is a 750 nm layer of silicon dioxide ( $\text{SiO}_2$ ); followed by 300 nm of polycrystalline silicon that forms the gate electrodes. Where the gate electrodes overlap, the thickness of the polysilicon doubles to 600 nm, this occurs in 11.1 % of the pixel structure and was accounted for in the following model. An 85 nm layer of silicon nitride ( $\text{Si}_3\text{N}_4$ ) acts as the gate dielectric for the pixel structure. Finally 85 nm of  $\text{SiO}_2$  separates the active silicon from the surface structures. A summary of the front illuminated CCD217 and CCD247 surface layers is shown in Table 6.4.

Layer	Thickness (nm)	Use
silicon dioxide ( $\text{SiO}_2$ )	750	Protective layer
polycrystalline silicon (Si)	300	Gate electrode
silicon nitride ( $\text{Si}_3\text{N}_4$ )	85	Dielectric
silicon dioxide ( $\text{SiO}_2$ )	85	Native
silicon (Si)	>162,000	Active material

**Table 6.4** Front illuminated CCD217 and CCD247 layer thicknesses

Each pixel is formed by a set of three electrodes and two channel stops. The electrodes measure 5.5  $\mu\text{m}$ , 5  $\mu\text{m}$  and 4.5  $\mu\text{m}$  in width for the electrodes  $\emptyset 1$ ,  $\emptyset 2$  and  $\emptyset 3$  respectively, with a 0.5  $\mu\text{m}$  overlap in each case. A vertical cross-section of the CCD pixel structure is shown in Figure 6.5.

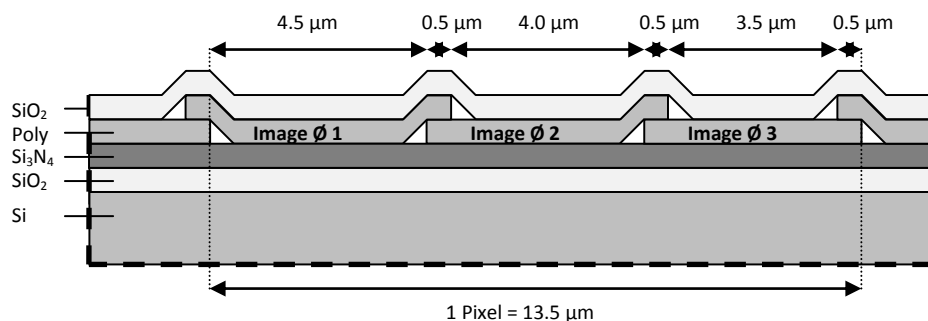


**Figure 6.5** CCD217/247 13.5  $\mu\text{m}$  pixel cross-section

Given the thicknesses of the different layers of material that form the CCD structure, it is possible to model the transmission of X-ray photons through each layer,  $I$ , from Beer's law:

$$I = 0.998 \times 0.992 \times I_0 e^{-\mu x} \quad (\text{vi-vii})$$

Where  $I_0$  is the incident photon flux,  $\mu$  ( $\text{cm}^{-1}$ ) is the linear attenuation coefficient for the material or compound and  $x$  (cm) is the overall thickness of the layer. The two constants, 0.998 and 0.9924, account for the absorption in the surface electrode structures and 0.5  $\mu\text{m}$  buried channel respectively.

In order to obtain the linear attenuation coefficient of a compound, such as silicon dioxide, it is necessary to find the sum of the linear attenuation coefficients of the elements in the compound. The linear attenuation coefficient of silicon dioxide,  $\mu_{SiO_2}$ , is:

$$\mu_{SiO_2} = \mu_{Si} + 2 \times \mu_O \tag{vi-viii}$$

The linear attenuation coefficient for silicon nitride,  $\mu_{Si_3N_4}$ , is:

$$\mu_{Si_3N_4} = 3 \times \mu_{Si} + 4 \times \mu_N \tag{vi-ix}$$

In the model the incident flux for each layer is the transmission through the previous layer of CCD material, starting at the silicon dioxide interface. Figures 6.6 and 6.7 show the modelled transmission of X-ray photons through the CCD structure for the characteristic lines of Cu-K $\alpha$  (8,047 eV), Ge-K $\alpha$  (9,885 eV) and Mo-K $\alpha$  (17,478 eV).

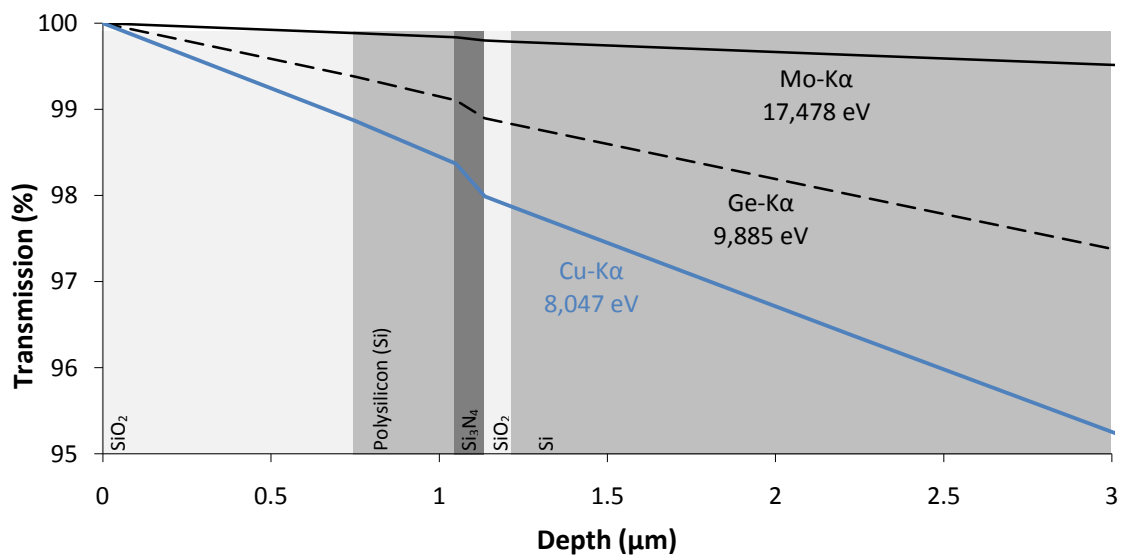


Figure 6.6 X-ray photon transmissions through the CCD

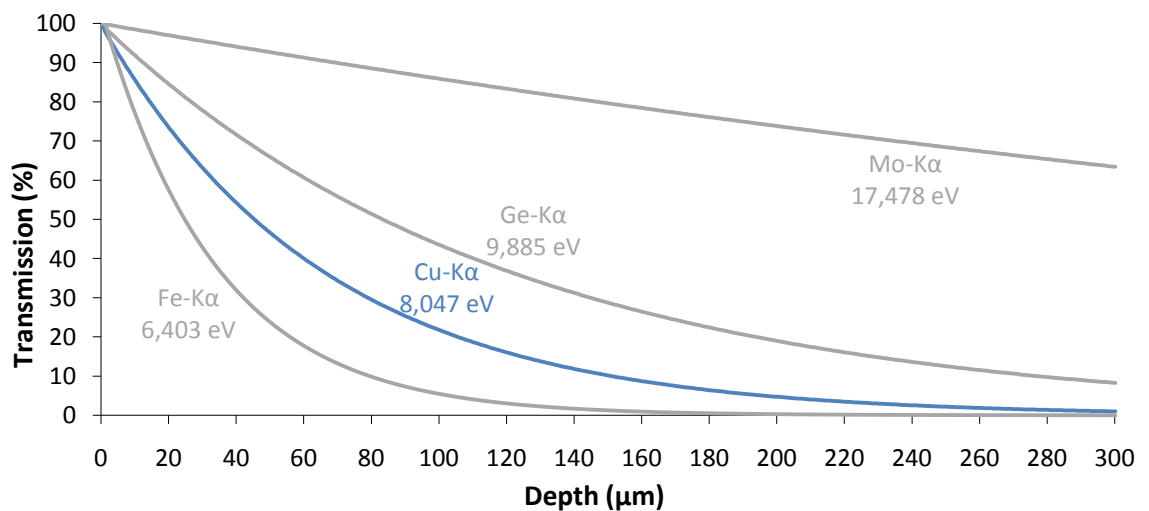


Figure 6.7 X-ray photon transmissions through the CCD

Figure 6.7 demonstrates that the higher the energy of the incident X-ray photon, the greater the thickness of silicon required to absorb the majority of photons.

## 6.5 X-ray split events

X-ray events in images are often observed to be spread across multiple pixels. This is caused by the charge cloud generated during photoelectric absorption traversing pixel boundaries during collection. There are three factors that will determine whether a charge cloud will cross the boundaries of a pixel on collection [Pavlov & Nousek 1999]:

- The **location** of where the cloud forms in the pixelated silicon structure.
- The **size** of the cloud generated in the silicon, due to the photo-electron range.
- The **distance** the charge travels through to collection.

Figure 6.8 demonstrates each of these factors in a vertical cross-section of the CCD.

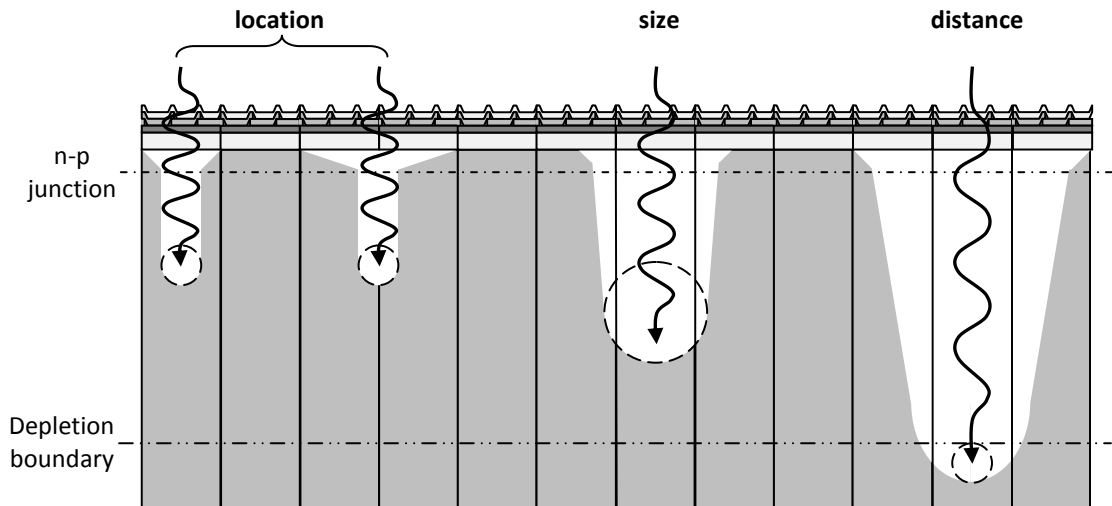


**Figure 6.8** Factors influencing X-ray split event types observed in CCDs

### 6.5.1 Location of ionisation (location)

The location of the charge cloud generated below the array of pixel structures has a direct impact on the probability of a split event. If the centre of a charge cloud generated by an X-ray event is directly below the centre of a pixel and has a diameter smaller than the width of the pixel, it has a very high probability of being collected in only that pixel. If the charge cloud is generated below the  $p^+$  channel isolation structure (channel stop), regardless of size and any diffusion, the charge has a very high probability of being split between two horizontal neighbouring pixels. Similarly if the charge was generated below any of the off-phase electrodes in the imaging area, it is highly likely to drift into the potential wells of vertical neighbouring pixels as the 2<sup>nd</sup> event example in Figure 6.8 demonstrates.

X-ray events that are split between neighbouring pixels due to the location of the interaction can be summed during post processing of the image to measure the full charge generated by the incident photon (assuming no piled-up events).

### 6.5.2 Size of e-h cloud (size)

The radius of the charge cloud in  $1\sigma_{\text{radius}}$  of events formed inside the depleted region can be approximated by [Hopkinson 1983]:

$$1\sigma_{\text{radius}} (\mu\text{m}) = \sqrt{\frac{2kT\epsilon_{Si}}{q^2N_A}} \ln\left(\frac{x_d}{x_d - x_{abs}}\right) \quad (\text{vi-x})$$

Where  $k$  is Boltzmann's constant,  $T$  is the temperature in degrees Kelvin. The distances  $x_d$  (cm) and  $x_{abs}$  (cm) are the depletion depth of the CCD and photon 1/e absorption depths (linear attenuation) respectively. The charge cloud radius and hence diameter will therefore vary with changes to the substrate potential and incident X-ray energy as these directly affect both  $x_d$  and  $x_{abs}$ .

Table 6.5 lists the  $1\sigma$  charge cloud diameters for a number of different incident photon energies at different depletion depths. Where the depletion depth ( $x_d$ ) is smaller than the absorption depth ( $x_{abs}$ ), equation vi-x cannot be satisfied and hence no result can be calculated.

$V_{SS}$	$x_d$ ( $\mu\text{m}$ )	1,487 eV ( $\mu\text{m}$ ) $X_{abs} = 7.7$	6,403 eV ( $\mu\text{m}$ ) $X_{abs} = 34.0$	8,047 eV ( $\mu\text{m}$ ) $X_{abs} = 65.7$	9,885 eV ( $\mu\text{m}$ ) $X_{abs} = 120.3$	11,221 eV ( $\mu\text{m}$ ) $X_{abs} = 175.3$	17,478 eV ( $\mu\text{m}$ ) $X_{abs} = 658.6$
+9	40	2.18	6.48	-	-	-	-
0	93	1.39	3.18	5.22	-	-	-
-20	156	1.06	2.34	3.49	5.73	-	-
-70	252	0.83	1.79	2.59	3.80	5.14	-
-100	295	0.77	1.65	2.37	3.41	4.48	-
-130	332	0.72	1.55	2.22	3.16	4.09	-

**Table 6.5**  $1\sigma_{\text{radius}}$  charge cloud diameters generated in depleted region of the CCD247

When the charge cloud diameter increases towards the dimensions of the pixel structure (13.5  $\mu\text{m}$ ) the probability of causing a split event in the image is also increased. A split event will certainly occur where incident photons generate a charge cloud with a diameter greater than the pixel size.

X-ray events that are split over neighbouring pixels due to a relatively large cloud diameter can also be summed during post processing of the image to measure the full charge generated by the incident photon (again, assuming events do not pile-up).

### 6.5.3 Charge diffusion to collection (distance)

Once generated by the photoelectric effect, the e-h charge cloud diffuses isotropically through the silicon until it is collected in potential wells or recombines in the bulk. The diameter of the charge cloud increases as it diffuses in the silicon, increasing its probability of growing larger than the pixel dimensions, resulting in a split event at collection. We know from the work of Pavlov and Nousek that the dominant diffusion effect occurs in the field-free region of the silicon (beyond depletion) as diffusion within the depleted region is small in comparison to the pixel size.

When the charge is generated within the strong electric field of the depleted region, it drifts entirely towards collection in one or more potential wells and can be summed during post processing to recover the entire charge generated by the incident photon. Charge clouds generated by incident photons that interact beyond the depletion region will have a large probability of charge loss, due to recombination in the bulk, and hence full charge recovery will not be possible during post processing. This effect is paramount to the X-ray spread event analysis method as it allows the ratio of photons absorbed beyond depletion to be estimated by finding the number of X-ray events in an image that sum to less than that expected from the incident photon.

## 6.6 Depletion depth estimate method

The CCD was illuminated by a beam of X-ray photons of a known energy. Images were stored for a number of different applied substrate potentials, and hence depletion depths, to generate a number of correlated transmission statistics. The minimum depletion depth for experimentation would be  $\sim 90 \mu\text{m}$  when applying 0 V to the substrate bias and therefore it was decided that energies below 8,047 eV would have already been sufficiently absorbed ( $\sim 93\%$ ) to make measurements unreliable. The Cu-K $\alpha$  line, at 8,047 eV, was therefore chosen as it gave a modelled transmission of between 2 % to 24 % over the substrate potentials of interest (0 V to -70 V). A 15  $\mu\text{m}$  nickel filter was used, as in the work of Chapter 5, to attenuate the other unwanted X-ray energies incident on the CCD.

The fraction of X-ray event patterns generated beyond the depletion region was found by post processing the recorded images to determine those events that have lost some portion of the charge packet through recombination in the bulk, such events being split between two or more neighbouring pixels and summing to less than  $3\sigma$  of the 8,047 eV average distribution. This fraction, the measured photon transmission, was then referenced to the theoretical

model, shown in Figure 6.7, to provide an estimate for the depletion depth at the applied substrate potential.

## 6.7 Event counting

In order to measure the fraction of X-ray events generated beyond the depletion region, it was necessary to develop a custom software tool to recognise and count the different types of X-ray events in the images. Initially, an automatic energy calibration was performed on the image to determine the background and X-ray charge levels. This was achieved by generating a histogram of the pixel levels and then fitting Gaussian profiles to both the background and X-ray peak distributions. A background threshold was then set  $6\sigma$  above the background peak to ensure the software would only count pixel events caused by X-ray interactions. Each pixel in the image was then sequentially checked to determine if it was above the background threshold. If so, a number of event pattern masks were applied to the pixel to check the different combinations of charge distribution among neighbouring pixels to determine the event type. These pattern masks are shown in Figure 6.9 and cover all the possible split event patterns a single X-ray photon can generate within a  $4 \times 4$  pixel area.

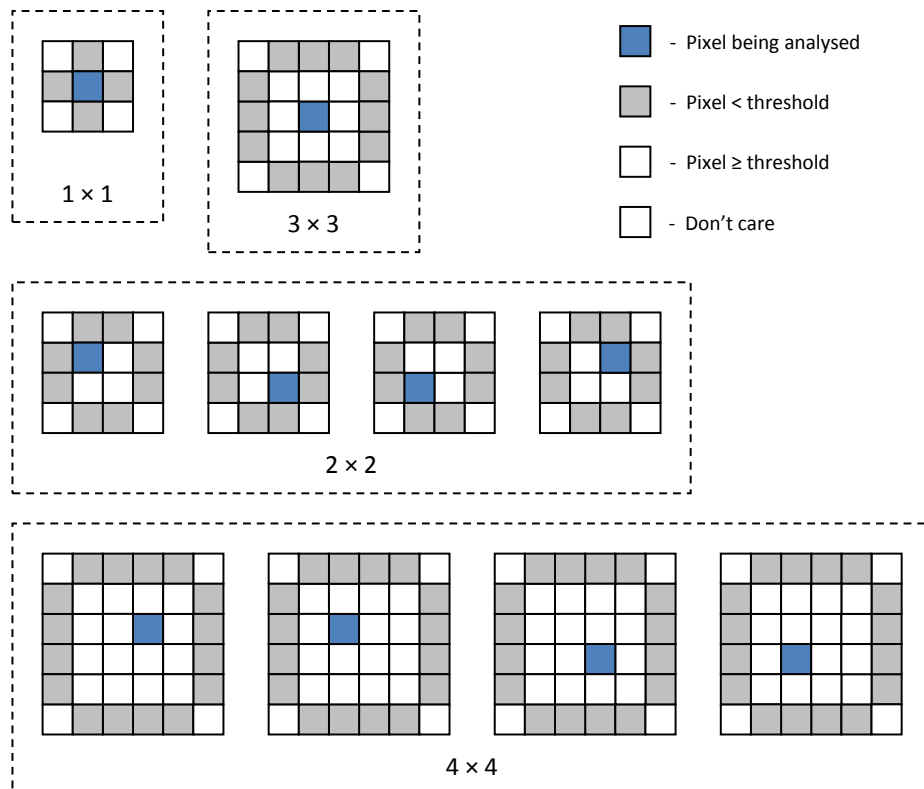


**Figure 6.9** Event pattern masks

For example, a  $1 \times 1$  (isolated) event was counted when there was no charge in the orthogonal neighbouring pixels above the background threshold. For events that were split between

multiple pixels, component pixel charges must sum to a value within  $3\sigma$  of the peak X-ray energy if the event were to be counted as occurring within the depletion region. If the summed value of the split event was lower than  $3\sigma$  of the X-ray peak, the event was counted as having occurred beyond depletion as there had been some charge loss to the bulk.

## 6.8 Results

### 6.8.1 Errors

There are a number of errors when estimating depletion depth by this method, summarised below:

It was assumed all X-ray photons collected in the image are 8,047 eV; however there are photons of other energies present from different sources. Table 6.6 lists these sources and their relative probability of occurrence compared to that of an 8,047 eV photon.

Energy (eV)	Source	Line	Fluorescence Yield	Filter Transmission	Probability	Relative Probability
8,047	XRF	Cu-K $\alpha$	44.6 %	53.5 %	23.9 %	100 %
8,904	XRF	Cu-K $\beta$	6.3 %	2.4 %	0.2 %	0.6 %
930	XRF	Cu-L $\alpha$	0.6 %	0.0 %	0.0 %	0.0 %
6,308	CCD	Cu-K $\alpha_{\text{escape}}$	4.7 %	5.4 %	1.1 %	4.7 %
7,165	CCD	Cu-K $\beta_{\text{escape}}$	0.7 %	2.4	0.2 %	0.7 %
1,739	CCD	Si-K $\alpha$	4.7 %	N/A	1.1 %	4.7 %
1,836	CCD	Si-K $\beta$	0.7 %	N/A	0.2 %	0.7 %

**Table 6.6** X-ray photon occurrence probabilities relative to Cu-K $\alpha$

The high absorption in the nickel window renders the Cu-L $\alpha$  photon count to be negligible. The Cu-K $\beta$  photons also have an insignificant probability due to their combined low fluorescence yield and high absorption in the nickel window. There was a higher probability of the silicon atoms in the CCD being fluoresced and generating Si-K $\alpha$  and Si-K $\beta$  photons at 1,739 eV and 1,836 eV respectively, although these energies are very close to the silicon K shell absorption edge of 1,838.9 eV and are also assumed to be negligible. The dominating source of undesired photons in the experiment was therefore the silicon escape peaks at 6,308 eV and 7,165 eV. These contribute a total uncertainty of  $4.7\% + 0.7\% = 5.4\%$  for the measured in-field X-ray flux.

Additionally there was an error in the counting of events that are generated beyond the depletion region. Some X-ray photons will be ionised so far beyond the depletion region that by the time the charge has drifted into a potential well, it has been sufficiently spread out to be effectively 'lost' in the noise. There was also a probability that some X-ray photons pass

through the CCD completely. For an 8,047 eV X-ray photon, the error reduces with increased depletion depth from 25 % at 90  $\mu\text{m}$  to 1 % at 300  $\mu\text{m}$ .

There are also systematic errors on the estimates due to the definition of the depletion depth. The theoretical depletion depth, described in Section 6.3.3, was based on the depth at which the electrostatic potential equals the applied substrate potential. However, the electrostatic potential has a parabolic decline that may fall to a level that was insufficient to fully collect photo-generated charge before the theoretical depletion.

### 6.8.2 Depletion boundary estimate example

A CCD217 that is illuminated by Cu-K $\alpha$  photons will produce an image similar to that shown in Figure 6.10. The X-ray events that were ionised within the depleted region are brighter and confined to within a few pixels; there are 66 such events in Figure 6.10. Those photons that interact beyond the depleted region produce the darker, 'blurry' events that share the original charge between many pixels; there are 49 of these events in this example.

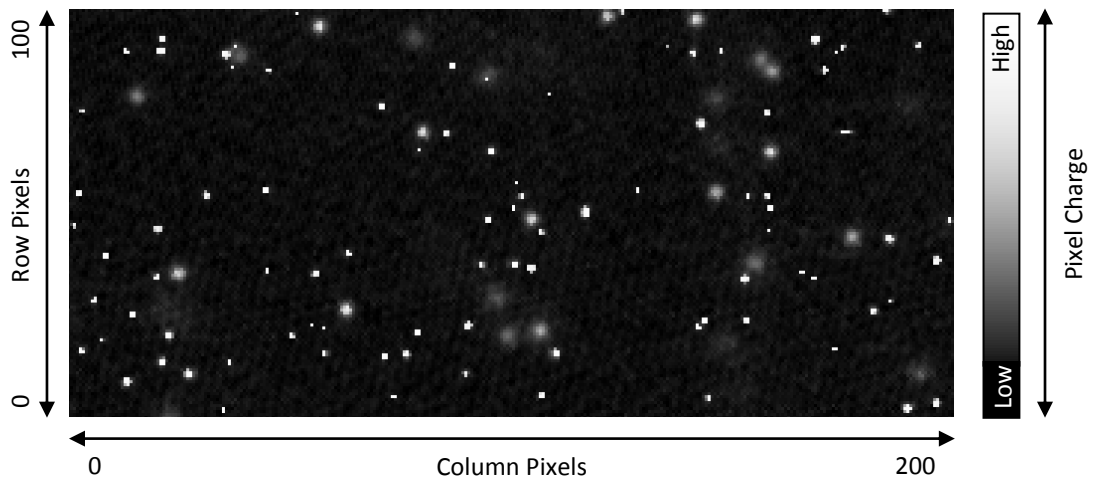


**Figure 6.10** Example of X-ray events collected by CCD

The transmission beyond the depleted region boundary is calculated by the number of events ionised beyond depletion (49) divided by the total number of events (66 + 49), that is 42.6 % in this example. This value is then referenced to the photon transmission model in Figure 6.7, to estimate the depletion boundary to be at  $\sim 56 \mu\text{m} \pm 3 \mu\text{m}$  at the applied field voltage of 0 V.

### 6.8.3 Estimates

Depletion depth estimates for the CCD247 based on experimental data are shown in Figure 6.11 and Table 6.7.

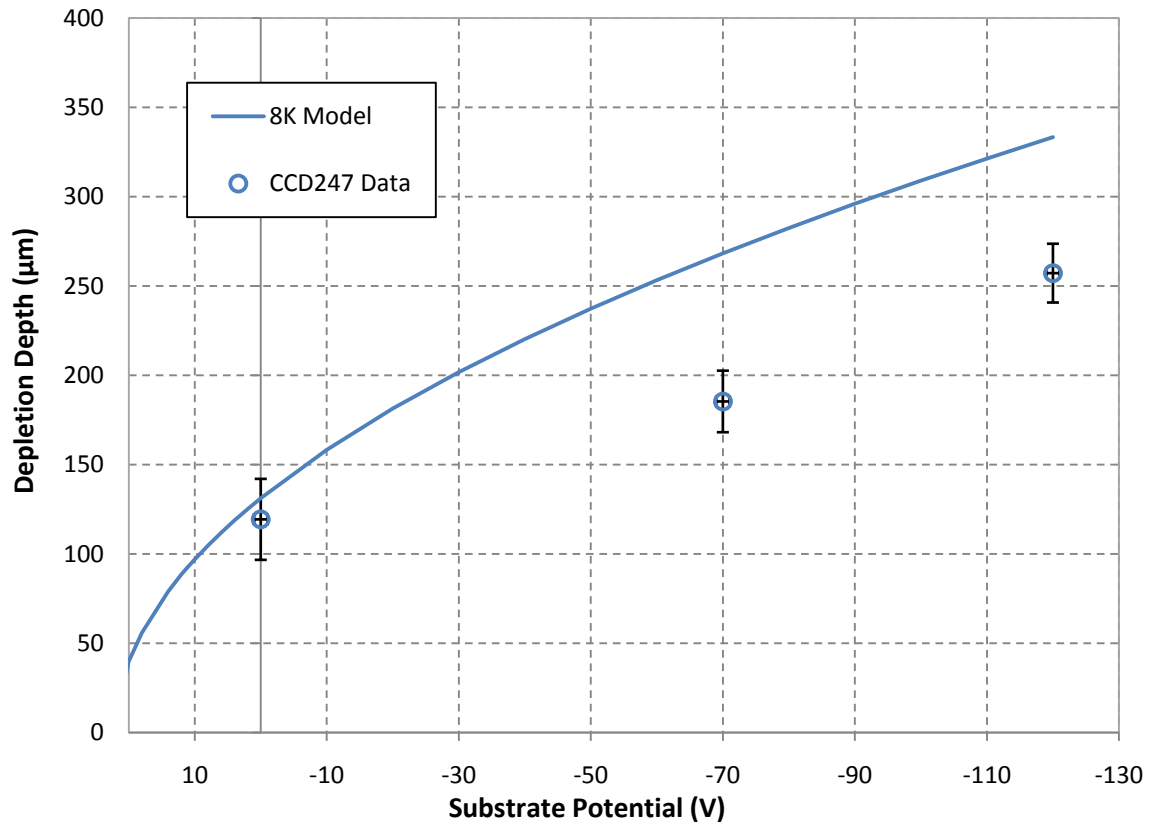


Figure 6.11 Depletion depth estimates

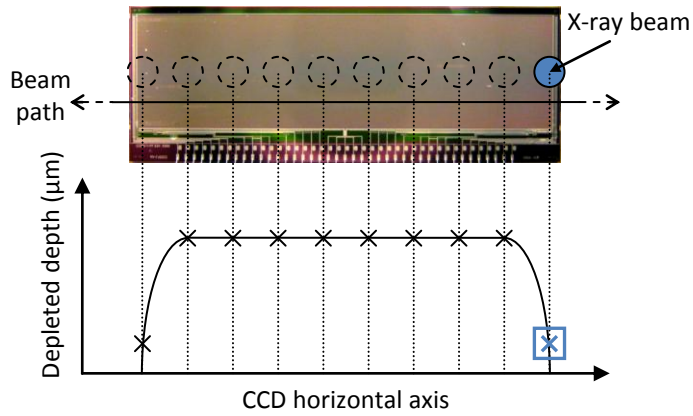
Substrate Potential (V)	Depletion Depth (μm)
0	120
-70	185
-120	257

Table 6.7 Depletion depth estimates

The fact that the measured values are lower than those predicted by the model maybe a consequence of the inherent errors in the method.

## 6.9 Depletion depth uniformity

The equipment developed for the QE work of Chapter 7 allowed the X-ray source to be moved across the horizontal imaging axis of the CCD during operation. Depletion depth estimates made by the method presented in this chapter were therefore obtained at various positions across the horizontal axis of imaging area of the CCD using this adapted test equipment. Figure 6.12 demonstrates the measurement positions that were available.



**Figure 6.12** Depletion depth uniformity estimates example

Initial estimates for the variation in depletion across the centre of the imaging area for the CCD247 are shown in Figure 6.13 using the method presented in this chapter.

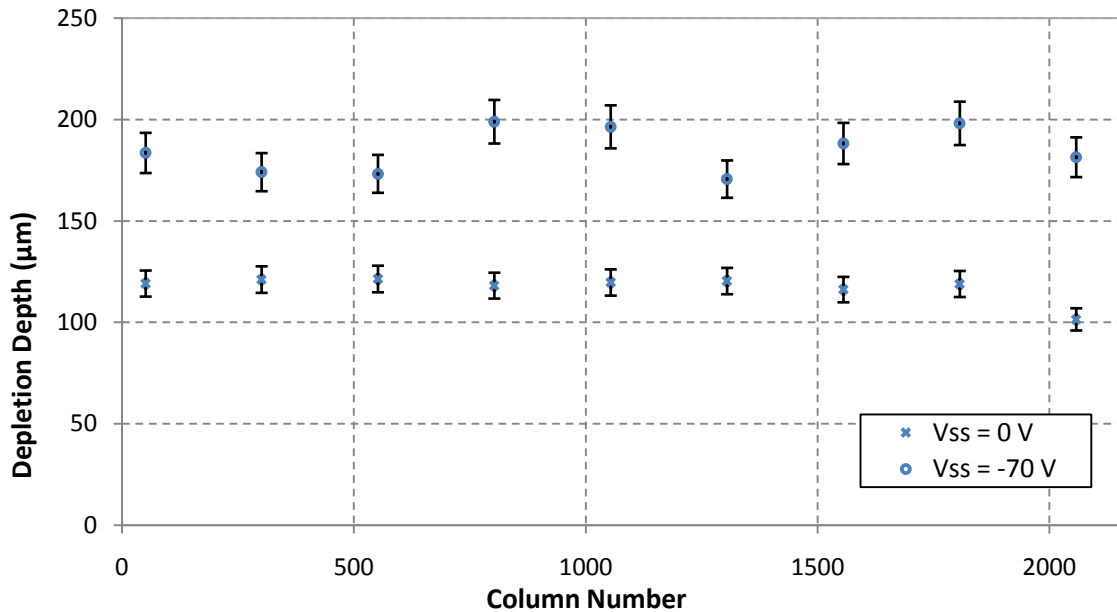


**Figure 6.13** Depletion uniformity measurements for CCD247

The initial results show the depletion depth to be uniform across the horizontal axis of the imaging area for a low gate to substrate potential. For larger gate to substrate potentials, the errors on the depletion depth estimates are increased due to the smaller change in transmission (used to make the estimate) through the depleted silicon for 8,047 eV photons. From the photon transmission model shown in Figure 6.7, the average change in transmission for an 8,047 eV photon was 1.43 % between 150 μm to 160 μm of depleted silicon, whereas a 9,885 eV photon would give 2.30 %. It would therefore be possible to increase the accuracy of all depletion depth estimates by tuning the incident photon energy to the expected depletion depth.

## 6.10 Conclusions

The depletion depth of a CCD is proportional to the root of the substrate potential. Where the substrate potential is taken more negative, hence increasing the electric field strength, the depleted region extends further into the p-region of the bulk silicon. Increased depletion depth increases the QE for X-rays and reduces the number of spread events observed in an X-ray image. Figure 6.14 shows example images of the same X-ray source taken at two different substrate potentials using a CCD247.



**Figure 6.14** X-ray event patterns observed by CCD247 at  $V_{ss} = 0$  V (left) and  $V_{ss} = -100$  V (right)

Both CCD217 and CCD247 devices performed well with substrate potentials as negative as -70 V. A depletion depth of approximately 185  $\mu\text{m}$  was estimated by split event analysis for the CCD247 when depleted by an applied substrate potential of -70 V. This was approximately 28  $\mu\text{m}$  less than the theoretical depletion depth at this substrate potential and can be explained, but not fully accounted for, by some of the errors inherent in the event analysis technique.

The depletion depth estimates are subject to systematic errors from the un-counted spread events, occurring deep in the substrate and by the low field tail leading to the electronic definition of the depletion boundary. There will be spread events that are so far beyond the depleted region they cannot be differentiated from the background noise. Therefore, the number of spread events counted experimentally can only be a minimum value. If the ratio of spread events were to be higher, this would correspond to a reduction in the depletion depth estimate. The methodology described in this chapter can however give a 'quick' indication of CCD depletion depth using typical X-ray CCD characterisation equipment.

A more accurate method for estimating the depletion depth of a CCD can be derived from QE measurements that are presented in Chapter 7.

### 6.11 Further work

The depletion uniformity could also be probed in the vertical imaging axis by adjusting the mounting of the CCD on the cold finger between experiments to enable a depletion map to be plotted for the device. Further work could investigate positioning the CCD on a translational mount to enable the probing of the entire imaging area without the downtime of physically moving the CCD on the cold finger.

### 6.12 References

- Awaki, H. et al., 2002. A novel method to estimate the thickness of the depletion layer of an X-ray CCD. *Nuclear Instruments and Methods*, Vol. A495, p. 232-239.
- Hopkinson, G.R., 1983. Charge diffusion effects in CCD X-ray detectors. I. Theory. *Nuclear Instruments and Methods*, Vol. 216, p. 423-429.
- Howes, M.J. & Morgan, D.V., 1979. Charge-coupled devices and systems. *Wiley*.
- Pavlov, G.G. & Nousek, J.A., 1999. Charge diffusion in CCD X-ray detectors. *Nuclear Instruments and Methods*, Vol. A428, p. 348-366.
- Prigozhin, G. et al., 1998. The depletion depth of high resistivity X-ray CCDs. *IEEE Transactions on Nuclear Science*, Vol. 45, p. 903-909.

## Chapter 7: X-ray quantum efficiency modelling & measurements

### 7.1 Introduction

The quantum efficiency (QE) of a CCD is a measure of the number of incident photons that are converted into electron-hole pairs and sampled by the device at different wavelengths. The X-ray QE of a front illuminated CCD is highly dependent on photon energy due to the transmission of photons through the different layers of surface structures, shown in Figure 7.1, that comprise the CCD.

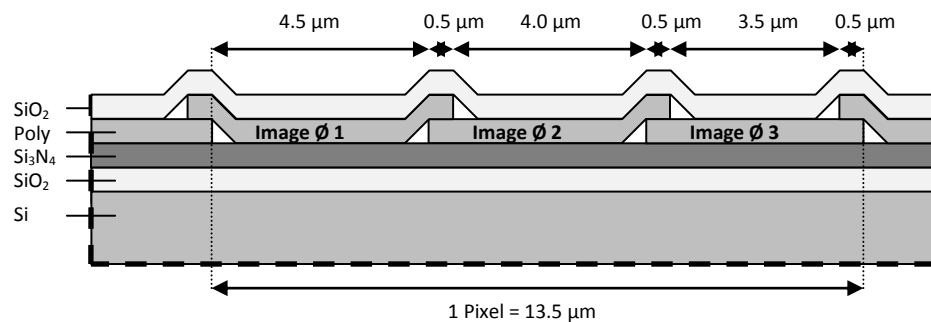


**Figure 7.1** CCD image area cross-section

In standard gate electrode devices, such as the CCD247, low energy photons ( $< 0.5$  keV) have less than a 10 % probability of reaching the active silicon and being detected. Open or thin electrode designs, such as the CCD22 (open electrode) and CCD66 (thin electrode), have been manufactured to improve this detection efficiency to  $\sim 50$  %. This is achieved by reducing the thickness of the 'dead' layers of silicon dioxide, polysilicon and silicon nitride the photons must traverse to reach the active silicon [Castelli 1990].

Higher energy photons ( $> 5$  keV) suffer the converse problem. They have a lower probability of being absorbed within the depleted region of the silicon, due to their energy being high enough to pass through the depleted region into the bulk, or even completely through the device. Electron-hole pairs that are created beyond the depleted region will diffuse and can only be partially collected and sampled by the CCD, yielding undeterminable incident photon energy degrading spectral resolution.

The design goal of the front illuminated CCD247 is to increase high energy QE whilst maintaining an acceptable level of spectral resolution [e2v technologies 2007]. This is achieved by increasing the depletion depth by manufacturing the device on high resistivity bulk silicon ( $\sim 8$  k $\Omega$  cm), allowing for operation at greater gate to substrate potentials, as described in Chapter 5.

The QE data presented in this chapter describes the spectral sensitivity of the front-illuminated CCD247 in the range 8,047 eV to 17,478 eV (Cu-K $\alpha$  to Mo-K $\alpha$ ) relative to that of a calibrated spectrometer.

### 7.2 Front illuminated CCD247 QE model

The QE of the front illuminated CCD247 can be modelled by knowledge of the transmission through the various layers comprising the CCD structure. The photon transmission through the surface structures is the product of the mass absorption law for each layer. The transmission through the depleted silicon is the result of mass absorption law for the depth of depleted silicon. QE is calculated at particular incident photon energies using [Burt 2006]:

$$QE_{ENERGY} = \underbrace{e^{-(\mu_{SiO_2} \cdot x_{SiO_2})} \cdot e^{-(\mu_{Si_3N_4} \cdot x_{Si_3N_4})} \cdot e^{-(\mu_{Si} \cdot x_{Si})}}_{\text{Surface layers transmission}} \cdot \underbrace{(1 - e^{-(\mu_{Si} \cdot x_{dSi})})}_{\text{Depletion}} \tag{vii-i}$$

Where  $\mu$  is the linear attenuation coefficient of the material for the incident photon energy,  $x$  is the thickness of the layer and  $x_d$  is the depth of the depleted region. Given the layer thicknesses comprising the CCD247 it is possible to accurately model the QE for the CCD over a range of photon energies. Table 7.1 gives a summary of the layer thicknesses comprising the CCD247.

Layer	Thickness (nm)	Use
Silicon dioxide (SiO <sub>2</sub> )	750	Protective layer
Polycrystalline silicon (Si)	300	Gate electrode
Silicon nitride (Si <sub>3</sub> N <sub>4</sub> )	85	Gate dielectric
Silicon dioxide (SiO <sub>2</sub> )	85	Gate dielectric
Depleted silicon (Si)	160,000	Active material

**Table 7.1** Layer thickness through cross-section of CCD217

The QE model shown in Figure 7.2 was derived from equation vii-ii:

$$QE_{ENERGY} = (e^{-(\mu_{SiO_2} \cdot 0.085 + 0.75)} \cdot e^{-(\mu_{Si_3N_4} \cdot 0.085)} \cdot (\frac{12}{13.5} \cdot e^{-(\mu_{Si} \cdot 0.3)} + \frac{1.5}{13.5} \cdot e^{-(\mu_{Si} \cdot 0.6)})) \cdot (1 - e^{-(\mu_{Si} \cdot 295)}) \tag{vii-ii}$$

Where the two numerical fractions are the constants used to account for the single and double layer electrode thickness in the regions where they overlap.

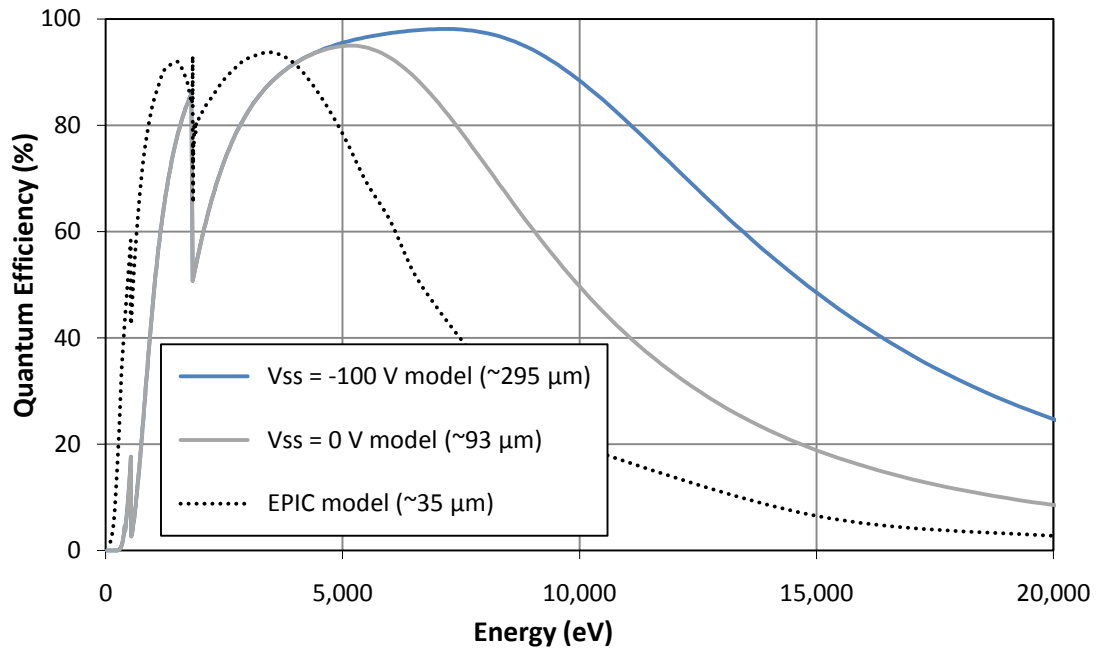


**Figure 7.2** FI-CCD247 quantum efficiency model (8 kΩ cm) compared to CCD22 (XMM/EPIC)

From the  $V_{SS} = 0$  V (8 kΩ cm) and EPIC CCD model (1.5 kΩ cm) plots in Figure 7.2, the effect of increased resistivity on device QE is apparent due to the increased depletion depth. It should be noted that the low energy QE of the EPIC device is higher due to the thin electrode structure used in the EPIC imaging area [Holland et al 1996]. Where the substrate potential is taken more negatively, the depletion region is further increased into the silicon, further increasing the higher energy ( $> 5$  keV) QE, shown by  $V_{SS} = -100$  V in Figure 7.2.

### 7.3 The QE measurement facility

The experiment was to provide data points to support the theoretical model of QE for the front illuminated CCD247 over the energy range 8,047 eV to 17,478 eV to within an accuracy of 10 %. A series of measurements were taken by both the CCD247 and a reference detector, illuminated by the same X-ray beam at differing photon energies to provide this data. The X-ray QE of the CCD was determined by the measured ratio of photons detected by the CCD to that acquired by the reference detector, ‘normalised’ to the detection efficiency of the reference detector. It was vital, during the experiment, to ensure that both CCD and reference detector were exposed to the same X-ray beam for an accurate comparison to be made. Ensuring an identical source illumination for both the CCD and reference detector is not possible to achieve practically as both CCD and reference detector cannot occupy the same position at the same time. Therefore the following points were taken into account before constructing the experimental setup:

- Temporal variations in flux from the X-ray tube source due to the anode temperature changing during operation and voltage transients in the electronics.
- Spatial variations due to the physical location of detectors from the X-ray source.

### 7.3.1 Possible QE measurement chamber designs

Three popular methods for taking QE measurements of CCDs are described in this section, all of which require some spatial or temporal displacement between the CCD and reference detector measurements. In the concurrent measurement setup, shown in Figure 7.3, the CCD and the reference detector are mounted at one end of a long vacuum chamber [Castelli 1990]. The X-ray source is located at the far end of the vacuum chamber, attempting to minimise the beam divergence between the two detectors. The difference in X-ray flux between the spacing of the detectors can be estimated based on the inverse square law of X-ray flux fall off and factored into the results by substituting the CCD with a second reference detector. Typically such designs require a vacuum chamber to be a number of meters in length needing a large amount of laboratory space.

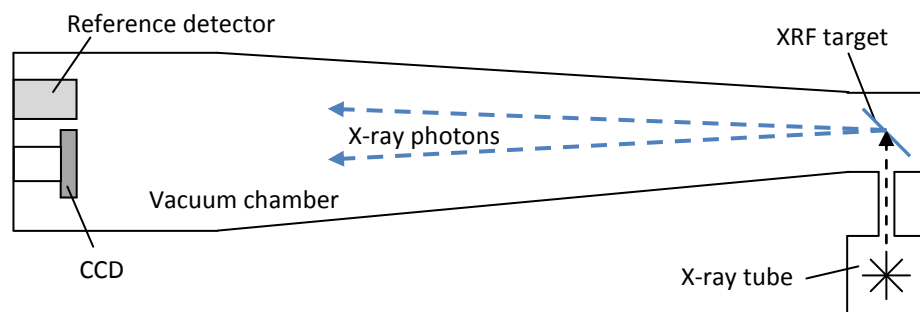


**Figure 7.3** Schematic of a side-by-side detector QE facility (plan view)

A second method is to translate the reference detector in front of the CCD, as shown in Figure 7.4. The reference detector will however be closer to the X-ray source than the CCD during the measurement [Martin 2005]. This must be corrected for during analysis, as the closer the reference detector is, the larger the X-ray flux per unit area that will be measured. It will also not be possible to take concurrent measurements using this method, so any temporal variations in source flux must also be accounted for in the results. The mechanical constraints of this design limit the type of reference detector that can be used, putting an upper limit on the energy detection range.

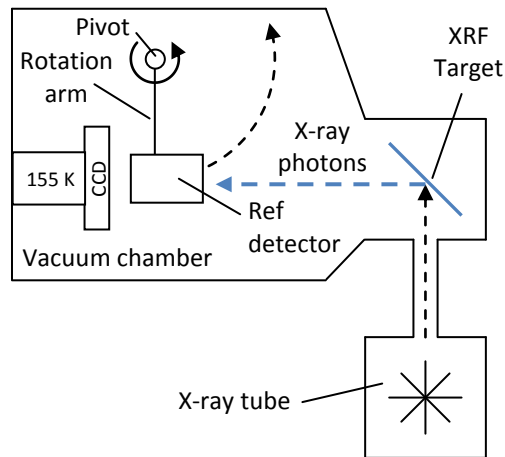


**Figure 7.4** Schematic of a translational detector QE facility (plan view)

A third method was employed at Massachusetts Institute of Technology (MIT) to make relative QE measurements for the ACIS CCDs of Chandra [Manning et al 1996]. The CCD and the reference detector are mounted onto a translation stage inside the vacuum chamber. This ensures that both the CCD and the reference detector are illuminated by an identical beam path. Again, any temporal variation in flux must be taken into account. This method can also impose restrictions on the X-ray energy range measured, due to the mechanical constraints of the detectors, plus the added complexity of cooling them whilst still being free to move along the translation stage.

### 7.3.2 The SiLi reference detector

In order to measure the increased X-ray QE sensitivity of deep depletion CCDs, such as the CCD247, a reference detector with a high QE ( $\sim 100\%$ ) up to 20 keV was required. The reference detector chosen was a lithium drifted silicon crystal (SiLi) that was depleted to  $\sim 4.5$  mm by applying a 500 V potential across the crystal. The SiLi detector has a collecting area of  $30\text{ mm}^2$ , allowing X-ray photons in the energy range 5 keV to 20 keV to be sampled with a QE of approximately 100% and is shown in Figure 7.5.



**Figure 7.5** The SiLi detector (courtesy of e2vsi)

The QE of the SiLi detector is modelled in the same way as the CCD247 described in Section 7.2, for the same energy range, taking into account X-ray photon absorption in the beryllium entrance window and nickel electrode contact. The beryllium entrance window is used to filter out the optical wavelengths and has a thickness of between 8  $\mu\text{m}$  and 12  $\mu\text{m}$ . The uncertainty of the beryllium thickness will have negligible impact on QE measurements taken in the energy range of interest ( $> 6 \text{ keV}$ ). The nickel electrode covering the entire crystal surface is used to apply the high bias potential to drive the depletion and has a thickness of  $\sim 8 \text{ nm}$ , although the exact thickness is unknown. Even though the nickel K-absorption edge (8,333 eV) is within the energy range of interest (8,047 eV to 17,478 eV), the error imposed by the uncertainty of the thickness is negligible due to its relatively small size [McMaster et al 1969].

Figure 7.6 shows the modelled QE for the SiLi detector with both 8  $\mu\text{m}$  and 12  $\mu\text{m}$  beryllium entrance windows [Bale 2006]. The true QE of the SiLi detector therefore lies somewhere between these two curves.

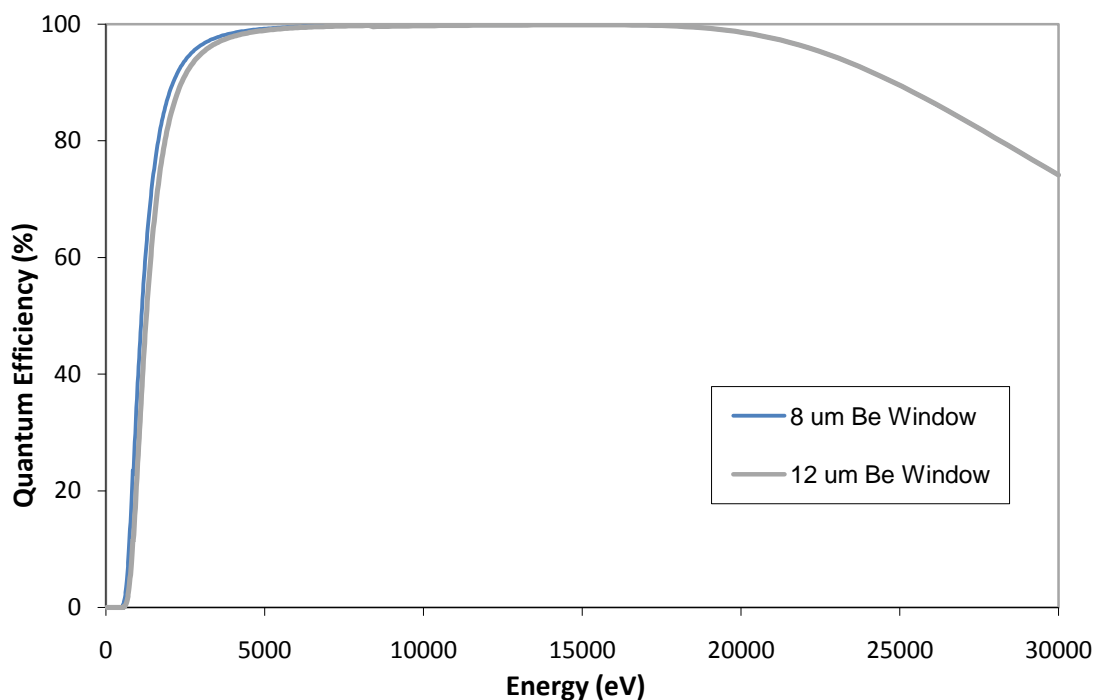


**Figure 7.6** Modelled SiLi detector X-ray QE

The SiLi crystal must be cooled during operation to suppress dark current; this is achieved by thermal conduction with liquid nitrogen that is stored in the insulated white tank shown in Figure 7.6. It was not possible to translate the SiLi detector inside a vacuum chamber due to this 3.8 Lt tank.

### 7.3.3 The design

The liquid nitrogen tank prohibits the SiLi detector from being translatable and was therefore permanently fixed onto a custom made vacuum flange with the CCD assembly mounted next to it. Figure 7.7 shows the internal face of this flange that is sealed within the vacuum chamber during operation.

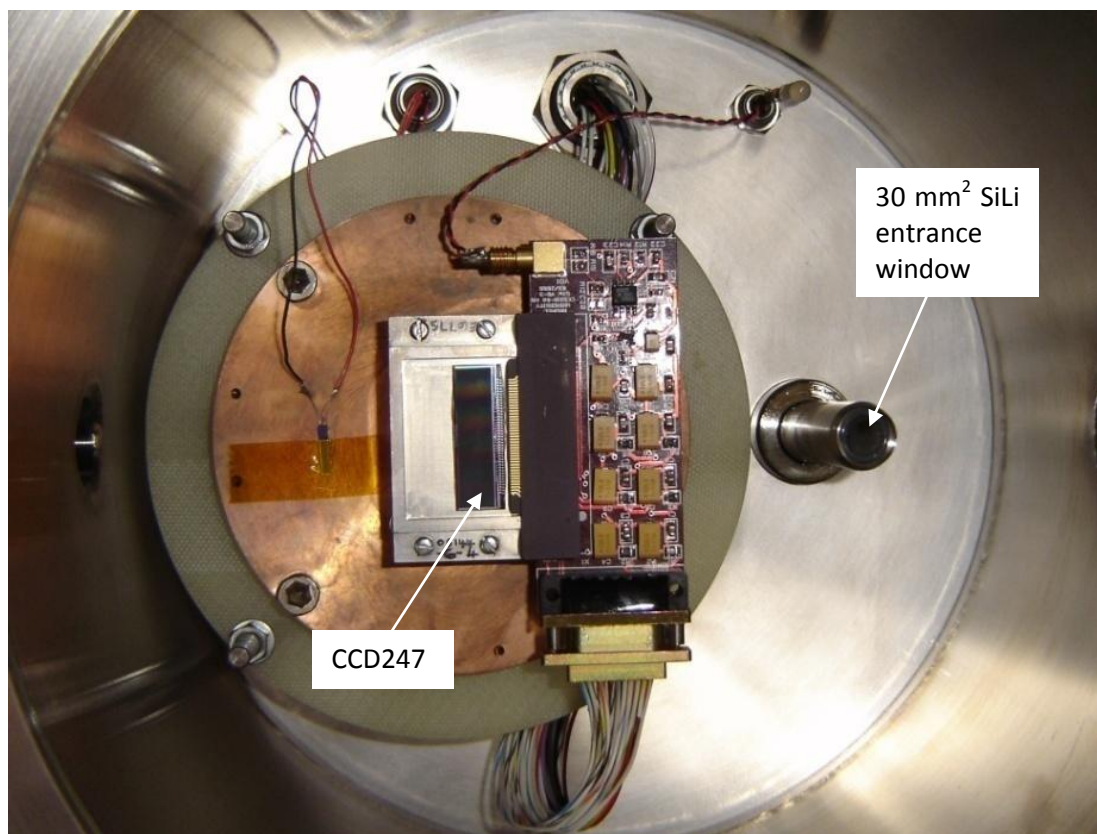


**Figure 7.7** The CCD247 and SiLi Detector mounted inside vacuum chamber

It was not desirable to have the length of a side-by-side design and not possible to have a translational detector design due to the cooling requirements of both detectors. Figure 7.8, 7.9 and 7.10 show the equipment that was developed under this work to allow for fixed position detectors, illuminated by a translatable X-ray source that could be moved between detectors within seconds. This final design addresses both the concerns of spatial displacement and minimising any effect of temporal variation. An X-ray fluorescence (XRF) target was used to allow various characteristic X-ray energy lines to be produced. The X-ray beam is translatable within the vacuum chamber to ensure an identical spatial displacement between source and detector for the reference and CCD measurements.

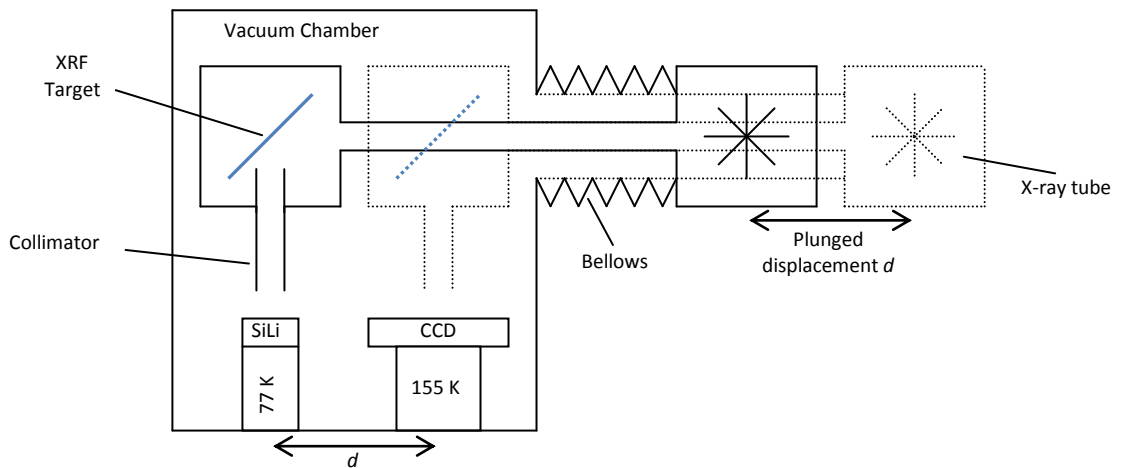


**Figure 7.8** Schematic of the translational XRF CCD QE facility (plan view)

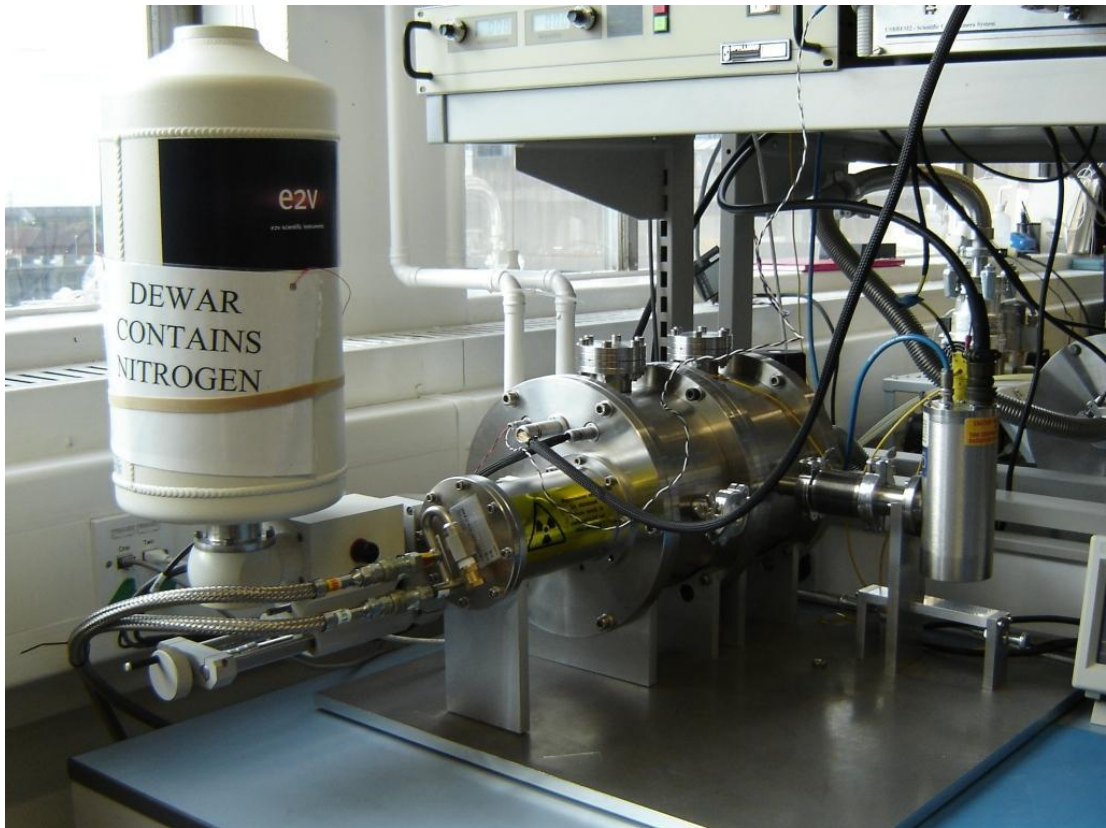


**Figure 7.9** Translational XRF CCD QE facility

The X-ray tube is connected by a solid steel tube (plunge arm) with a wall thickness of 4 mm to an XRF target box that has a collimated output at  $90^\circ$  towards the detector plane. A bellows surrounds the plunge arm between the vacuum chamber and the X-ray tube to maintain the pressure inside the chamber during movement. The assembly can be moved along the  $x$ -axis of the chamber to an extent of  $d = 90$  mm, allowing corresponding distance between the detectors.

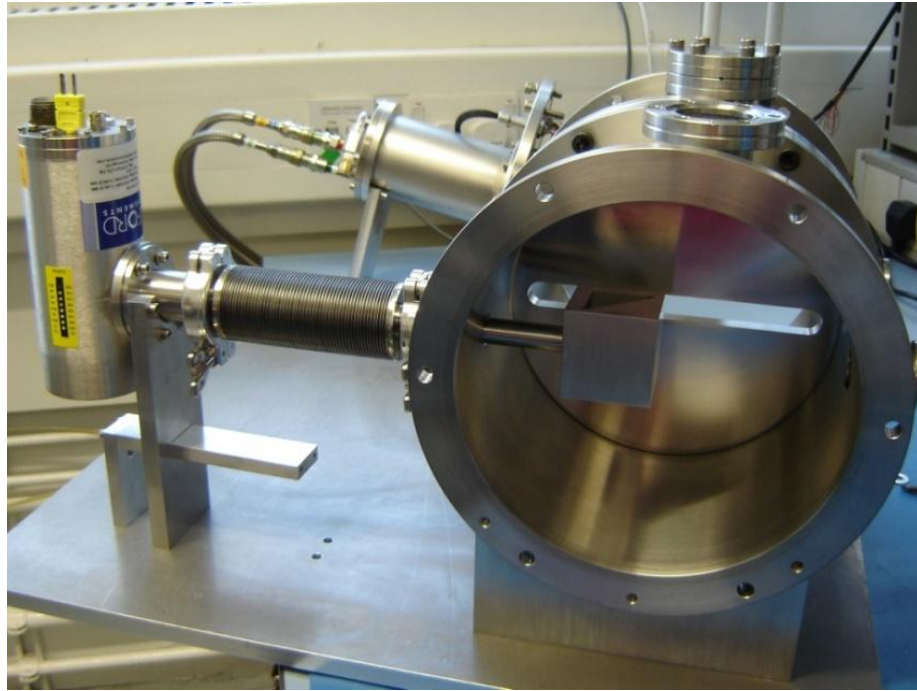


**Figure 7.10** X-ray fluorescence target box (from rear)

The fluorescence target material can be substituted between experiments to acquire data for different photon energies. The X-ray tube generates a continuous spectrum of photons from 0 keV to 25 keV. Various target materials were fluoresced to illuminate the detectors with their characteristic X-ray lines, given in Table 7.2.

Atomic Number	Element	Line	Photon Energy (eV)
22	titanium	Ti-K $\alpha$	4,510
23	vanadium	V-K $\alpha$	4,952
24	chromium	Cr-K $\alpha$	5,414
26	iron	Fe-K $\alpha$	6,403
26	iron	Fe-K $\beta$	7,057
28	nickel	Ni-K $\alpha$	7,478
29	copper	Cu-K $\alpha$	8,047
29	copper	Cu-K $\beta$	8,904
30	zinc	Zn-K $\alpha$	8,638
32	germanium	Ge-K $\alpha$	9,885
32	germanium	Ge-K $\beta$	10,981
34	selenium	Se-K $\alpha$	11,221
42	molybdenum	Mo-K $\alpha$	17,478

**Table 7.2** X-ray fluorescence energies

### 7.3.4 The X-ray source

The source of X-ray radiation was an Oxford Instruments XTF5011 X-ray tube with a tungsten target, shown in Figure 7.11. This tube was used to fluoresce various materials in turn to provide known photon energies to illuminate the CCD and reference detector.



**Figure 7.11** X-ray tube (left) and power supply (right) (Oxford Instruments)

Figure 7.12 shows the variation of the X-ray tube output observed over a 2 hour period from the initial start up. The warm up period of the X-ray tube anode and electronics was found to take approximately 1 hour 20 minutes when operating at 16 kV and 0.08 mA. It was found during the stable period after this time that the fluoresced X-ray count rate could be  $\pm 4.6\%$ .

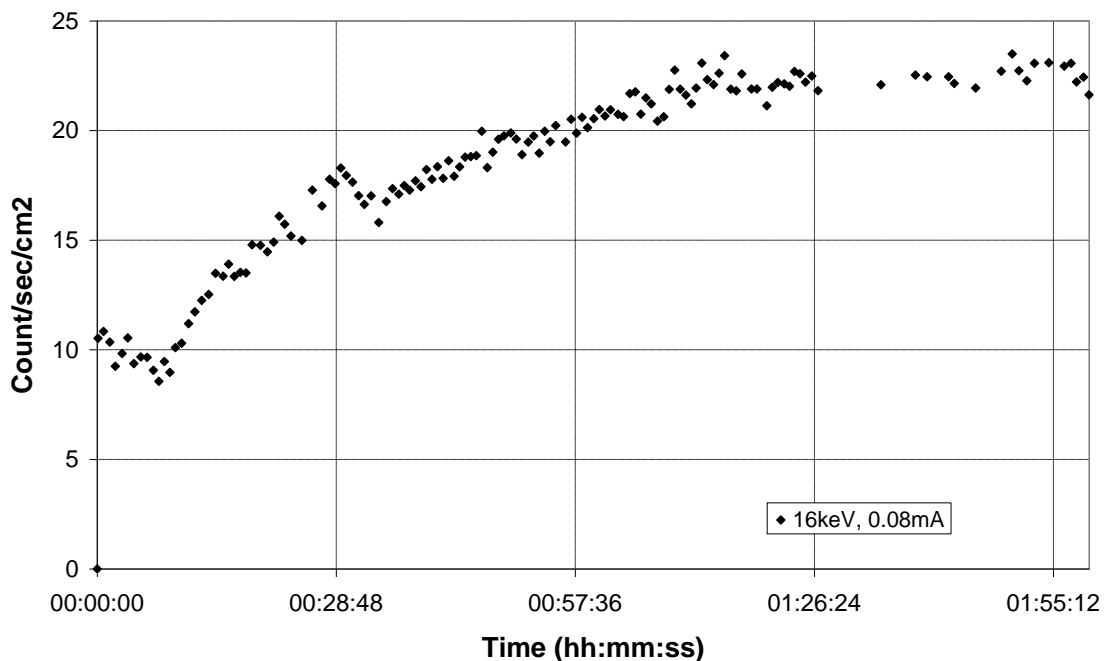


**Figure 7.12** Variation in X-ray flux during warm up

The error imposed by temporal variations in flux can be reduced by taking both measurements concurrently or by averaging a set of results taken for individual detectors.

### 7.3.5 Radiation safety

The X-ray tube was electronically limited to a maximum output of 25 kV to prevent significant transmission of X-ray photons up to this energy to the external environment when the vacuum chamber was sealed. The schematic shown in Figure 7.13 labels the key X-ray filters to the external environment and gives estimates of the maximum transmission,  $T_x$ , when operating at 25 keV.

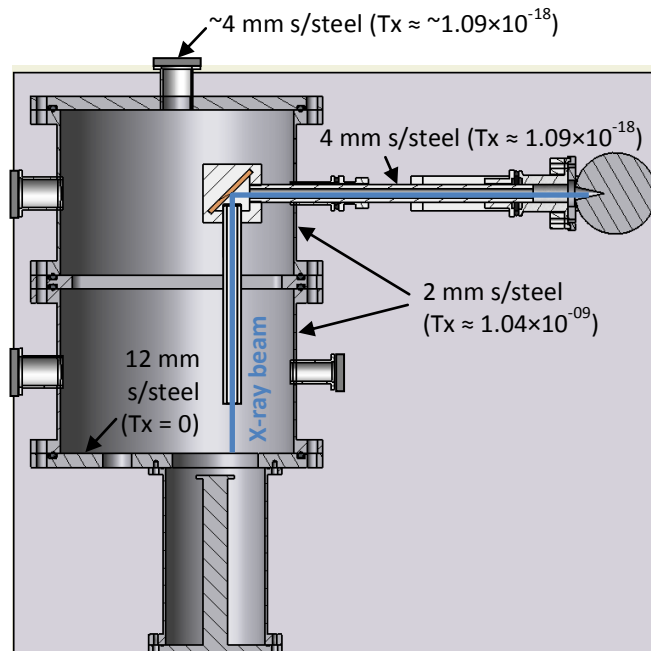


**Figure 7.13** QE facility X-ray transmission filters

Two interlocks were included to minimise the health and safety risk. A vacuum interlock prevented the generation of any X-rays until a sufficient vacuum was present, ensuring the vacuum chamber had been sealed and hence all the filters shown in Figure 7.13 were in place. A simple key switch prevented the unauthorised generation of X-ray photons. Figure 7.14 demonstrates the interlock system developed for the X-ray QE facility.

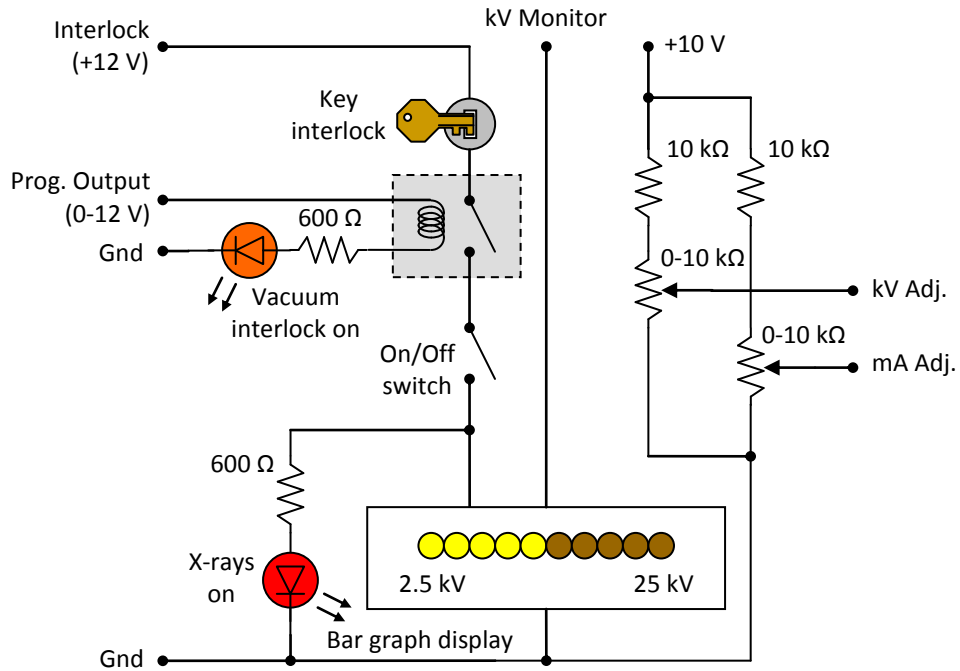


**Figure 7.14** X-ray tube control box circuit

## 7.4 Method

X-rays were collimated into a  $50 \text{ mm}^2$  spot that could be translated across the horizontal plane of the CCD imaging surface and across the SiLi. A correction factor would later be applied to the QE measurement to account for the smaller ( $30 \text{ mm}^2$ ) SiLi entrance window.

Alignment of the X-ray collimator to the SiLi was checked by exposing a piece of Gaphchromic film placed over the beryllium entrance window for  $\frac{1}{2}$  hour. This produced a blue mark at the point of focus for the collimated X-rays. Adjustments were made to the external depth stop screws to ensure the collimated beam was directly aligned to the SiLi entrance window. Precise alignment of the CCD was not necessary as the imaging area was large in comparison to the collimated beam and, as the beam was 'imaged', the correct alignment could be observed during the data processing.

The QE facility was then sealed, evacuated and the CCD cooled. During the cool-down period ( $\sim 2$  hours), the X-ray source was turned on to allow the output to stabilise.

The X-ray source was initially aligned to the CCD and clamped into place. The clamp was necessary to prevent the atmospheric pressure from constricting the bellows and pulling the X-ray source away from the CCD.

### 7.4.1 Data acquisition

Images were acquired by the CCD247 at both substrate potentials of 0 V and -100 V to provide QE data points at depleted depths of 93  $\mu\text{m}$  and 295  $\mu\text{m}$  respectively.

CCD images were acquired in continuous, full-frame mode (TDI), with zero additional integration between rows/frames. This allowed the collimated 50  $\text{mm}^2$  X-ray exposure to be 'effectively' distributed across the vertical axis of the imaging area, reducing the probability of pile-up events. The integration period of the CCD image was calculated by multiplying the row readout time, including the parallel transfer time for the next row into the readout register, by the number of rows in the image.

After acquisition of the CCD image, the X-ray source was immediately repositioned to align with the SiLi detector entrance window, taking approximately 5 seconds. A corresponding SiLi spectrum was then acquired for the X-ray beam for the same integration period as the CCD image.

A number of CCD images and corresponding SiLi spectrums were obtained to increase the photon statistics for each of the X-ray energies measured.

### 7.4.2 Data processing

Software was developed using Matlab to count the number of X-ray photons at a particular energy in both the CCD image and the corresponding SiLi spectrum and is described below:

The CCD image was read into a two-dimensional Matlab array. Pixel values were put into a histogram and plotted as a spectrum. The energy scale was then obtained by calibration to the background distribution and a known X-ray peak, typically the Fe-K $\alpha$  (6,403 eV) peak prevalent in all acquisitions due to fluorescence from the collimator. This involved selecting the high and low points of the X-ray peak and then fitting a Gaussian profile to the data points in the peak. A background threshold was set to  $6\sigma$  to facilitate the event recognition algorithms described in Chapter 6. Each event pattern was then processed to count each event type and then summed into the equivalent isolated ( $1 \times 1$ ) event. A second histogram of the CCD image was then produced for the isolated events only; this was used to select the  $\pm 3\sigma$  boundaries of the photon energy of interest. The cumulative count between these two boundaries was then found to determine the detected X-ray flux at that energy. The silicon escape and pile-up peak energies were also calculated to  $\pm 3\sigma$  and added to this count where possible, shown in Figure 7.15.

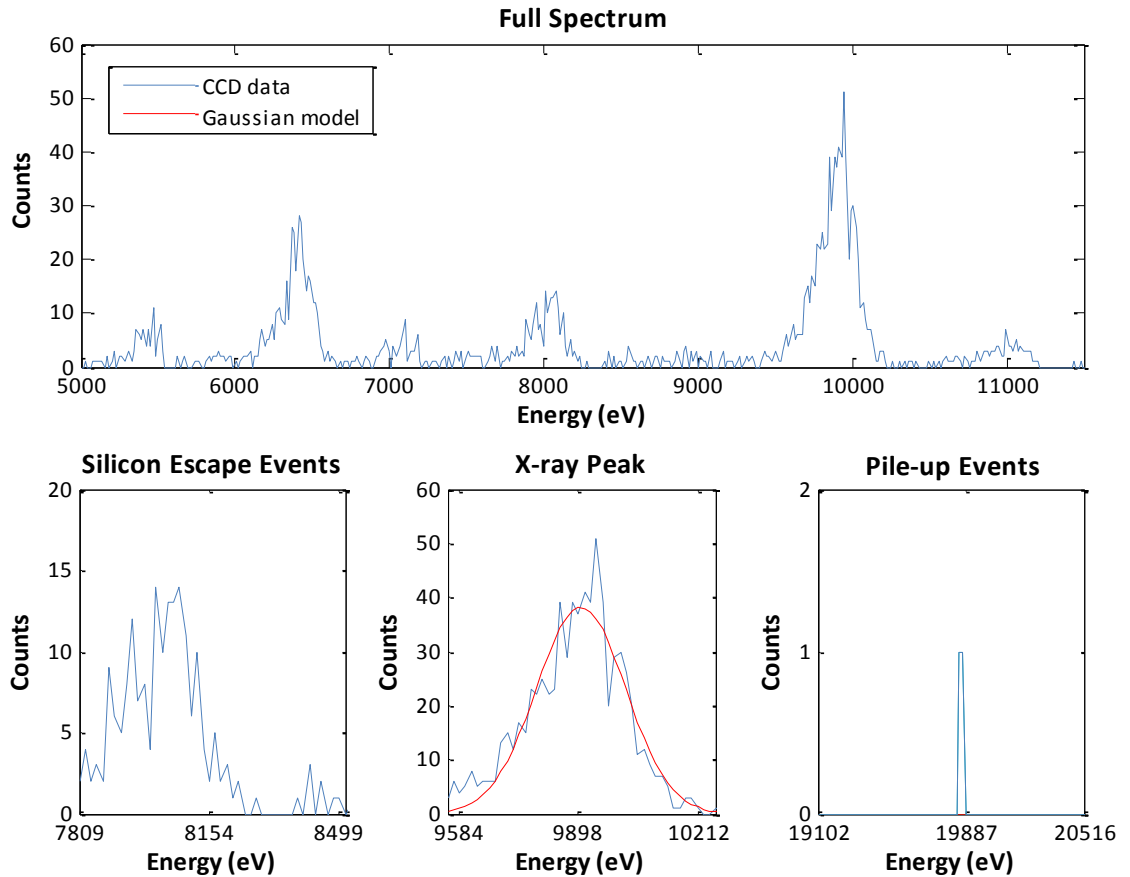


**Figure 7.15** The energy count summary with zoomed Ge-K $\alpha$  sections

In some instances where the characteristic lines of multiple elements were close together some overlap occurred between the silicon escape peak and another characteristic peak. This rendered the count indeterminable and hence such data were excluded. For example, where the X-ray energy of interest was Cu-K $\alpha$  (8,047 eV), the silicon escape peak was located at 6,307 eV. With the additional Fe-K $\alpha$  peak generated by fluorescence of the collimator, at 6,403 eV and having a typical spectral resolution of  $\sim 145$  eV (CCD247), the lower boundary of the X-ray peak would be approximately 6,331 eV. The upper boundary of the silicon escape peak for Cu-K $\alpha$  could be  $\sim 6,401$  eV factoring in a spectral resolution of  $\sim 188$  eV, significantly overlapping the two energy sources.

The total photon count in the CCD image at the selected energy was then normalised into counts / second / cm<sup>2</sup>.

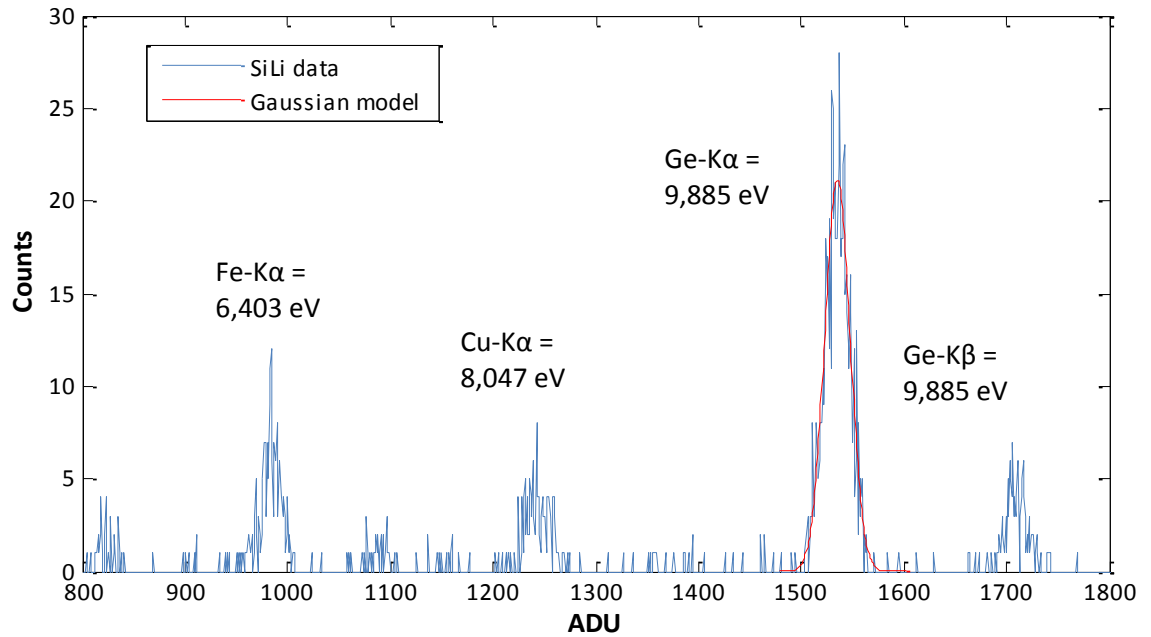


**Figure 7.16** SiLi input spectrum with fitted Gaussian profile to known X-ray line

The spectral data acquired from the SiLi was then imported into another Matlab array. Similar operations were performed to establish the total photon count at the same energy selected for the CCD image. However the energy calibration was slightly different as there is no background peak in the spectrum due to the discrimination of the SiLi output processing electronics. Two known X-ray peaks were used to make the energy calibration. Total counts in the SiLi spectrum for the energy selected were again normalised into counts / second /  $\text{cm}^2$ . A Gaussian profile fitted to a known X-ray line in the SiLi spectrum is shown in Figure 7.16.

Finally the calculated flux at the CCD was then divided by that obtained from the corresponding SiLi spectrum to calculate the relative QE. This was then multiplied by the modelled SiLi QE at that energy to determine an absolute CCD QE for the selected energy.

### 7.4.3 Errors

**Photon statistics** – Approximately 600 X-ray photons in the peak were required for the Gaussian fitting algorithm. For many of the elements listed in Table 7.2 the fluorescence yield was too low to acquire enough data.

**Output flux** – The output from the X-ray tube was measured to have a variation in flux of  $\pm 4.6\%$  in steady state operation, the tube was given  $\sim 2$  hrs to reach a steady state before measurements were made. A number of repeat measurements were made between detectors to also minimise the effect. Variations in flux were made with the SiLi and were found to be  $\pm 4.6\%$  over the course of 1 minute. This error was factored into the error bars of Figure 7.17.

Filter transmission - The uncertainty of the low energy QE for SiLi detector due to the thickness of the beryllium window would have an effect on QE measurements made between 0 keV to  $\sim 6$  keV, reducing in magnitude towards 6 keV. This could be estimated based on the two extremes of the window thickness, for a given energy, although was not considered for the results presented in this chapter as all the data points were for energies above 6 keV.

Counting - For some energies, silicon escape events could not be included in the total count, where such energies conflicted with the characteristic lines of other elements in the X-ray source. This could potentially contribute a positive error of 5 %, due to the K-shell fluorescence yield of a silicon atom, however as the error will be the same for the SiLi, the effect is negligible. Pile-up events were not found to conflict with any of the characteristic energy lines of the XRF samples used.

## 7.5 Results

QE measurements were successfully taken for Cu-K $\alpha$ , Ge-K $\alpha$ , Ge-K $\beta$  and Mo-K $\alpha$  and are shown in Figure 7.17 and are listed in Table 7.3.

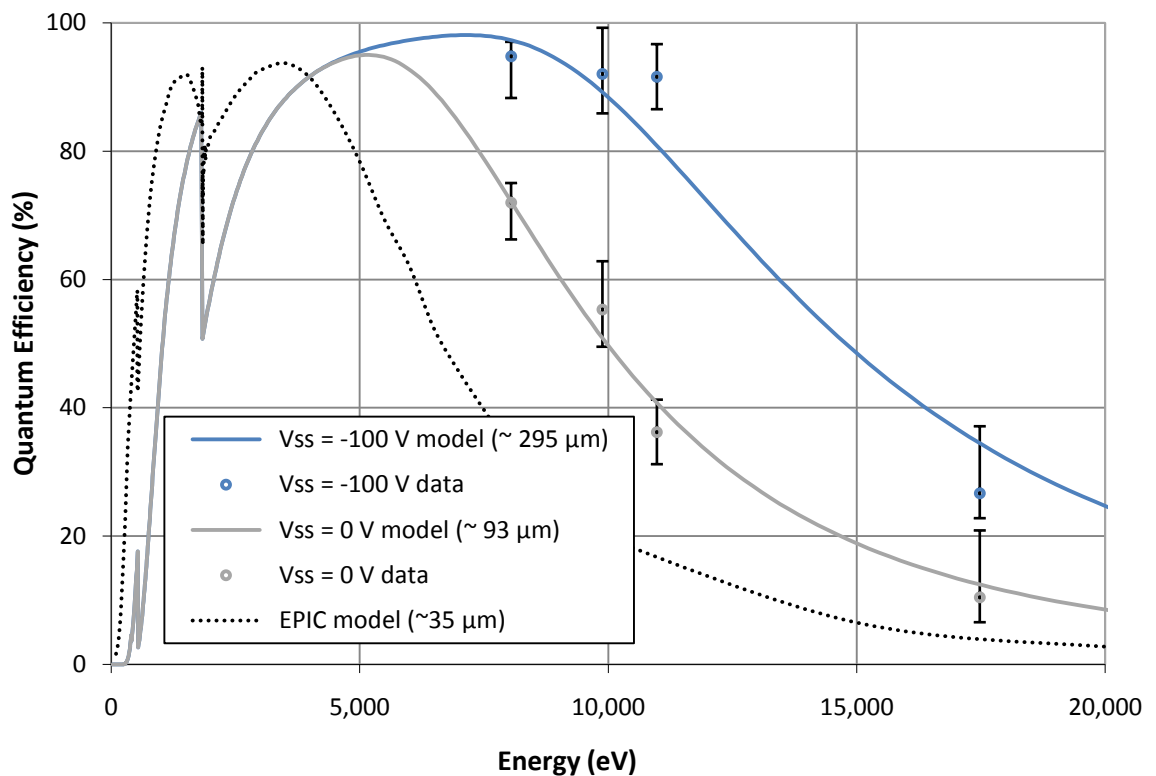


**Figure 7.17** Summary of X-ray QE measurements for CCD247

It may be noted that the agreement with theoretical depletion is better than achieved with the method described in Chapter 6. The results suggest that the depletion predictions are in fact reasonably accurate.

Atomic Number	Line	Photon Energy (eV)	QE (VSS = 0V) %	QE (VSS = -100 V) %
29	Cu-K $\alpha$	8,047	70.5	94.8
32	Ge-K $\alpha$	9,885	56.0	92.0
32	Ge-K $\beta$	10,981	36.2	91.6
42	Mo-K $\alpha$	17,478	10.5	26.7

**Table 7.2** X-ray fluorescence energies

## 7.6 Conclusions

Quantum efficiency measurements of X-ray photons were taken about the centre of the CCD imaging area using the QE facility developed under this work; to within a maximum error of 9.6 % (< 10 % was desired).

Data points were plotted in Figure 7.17 alongside the modelled QE curve for the CCD247 that was assumed to have been fabricated on 8 k $\Omega$  cm bulk p-type silicon. Due to the similarity between the data points and the model, a device depletion of 93  $\mu$ m and 295  $\mu$ m is believed for the CCD247, when substrate potentials of 0 V and -100 V are applied respectively. This method provides a closer agreement with the theoretical depletion depth than the spread event method presented in Chapter 6.

An improvement in QE is shown for the higher energies (> 5 keV), with an increase of  $\sim$  70 % at 10 keV compared to that of the EPIC-MOS device onboard XMM-Newton, demonstrating the suitability of high-resistivity bulk silicon technology in future CCD based X-ray missions.

## 7.7 Further work

The facility could be adapted to measure the QE of future devices in the MOS CCD development programme for XEUS. This would include extending the energy range of calibration lines, particularly to lower energies down to carbon/oxygen (277/525 eV) using low energy electron gun and monochromator as the source of X-ray photons. This will enable the QE of thin and open electrode technologies to be evaluated. Other new detectors such as the family of swept charge devices (SCDs) could also be evaluated as they will have a different QE curve due to their inverted mode operation.

The experimental downtime ( $\sim$  3.5 hrs), experienced whilst changing the XRF target, could be significantly reduced by replacing the target box with one that includes a rotational target wheel, allowing multiple XRF targets to be positioned into the beam. The target wheel could not be rotated by a traditional vacuum feed-through due to the translation of the target box assembly during operation. Therefore a stepper motor unit would be required to sit inside the

target box and rotate the wheel between samples when required. The stepper motor would have to be suitable for vacuum applications (no out-gassing of lubricants and components).

By including a rotational target wheel, the QE facility could be further enhanced to allow for optical QE measurements. This could be achieved by including a mirror surface on the target wheel that would reflect light onto the detectors from a band-pass light filtered source entering the vacuum chamber from the opposite port to that used for the X-ray beam. A second reference detector, such as calibrated photodiode (PD), would be required to take the relative flux measurements, as the beryllium window blocks the optical wavelengths. These potential modifications to the CCD QE facility are shown in Figure 7.18.

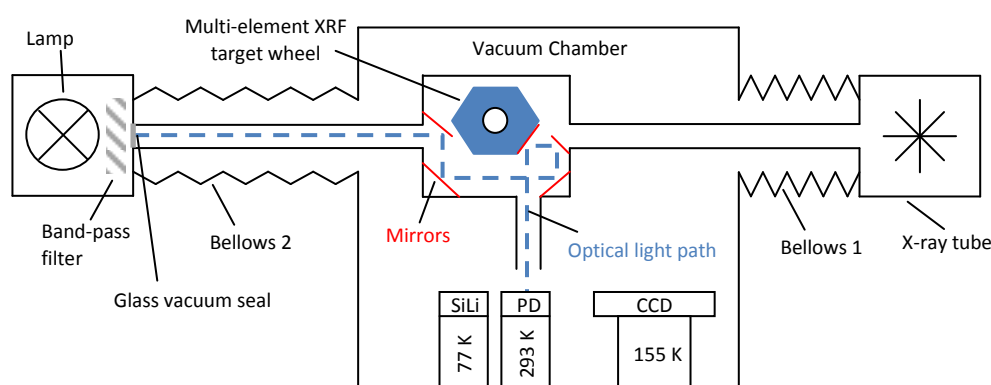


**Figure 7.18** Schematic of the CCD QE facility modified to include optical

## 7.8 References

Bale, G., 2006. Private communication.

Burt, D.J., 2006. Private communication.

Castelli, C.M., 1990. The soft X-ray performance of CCD detectors. *University of Leicester*, Ph.D. thesis.

e2v technologies, 2007. High rho project progress summary. *Commercial in Confidence*.

Holland, A.D. et al., 1996. MOS CCDs for the EPIC on XMM. *Proc. SPIE*, Vol. 2808, p. 414-420.

Manning, H.L. et al., 1996. Quantum efficiency calibration of AXAF CCDs from 2 to 10 keV. *Proc. SPIE*, Vol. 2808, p. 23-33.

Martin, A.D., 2005. Private communication.

McMaster, W.H. et al., 1969. Compilation of X-ray cross sections. *Atomic data and nuclear data tables*.

## Chapter 8: High throughput video processing ASICs

### 8.1 Introduction

Advances in CCD manufacture have allowed for image areas that are only limited by the dimensions of the wafer on which they are fabricated. ‘Stitching’ is the industrial term used to describe the method that allows large area CCDs to be manufactured from a small number of photolithographic masks. An example of a large area CCD manufactured using the stitching process is shown in Figure 8.1.

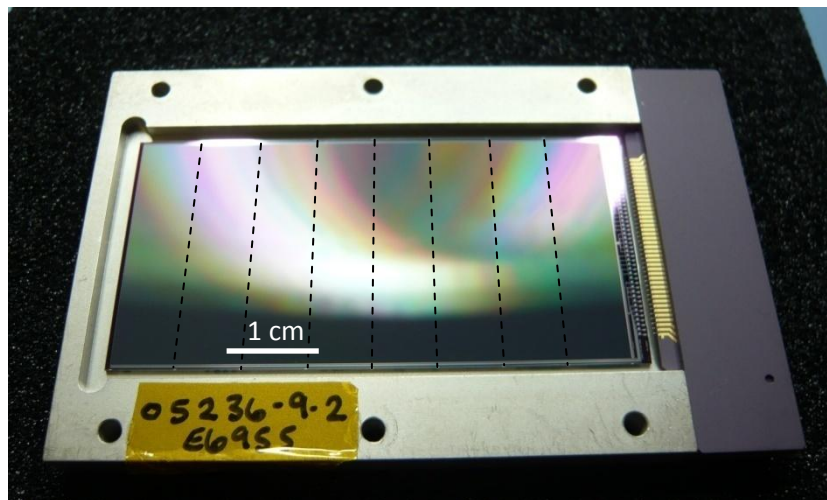


**Figure 8.1** CCD227-FI 8 stitched image sections

A larger imaging area usually corresponds to a larger number of pixels that need to be read out from the device and hence a longer image read time, that is often undesirable. Therefore in many applications, application specific integrated circuits are beneficial to accommodate the following:

#### 8.1.1 High pixel throughput

The pixel readout rate can be increased by simply reducing the clock periods of the read out circuit electronics. Typical CCD output amplifiers are however unsuitable for being driven at such speeds due to their relatively high capacitance. Manufacturers are therefore including a second stage in the source follower amplifier to reduce capacitive loading and hence provide a better impedance match to the readout electronics, allowing pixels to be readout at speeds up to 3 MHz whilst maintaining an acceptable  $< 10 e^-$  r.m.s. read noise [Janesick 2001]. Figure 8.2 shows the standard 2-stage circuit schematic included in e2v’s scientific CCDs.

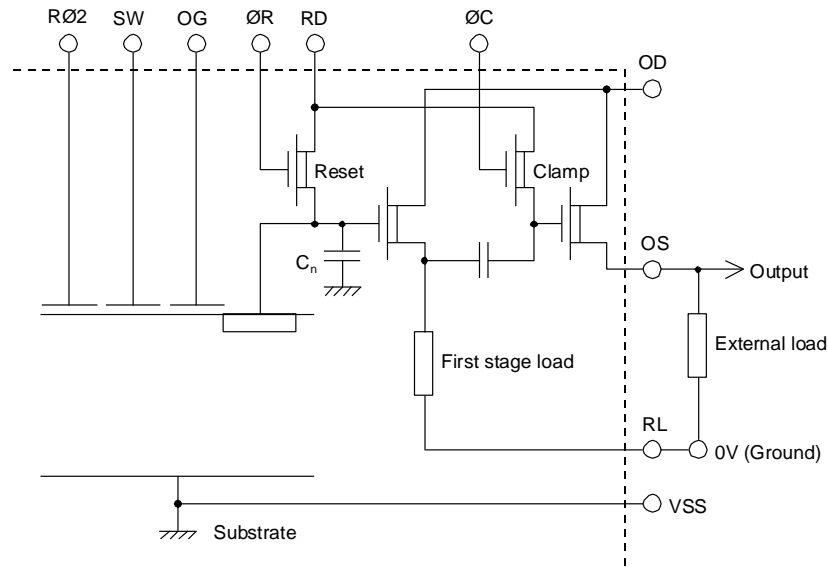


**Figure 8.2** CCD two-stage output circuit (courtesy of e2v technologies)

**8.1.2 Multiple readout channels**

The need for multiple channel readout electronics is necessary for two reasons. The inclusion of multiple output nodes is now common place in large area CCDs to increase image throughput by exploiting parallelism. Original ‘multi-node’ designs have two output nodes at the lower corners of the left and right side of the imaging area to output their respective half of the image. The latest CCD designs have an output node at each corner so that the read time can be reduced by a factor four as each node needs only to readout ¼ of the image area [e2v technologies 2007]. Figure 8.3 demonstrates the use of multiple output nodes to read out a large area CCD.

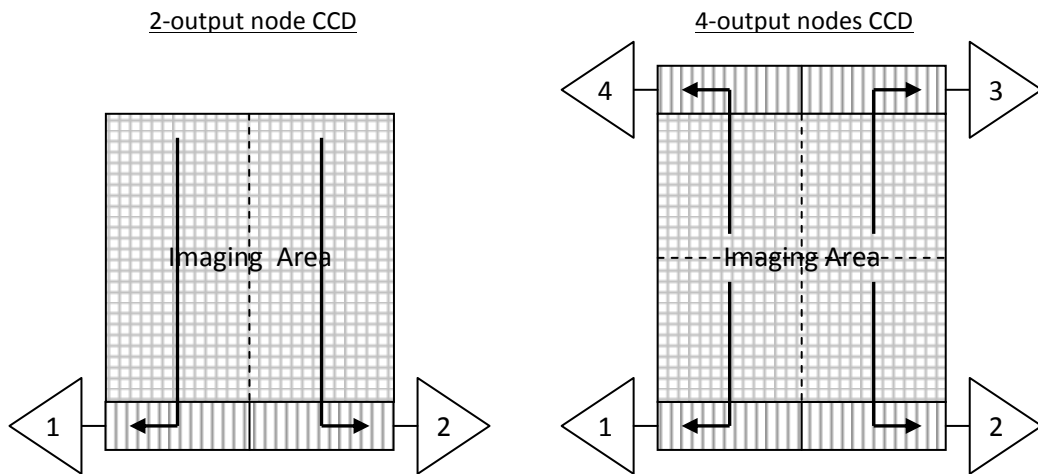


**Figure 8.3** CCD multiple output node examples, e.g. CCD42 (left) and CCD230 (right)

The second requirement for multi-channel read out electronics is for CCD arrays such as that assembled for the focal plane in the ESA Gaia mission that has an area of approximately  $0.5 \text{ m}^2$ , constructed from  $\sim 90$  CCDs an example of which is shown in Figure 8.4 [Short et al 2005]. Each CCD needs to be read out concurrently to meet the timing requirements of the mission. Multiple channel video processing electronics are required to accommodate such concurrency and enable focal plane arrays to be assembled in a ‘modular’ fashion.

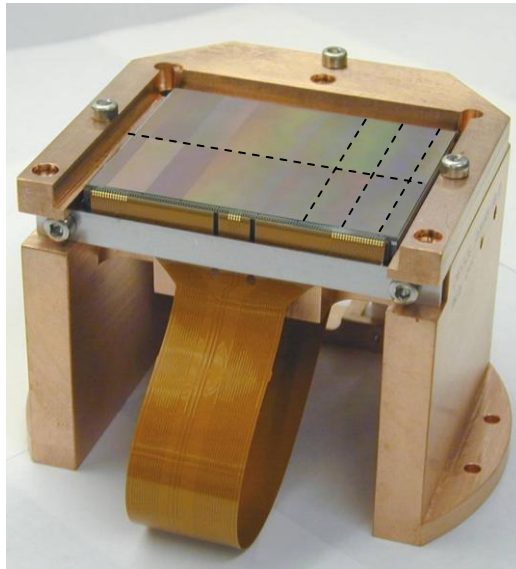


**Figure 8.4** Gaia astrometric field ‘stitched’ CCD in transportation packaging (e2v technologies)

### 8.1.3 Reduced mass

Space hardware is typically designed to have the minimum mass necessary to complete the mission objectives to minimise the fuel load required to launch into space. ASICs offer a significant reduction in size and mass over traditional components [Rabaey et al 2003]. Figure 8.5 compares a single video processing circuit to an ASIC equivalent.

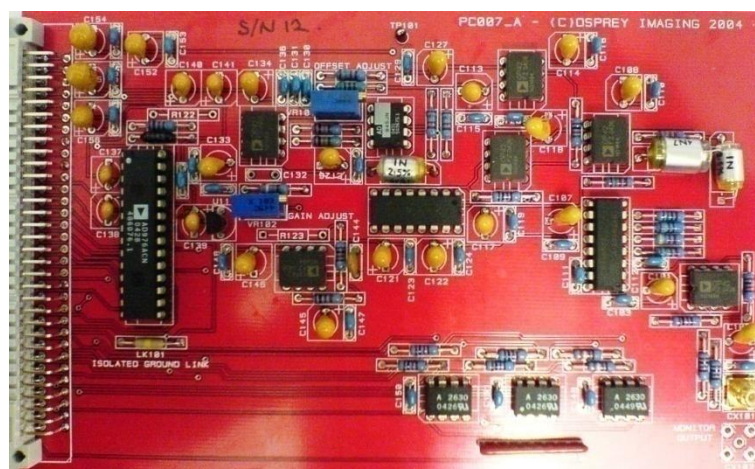


**Figure 8.5** Traditional components (left) vs. ASIC (right)

### 8.1.4 Reduced power consumption

Power consumption of space based instrumentation has to be kept to a minimum due to the limited power budget of spacecraft. ASICs typically require less power than traditional electronics [Rabaey et al 2003].

### 8.1.5 Reduced noise through layout

X-ray spectroscopy applications typically have a minimum noise requirement of  $\leq 5 e^-$  r.m.s. [Lumb et al 1991]. It is vital to minimise exposure of the analogue signal path to any spurious noise sources before digitisation to achieve minimal noise whilst reading out the CCD. This is achieved by considerate layout of the camera system electronics and ensuring the analogue path length is kept to an absolute minimum to avoid pickup of any spurious electro-magnetic interference. Connecting the output of the CCD directly into an ASIC gives the minimal possible analogue signal path.

### 8.1.6 Reduced noise through CDS

Reset level noise has the largest impact on the SNR and must be eliminated to make X-ray spectroscopy with CCDs at all possible. Reset noise is found on all CCD output signals caused by Johnson noise ( $kTC$ ) in the reset FET [Johnson 1928]. This noise causes a variation in the charge flowing through the FET from the potential bias of the reset drain to the output node and causes a non-deterministic reset value to be stored in the output node when the FET closes. Figure 8.6 shows an example of how the modulation of the reset FET can affect the charge stored in the output node.

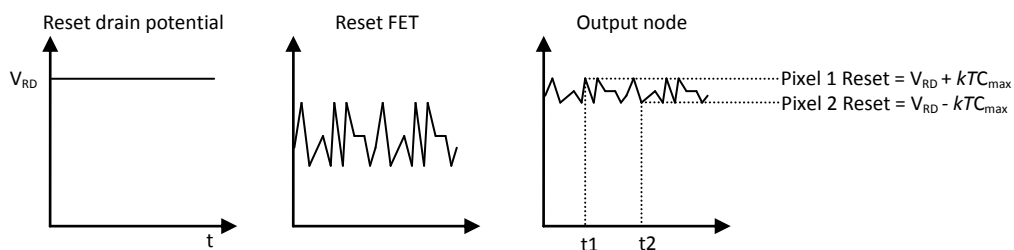


**Figure 8.6**  $kTC$  noise modulation of output node

When the signal charge of a pixel, shown in Figure 8.7, is added to the reset level held in the output node capacitance during the serial clocking operation, both the reference and signal levels contain the same reset noise component. Correlated double sampling (CDS) removes reset noise by differencing the charge measured by the output FET upon reset and after the charge packet has been added [Janesick 2001].

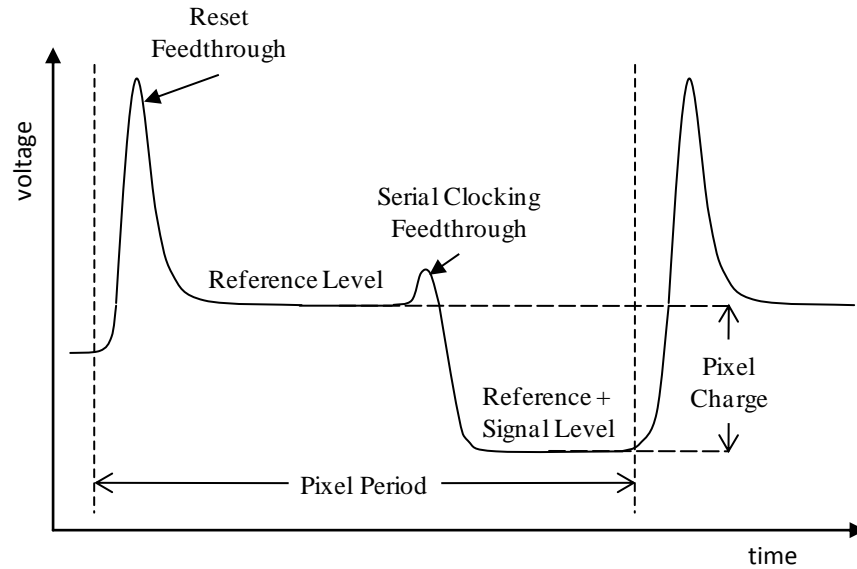


**Figure 8.7** Schematic of a 1 pixel CCD output waveform

Brunel University, in collaboration with STFC, designed and developed a number of ASIC designs capable of reading out a CCD video signal by the CDS method. The design and performance of three such ASICs are presented in the following sections.

## 8.2 The 2-channel CDS ASIC

The 2-channel CDS ASIC was designed by J. Calafell at Brunel University in collaboration with STFC under the PIPSS programme in 2004 [Calafell et al 2005]. It has two differential inputs with programmable on-chip gain, although only one input can be used at a time. The reason for the second input was to allow for redundancy should the programmable  $\pm 500$  mV offset via the 10-bit DAC of input 1 fail. The offset for input 2 was set by external bias potentials. The basic block diagram of the 2-channel CDS ASIC is shown in Figure 8.8.

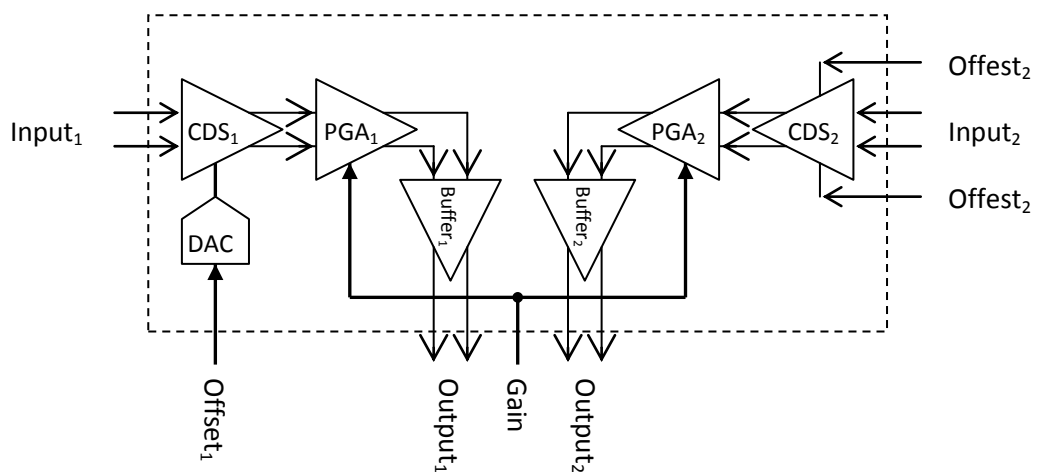


**Figure 8.8** The 2-channel CDS ASIC block diagram

The design specification of the 2-channel ASIC was to read a single output channel from an X-ray CCD at pixel rates of up to 1 MHz, whilst maintaining a system noise of  $< 10 e^-$ . The CDS stage had a fixed gain of 4.4 and the programmable stage of between 1 and 2.98. The 2-channel ASIC would consume less than 130 mW from a 3.3 V power supply.

The CDS processor is the first stage of the ASIC; it has a fully differential preamplifier stage with a fixed gain of 4.4 and a sample and hold CDS circuit design. This enables the use of the common mode rejection (CMR) for CCDs equipped with ‘dummy’ outputs to further suppress the extraneous noise of the camera system (CDS and CMR are discussed in Chapter 4). The input to the preamplifier is A.C. coupled to isolate the high output bias voltage of the CCD ( $V_{RD}$ ) used to create the output node (17 V to 20 V). The programmable offset available on input 1 can be set by the bit patterns in Table 8.1 to increase the dynamic range of the ASIC, correcting for the background of the CCD image caused by dark current.

Input 1 (10-bit DAC)	Input 2 + (V)	Input 2 – (V)	Offset (V)
0000000000	0.5	2.5	-0.5
1000000000	1.5	1.5	0
1111111111	2.5	0.5	+0.5

**Table 8.1** Programmable offset input values for the 2-channel CDS ASIC

The programmable gain stage allows the full dynamic range of the CDS ASIC to be quantised by a  $\pm 2.5$  V ADC, maximising the resolution of the readout for incoming X-ray photons up to 25 keV. The PGA is made from a binary weighted capacitor array that acts as the input capacitance for an operational amplifier. Values for the switched capacitances are designed to give a gain between 1 and 2.98 at 7-bits of resolution. Examples of the 7-bit programmable gain settings are shown in Table 8.2.

Input (7-bit)	PGA Gain
0000000	1
1000000	2
1111111	2.98

**Table 8.2** Programmable gain amplifier input values for 2-channel CDS ASIC

A buffer stage is included before the output to ensure the ASIC can drive a typical input capacitance of 5 pF for the ADC stage [Linear Technology 2000].

### 8.2.1 Testing and results

An evaluation board was designed and manufactured to test the 2-channel ASIC which included a programmable pre-amplifier stage to raise the SNR of the CCD video signal and a 14-bit ADC (LTC1414) to sample the ASIC output. The CDS sequencing clocks were input via optical isolators to protect the ASIC from voltage transients. The 2-channel ASIC programmable gain and offsets were set by dual in-line package (DIP) switches [Calafell et al 2005].

Functional tests were initially carried out to confirm the correct operation of the 2-channel ASIC. The system noise was then evaluated using input from a CCD57 and was measured to be  $\sim 6 e^-$  r.m.s. at a pixel frequency of 300 kHz. An independent camera system was used to measure the noise performance of the same CCD57 and was found to be  $\sim 4 e^-$  r.m.s. The extra noise of the ASIC system was attributed to the layout of the evaluation board [Calafell et al 2005].

The noise equivalent signal (NES) contribution of the 2-channel ASIC and evaluation board to the complete system were then measured at various pixel frequencies by grounding the input, following an initial energy calibration. It was found that the CCD noise dominated for pixel frequencies below  $\sim 500$  kHz. The total system noise would be expected to be in excess of  $10 e^-$  r.m.s. for pixel frequencies above 500 kHz [Calafell et al 2005].

### 8.3 The 4-channel CDS ASIC

The 4-channel CDS ASIC was also designed by J. Calafell at Brunel University in collaboration with STFC for the PIPSS programme [Calafell et al 2005]. Based on the 2-channel CDS ASIC design, four independent CCD video signals can be processed concurrently but share the same programmable gain and offset as shown in Figure 8.9. The specification and input parameters are otherwise the same as the 2-channel ASIC listed in Tables 8.1 and 8.2.

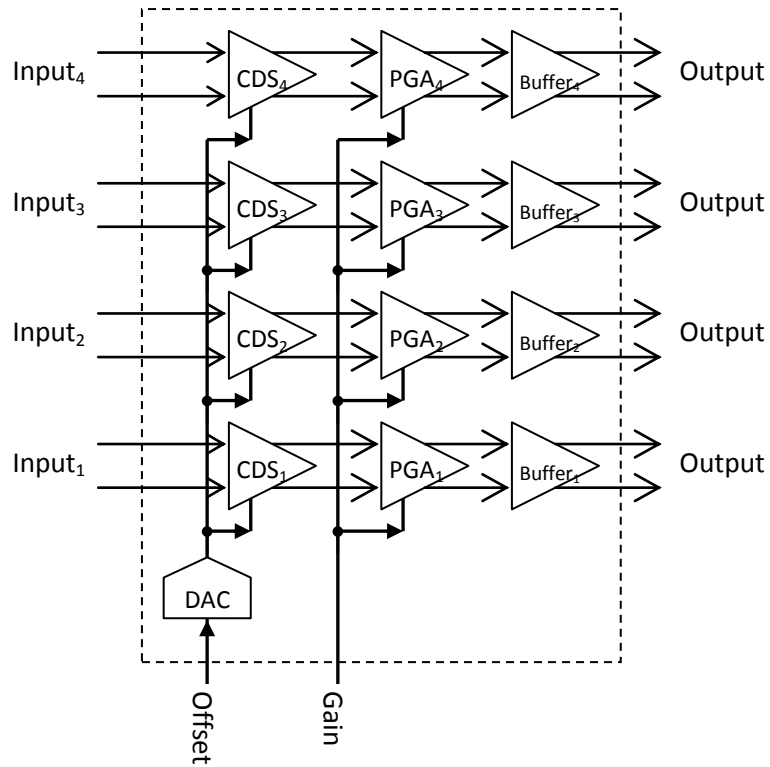


**Figure 8.9** 4-Channel CDS ASIC block diagram

The design bit-slice incorporating the CDS amplifier, programmable gain and output buffer stages has been repeated in the layout to allow for four different CCD video signals to be processed concurrently. The 4-channel CDS ASIC die with overlaid function blocks is shown in Figure 8.10. Each of the four channels shares the same user programmable gain and voltage offset and must be sequenced by the same camera system to ensure correct timing of the CDS operation.

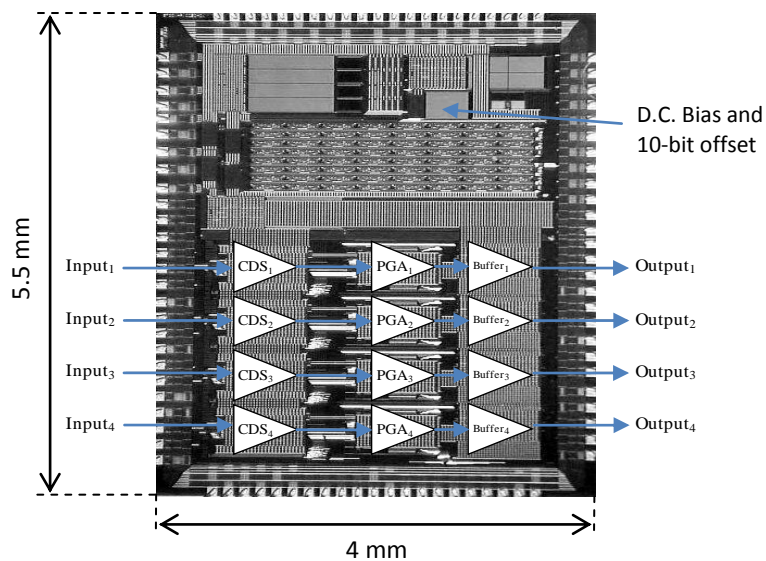


**Figure 8.10** 4-channel CDS ASIC die

The connections to the ASIC are listed in Table 8.3.

Pad Number	ZIF Socket	Pin	Value	Description
1	B12	Gnd	0 V	Analogue Ground
2	A12	Vdd	3.3V	Analogue VDD
3	B11	Gnd	0 V	Analogue Ground
4	A11	Vdd	3.3V	Analogue VDD
5	B10	Gnd	0 V	Analogue Ground
6	A10	Vdd	3.3V	Analogue VDD
7	B9	Gnd	0 V	Analogue Ground
8	A9	Vdd	3.3V	Analogue VDD
9	C8	Gnd	0 V	Analogue Ground
10	B8	VoffP1	500mV	Positive Offset reference
11	A8	VoffN1	500mV	Negative Offset reference
12	B7	Vcasc	0-3.3V	Cascade Bias Voltage
13	C7	Vcm	0-3.3V	Common Mode Bias Voltage
14	A7	INP1	0-1V	CCD1 Ground Input
15	A6	INN1	0-1V	CCD1 Signal Input
16	B6	Gnd	0 V	Analogue Ground
17	C6	INP2	0-1V	CCD2 Ground Input
18	A5	INN2	0-1V	CCD2 Signal Input
19	B5	Gnd	0 V	Analogue Ground
20	A4	INP3	0-1V	CCD3 Ground Input
21	B4	INN3	0-1V	CCD3 Signal Input
22	A3	Vdd	3.3V	Analogue VDD
23	A2	Gnd	0 V	Analogue Ground
24	B3	INP4	0-1V	CCD4 Ground Input
25	A1	INN4	0-1V	CCD4 Signal Input
26	B2	Vdd	3.3V	Analogue VDD
28	C2	Vdd	3.3V	Analogue VDD
29	C1	Gnd	0 V	Analogue Ground
30	D2	Vdd	3.3V	Analogue VDD
31	D1	Gnd	0 V	Analogue Ground
32	E2	Vdd	3.3V	Analogue VDD
33	E1	Gnd	0 V	Analogue Ground
34	F3	Clp	0-3.3V	CDS Clamp
35	F2	Phi1	0-3.3V	CDS Sample Clock 1
36	F1	Phi2	0-3.3V	CDS Sample Clock 2
37	G2	Aclk	0-3.3V	ADC Clock
38	G3	Vdd	3.3V	Analogue VDD
39	G1	Gnd	0 V	Analogue Ground
40	H1	Gain<0>	0-3.3V	Gain Select (LSB)
41	H2	Gain<1>	0-3.3V	Gain Select (Bit 1)
42	H3	Gain<2>	0-3.3V	Gain Select (Bit 2)
43	J1	Gain<3>	0-3.3V	Gain Select (Bit 3)
44	J2	Gain<4>	0-3.3V	Gain Select (Bit 4)
45	K1	Gain<5>	0-3.3V	Gain Select (Bit 5)
46	K2	Gain<6>	0-3.3V	Gain Select (MSB)
47	L1	Gnd	0 V	Analogue Ground
48	M1	Vdd	3.3V	Analogue VDD
50	N1	Gnd	0 V	Analogue Ground

51	M2	OUTP4	±2.5V	Positive Differential Output
52	N2	OUTN4	±2.5V	Negative Differential Output
53	M3	Gnd	0 V	Analogue Ground
54	N3	Gnd	0 V	Analogue Ground
55	M4	OUTP3	±2.5V	Positive Differential Output
56	N4	OUTN3	±2.5V	Negative Differential Output
57	M5	Gnd	0 V	Analogue Ground
58	N5	OUTP2	±2.5V	Positive Differential Output
59	L6	OUTN2	±2.5V	Negative Differential Output
60	M6	Gnd	0 V	Analogue Ground
61	N6	OUTP1	±2.5V	Positive Differential Output
62	M7	OUTN1	±2.5V	Negative Differential Output
63	L7	VREFL	0-3.3V	Low ADC Reference
64	N7	VREFH	0-3.3V	High ADC Reference
65	N8	VREFM	0-3.3V	Mid ADC Reference
66	M8	Offset<9>	0-3.3V	Offset Select (MSB)
67	L8	Offset<8>	0-3.3V	Offset Select (Bit 8)
68	N9	Offset<7>	0-3.3V	Offset Select (Bit 7)
69	M9	Offset<6>	0-3.3V	Offset Select (Bit 6)
70	N10	Offset<5>	0-3.3V	Offset Select (Bit 5)
71	M10	Offset<4>	0-3.3V	Offset Select (Bit 4)
72	N11	Offset<3>	0-3.3V	Offset Select (Bit 3)
73	N12	Offset<2>	0-3.3V	Offset Select (Bit 2)
74	M11	Offset<1>	0-3.3V	Offset Select (Bit 1)
75	N13	Offset<0>	0-3.3V	Offset Select (LSB)
77	M13	Vdd	3.3V	Analogue VDD
78	L12	Gnd	0 V	Analogue Ground
79	L13	PonRst	0-3.3V	Power-on-reset
80	K12	Gnd	0V	Analogue Ground
81	K13	Vdd	3.3V	Analogue VDD
82	J12	Gnd	0V	Analogue Ground
83	J13	Vdd	3.3V	Analogue VDD
84	H11	Gnd	0 V	Analogue Ground
85	H12	Vdd	3.3V	Analogue VDD
86	H13	Gnd	0 V	Analogue Ground
87	G12	Vdd	3.3V	Analogue VDD
88	G11	Ibias	0-3.3V	Bias Current (300uA)
89	G13	Vdd	3.3V	Analogue VDD
90	F13	Gnd	0 V	Analogue Ground
91	F12	Vdd	3.3V	Analogue VDD
92	F11	Gnd	0V	Analogue Ground
93	E13	Vdd	3.3V	Analogue VDD
94	E12	Gnd	0V	Analogue Ground
95	D13	Vdd	3.3V	Analogue VDD
96	D12	Gnd	0V	Analogue Ground
97	C13	Vdd	3.3V	Analogue VDD

Table 8.3 4-channel CDS ASIC pin connections

### 8.3.1 Initial 4-channel CDS ASIC Evaluation board

A prototyping board was developed under this work to accommodate the 4-channel ASIC with four independent inputs for characterisation and is shown in Figure 8.11.

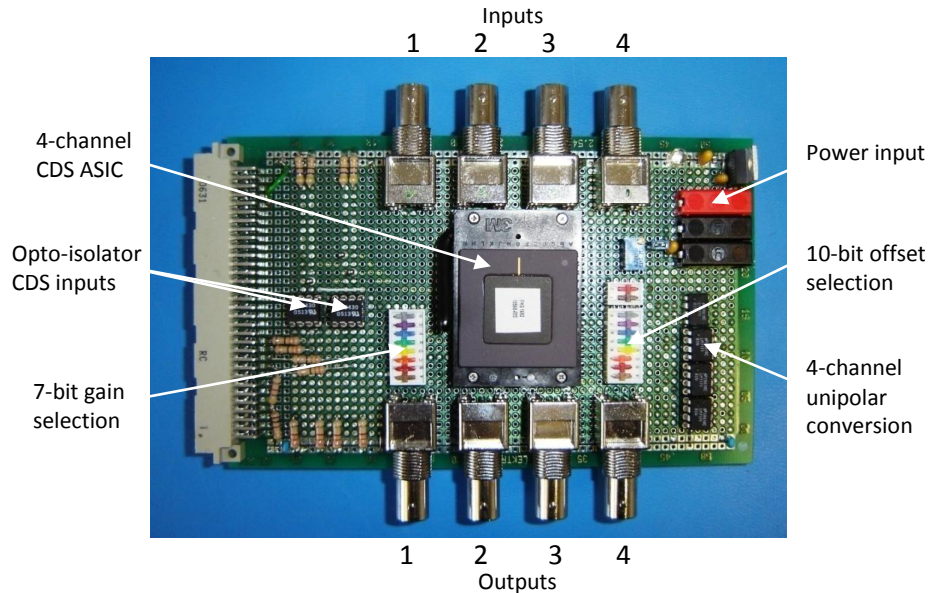


**Figure 8.11** Evaluation board developed under this work to test the 4-channel CDS ASIC

The video signals output by the CCDs are initially A.C. coupled into a pre-amplifier on the CCD headboard by a gain of 11 (see Chapter 4). DIP switches can be set to the desired bit patterns to set the programmable gain and offset. Two optical isolator ICs were used to protect the ASIC from any undesirable voltage transients on the  $\Phi_{i1}$ ,  $\Phi_{i2}$ ,  $Clp$  and  $Aclk$  inputs from the sequencing electronics. The outputs from the ASIC are bipolar and therefore four differential input, high speed operational amplifiers (LM7171) were included with unity gain to convert each output into unipolar for a ground referenced ADC (DAS4020/12). The conversion of the differential outputs, labelled  $OutP_{ASIC}$  and  $OutN_{ASIC}$ , into a unipolar form is shown in Figure 8.12.

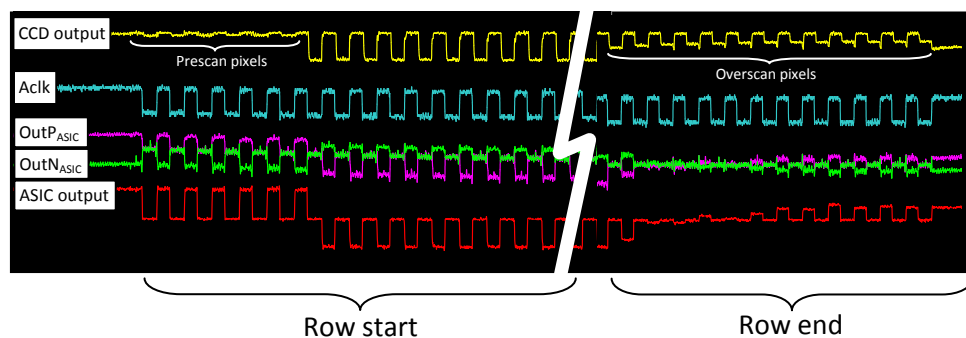


**Figure 8.12** Oscilloscope traces of CCD and corresponding unipolar ASIC output

### 8.3.2 Initial setup

The first task was to establish the correct functioning of the 4-channel CDS ASIC. Each channel was initially tested individually in turn using the input from a CCD62 (a basic, easy to use device for system characterisation). The input to 1 channel of the evaluation board was connected to a CCD62 headboard via a short twisted pair cable. The unipolar output of the corresponding channel was then input directly into an ADC connected to a PCI bus. Pixel data was acquired by the DAS4020/12 method described in Chapter 4. Modifications to the standard CCD sequencer program were necessary due to the different timings of the ASIC CDS operations compared to the standard system, also described in Chapter 4. A schematic of the initial experimental setup is shown in Figure 8.13.

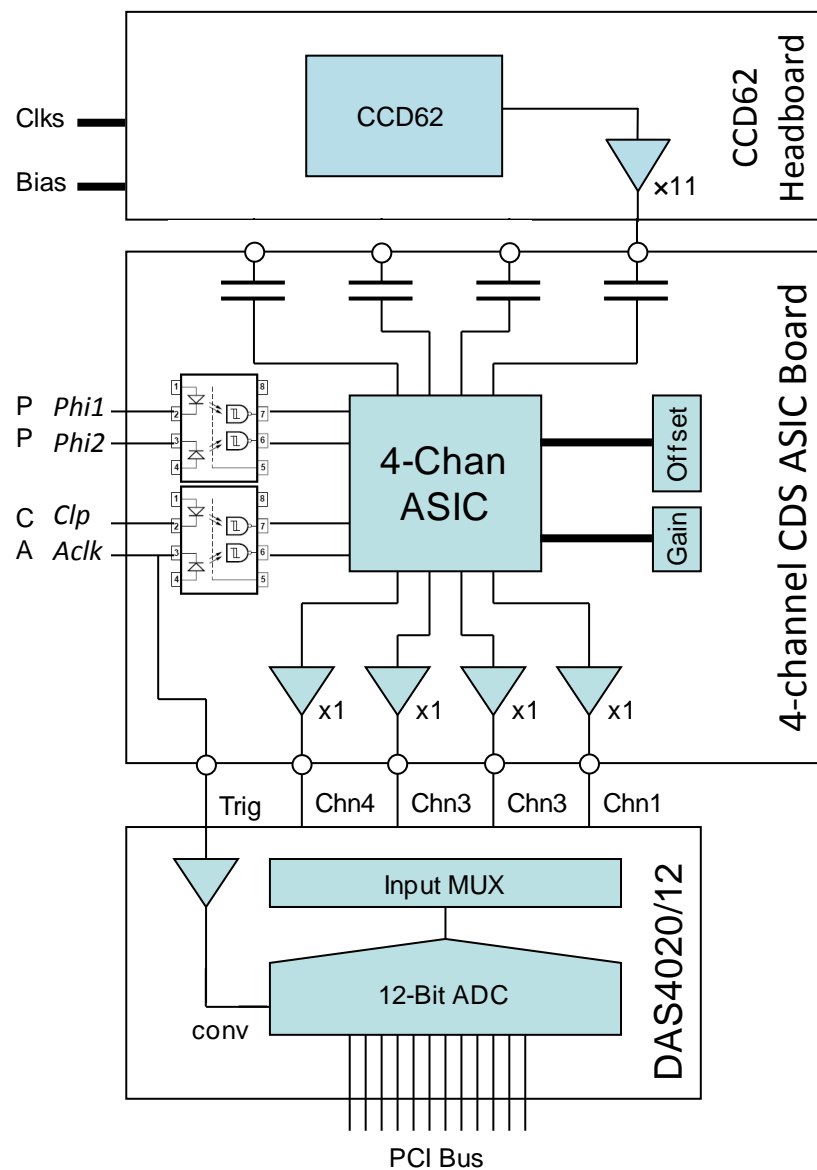
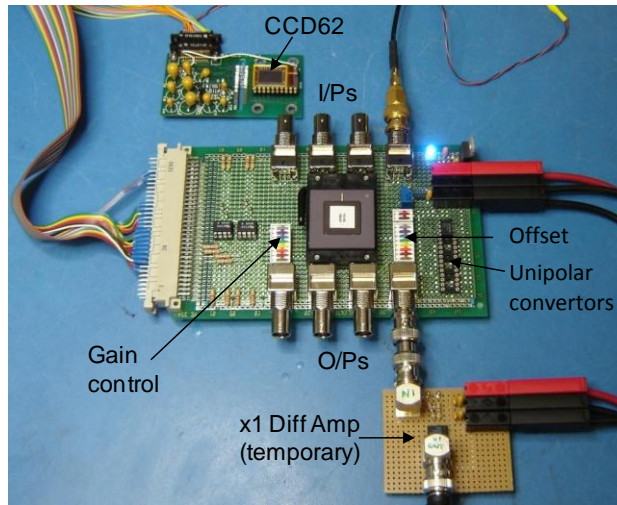


Figure 8.13 4-channel CDS ASIC experimental setup block diagram

During the initial testing of the 4-channel CDS ASIC the bipolar conversion circuits on the evaluation board were failing due to a soldering error and hence a temporary off-board conversion circuit was made, shown in Figure 8.14.



**Figure 8.14** Initial setup for 4-channel CDS ASIC testing with temporary unipolar converter

### 8.3.3 Operation

Sequencing of the required inputs to the CDS stage was performed by a DSP in the camera drive electronics. The CDS function requires four such inputs. An internal clamp (*Clp*) was used to reset the input bias to midway between the differential reference potentials, required for the operation of the ASIC from a single + 3.3 V supply when using a differential input of  $\sim \pm 1$  V after A.C. coupling. The *Clp* was activated once per pixel during the reset of the CCD output node. The output node reference level, including any *kTC* noise, was sampled on the falling edge of *Phi1*. The pixel charge packet was then sampled at the falling edge of *Phi2*, after the appropriate clocking of the CCD serial register. The difference of the two stored values was then amplified in the CDS stage amplifier for the high period *Phi2*. The final input, *Aclk* determines the timing of a valid output of the ASIC for the ADC to samples and was valid for the pixel that precedes it. Further amplification was then performed by the PGA stage depending on the 7-bit user input. The relative timings of the inputs to the CDS stage to the CCD output are shown in Figures 8.15 and 8.16.

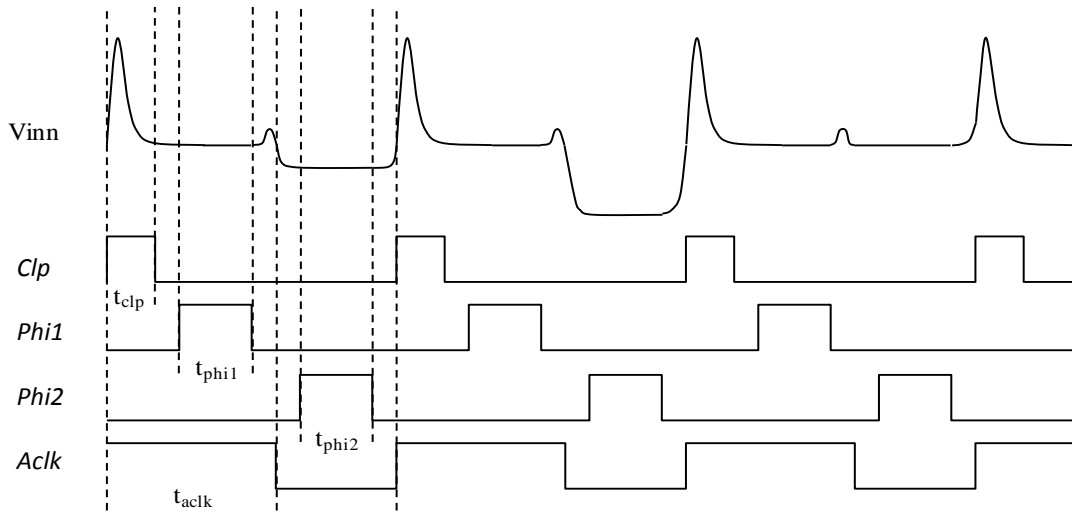


Figure 8.15 Sequence timings for CDS

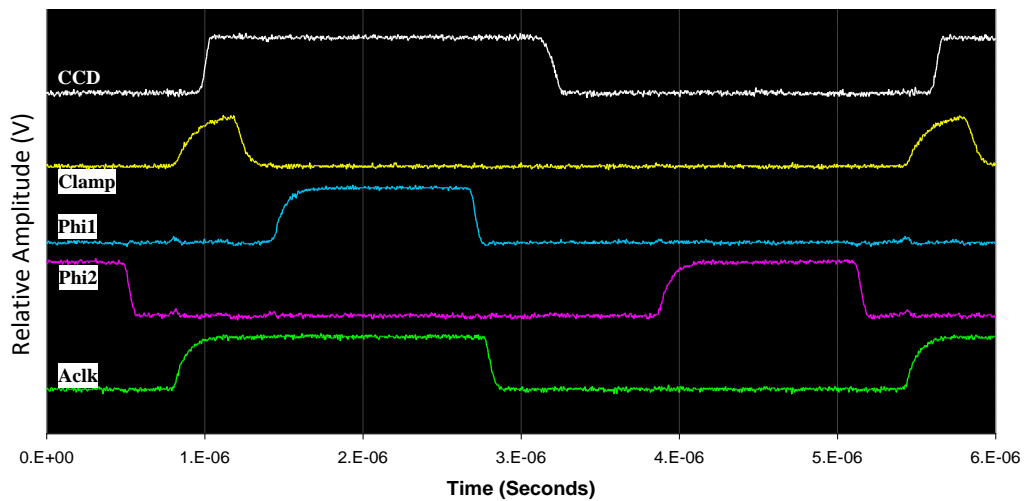


Figure 8.16 Oscilloscope voltage traces for CDS of 1 pixel

The minimum time periods between operations for correct operation of the 4-channel CDS ASIC, are shown in Table 8.4.

Name	Min Time (ns)
t <sub>clp</sub>	50
t <sub>phi1</sub>	100
t <sub>phi2</sub>	300
t <sub>aclk</sub>	250

Table 8.4 Minimum timings for the correct operation of the 4-channel CDS ASIC

The output of the 4-channel CDS ASIC relative to that of the CCD is shown in Figure 8.17. The input to the ADC had a voltage swing of ± 1.7 V, where zero pixel charge was +1.7 V and full well was -1.7 V.

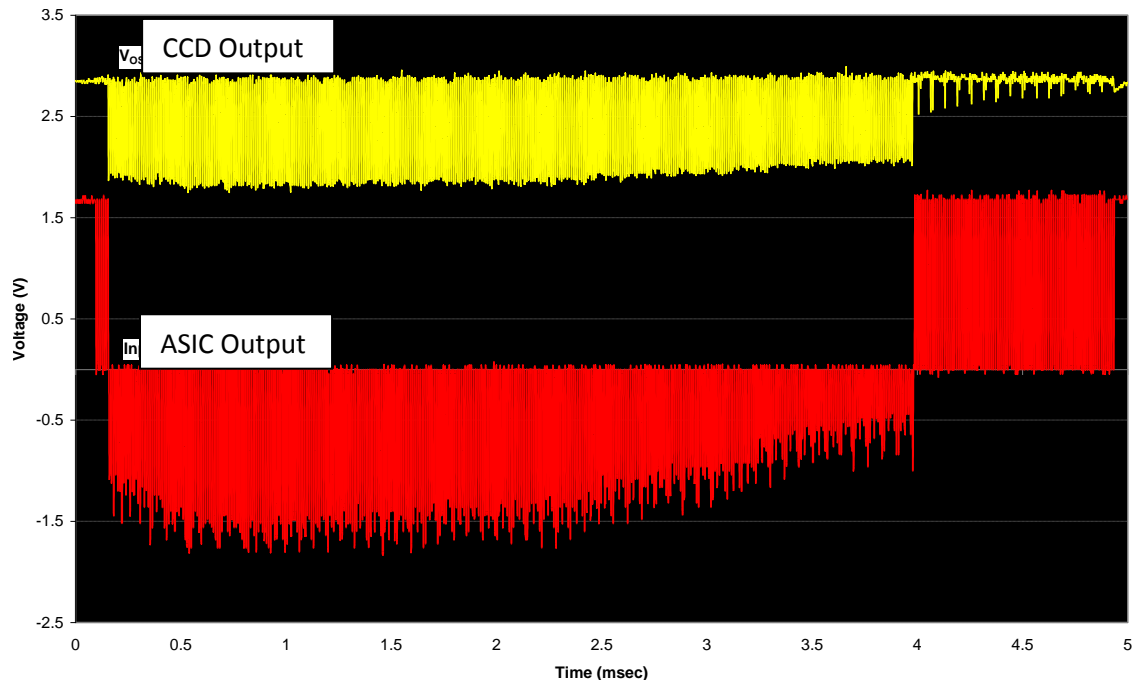


**Figure 8.17** Oscilloscope trace of a 1 row output from the CCD and the 4-channel CDS ASIC

### 8.3.4 Data acquisition and processing

The effect of noise pickup on the analogue path can be reduced by  $\sqrt{N}$  when averaging a number ( $N$ ) of samples for each pixel value. In order to operate the ADC at a suitable sampling rate of greater than four samples per pixel for consecutive pixels, it was necessary to sample an entire row at a time using the triggered input scan function and to later recover the pixel data during post processing. This was due to the large latency ( $\sim 1$  ms) of the DAS4020/12 between setting up a trigger, triggering and then beginning to acquire the samples. At such latency, many pixels would have been missed between consecutive triggers. Therefore a large memory buffer was created to hold the samples for the entire row output by the ASIC, plus the *Aclk* clock to enable synchronisation during post processing to valid pixel data. The capture of row data was triggered by the *Line-Sync* pulse, supplied by the drive electronics that precedes the readout of each row. Figure 8.18 shows the relative timings of the operations to acquire one row containing four pixels.

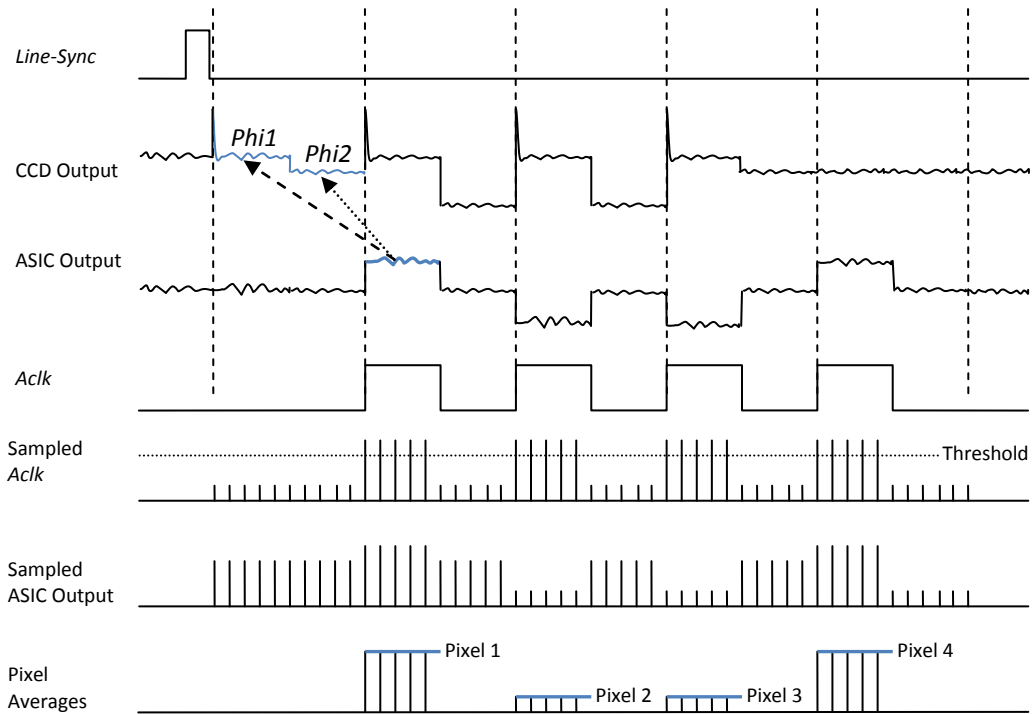


**Figure 8.18** DAS4020/12 ASIC pixel acquisitions

A Matlab routine was developed to process the samples acquired for the *Aclk* and ASIC outputs into a 2-D array of pixels comprising the CCD image. The *Aclk* samples were initially converted into an array of logic ones and zeros and then multiplied by the ASIC output samples to zero the undesired data between pixels for each row. Each set of pixel samples, now separated by zeros, was averaged to give single values for each pixel that were then stored into the 2-D image array. Figure 8.19 shows an example of two consecutive rows of 385 pixels, separated by the prescan pixels of the CCD.

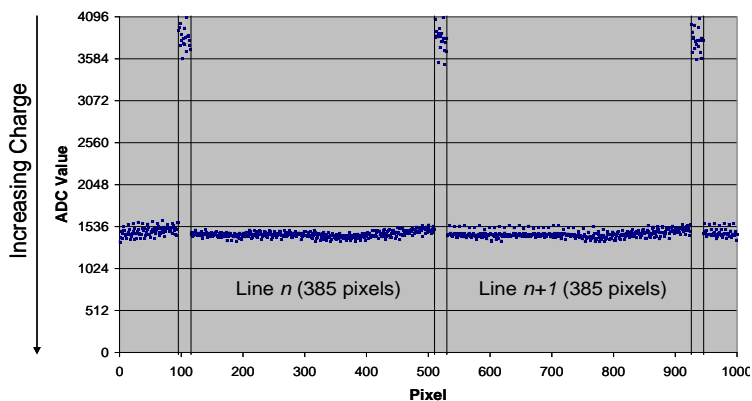


**Figure 8.19** Two row acquisition of CCD62 image with 4-channel CDS ASIC

The parallel transfer time for the CCD to shift the next row of pixels into the serial register was sufficient for the DAS4020/12 to set up the triggered input scan for the subsequent row of pixels.

### 8.3.5 Channel cross-talk evaluation

The first experiment undertaken with the 4-channel CDS ASIC was to measure the cross-talk between channels when performing CDS on multiple video input signals. One of the four channels was input a square wave of amplitude 1 V to simulate a full well pixel charge of the CCD and hence give a corresponding full scale output of the ASIC. The square wave was uncorrelated to the CDS and therefore the period was set to span a number of pixels, allowing the  $\Phi_1$  sample to be taken the high level of the square wave and the  $\Phi_2$  at the low level at regular intervals. This simulated a full well pixel charge and gave a full scale output of the ASIC, demonstrated in Figure 8.20.

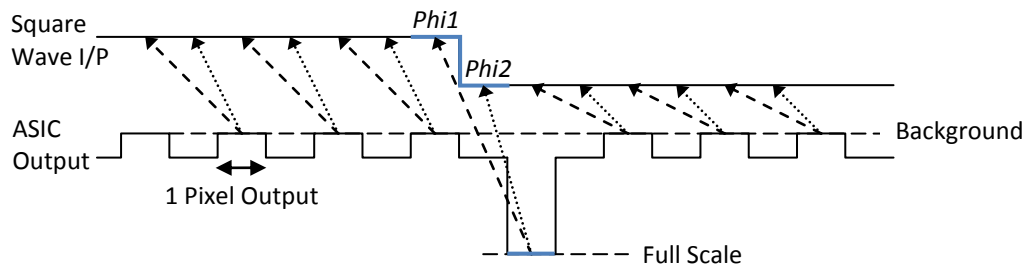


Figure 8.20 Cross-talk input/output waveforms

The remaining three channels had a common square wave input with a different period, carefully chosen not to give a full scale output at the same time as the channel under investigation. The output of the said channel can be directly compared to those of the common three to analyse any pickup occurring within the ASIC. A block diagram of the experimental setup is shown in Figure 8.21.

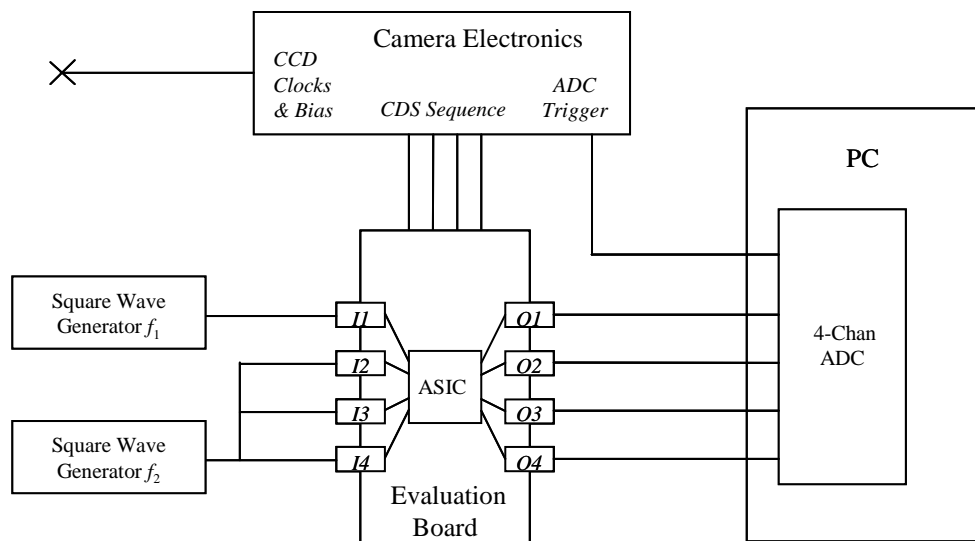


Figure 8.21 Cross-talk experiment block diagram

The outputs from the 4-channel CDS ASIC were sampled by the ADC and analysed to determine the background signal distribution produced by the ASIC. This was the noise component of the ASIC and is given in Volts r.m.s. Where a full scale output occurred on the isolated channel the remaining three common channels were found to have no measurable pickup of this signal above the background level. Similarly, a full scale output on the common channels had no measurable effect on the isolated channel. Table 8.5 and figure 8.22 gives an example of the measured 4-channel ASIC cross-talk for two pixels *a* *b*, simulated by square wave generators [Murray et al 2007].

Example	Channel	Input	Background (ADU)	Pixel (ADU)	Change (ADU)	%	Isolation
<i>a</i>	1	Common	2156	2162	+ 6	+ 0.278	369:1
<i>a</i>	2	Common	2126	2132	+ 6	+ 0.282	354:1
<i>a</i>	3	Common	2125	2126	+ 1	+ 0.047	2125:1
<i>a</i>	4	Isolated	2079	2614	+ 535	+ 25.734	N/A
<i>b</i>	1	Common	2156	2667	+ 511	+ 23.701	N/A
<i>b</i>	2	Common	2126	2638	+ 512	+ 24.083	N/A
<i>b</i>	3	Common	2125	2635	+ 510	+ 24.000	N/A
<i>b</i>	4	Isolated	2079	2075	- 4	- 0.192	520:1

Table 8.5 ASIC output and background

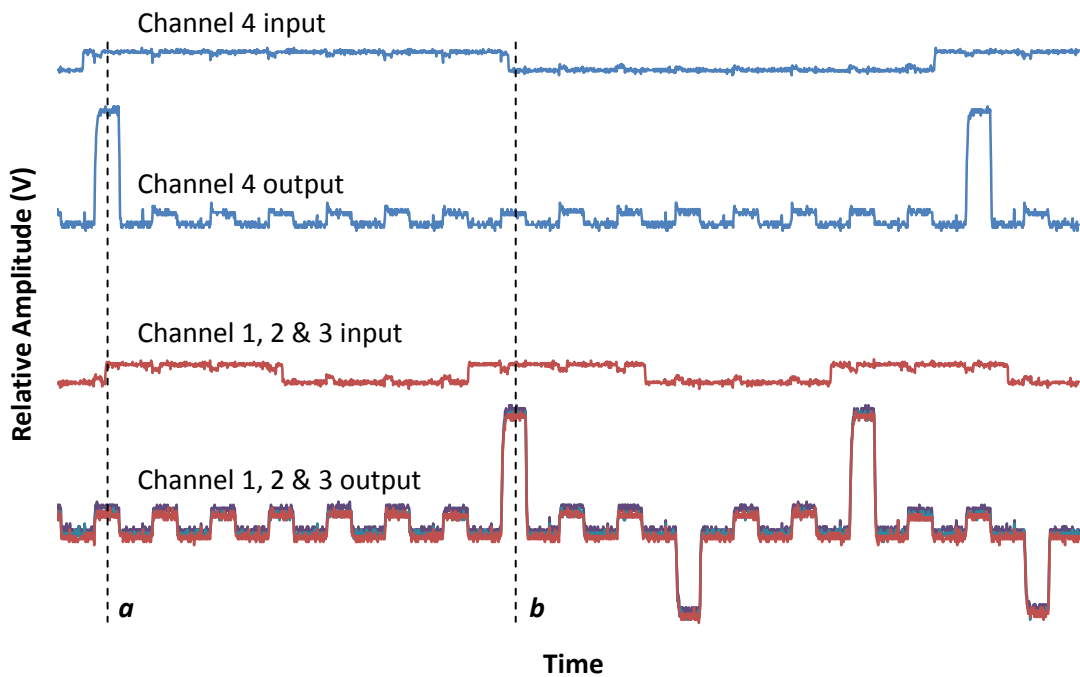
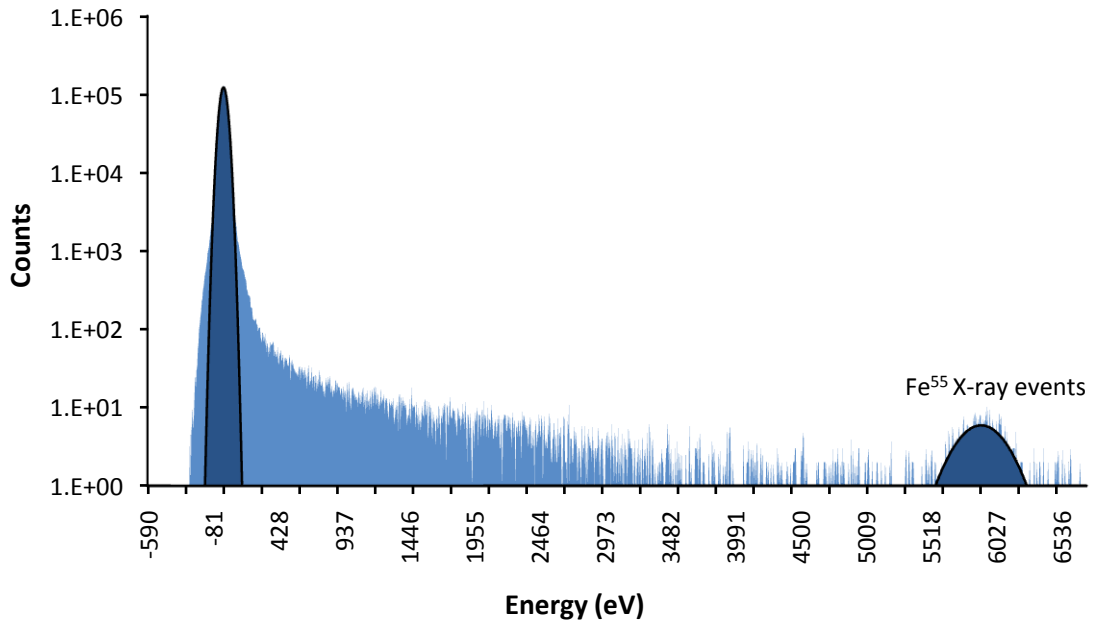


Figure 8.22 Input output captured waveforms of the cross-talk investigation

### 8.3.6 Noise contribution

An  $\text{Fe}^{55}$  source was used to calibrate the energy scale for images read out from a CCD47 using the 4-channel ASIC. Gaussian models were fitted to a histogram of the pixel data in the image to determine the 5,898 eV source to background distribution and hence the energy resolution of the ADC. The FWHM of the modelled background peak was measured and used to determine the sigma of the background noise distribution. The system noise of the camera was measured to be  $8.1 e^- \pm 0.2 e^-$  r.m.s. from the relationship  $1 e^-$  was generated for every 3.68 eV of charge deposited in silicon at 173 K. The energy spectrum obtained by the 4-channel ASIC is shown in Figure 8.23. It should be noted the responsivity of the CCD47 was low and hence the noise and spectral performance was poor [Murray et al 2007].



**Figure 8.23**  $\text{Fe}^{55}$  spectrum read by the 4-channel CDS ASIC and low responsivity CCD47

The ASIC noise component was determined by subtracting the other known noise contributions to the camera system and is shown in Figure 8.24. The ADC noise component was measured by grounding its input and reading a number of samples. The CCD noise is specified by e2v technologies for a given pixel read out rate.

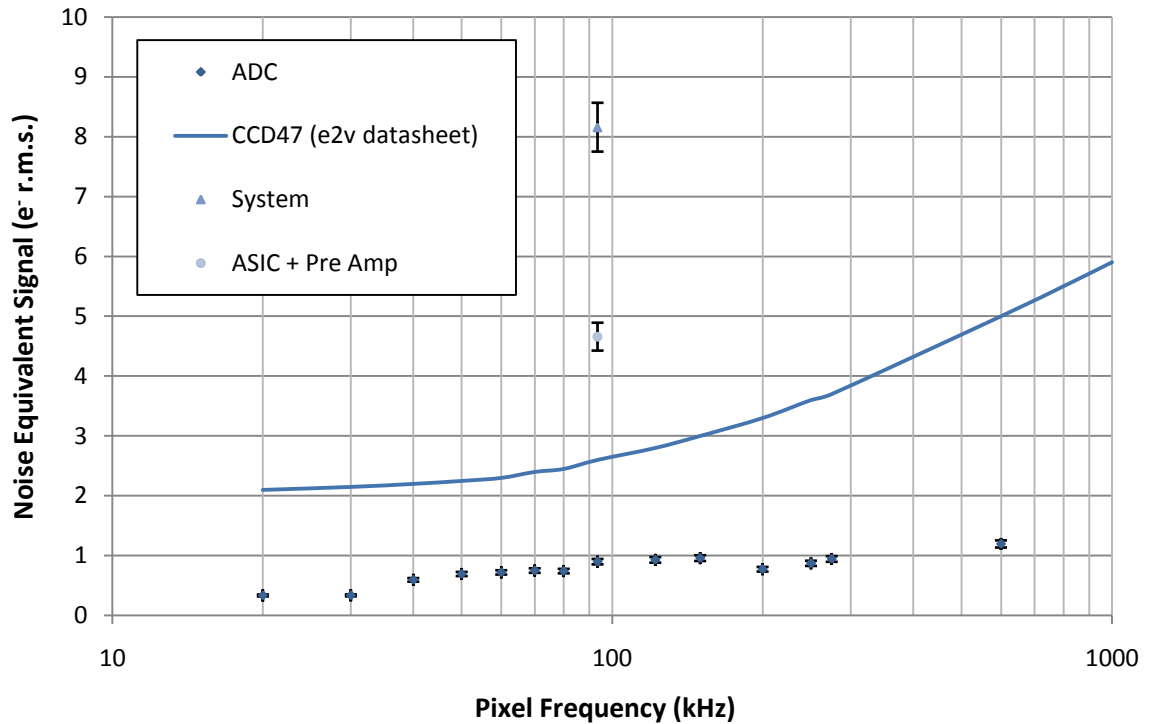


**Figure 8.24** Noise vs. pixel readout frequency

## 8.4 Conclusions

The noise performance of the 2-channel ASIC system was found to be acceptable ( $< 10 e^-$  r.m.s.) at pixel frequencies below 500 kHz. The 2-channel ASIC system is expected to offer an equivalent performance to EPIC-MOS (160 kHz) up to a pixel frequency of 375 kHz [Calafell et al 2005].

The 4-channel CDS ASIC was measured to contribute a noise equivalent signal of  $< 5 e^-$  r.m.s. to the system when operated at a read out of  $\sim 100$  k pixels per second. It is believed that the ASIC will perform with an acceptable  $< 10 e^-$  r.m.s. for pixel rates up to 500 kHz, due to the nature of the clamp and sample technique employed by the ASIC.

The isolation between channels within the 4-channel ASIC was measured on average to be greater than 800:1. This is sufficient isolation for use with multiple X-ray CCD video channels. At this level of isolation, if one channel measures the charge generated by one 5,898 eV X-ray photon, any potential cross channel pickup would be equivalent to a maximum of  $2 e^-$  r.m.s. This is far lower than the  $1\sigma$  noise that has been measured for the X-ray camera system ( $\sim 8 e^-$  r.m.s.) A  $5\sigma$  threshold is typically used for such an X-ray detection system, therefore any cross channel pickup is truly in the noise.

The performance confirms the 4-channel CDS ASIC's suitability for X-ray photon counting spectroscopy, hence the reduced size and mass of this multiple channel ASIC would be of great benefit to any space based X-ray CCD focal plane array such as that proposed for XEUS [Holland et al 2005].

The sample and hold CDS technique employed by the ASICs allowed some high frequency noise signal of amplitude  $\pm 20$  mV on the video signal to be sampled during CDS. This effect was reduced by re-routing and shortening connections to the ASIC, although could not be entirely eliminated. A dual slope integrator design would be less susceptible to the effects of this high frequency noise as the reference level and charge packet samples are effectively an average of samples over a short time. Therefore any repetitive high frequency signal occurring during the integration time would appear in both samples and be removed by CDS.

## 8.5 Further work

Further to the work undertaken, measurements of the 4-channel CDS ASIC noise component could be obtained at pixel frequencies of 150 kHz to 1 MHz and without using the pre-amplifier on the CCD headboard. It would also be beneficial to incorporate a 16-bit ADC into the evaluation board to minimise the analogue signal path, reducing the effect of the high frequency noise pickup.

STFC provided 2 samples of their Mk8 CDS/ADC ASIC to Brunel for characterisation during the work described in this thesis. The Mk8 provides a single chip solution for processing the raw analogue output of the CCD into digital pixel values. Similar to the two ASIC designs discussed in this chapter, the ASIC performs CDS on the analogue signal to remove  $kTC$  noise and block low frequency noise. It has the same 10-bit offset to correct for dark current and 7-bit programmable gain to scale to the input range of the ADC. The output from the programmable gain amplifier is then fed directly into a 16-bit ADC that can operate at pixel rates up to 2.5 MHz. Designed with space applications in mind, triple-voting logic gates are included to protect against single event upsets that can be caused by proton damage in the space environment. The digital error correction block (DEC) digitally divides the CDS value by the gain used in the PGA stage and then adds or subtracts the offset voltage applied in the CDS amplifier to output a true digital representation of the analogue input [Waltham et al 2005]. Figure 8.25 shows a block diagram of the Mk8 CDS/ADC ASIC.

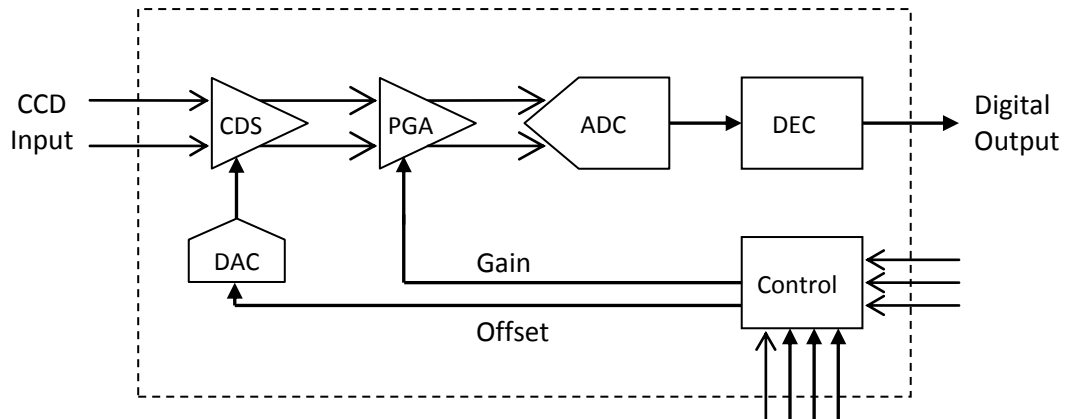


**Figure 8.25** Mk8 CDS/ADC ASIC Block Diagram (STFC)

The evaluation board shown in Figure 8.25 was designed and manufactured under the work of this thesis in preparation for the characterisation of the Mk8 CDS/ADC ASIC.

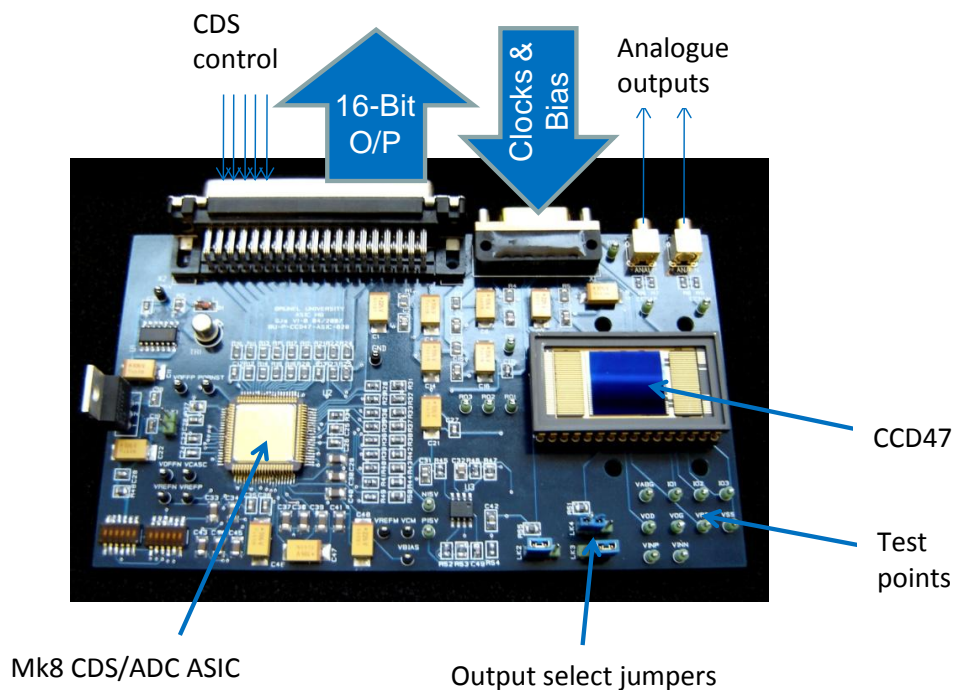


**Figure 8.26** Evaluation board developed to test the Mk8 CDS/ADC ASIC

The programmable gain and offset are set externally by communication over a 3 wire interface, compatible with the Philips I<sup>2</sup>C standard, eliminating the necessity to include mechanical DIP switches. It is envisaged that multiple ASICs of this type will be employed to read out a space based CCD focal plane array and therefore this reduction of external components is particularly beneficial. The ASIC is powered from a single 3.3 V supply, typically consuming 413 mW and as such the D.C. restoration of the A.C. coupled input signal is the same as in the 4-channel CDS ASIC. The input referred noise has been measured by STFC to be less than 3 ADU r.m.s. [Waltham et al 2005]. This could be measured in terms of noise equivalent signal by energy calibration with X-ray photons.

## 8.6 References

- Calafell, J. et al., 2005. A Readout ASIC for X-ray CCDs. *Proc. SPIE*, Vol. 5898.
- e2v technologies, 2007. Datasheet: CCD230-84 scientific CCD sensor front illuminated, 4096x4096 pixels, four outputs and inverted mode operation. A1A-100049, Version 3.
- Holland, A.D. et al., 2005. MOS CCDs for the wide field imager on the XEUS spacecraft. *Proc. SPIE*, Vol. 5898.
- Janesick, J.R., 2001. Scientific charge-coupled devices. *SPIE*.
- Johnson, J.B., 1928. Thermal agitation of electricity in conductors. *Physical Review*, Vol. 32, p. 97-109.
- Linear Technology, 2000. Datasheet: LTC1608 High speed, 16-Bit, 500 ksps sampling A/D converter with shutdown.
- Lumb, D.H. et al., 1991. Charge-coupled devices (CCDs) in X-ray astronomy. *Experimental Astronomy*, Vol. 2, p. 179-201.
- Murray, N.J. et al., 2007. High-throughput video processing ASICs for X-ray CCDs. *Proc. SPIE*, Vol. 6686.
- Rabaey, J.M. et al., 2003. Digital integrated circuits. *Prentice Hall Electronics and VLSI Series*, 2<sup>nd</sup> Ed.
- Short, A. et al., 2005. Gaia astrometric CCDs and focal plane. *Proc. SPIE*, Vol. 5902.
- Waltham, N.R. et al., 2005. A Single-Chip CDS and 16 Bit ADC CCD Video Processing ASIC. *Rutherford and Appleton Labs*.

## Chapter 9: Conclusions and further work

This chapter summarises the main conclusions of the studies carried out for this thesis and indicates directions for possible further work in each case.

### 9.1 Electro-optic characterisation of high resistivity CCDs

High resistivity CCDs were characterised to assess their design and general performance. Some of the key findings from this work were as follows:

- The CCD217 was successful in proving the concept of fabricating CCDs using e2v's standard processes on high resistivity bulk silicon, that could be operated at large negative substrate potentials (-70 V) to increase the depletion depth of the device. The extra spacing of the output circuit layout led to increased parasitic capacitance of the output node, reducing output amplifier responsivity to  $\leq 2 \mu\text{V}/e^-$  that had a negative impact on the noise, which in turn hindered the spectral performance of the device.
- Modifications to the CCD247 design allowed the layout of the output circuit to be reduced to a similar size to the CCD42, whilst retaining the ability to operate at large negative substrate potential. Responsivity was therefore increased, almost halving the noise and increasing the spectral resolution to an acceptable 140 eV at 6.4 keV. The guard drain structure however was found not to completely isolate the output circuit from the main substrate.
- The CCD247 was found to function correctly for substrate potentials between 0 V and -130 V. It was found that the most negative substrate potential that could be applied to the CCD247 whilst maintaining an acceptable  $< 5 e^-$  system noise was -100 V. The local substrate potential was found have little impact on the noise in the range 0 V to 8 V, at higher potentials it is believed the onset of clock induced charge is observed, increasing the noise measurement. The CCD247 was never intended to operate with a local substrate potential of  $> 7 \text{ V}$  and therefore further investigation was not necessary.
- Leakage current generation occurred at the expected rate for substrate potentials less negative than -90 V. Where the substrate potential was taken more negative an extra leakage effect was observed at the bottom left hand side of the imaging area. The severity of this effect was proportional to substrate potentials more negative than -90 V. From this work, e2v now recognise a redesign of the CCD247 is necessary to avoid this problem.

- In both CCD217 and CCD247 designs, it was observed that the pixel size should be matched to the incident X-ray energy for optimum performance to prevent the oversampling of the event generated. For high energy X-ray applications (up to 20 keV), it would be desirable to have 40  $\mu\text{m}$  to 50  $\mu\text{m}$  pixels.
- Modifications were made to existing laboratory equipment to operate the p-channel devices with a complete set of inverted inputs. Images were acquired, although the leakage current was found to be a factor 5 times higher than the equivalent n-channel CCDs, showing a greater dependence on the gate to substrate potential. Cosmetic quality was also found to be considerably poorer than that of the n-channel devices. A possible explanation is that the silicon material was of inferior quality. It was not possible to adequately suppress the leakage current to observe X-ray photons.

Further work would be to investigate the I-V characteristics of both the guard drain to main substrate and guard drain to local substrate of the CCD247, to ascertain the source of the extra leakage current observed at  $V_{SS} < -90$  V. This could lead to a modification of the design that would allow substrate potentials down to -130 V, whilst maintaining a  $< 5$   $e^-$  r.m.s.

Further work would also include a comparative proton irradiation study of both p-channel and n-channel variants of the high resistivity CCDs to investigate the reduction in charge transfer inefficiency (CTI) in the p-channel devices.

## 9.2 Depletion depth modelling and estimates by event analysis

Depletion depth estimates were made by spread event analysis of X-ray photons for a range of substrate potentials. Some of the key findings from this work were as follows:

- The depletion depth of a CCD is proportional to the root of the substrate potential. Where the substrate potential is taken more negative, hence increasing the electric field strength, the depleted region extends further into the p-region of the bulk silicon. Increased depletion depth increases the QE for X-rays and reduces the number of spread events observed in an X-ray image.
- Both CCD217 and CCD247 devices performed well with substrate potentials as negative as -70 V. A depletion depth of approximately 185  $\mu\text{m}$  was estimated by split event analysis for the CCD247 when depleted by an applied substrate potential of -70 V. This was approximately 28  $\mu\text{m}$  less than the theoretical depletion depth at this substrate potential and can be explained, but not fully accounted for, by some of the errors inherent in the event analysis technique.

- The depletion depth estimates are subject to systematic errors from the un-counted spread events, occurring deep in the substrate and by the low field tail leading to the electronic definition of the depletion boundary. There will be spread events that are so far beyond the depleted region they cannot be differentiated from the background noise. Therefore, the number of spread events counted experimentally can only be a minimum value. If the ratio of spread events were to be higher, this would correspond to a reduction in the depletion depth estimate.

Using the adapted test equipment described in Chapter 7, the depletion depth estimates made by the method presented in this chapter were obtained at various positions across the horizontal axis of imaging area of the CCD. Further modifications could be made to allow the CCD to be shifted in the vertical imaging axis direction to allow the depletion uniformity across the entire imaging area.

### 9.3 X-ray quantum efficiency modelling and measurements

Quantum efficiency measurements were made of the CCD247 of photon energies between 8,047 eV and 17,478 eV by taking relative measurements between the CCD and a SiLi detector. Some of the key findings from this work were as follows:

- Quantum efficiency measurements of X-ray photons were taken about the centre of the CCD imaging area using the QE facility developed under this work, to within a maximum error of  $\pm 9.6\%$  ( $< 10\%$  was desired).
- Data points were plotted alongside the modelled QE curve for the CCD247 that was assumed to have been fabricated on 8 k $\Omega$  cm bulk p-type silicon. Due to the similarity between the data points and the model a device depletion of 93  $\mu\text{m}$  and 295  $\mu\text{m}$  is believed for the CCD247 when substrate potentials of 0 V and -100 V are applied respectively. This method provides a closer agreement with the theoretical depletion depth than the spread event method presented in Chapter 6.
- An improvement in QE was shown for the higher energies ( $> 5$  keV), with an increase of  $\sim 70\%$  at 10 keV compared to that of the EPIC-MOS devices onboard XMM-Newton. Demonstrating the suitability of high-resistivity bulk silicon technology in future CCD based X-ray missions.

Further work would include adapting the QE facility to measure future devices in the MOS CCD development programme for XEUS. This would include extending the energy range of calibration lines, particularly to lower energies down to carbon/oxygen (277/525 eV) using low energy electron gun and monochromator as the source of X-ray photons. This will enable the

QE of thin and open electrode technologies to be evaluated. Other new detectors such as the family of swept charge devices (SCDs) could also be evaluated as they will have a different QE curve due to their inverted mode operation.

The experimental downtime ( $\sim 3.5$  hrs), experienced whilst changing the XRF target, could be significantly reduced by replacing the target box with one that includes a rotational target wheel, allowing multiple XRF targets to be positioned into the beam. Due to the translation of the target box assembly during operation, the target wheel could not be rotated by a traditional vacuum feed-through. Therefore a stepper motor unit would be required to sit inside the target box and rotate the wheel between samples when required. The stepper motor would have to be suitable for vacuum applications (no out-gassing of lubricants and components).

By including a rotational target wheel, the QE facility could be further enhanced to allow for optical QE measurements. This could be achieved by including a mirror surface on the target wheel that would reflect light onto the detectors from a band-pass light filtered source entering the vacuum chamber from the opposite port to that used for the X-ray beam. A second reference detector, such as calibrated photodiode, would be required to take the relative flux measurements, as the beryllium window blocks the optical wavelengths.

#### 9.4 High throughput video processing ASICs

The 4-channel CDS ASIC designed by J. Calafell in collaboration with STFC was characterised in terms of noise equivalent signal and channel cross-talk. Some of the key findings from this work were as follows:

- The 4-channel CDS ASIC was measured to contribute a noise equivalent signal of  $< 5 e^-$  r.m.s. to the system when operated at a read out of  $\sim 100$  k pixels per second. It is believed that the ASIC will perform with an acceptable  $< 10 e^-$  r.m.s. for pixel rates up to 500 kHz, due to the nature of the clamp and sample technique employed by the ASIC.
- The isolation between channels within the 4-channel ASIC was measured on average to be greater than 800:1. This is sufficient isolation for use with multiple X-ray CCD video channels. At this level of isolation, if one channel measures the charge generated by one 5,898 eV X-ray photon, any potential cross channel pickup would be equivalent to a maximum of  $2 e^-$  r.m.s. This is far lower than the  $1\sigma$  noise that has been measured for the X-ray camera system ( $\sim 8 e^-$  r.m.s.) For such an X-ray detection

system a  $5\sigma$  threshold is typically used, therefore any cross channel pickup is truly in the noise.

- The performance confirms the 4-channel CDS ASIC's suitability for X-ray photon counting spectroscopy, hence the reduced size and mass of this multiple channel ASIC would be of great benefit to any space based X-ray CCD focal plane array such as that proposed for XEUS.
- The sample and hold CDS technique employed by the ASICs allowed some high frequency noise signal of amplitude  $\pm 20$  mV on the video signal to be sampled during CDS. This effect was reduced by re-routing and shortening connections to the ASIC, although could not be entirely eliminated. A dual slope integrator design would be less susceptible to the effects of this high frequency noise as the reference level and charge packet samples are effectively an average of samples over a short time. Therefore any repetitive high frequency signal occurring during the integration time would appear in both samples and be removed by CDS.

Further to the work undertaken, measurements of the 4-channel CDS ASIC noise component could be obtained at pixel frequencies of 150 kHz to 1 MHz and without using the pre-amplifier on the CCD headboard. It would also be beneficial to incorporate a 16-bit ADC into the evaluation board to minimise the analogue signal path, reducing the effect of the high frequency noise pickup.

Further work would also characterise the performance of the Mk8 CDS/ADC ASIC in terms of noise equivalent signal by energy calibration with X-ray photons.

"This thesis has been completed on Veteran, Legendary and Insane" D.R. Smith, 2008